

# **An Investigation of Fine Structure Effects in CCDs developed for JET-X**

**by**

**Adam Keay**

A Thesis submitted to the University of Leicester for the degree of Doctor of Philosophy

September 1997

X-Ray Astronomy Group  
Department of Physics and Astronomy  
University of Leicester

UMI Number: U103779

All rights reserved

INFORMATION TO ALL USERS

The quality of this reproduction is dependent upon the quality of the copy submitted.

In the unlikely event that the author did not send a complete manuscript and there are missing pages, these will be noted. Also, if material had to be removed, a note will indicate the deletion.



UMI U103779

Published by ProQuest LLC 2013. Copyright in the Dissertation held by the Author.  
Microform Edition © ProQuest LLC.

All rights reserved. This work is protected against  
unauthorized copying under Title 17, United States Code.



ProQuest LLC  
789 East Eisenhower Parkway  
P.O. Box 1346  
Ann Arbor, MI 48106-1346

## **Declaration**

I hereby declare that no part of this thesis has been previously submitted to this or any other University as part of the requirements for a higher degree. Work described here was conducted by the undersigned except for the contribution of colleagues indicated in the text.

Adam Keay  
September 1997

A handwritten signature in black ink, appearing to read 'Keay', with a long, sweeping underline that extends to the right.

## Dedication

This thesis is dedicated to my family, to Mops, Pops and Jamie, and, of course, to Lisa. Its difficult to say how much of this is due to the four of you but I suspect a lot of it. For Lisa, thank you for giving meaning to my whole life, without you I wouldn't, and couldn't, have completed such a piece of work. **Thank you for everything.** For my Mum, Dad and Brother, thank you for all your help, support and encouragement throughout my degree and PhD. **You all know how important you are to me.**

## Acknowledgements

I extend my thanks firstly to my supervisor, Alan Wells, for giving me the opportunity to carry out this thesis and for all his help and advice. Thanks to Alan Owens whose drive and determination ensured that the synchrotron investigations of CCDs were carried out and who helped me prepare papers for publication. Thanks must also go to Kieran McCarthy for his help during the synchrotron campaigns and for his gentle advice. Thanks also to all the technical staff at Leicester, especially Tony and Dave, for all their help.

For all the "pleasures" of undertaking my PhD, none can compare with the two most important: football and the coffee club. As much as anything else football has helped me keep a sense of perspective during the PhD. As a famous man said, "you don't have to break the net to score a goal". The coffee club has provided the friends to talk to and the time in which to talk (and mince pies and sherry at christmas, of course). I would like to thank John (longest serving member and co-footballer), Andrew, Mike and Gillian (who brought a hitherto unknown, refined quality to coffee break discussions). To Rick, a late arrival, who made us realise how different Americans are from us Brits. Thanks to Jo who made work less pants than it could have been, for unfailingly bearing the brunt of our vegetarian jokes, for games of tennis, for DESY (!) and for making the coffee. To Nick for the (relatively) intelligent conversation, for the mutant courgettes, for a shared love of films and for always looking suitably Sea-Devil'y. To Chris for being Chris a.k.a. Dr. X, for helping out (sometimes) and always running for his phone. To Sarah and Ian for games of bridge and polite company. To Jason for making Daresbury night-shifts bearable, for Fantasy Football and for our football chats. Finally to Alex and Helen for (in no particular order) Bridge, films, Hi-Fi, music, Beavis and Butt-Head (huh! huh!), christmas films and mulled wine, Lord of the Rings ("I am Gandalf, see"), coffee that was even more lethal than usual, getting married and deliberately taking longer over the PhD to make me feel better. **Most importantly, thank you all for friendship.**

## List of Publications

Some of the work included in this thesis has been incorporated in the following papers.

1. "Exploring macroscopic surface structures on x-ray CCDs using silicon absorption edge quantum efficiency measurements",  
A. Keay, A. Owens, S. Gurman, G. Fraser, K. McCarthy and A. Wells,  
Nucl. Instr. and Meth. **B 97** (1995) 316 - 321
2. "Mapping X-Ray Absorption Fine Structure in the quantum efficiency of an X-Ray CCD",  
A. Owens, G. Fraser, A. Keay, A Wells, K. McCarthy, S. Hill, E. Hughes, A. Smith, V. Suller and M. Surman,  
X-Ray Spectrometry **25** (1996) 33 - 38
3. "The x-ray energy response of silicon (B): Measurements",  
A. Owens, G. Fraser, A. Abbey, A. Holland, A. Keay, K. McCarthy and A. Wells,  
Nuclear Instruments and Methods **A 382** (1996) 503 - 510
4. "The Effect of XAFS in soft x-ray astronomical telescopes",  
A. Owens, M. Denby, A. Keay, A. Wells, D. Graessle and R. Blake,  
Astrophysical Journal **476** (1997) 924 - 931
5. "Investigating chemical structure in a silicon CCD using Extended X-Ray Absorption Fine Structure",  
A. Keay, A. Wells, A. Owens and K. McCarthy,  
Nucl. Instr. and Meth. **B 124** (1997) 615 - 623
6. "Escape peak ratios in silicon x-ray CCDs",  
K. McCarthy, A. Owens and A. Keay,  
Nucl. Instr. and Meth. **A 384** (1997) 403 - 409
7. "On the experimental determination of the Fano factor in silicon at soft x-ray wavelengths",  
A. Owens, G. Fraser, A. Keay and K. McCarthy,  
to appear in Nucl. Instr. and Meth. (1997)
8. "Imaging x-ray fluorescence using microchannel plate (MCP) relay optics",  
A. P. Martin and 10 co-authors  
to appear in Jour. of X-Ray Spectr. (1997)

# Abstract

Charge Coupled Devices (CCDs) are low power, robust detectors promising medium spectral resolution, high spatial resolution and a high signal to noise ratio. It is for this reason that CCDs have become the preferred focal plane detector in all x-ray astronomy missions due for launch in the 1990s and early in the next millennium. The absorption of x-rays by a CCD is modulated by the transmission of the complex electrode structures and passivation layers on its front surface. Since the path length of soft x-rays (0.1 - 2 keV) is of the same order as the thickness of these layers, fine structure in the quantum efficiency ( $Q(E)$ ) around absorption edges can have a profound influence on the response of the CCD. This thesis presents the work done in investigating fine structure effects in the  $Q(E)$  of x-ray CCDs and the impact that these effects will have on astronomy missions. The state of x-ray astronomy as we move into the CCD-mission era is reviewed in Chapter 2. The operation of a CCD as an x-ray detector is then described. The extensive set of experiments carried out at the Daresbury Synchrotron Radiation Source (SRS) to map the  $Q(E)$  of JET-X CCDs are detailed, including a description of the first use of the new, low beam current mode of SRS operation. Chapter 5 describes the origins and expression of X-ray Absorption Fine Structure (XAFS) in the CCD response. The instruments that make up the JET-X Focal Plane Cameras are then reviewed. In Chapter 7 the importance of calibrating JET-X accurately is shown by analysing the impact of XAFS in the detector sub-systems. It is shown that XAFS threaten the scientific return from current and future x-ray astronomy missions. In Chapter 8 the information contained by the fine structure in the CCD  $Q(E)$  is extracted and analysed to obtain the thickness and structure of the inert layers on the surface of the CCD, and also to improve models of the CCD response. Finally the work is summarised and additional further work is suggested.

# Contents

<b>1 Introduction</b>	<b>1</b>
1.1 X-Ray Astronomy and CCDs .....	1
1.2 Thesis Organisation.....	5
<b>2 X-Ray Astronomy and CCDs</b>	<b>7</b>
2.1 Introduction.....	7
2.1.1 Background.....	7
2.1.2 X-ray spectroscopy.....	9
2.2 X-Ray Astronomy before CCDs detectors .....	11
2.2.1 The gas counter.....	14
2.2.2 Einstein .....	15
2.2.3 BBXRT.....	16
2.3 X-Ray Astronomy with CCDs.....	17
2.3.1 Introduction .....	17
2.3.2 ASCA.....	17
2.3.3 AXAF.....	18
2.3.4 SPECTRUM XG.....	19
2.3.5 XMM .....	19
2.3.6 ASTRO-E.....	20
2.3.7 ABRIXAS.....	20
2.4 Conclusions .....	21
<b>3 The production, operation and testing of CCDs</b>	<b>22</b>
3.1 Introduction.....	22
3.2 CCD detectors.....	22
3.2.1 Introduction .....	22
3.2.2 CCD production .....	22
3.2.3 Charge storage.....	24
3.2.4 Charge coupling.....	25
3.2.5 Charge measurement .....	27
3.2.6 Noise.....	28
3.3 The JET-X CCD design.....	30
3.4 CCD operation.....	32
3.4.1 The CCD cryostat .....	32

3.4.2 Drive electronics .....	34
3.4.3 Software .....	35
3.5 The JET-X calibration facility .....	38
3.5.1 Introduction .....	38
3.5.2 X-ray production.....	39
3.6 The use of the SRS.....	41
3.6.1 Introduction .....	41
3.6.2 Low beam current mode.....	42
<b>4 Synchrotron Investigations of X-Ray CCDs</b>	<b>43</b>
4.1 Introduction.....	43
4.2 First Tests.....	43
4.2.1 Introduction .....	43
4.2.2 Devices .....	43
4.2.3 Experimental Set-Up .....	45
4.2.4 Results .....	47
4.2.5 Discussion .....	51
4.3 Low Energy Tests .....	51
4.3.1 Introduction .....	51
4.3.2 Devices .....	52
4.3.3 Experimental Set-Up .....	54
4.3.4 Results .....	57
4.3.5 Discussion .....	64
4.4 Extended Energy Range, Si K Edge Tests .....	65
4.4.1 Introduction .....	65
4.4.2 Devices .....	66
4.4.3 Experimental Set-Up .....	66
4.4.4 Results .....	67
4.4.5 Discussion .....	69
4.5 Conclusions .....	69
<b>5 X-ray Absorption Fine Structure</b>	<b>71</b>
5.1 Introduction.....	71
5.2 X-ray absorption.....	72
5.3 Absorption Fine Structure .....	74
5.4 Extended X-ray Absorption Fine Structure .....	76
5.5 X-ray Absorption Near-Edge Structure .....	78
5.6 “White lines” and edge shifts.....	78
5.7 Heuristic derivation of the EXAFS function, $\chi(E)$ .....	79



<b>6 The JET-X Focal Plane Cameras</b>	<b>83</b>
6.1 Introduction.....	83
6.1.1 JET-X.....	83
6.1.2 Status of JET-X .....	86
6.2 Instrumental performance.....	86
6.2.1 Mirror system.....	87
6.2.2 The x-ray filters.....	91
6.2.3 The x-ray detectors.....	93
6.3 The instrument response matrix .....	96
6.3.1 CCD redistribution matrix.....	97
6.3.2 Telescope response.....	98
6.4 In-orbit calibrations .....	100
6.5 Conclusions .....	100
<b>7 XAFS and the interpretation of astronomical x-ray sources</b>	<b>101</b>
7.1 Introduction.....	101
7.1.1 Calibration of JET-X .....	102
7.1.2 Future missions.....	102
7.2 Modelling.....	104
7.2.1 Introduction .....	104
7.2.2 XSPEC .....	104
7.3 Results .....	107
7.3.1 The effect of Si K edge XAFS on deconvolved cosmic x-ray spectra .....	107
7.3.2 Further results of modelling.....	109
7.4 Discussion.....	112
<b>8 Investigating the composition and structure of materials in an x-ray CCD</b>	<b>116</b>
8.1 Introduction.....	116
8.2 Utilising XANES in the Q(E) to investigate an x-ray CCD .....	117
8.2.1 Measurements of near-edge structure.....	117
8.2.2 Phenomenological interpretation of near-edge structures.....	119
8.2.3 A more detailed analysis of the near-edge structure .....	121
8.2.4 Results .....	123
8.2.5 Deductions from this analysis .....	125
8.3 Analysis of chemical structures using EXAFS .....	127
8.3.1 Reducing CCD Q(E) to inactive layer absorption .....	127
8.3.2 Extracting and analysing the EXAFS signal.....	130
8.3.3 Results.....	131
8.3.4 Deductions about structural chemistry from the best-fit analysis .....	133

8.4 Discussion.....	134
<b>9 Conclusions and future work</b>	<b>136</b>
9.1 Conclusions .....	136
9.2 Future work .....	138
<b>10 Bibliography</b>	<b>140</b>

*“This animal, common in the north... its eyes are scarlet and its fur jet black... it is marked by a curious instinct - the taste for... ink. When a person sits down to write, the monkey squats cross-legged near by with one forepaw folded over the other, waiting until the task is over. Then it drinks what is left of the ink, and afterwards sits back on its haunches, quiet and satisfied.”*

Wang Tai-Hai (from “The book of imaginary beings” by J. L. Borges)

*“The will to truth, which is still going to tempt us to many a hazardous enterprise... What questions this will to truth has already set before us! What strange, wicked and questionable questions! It is already a long story - yet does it not seem as if it has only just begun?”*

F. Nietzsche

*It is better to light one candle than to curse the darkness*

Adage

# 1

## Introduction

### 1.1 X-Ray Astronomy and CCDs

The last four decades have seen x-ray astronomy develop into one of the most important fields in astrophysics. The first minute-long experiments used simple recording devices with crude collimators and only set out to discover if there were x-ray sources in the sky. Since the discovery of Scorpius X-1 in 1962, the number of known x-ray sources has risen from three (the Sun, the x-ray background and Sco X-1) to over one hundred thousand. During this period, x-ray astronomical experiments have developed into large observatories, capable of observing the sky with arc second spatial resolution using high spectral resolution detectors over lifetimes measured in years. At the present time high resolution detectors, high quality mirrors and other technological developments promise the ability to observe the x-ray universe in unparalleled detail.

The recent improvement in instrument sensitivity and resolution has gone hand in hand with the maturing of x-ray astronomy as an observational science. As the power to measure the astrophysical properties of cosmic x-ray sources is realised, theoretical models are continually improved. High resolution x-ray spectroscopy gives access to the huge amount of information contained in x-ray spectral lines which dominate the x-ray emission of hot, optically thin astrophysical plasmas. These spectral lines reflect the density, elemental abundance, temperature distribution, ionisation state and velocity associated with the hot, emitting gas. Gas at temperatures from  $10^6$  K to  $10^8$  K is found in sources ranging in scale from stellar coronas to clusters of galaxies, and in active galactic nuclei (AGN), supernovae remnants and accretion disks surrounding compact objects. Cosmic x-rays are also thought to arise from synchrotron radiation, from electron-photon collisions and from energy transitions in excited atomic nuclei. It is clear therefore why x-ray spectroscopy has become a prime objective of virtually every major mission that is currently being built or is planned for the future. This ensures that x-ray astronomy missions will account for a significant fraction of the total resources that the world will devote to astronomy over the next two decades [Gorenstein & Zombeck, 1990].

The introduction of CCDs to the field of x-ray astronomy in the last ten years has led to the possibility of carrying out spectroscopy across the whole of the XUV/soft x-ray bands with positional and spectral resolutions better than 30 arcsecs and 5% FWHM, respectively. This has been a significant step forward since these figures are at least a factor of ten better than those obtained with current detection systems which employ position

sensitive proportional counters (PSPCs), scintillators or microchannel plates. Largely because of the inability of gas and scintillation counters to resolve predicted structure in the x-ray spectra of astrophysical sources, x-ray astronomy has been quick to take advantage of CCD detectors. Around the middle of the 1980s it was realised that the energy resolution of silicon could be combined with the imaging capability of a CCD to provide both high spatial and high spectral resolution [Chowanietz, 1986]. When coupled with the advantages of semiconductor technology, such as low power, robustness and high signal-to-noise ratio, the benefits of CCDs promise to be pervasive and potentially very important. As a result, CCDs have emerged as the preferred detectors in all major x-ray missions due for launch in the 1990's [Weisskopf, 1987; Wells, 1988; Bignami, 1990; Inoue, 1992].

The CCD concept can ultimately be traced to two workers at Bell Laboratories, Willard S. Boyle and George E. Smith. During the late '60s Boyle and Smith were investigating silicon as a potential imaging material when the idea of an electric analogue to the magnetic bubble memory (*i. e.* charge-coupling) was first conceived. The paper detailing their work began, "A new semiconductor device concept has been devised which shows promise of having wide application" [Boyle, 1970]. Initially it was thought that CCDs would find many uses in the field of electronics, especially in computer memories, but the invention of solid state memory chips, which were cheaper and faster, prevented this. In the early years many astronomy and space science groups provided a useful stimulus in the pioneering development of CCDs.

The first astronomical CCD images were obtained by Jim Janesick and Fred Landauer of the Jet Propulsion Laboratory and Bradford Smith at the University of Arizona. Particularly impressive were the "doughnut-like", limb-brightened images of Uranus through a methane-band filter; images which showed for the first time the superior potential of CCDs over other imaging equipment [McLean, 1994]. Since those early years the CCD has virtually replaced optical imaging technologies such as Vidicon tubes, photographic plates and other solid-state technologies such as interline transfer devices (ITD) or charge injection devices (CID). CCDs have been used to image everything from planets, satellites and comets to galaxies and gravitationally lensed quasars.

There is now a plethora of CCDs for astronomical purposes. Pixel sizes reach as low as 2.5  $\mu\text{m}$ . Array sizes reach up to  $2048 \times 4096$  pixels, with a physical size of 28 mm  $\times$  55 mm [Heyes, 1997], taking up whole silicon wafers. Many improvements in CCD design have been specifically for x-ray astronomical operation and have demanded major technological innovations. For example, thinned and open electrode technologies were necessary to increase the low energy  $Q(E)$  of CCDs [Castelli, 1991]. High resistivity, deep depletion regions have increased the high energy  $Q(E)$  [Chowanietz, 1986]. Charge transfer efficiency now regularly exceeds 99.9999% and cooled, low noise performance, below 3.5 electrons rms, has been achieved. However, it is only in the last 10 years that

x-ray CCDs have been able to achieve truly Fano-optimised operation with adequate quantum efficiency.

As the sensitivity of CCD detectors improve, instrument-induced structure in their quantum efficiency becomes an increasingly significant limitation on the sensitivity of the telescope system. In particular, x-ray absorption fine structure (XAFS) effects, which are a consequence of the quantum mechanical nature of x-ray photon absorption, can appear as artefacts in the telescope response. Part of this thesis will argue that XAFS will be important for all current and future x-ray astronomy missions based on semiconducting or superconducting technologies.

The work in this thesis is mainly carried out on CCDs being developed for the JET-X project. JET-X [Wells, 1990] is to be the link between the successful science missions of the 1980s and the large science missions due to be launched at the end of the 20th century and at the beginning of the next millennium. JET-X is one of three core instruments, JET-X, SODART [Schnopper, 1990] and MOXE [Priedhorsky, 1989], which comprise the science payload of the Russian Spectrum Roentgen-Gamma (SRG) mission [Cruise, 1990]. The Spectrum series of Automated Space Vehicles form the cornerstone of the CIS' astrophysics program and continue the line of successful Soviet satellites such as ASTRON [Babichenko, 1990], KVANT [Sunyaev, 1990] and GRANAT [Roques, 1990].

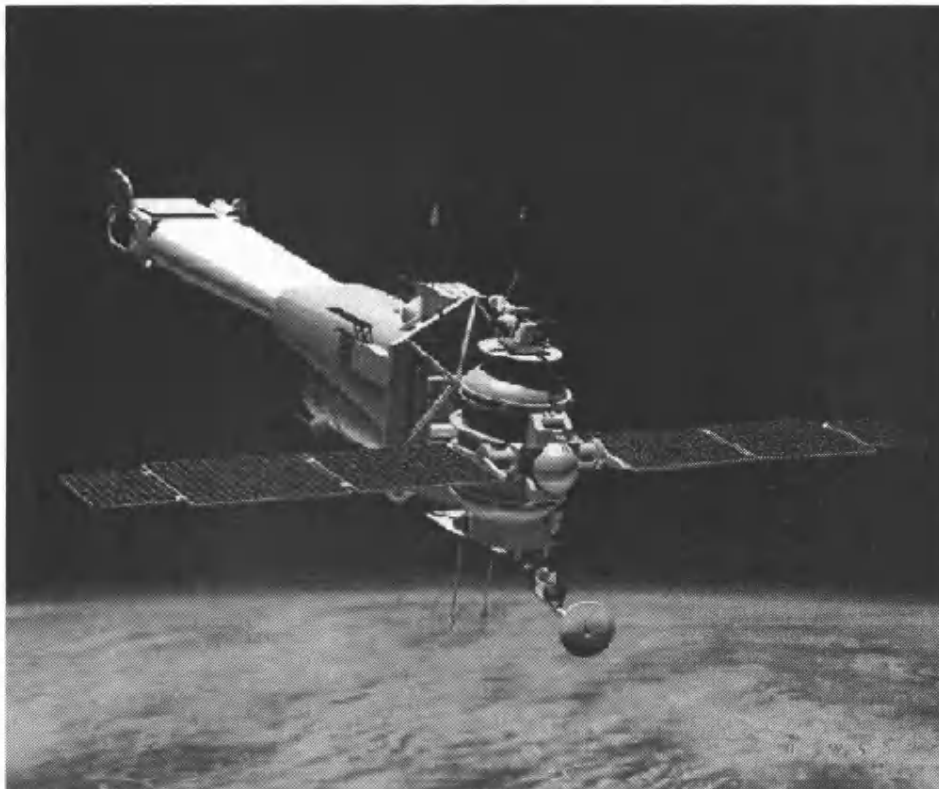


**Figure 1.1** Spectrum Xr

The Joint European X-ray Telescope (JET-X) is currently scheduled to be launched aboard SRG in December 1998.

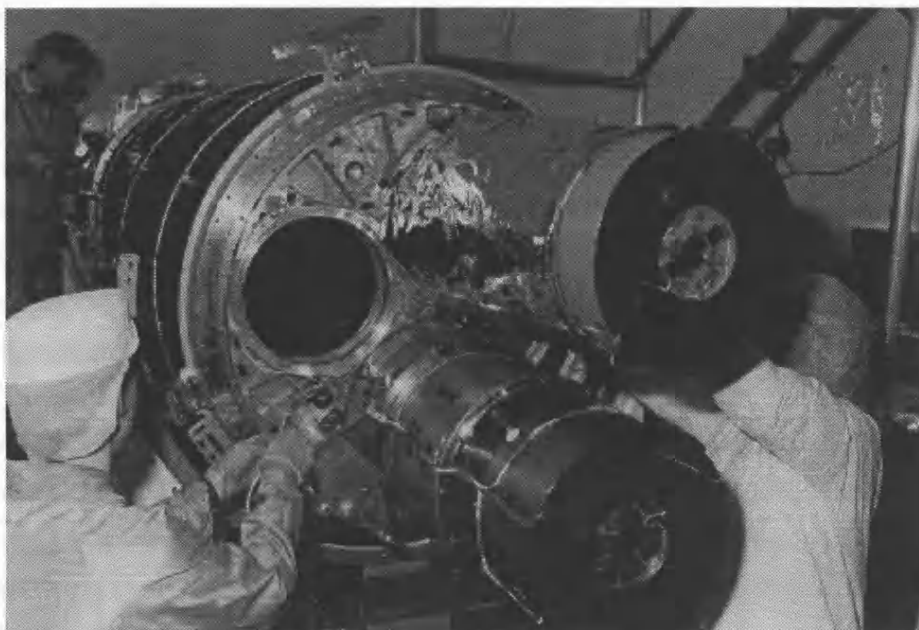


**Figure 1.2** A JET-X engineering model telescope in the clean room at Leicester

JET-X will utilise Wolter I mirror technology with Si CCD detectors at the focal plane. The core science will include x-ray spectroscopy of medium/bright sources and imaging of extended, low surface brightness regions.

The spacecraft will be launched from the Baikonur launch facility in Kazakhstan aboard a PROTON rocket. After separation and injection into a phasing orbit, the spacecraft will execute a double lunar swing-by before being moved into a highly elliptical orbit, with a perigee of  $\sim 6,000$  km evolving to  $40,000$  km after 6 months and an apogee of  $200,000$  km. It will have a  $51.5^\circ$  inclination and an orbital period of  $\sim 4$  days. These orbital parameters ensure SRG will provide an ideal platform for JET-X from both a scientific and engineering point of view [JET-X/FDR (1995)].

For such a high apogee orbit there will be no shielding from solar flares and galactic cosmic ray protons by the Earth's magnetic field. JET-X will therefore encounter the trapped radiation belts where proton fluxes reach values of  $2 \times 10^5 \text{ cm}^{-2}\text{s}^{-1}$  above  $10 \text{ MeV}$  at  $\sim 1.8 R_e$  along the plane of the geomagnetic equator. For the nominal SRG orbit, values of  $\sim 10^3 \text{ cm}^{-2}\text{s}^{-1}$  may be expected for short intervals during solar flares. Out of the belts ( $> a \text{ few } R_e$ ) the primary contribution to the ambient background are the solar-cycle modulated galactic cosmic rays, which at solar minimum, have an integral fluence of  $\sim 4 \text{ cm}^{-2}\text{s}^{-1}$  above  $10 \text{ MeV}$ . The calculated total dose (including 2 large solar flares) is  $\sim 8 \text{ krad}$  over three years, as opposed to a few krad per year expected in a typical  $28^\circ$  inclination,  $500 \text{ km}$ , low Earth orbit [Owens, 1992].

The prime up-link facility will be located at Kalyazin and the down-link at Bear Lake, both on the outskirts of Moscow. The main elements of the Ground System are:

- The Ground Station which will handle direct contact with the spacecraft

- The ‘Quick Look Facility’ (QLF) which will perform quick look analysis, command procedure generation, health monitoring, and act as the JET-X consortium interface with IKI.
- The UK Data Centre for routine processing and distribution of JET-X data.
- The Instrument Analysis Centre, at Leicester University, for full and long-term health and performance monitoring of the JET-X instruments, JET-X calibration, science analysis and large-scale background analysis.
- Consortium Institutes in the UK and non-UK for scientific analysis, interpretation and archival of the observation database.

Data will be telemetered to the ground station during the perigee pass where they can be sorted and formatted by the Quick Look Facility before being transferred to the UK Data Centre for processing and distribution. During the down-link, commands defining the instrumental configuration will also be uploaded for the next observation period. It is anticipated that the mission lifetime will be approximately 5 years.

The JET-X project, led by Leicester University, is being developed by many groups around the world, including, the University of Birmingham, the Rutherford Appleton Laboratory, the Mullard Space Science Laboratory, ESTEC in Holland, the Institute for Space Research in Russia and CNR and the Universities of Milan, Rome and Palermo in Italy.

## 1.2 Thesis Organisation

Previous theses on CCD studies within the group at Leicester have included; the work of Lumb [Lumb, 1983] in which the feasibility of detecting x-rays with conventional video CCDs was investigated, the work of Chowanietz [Chowanietz, 1986] in which the impact of high resistivity silicon was investigated, the work of Holland [Holland, 1990] which investigated developments of the CCD for space applications including radiation damage effects and the work of Castelli [Castelli, 1991] which was an investigation of the soft x-ray response of CCDs.

The work in this thesis continues the CCD theme with more detailed investigations of the x-ray performance of CCDs. The main aims include: the detailed measurement of the detection efficiency of the CCDs, the investigation of the impact in x-ray astronomy of fine structure effects in the telescope response and the derivation of structural information from absorption fine structure in the CCD response.

The thesis is organised into 9 chapters, including this introduction. Chapter 2 is a summary of the state of x-ray astronomy as we move into the CCD era. In particular an attempt is made to place the arrival of the CCD, as an important focal plane, x-ray detector, into context. This includes summarising previous missions using detectors based on alternative technologies, and a survey of the missions at the end of the 20th century which will



use CCDs. Chapter 3 describes the use of CCDs as x-ray detectors with emphasis on the way in which CCDs are tested, and the requirements for the JET-X CCDs, which have led to the synchrotron calibration program at the Synchrotron Radiation Source (SRS) at Daresbury. The physics behind CCD operation and manufacture are also considered.

Chapter 4 outlines in detail the aspects of the CCD calibration program that were carried out at the SRS in the period October 1993 to January 1996. Emphasis is placed on describing the experiments carried out at the two Beamlines used, Beamlines 1.1 and 3.4. The realisation that x-ray absorption fine structure (XAFS) effects are present in the CCD response and measurable when using the SRS is discussed. This leads on to the theoretical description of XAFS and other fine structure effects in Chapter 5.

The work in this thesis has been intimately linked with work for the JET-X project. Many aspects of the thesis have had a bearing on the way in which the calibration program has been carried out and will continue to be of relevance when JET-X begins collecting data (*e. g.* detector induced structure in cosmic spectra). Chapter 6 therefore summarises parts of the JET-X work that have occurred during the period October 1993 to the present day. This also provides the background and context of the work presented in Chapter 7.

Chapter 7 is a report of the significance of the pseudo-emission or -absorption features introduced in to cosmic spectra by the elements in the optical path of JET-X, particularly the CCDs. It is shown that unfolding source spectra with an over-simplified response matrix causes spectral artefacts that can at the very least limit the accuracy of model fitting procedures.

Chapter 8 is a more detailed investigation of the information contained within the fine structure associated with the CCDs. The chapter is split in to two sections; the first deals with fitting data to the CCD response in order to derive detector parameters, whilst the second shows how extended x-ray absorption fine structure (EXAFS) has been used to probe the structure of the chemicals in the overlying dead regions of the CCD.

In the final chapter, Chapter 9, the main achievements of the thesis are summarised and directions for future work are assessed.

## X-Ray Astronomy and CCDs

### 2.1 Introduction

#### 2.1.1 Background

Since the first extra-solar x-ray source, Sco X-1, was discovered in 1962 [Giacconi, 1962], the study of cosmic x-ray sources has undergone rapid expansion, and is now an essential tool in astronomy. Many excellent reviews of the history of x-ray astronomy have been published [Bradt, 1992; Pounds, 1997]. Tables 2.1 and 2.2 show missions that have studied the x-ray universe since the early years.

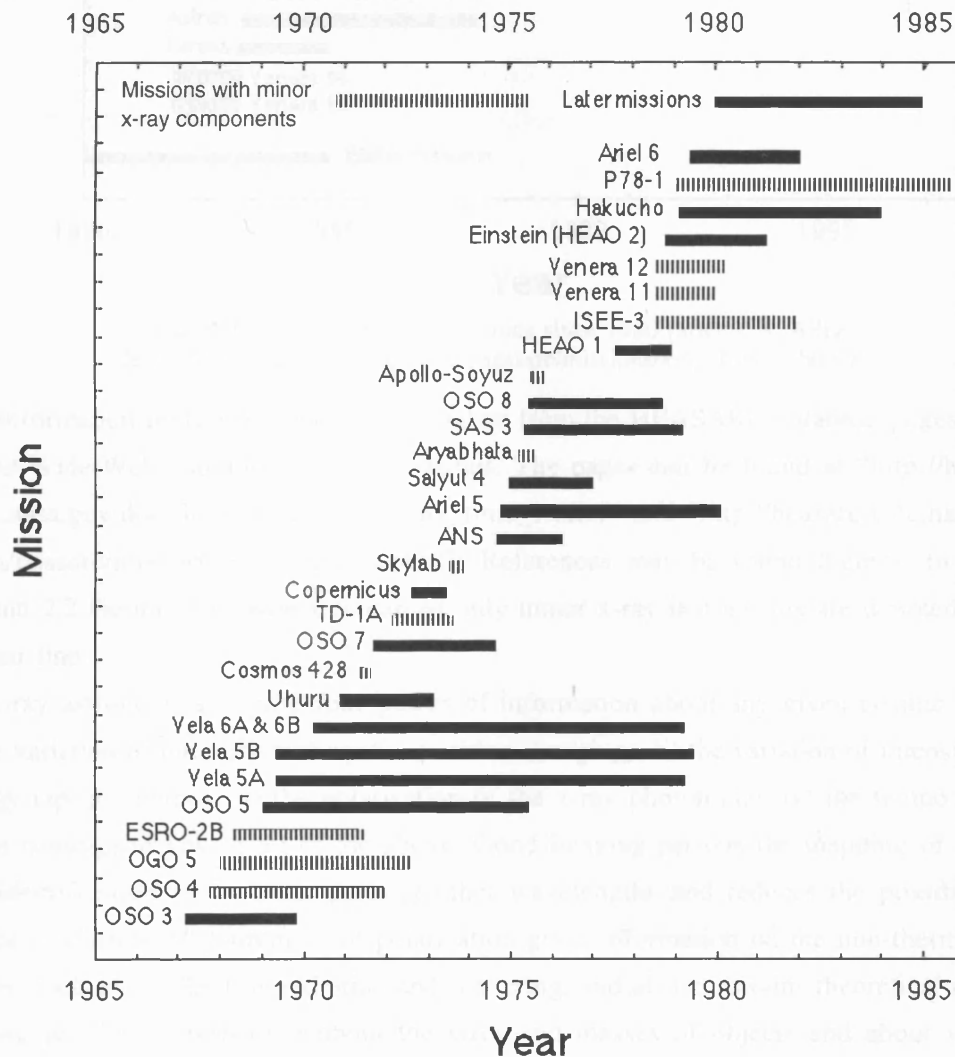


**Table 2.1** X-ray astronomy missions pre-1980 [after J. S. Allen  
([http://heasarc.gsfc.nasa.gov/docs/heasarc/missions/xray\\_time\\_1.html](http://heasarc.gsfc.nasa.gov/docs/heasarc/missions/xray_time_1.html))]

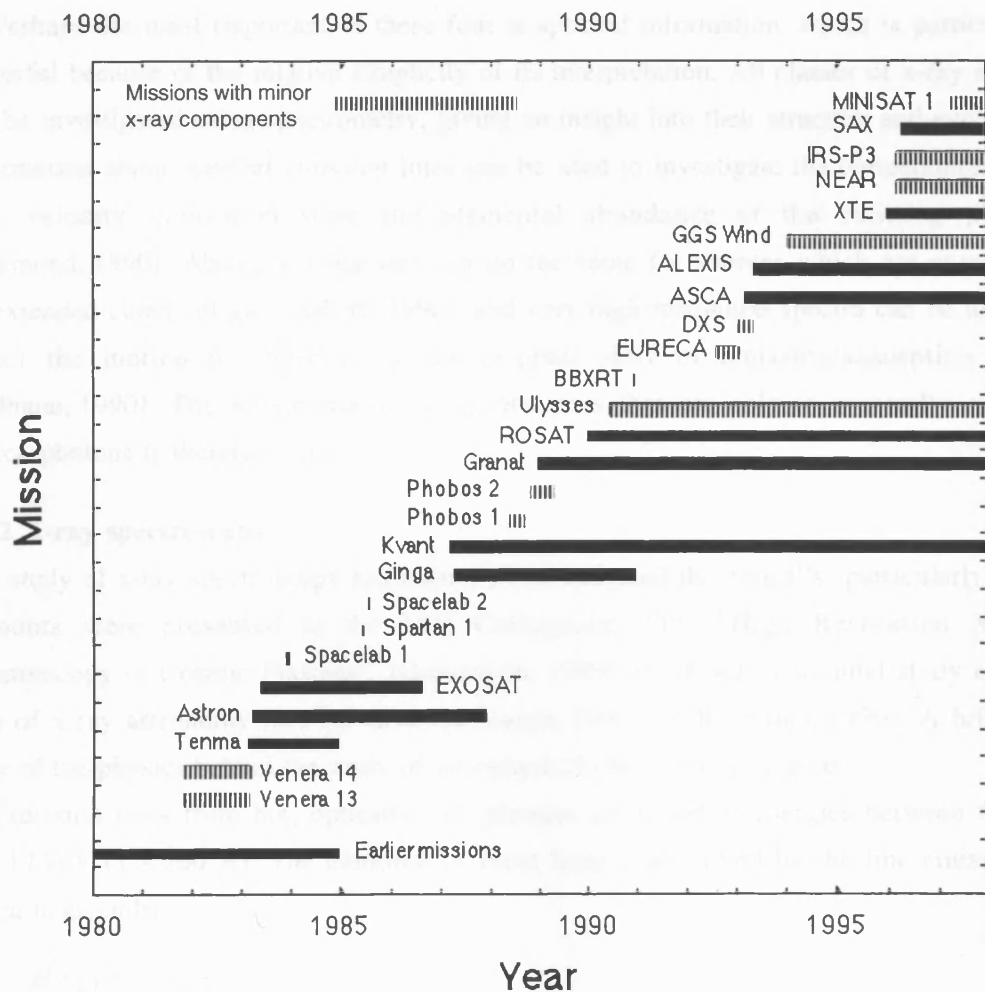


**Table 2.2** X-ray astronomy missions since 1980 [after J. S. Allen  
([http://heasarc.gsfc.nasa.gov/docs/heasarc/missions/xray\\_time\\_2.html](http://heasarc.gsfc.nasa.gov/docs/heasarc/missions/xray_time_2.html))]

The information in Tables 2.1 and 2.2 is taken from the HEASARC database pages on the World-Wide-Web maintained by J. S. James. The pages can be found at “[http://heasarc.gsfc.nasa.gov/docs/heasarc/missions/xray\\_time\\_1.html](http://heasarc.gsfc.nasa.gov/docs/heasarc/missions/xray_time_1.html)” and “[http://heasarc.gsfc.nasa.gov/docs/heasarc/missions/xray\\_time\\_2.html](http://heasarc.gsfc.nasa.gov/docs/heasarc/missions/xray_time_2.html)”. References may be found therein. In Tables 2.1 and 2.2 the missions which contained only minor x-ray instruments are denoted with a broken line.

X-ray astronomers require four pieces of information about any given cosmic source: i) the variation of intensity with spatial position (imaging), ii) the variation of intensity with energy (spectrometry), iii) the polarisation of the x-ray photon and, iv) the temporal evolution (timing) of any or all of the above. Good imaging permits the mapping of regions and identification with counterparts at other wavelengths and reduces the possibility of source confusion. Measurement of polarisation gives information on the non-thermal processes, such as synchrotron radiation and scattering, and also constrains theoretical models. Timing provides information about the sizes and masses of objects and about variable phenomena such as pulsars and the orbital parameters of binary systems.

Perhaps the most important of these four is spectral information, which is particularly powerful because of the relative simplicity of its interpretation. All classes of x-ray source can be investigated using spectrometry, giving an insight into their structure and evolution. Information about spectral emission lines can be used to investigate the temperature, density, velocity, ionisation state and elemental abundance of the emitting plasma [Raymond, 1990]. Absorption features can do the same for sources which are enveloped by extended clouds of gas [Haberl, 1990], and very high resolution spectra can be used to detect the motion of sources via the Doppler shift of emission/absorption lines [Culhane, 1990]. The importance of x-ray detectors that are able to spectrally resolve source photons is therefore clear.

### 2.1.2 X-ray spectroscopy

The study of x-ray spectroscopy has been well investigated theoretically, particularly good accounts were presented at the IAU Colloquium 115, “High Resolution X-Ray Spectroscopy of Cosmic Plasmas”, [Gorenstein, 1990] which was a seminal study of this area of x-ray astronomy [see for instance Mason, 1990 and Raymond, 1990]. A brief review of the physics behind the study of astrophysical plasmas is now given.

Emission lines from hot, optically thin plasmas are found at energies between 60 eV and 12 keV (1 - 200 Å). The emission of these lines is described by the line emissivity, which is given by

$$\epsilon(\lambda_{ij}) = N_j A_{ji} \frac{hc}{\lambda_{ij}} \quad 2-1$$

where  $\epsilon(\lambda_{ij})$  is measured per unit volume and per unit time.  $A_{ji}$  is the probability of a spontaneous transition between levels  $j$  and  $i$ ,  $h$  is Planck's constant,  $c$  is the velocity of light and  $\lambda_{ij}$  is the wavelength of the transition  $i$  to  $j$ .  $N_j$  is the number density of level  $j$  and is given by

$$N_j(X^{+m}) = \frac{N_j(X^{+m})}{N(X^{+m})} \frac{N(X^{+m})}{N(X)} \frac{N(X)}{N(H)} \frac{N(H)}{N_e} N_e \quad 2-2$$

where the first term on the right describes the population of level  $j$  relative to the total population of the ion species  $X^{+m}$ . The second term in Equation (2-2) describes the ionisation ratio of the  $X^{+m}$  species relative to the total number density of element  $X$ . The third is a measure of the abundance of element  $X$  relative to hydrogen and the fourth is the relative abundance of hydrogen.  $N_e$  is the electron number density. In Equation (2-2), term 1 is a function of temperature and electron density, term 2 depends on temperature alone and term 3 is usually taken to be a constant [Mason, 1990]. The intensity of a particular line, which is given by

$$I(\lambda_{ij}) = \int_V \epsilon(\lambda_{ij}) dV \quad 2-3$$

can be rewritten as

$$I(\lambda_{ij}) = \int_V \left[ \frac{N_j(X^{+m})}{N(X^{+m})} \frac{N(X^{+m})}{N(X)} \frac{N(X)}{N(H)} \frac{N(H)}{N_e} N_e A_{ji} \frac{hc}{\lambda_{ij}} \right] dV \quad 2-4$$

which, in the simple case of a two level ion in coronal equilibrium, can be simplified to

$$I(\lambda_{ij}) = \int_T G(T) \phi(T) dT \quad 2-5$$

where  $\phi(T)$  is a measure of the distribution of material as a function of temperature, called the differential emission measure [Mason, 1990].

Using the above equations the characteristics of the emitting plasma may be analysed from spectral line measurements. The intensity of a line depends on the temperature, density and elemental abundance of the plasma. The relative abundance of two or more lines can also be used as a diagnostic of plasma temperature, electron density and equilibrium state [Mason, 1990]. Emission line width, shift and asymmetry, are functions of plasma temperature as well as micro-turbulence and waves.

An example of a representative emission line spectrum can be seen in Figure 2.1.

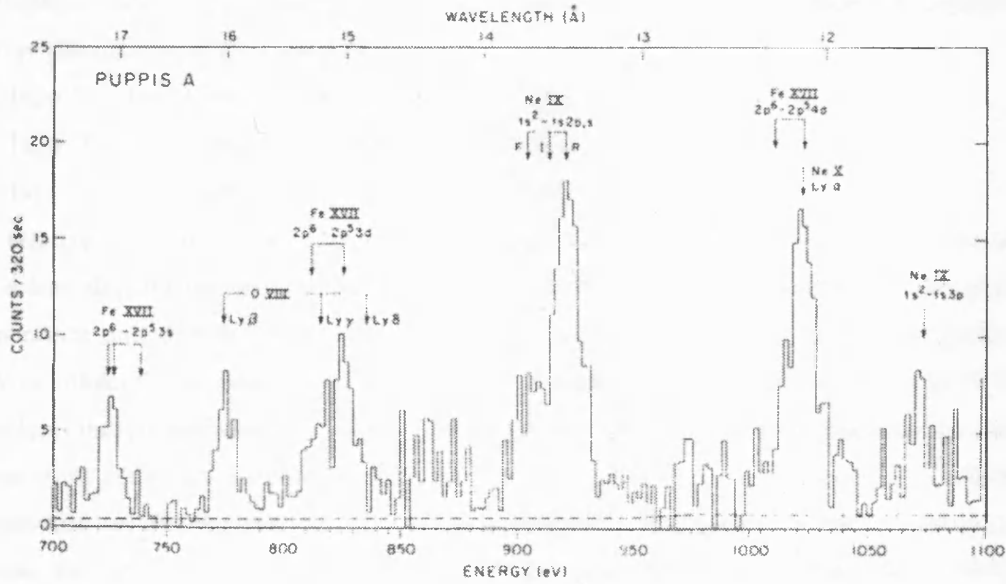


**Figure 2.1** The FPCS spectrum of Puppis A [Winkler *et. al.* 1981]

Figure 2.1 shows the Einstein Focal Plane Crystal Spectrometer (FPCS) spectrum of the highly ionised Fe lines in the range 700 eV to 1100 eV from Puppis A. The Fe XVII lines are clearly resolved.

The He-like ion emission lines are a typical diagnostic of cosmic plasmas [Mason, 1990]. In general, the H-like and He-like ions in plasmas have been well studied and there are extensive theoretical calculations providing excitation rates that are understood to the 10 - 20% level [Raymond, 1990]. Thus, at temperatures of around  $10^7$  K the strongest emission lines in cosmic plasmas, from O (VII and VIII), Si (XIII and XIV) and

Fe (XXV and XXVI), are also the easiest to interpret. The ratios of the forbidden, resonance and intercombination lines of He-like ions are especially useful [Gabriel and Mason, 1982]. Figure 2.2 shows a schematic energy level diagram of an He-like ion [adapted from Warwick, 1994].

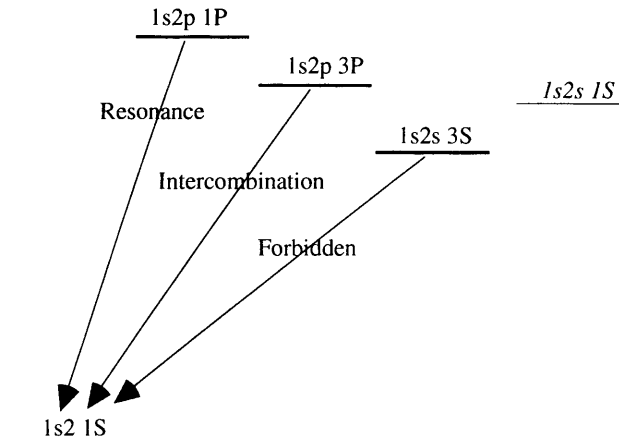


**Figure 2.2** A schematic diagram of the energy levels in an He-like ion [after Warwick, 1994]

Transitions from the  $n=2$  state to the ground state in He-like ions which are commonly used as plasma diagnostics are [Holt, 1990]:

- $1s2p\ ^1P - 1s^2\ ^1S$  which forms the resonance line,  $r$
- $1s2p\ ^3P - 1s^2\ ^1S$  which forms the intercombination line,  $i$
- $1s2s\ ^3S - 1s^2\ ^1S$  which forms the forbidden line,  $f$ .

The relative strengths of the forbidden and intercombination lines compared to the resonance line depend on the populations of each of the upper levels and hence the plasma temperature and density [Canizares, 1990]. The  $1s2p\ ^3P$  and  $1s2s\ ^3S$  levels are preferentially populated by recombination (electron + ion  $\rightarrow$  photon + atom) while the  $1s2p\ ^1P$  state is preferentially populated by collisions [Canizares, 1990]. Since the recombination rate is temperature sensitive [Canizares, 1990], the ratio  $(i+f)/r$  is a useful monitor of electron temperature. In He-like ions the  $^3S$  level is collisionally de-excited so that in high density plasmas the ratio  $f/i$  is a sensitive measure of plasma density [Schmitt, 1990; Holt, 1990].

## 2.2 X-Ray Astronomy before CCDs detectors

As with other areas of observational science, the expansion of knowledge in x-ray astronomy has been, and continues to be, dependant on advances in detector science. The evolution of detectors for x-ray astronomy and their use has been thoroughly reviewed in numerous sources. Good examples may be found in Fraser's book [Fraser, 1989] and the paper by Ramsey, Austin and Decher [Ramsey, 1994].

Name and Lifetime	Detector systems	Detector parameters	Energy	Science
SAS-1 (Uhuru) Dec 1970 - Mar 1973	Two Be-window, collimated proportional counters	-	2-20 keV	Sky survey of 150 x ray sources
Arrel V Oct 1974 - Mar 1980	1. Rotational Modulation Collimator (RMC) 2. High resolution proportional counter 3. Polarimeter/Spectrometer 4. Scintillator telescope 5. All sky monitor 6. Sky survey prop. counter	- 2. 128 pulse height channels 3. 3% sensitivity (polarisation) 5. 1cm <sup>2</sup> pinhole camera	1. 0.3 - 20 keV 2. 2 - 30 keV 3. 2 - 8 keV 4. 40 keV 5. 3 - 6 keV 6. 1.5 - 20 keV	Long period pulsars, black hole candidates, Seyfert I galaxies, 250 x-ray sources
SAS-3	1. Five collimators 2. A gas flow, low energy detector 3. Three tube collimators	1. Spatial res. better than 2' - -	1. 0.15 - 1 keV 2. 0.15 - 60 keV	Precise locations of ~60 x-ray sources and a dozen x-ray bursts
OSO-8 Jun 1975 - Sep 1978	1. Cosmic X-ray Spectrometer 2. High Energy Celestial X-ray Experiment 3. Soft X-ray Background Radiation experiment	- - -	1. 2 - 60 keV 2. 0.01 - 1 MeV 3. 0.15 - 45 keV	Solar studies. X-ray background, source spectra, iron line emission
HEAO-1 Aug 1977 - Jan 1979	1. A1 - Seven detectors 2. A2 - Six multi-layer, collimated proportional counters 3. A3 - Two modulation collimators 4. A4 - Seven inorganic Phoswich detectors	1. Spatial res. $\approx 1'$ 2. Area = 4000 cm <sup>2</sup> 3. Spatial res. = 30" and 2', Area = 700 cm <sup>2</sup> 4. Area = 480 cm <sup>2</sup>	1. 0.25 - 25 keV 2. 0.15 - 60 keV 3. 0.9 - 13.3 keV 4. 15 keV - 10 MeV	Discovery of more than a thousand x-ray sources, including AGN, galactic clusters, transients, bursters and pulsars. Studied variabilities and diffuse x-ray background
HEAO-2 (Einstein) Nov 1978 - Apr 1981	1. Two Imaging Proportional Counters (IPC) 2. Three High Resolution Imagers (HRI) 3. Solid State Spectrometer (SSS)	1. Spatial res. = 1', Area = 200 cm <sup>2</sup> , Time res. = 63 msec 2. Spatial res. = 2", Area = 20 cm, Time res. = 8 msec 3. Spatial res. = 1', Energy res. = 160 eV, 128 pulse height channels	1. 0.4 - 4 keV 2. 0.15 - 3 keV 3. 0.5 - 4.5 keV	First fully imaging x ray telescope in space. Observed over 5000 targets including AGN, x-ray binaries, CVs and SNRs, and many thousand "serendipitous" discoveries.

**Table 2.3** Major x-ray astronomy missions from Uhuru to Einstein

The major space missions which have included an x-ray observing element are summarised in Tables 2.3 and 2.4. Included in the tables are the detector parameters and the main science objectives and achievements. The information in these tables has been gathered from various sources including the following references [Pounds, 1997; Bradt, 1992] and the information supplied in the HEASARC database on the World-Wide-Web<sup>1</sup>.

<sup>1</sup> The address of the index of these pages is "<http://heasarc.gsfc.nasa.gov/docs/heasarc/missions/>". References may be found therein.

Name and Lifetime	Detector systems	Detector parameters	Energy	Science
Astro-B (Tenma) Feb 1983 - late 1984	1. Scintillation Proportional Counter (10 GSPCs)  2. X-ray Focusing Collector 3. Transient Source Monitor	1. Area = 720 cm <sup>2</sup> , Energy res. $\approx$ 10% @ 6 keV 2. Area $\approx$ 7 cm <sup>2</sup> -	1. 2 - 60 keV  2. 0.1 - 2 keV 3. 2 - 10 keV	Iron line studies in many classes of x-ray source
EXOSAT May 1983 - April 1986	1. Two Low Energy imaging telescopes (LE) 2. A Medium Energy proportional counter array (ME) 3. A Gas Scintillation Proportional Counter (GSPC)	1. Area = 0.1 - 11.1 cm <sup>2</sup> Spatial res. = 18" 2. Area = 1500 cm <sup>2</sup> , Spatial res. = 3' 3. Area = 150 cm <sup>2</sup> , Spatial res. = 3'	1. 0.04 - 2 keV  2. 1- 50 keV 3. 2- 40 keV	First long, uninterrupted, x-ray observations of the sky. Approx. 1800 observations including white dwarfs, x-ray binaries and the first obs. in the UV band
Astro-C (Ginga) Feb 1987 - Nov 1991	1. Large Area Proportional Counter (LAC)  2. All Sky Monitor (ASM)	1. Area = 4000 cm <sup>2</sup> , Energy res. = 18% @ 6 keV and <1 msec time res. -	1. 1 - 37 keV  2. 1 - 20 keV	Time variabilities and source spectra. 100 observations of 350 sources
GRANAT Dec 1989 - Present	1. SIGMA - coded mask hard x-ray telescope 2. ART-P coded mask telescope - Four MWPCs  3. ART-S spectrometer - Four x-ray proportional counters 4. WATCH - all sky monitor	1. Spatial res. 10", Area = 800 cm <sup>2</sup> 2. Spatial res. 5", Area = 600 cm <sup>2</sup> per module, Time res. = 4msec 3. Area = 2400 cm <sup>2</sup> @ 10 keV, 200 msec time res. 4. 36 channels, 30 energy res. @ 60 keV	1. 30 - 1300 keV 2. 4 - 60 keV imaging, 4 - 100 keV spectroscopy 3. 3 - 100 keV 4. 6 - 180 keV	Many galactic and extra-galactic sources particularly deep imaging and spectroscopy of galactic centre, black hole candidates and x ray novae
ROSAT Jun 1990 - Present	1. Position Sensitive Proportional Counter (PSPC) 2. High Resolution Imager (HRI) cascaded MCPs 3. Wide Field Camera	- 2. 2" spatial res., 61 msec time res. 3. 2.3' spatial res. (HEW)	1. and 2. 0.1 - 2.4 keV  3. 0.03 - 0.1 keV	All sky surveys in x-ray and EUV. Over 9,000 observations with more than 100,000 individual sources. Deep imaging
Ulysses October 1990 - Present	1. Two CsI hard x-ray detectors  2. Two Si soft x-ray detectors	1. 8 or 32 msec time res., 16 channel energy spectra 2. 500 $\mu$ m Si surface barrier, 6 energy channels	1. 15 - 150 keV  2. 5 - 20 keV	Designed for solar studies as well as carrying instruments to study x and $\gamma$ -rays from solar and cosmic sources

**Table 2.4** Major x-ray astronomy missions from Tenma to Ulysses

As mentioned in the Section 2.1, a characteristic of primary importance for x-ray detectors is energy, or spectral, resolution. The resolving power of various detectors used in x-ray astronomy is summarised in Figure 2.5 [after Wells, 1997]. In this plot are shown both statistics limited (*e. g.* CCDs) and noise limited (*e. g.* bolometer) detectors, along with



dispersive devices (*e. g.* grating spectrometers). The performance of other semiconductor materials, such as CdTe and GaAs, is also included. The improvement of resolution from scintillators to proportional counters (PC), to the modern CCDs that will be used in contemporary x-ray missions (*e. g.* JET-X), is clear.

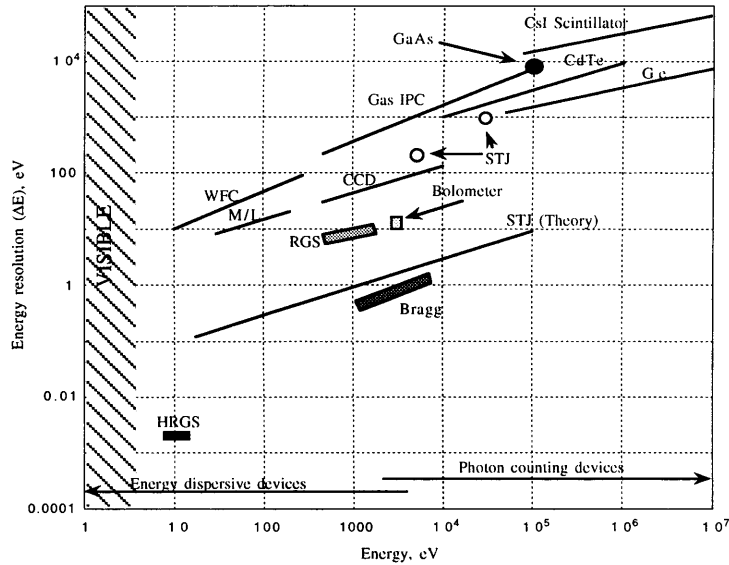


**Figure 2.2** The resolving power of the various types of x-ray detector (after Wells, 1997)

The first x-ray missions were simple Geiger counters, lifted above the earth's atmosphere by sounding rockets. In fact the rapid growth of x-ray astronomy in the early years depended mainly on sounding rockets for carrying detectors [Pounds, 1997]. After the discovery of Sco X-1, by a gas detector on board such a rocket, it soon became clear that extra-solar x-ray sources existed and that they were both extended and variable in time. Detection systems were then built which, in conjunction with arcminute resolution (mechanical collimators), could provide energy resolution which was low (gas counters) or medium (semiconductors). Later, the adoption of grazing incidence optics allowed the source photons to be focused onto a small area on the detector plane. This reduced the relative background rate, permitted the use of small, high performance detectors and also allowed the observation to be limited by the statistics of the source photons [Ramsey, 1994].

### 2.2.1 The gas counter

In the field of solar studies where photon fluxes can be high, the power of high resolution x-ray spectroscopy has been well demonstrated [Linsky, 1990]. However, for astrophysical sources other than the sun, the low resolution Gas filled Proportional Counter (GPC) was mainly used. The gas counter was the workhorse detector for most of the early years (1962 - 1969) and the era of the small satellites (1967 - 1977) and continues to be used today (*e. g.* on ROSAT and ASCA).

Gas counters detect the liberated charge from an x-ray photon interacting in a gas [Fraser, 1989]. Typically  $\sim 25$  eV are needed to produce one electron-ion pair, *i. e.*  $\sim 500$  electrons for a 10 keV photon. Gas Proportional Counters (GPCs) consist of a windowed gas cell, sub-divided into high and low field regions by an arrangement of electrodes. The electrodes measure the signals caused by electrons and ions in the gas, which contain information on the photons transmitted through the window [Fraser, 1989]. X-rays interact with the molecules of the gas, releasing a primary photoelectron along with fluorescent photons and/or Auger electrons. The energy of the x-ray photon is then converted into a cloud of secondary electrons that are confined to a region near the initial interaction site. The secondary electron cloud then drifts into a high field region near an electrode. In a conventional proportional counter the electrons gain enough energy between collisions to excite the molecules of the gas and an electron avalanche is thereby propagated to the anode. Provided the gas gain is not too high, the final pulse is directly proportional to the number of electrons produced by the incident x-ray [Fraser, 1989].

The energy resolution of a gas proportional counter consists of two components, i) a component due to the statistics of the initial electron cloud production and ii) a component due to the avalanche multiplication factor. This second term dominates and limits the FWHM resolution to  $\sim 900$  eV at 6.4 keV [Ramsey, 1994]. The Gas Scintillation Proportional Counter operates with a lower electric field so that the atoms of the gas are excited rather than ionised. The excited atoms emit ultraviolet radiation which is measured by a quartz window photomultiplier [Fraser, 1989]. The advantage of this technique is that the statistics are not dependant on the avalanche process. This improves the resolution to  $\sim 500$  eV @ 6 keV [Ramsey, 1994].

### 2.2.2 Einstein

The launch of the first truly imaging x-ray telescope, Einstein, provided a wealth of new data [Giacconi, 1978]. The superior signal-to-noise ratio provided by the grazing incidence optics employed on Einstein, allowed x-rays to be observed from a wide range of normal stars and galaxies, as well as the usual powerful x-ray objects [Pounds, 1997]. Spectroscopic resolution was provided by a Focal Plane Crystal Spectrometer (FCPS) (high) and a Solid State Spectrometer (SSS) (medium). This was a significant step forward from the era of proportional counters. Thus with the launch of Einstein, x-ray astronomy became, for the first time, a mainstream part of astronomy.

Although the FPCS provided a limited amount of data, the scientific return from Einstein's SSS hinted at the power of high resolution spectroscopy for the first time. The SSS consisted of parallel High Purity Ge (HPGe) and Si(Li) diodes operated in anti-coincidence. It provided a broad-band coverage from 0.5 to 5 keV with an in-flight resolution of 160 eV at 5.9 keV although with limited angular resolution [Joyce, 1978]. The energy resolution compared favourably with the GSPC on ASCA ( $\sim 550$  eV at

5.9 keV) and the GINGA Large Area Counter and proportional counters in general ( $\sim 900$  eV at 5.9 keV).

### 2.2.3 BBXRT

BBXRT, the Broad-Band X-ray Telescope, was part of the ASTRO-1 payload on shuttle Columbia, launched in December 1990 [Weaver, 1995]. During its 9 day mission BBXRT made approximately 116 observations of 76 galactic and extra-galactic sources in the range 0.3 - 12 keV. It had a collecting area  $\sim 750$  cm<sup>2</sup> @ 1.5 keV and 300 cm<sup>2</sup> @ 7 keV. By the time of launch, BBXRT was equipped with high quality segmented Si(Li) detectors with thin gold contacts. The detectors were modelled on the SSS on Einstein but with an improved resolution, 10% compared to 20% at  $\sim 1$  keV. The maximum spatial resolution was 2' and the temporal resolution was 63  $\mu$ s. Unfortunately pointing problems limited the return to 30% of the planned science, although high quality spectra from 50 sources, both galactic and extra-galactic, were obtained.

The science objectives of BBXRT were to observe x-ray spectral features with particular emphasis on the Fe K lines around 6 keV and to study broad band spectral variability. However, the results from BBXRT were somewhat compromised by the problems it encountered during the mission, which prevented full calibration. One of the problems, which is of particular interest in this thesis and to the JET-X calibration program, are the  $\sim 5\%$  residuals seen in deconvolved Crab data at the O (0.54 keV), Al (1.5 keV), Si (1.8 keV) and Au (2.2 - 3.5 keV) edges [Weaver, 1995]. Some of these features can be seen in the plot of a BBXRT spectrum from the Crab nebula in Figure 2.3. It will be shown in Chapter 7 that instrument induced spectral features are a potential cause of absorption- and emission-like features in cosmic x-ray spectra at a level similar to those observed in BBXRT spectra of the Crab nebula, such as in Figure 2.3.

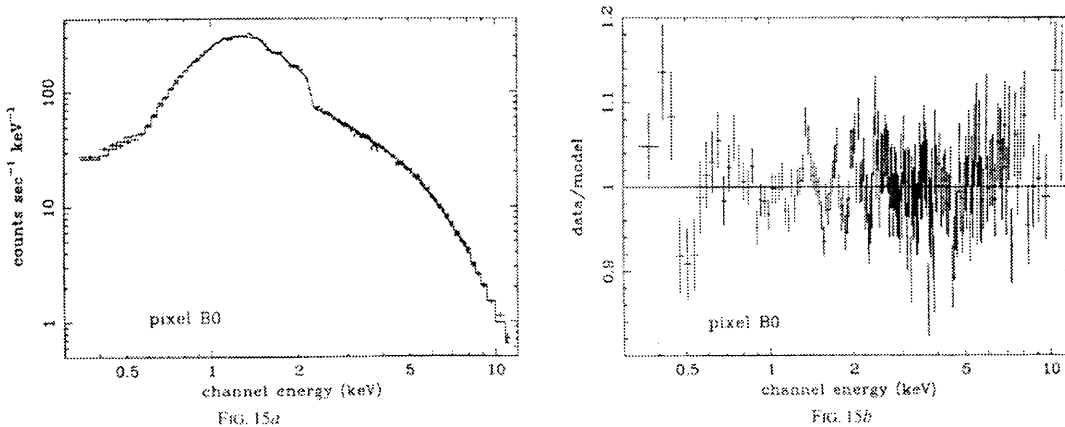


**Figure 2.3** A measured BBXRT spectrum of the Crab nebula with a plot of the deconvolved residual spectrum to the right [Weaver, 1995].

## 2.3 X-Ray Astronomy with CCDs

### 2.3.1 Introduction

The results from Einstein and the improvements to spectral and spatial resolution promised by CCDs set the stage for a new era in x-ray astronomy with CCDs as the prime focal plane detectors. By the middle of the 1980s x-ray astronomers realised that CCDs could combine the energy resolution of a silicon detector (4-5 times better than PCs or GSPCs) with the possibility of high resolution imaging [Wells, 1985]. The improved resolution of silicon based detectors arises from the more efficient use of the incident x-ray energy over gas counters. The average energy required to generate an electron-hole pair in silicon is only  $\sim 3.68$  eV at room temperature compared to  $\sim 25$  eV for Argon/Methane, which is typically used in GPCs. However, because of the small band-gap, silicon detectors, like other semiconductor detectors, must be cooled to cryogenic temperatures in order to reduce the number of thermally generated electrons.

Currently there are five operational x-ray missions: ROSAT, EUVE, ROSSI-XTE, SAX and ASCA with a further 6 planned for the near future: Spectrum X $\Gamma$ , XMM, ASTRO-E, INTEGRAL, AXAF and ABRIXAS. Of these ABRIXAS, ASCA, ASTRO-E, AXAF, SPECTRUM X $\Gamma$  and XMM have or are planning to have CCDs as focal plane detectors. These missions are now discussed, with emphasis on the CCD operation.

### 2.3.2 ASCA

Astro-D, or ASCA (Advanced Satellite for Cosmology and Astrophysics), which is currently in use, was launched on February 20th 1993. It was placed into a circular orbit with a period of 96 minutes [Tanaka, 1994]. ASCA carries four large-area x-ray telescopes with identical 119 layer, conical, thin-foil mirrors. The focal length of the mirrors is 3.5 m and they have a modest angular resolution of  $3'$ . All four mirrors have imaging spectrometers at their focal plane. At the focus of two of the telescopes are Gas Imaging Spectrometers (GIS), while Solid-state Imaging Spectrometers (SIS) are at the focus of the other two. The GISs are gas scintillation proportional counters, based on the GSPC that flew on the second Japanese x-ray astronomy mission, TENMA.

The construction of ASCA's two SISs was a joint effort on the part of MIT, ISAS and Osaka University. Each SIS camera is based around four, 420 by 422 pixel CCD chips with  $27\text{ }\mu\text{m}$  pixels, abutted side-by-side and operated in frame-store mode. The useful energy range of the front-side illuminated CCDs is 0.4 keV to 10 keV and they have resolution  $E/\Delta E \sim 50$  at 6 keV and  $\sim 20$  at 1.5 keV. The field of view of the SISs is 22 by 22 arcmin square.

ASCA is the first x-ray astronomy mission to use CCDs for x-ray astronomy. The mission combines imaging capability with a broad pass band, good spectral resolution, and a large effective area. With these properties, the primary scientific purpose of ASCA is spec-

troscopy of astrophysical plasmas, especially the analysis of emission lines and absorption edges.

### 2.3.3 AXAF

NASA's Advanced X-ray Astrophysics Facility (AXAF), scheduled to be launched and deployed by the Space Shuttle in August 1998, will be the most sophisticated x-ray observatory ever built [Weisskopf, 1987]. AXAF is designed to operate for at least 15 years with maintenance provided by NASA's space shuttle, which should also allow the incorporation of more powerful instruments as they are built. AXAF will be launched into an elliptical, high-earth orbit with an orbital period of ~64 hours. The spacecraft will spend 85% of its orbit above the belts of charged particles that surround the Earth and uninterrupted observations for as long as 55 hours, should be possible.

The x-ray telescope will consist of four nested Wolter-I pairs with a focal length of 10 m, an angular resolution better than 0.35 " (50% encircled energy) and a geometrical area of 1700 cm<sup>2</sup>. There will be two focal plane instruments: a High Resolution Camera (HRC) and the AXAF CCD Imaging Spectrometer (ACIS). The HRC will be similar to the HRIs on EINSTEIN and ROSAT but with a lower background rate [Fraser, 1996]. It will be used for making detailed or high resolution images and will have a limited ability to distinguish between the energies of incoming x-rays. The HRC is a natural extension of proven technology based on Micro-Channel Plate (MCP) imaging x-ray detectors and is the instrument of choice for reading out the Low Energy Transmission Grating Spectrometer (LETGS).

The critical active elements in the ACIS are the CCDs. The ACIS pixels are 24  $\mu$ m square with no dead area between pixels. The ACIS instrument has 4 primary imaging chips in a 2-D array. 6 chips in a linear array will provide spectroscopy. Since the optimal focal surfaces for imaging and spectroscopy are different, there will be separate CCD arrays optimised for each application. The ACIS-I array offers the largest field of view with best imaging performance across the field. The ACIS-S array follows the Rowland Circle defined by the gratings, and gives the best spectroscopic energy resolution. When a transmission grating is introduced into the light path between the x-ray mirrors and ACIS, the image of sources becomes dispersed thereby providing higher spectral resolution ( $E/\Delta E \sim 500$ ). The CCDs will be constructed on high resistivity silicon (10,000  $\Omega$ cm) in order to achieve a deep depletion depth, giving 80% detection efficiency at 6 keV.

The scientific objectives of AXAF are to investigate [Weisskopf, 1988]:

- The nature and origin of the cosmic x-ray background and the relative contributions of quasars, primordial galaxies and diffuse gas at cosmological epochs.
- The nature and origin of nuclear activity in galaxies and quasars, and the physical relationships between AGNs and their host galaxies.

- The structure and evolution of galaxy clusters and superclusters as probes of the formation of galaxies and theories of the early universe.
- The mass and nature of haloes of galaxies as derived from studies of the hot gas they contain and from the x-ray properties of cluster galaxies.
- The origin of stellar activity as manifested in the x-ray emission from winds and coronae of stars.

#### 2.3.4 SPECTRUM XT

There are 7 main experiments on Spectrum XT, including JET-X, which will use CCDs for its focal plane imaging detectors. The JET-X CCD program is mentioned in Chapters 3 and 4 of this thesis while the focal plane cameras of JET-X are discussed in detail in Chapter 6. The primary science objectives of JET-X, put briefly, are detailed imaging and spectroscopic measurements of cosmological sources, imaging of extended low surface brightness regions and spectral variability studies. The principal design criteria are [Wells, 1990]:

- Imaging with  $< 30$  arc sec resolution with a limiting sensitivity at 1 keV of  $\sim 0.5$  nJy.
- Medium spectroscopic resolution ( $E/\Delta E > 10$ ) in the 0.3 to 10 keV band with emphasis on high sensitivity and spectral resolution ( $E/\Delta E > 50$ ) around the Fe-line complex.
- Temporal resolution sufficient to map x-ray time variability on timescales ranging from milliseconds to months.

The principal science goals will be [JET-X/FDR (1995)]:

- Deep source counting, population studies, broad-band spectrophotometry of faint sources and optical follow up.
- Plasma diagnostics using CCD spectroscopy.
- Spatially resolved spectroscopy of extended sources; medium-high Z clusters, galaxies and supernovae remnants.
- Long baseline/high time resolution variability studies.

#### 2.3.5 XMM

XMM will be the second ESA Horizon-2000 Cornerstone mission and is due to be launched in late 1999 from an Ariane V rocket. The satellite will be put into a highly elliptical orbit with up to 32 hours continuous observations. The predicted lifetime of the mission is 10 years. The payload is made up of the European Photon Imaging Camera (EPIC), the Reflection Grating Spectrometer (RGS) and an Optical Monitor (OM).

EPIC is the main focal plane instrument at the foci of the three XMM mirror systems, with two Metal-Oxide Semiconductor (MOS) CCD (see Chapter 4) arrays and one pn-CCD array (EPIC-Maxi) [Bignami, 1990]. The RGS has gratings mounted on the rear of two of the mirrors with two CCDs mounted in the focal plane to measure the dispersed spectra.

Each of the mirror modules on XMM will be capable of an angular resolution of under 10 " (FWHM) with an effective area of  $\sim 1500 \text{ cm}^2$  at 1 keV.

The final iteration of the MOS CCD camera on EPIC is a 7 CCD design with the central CCD lowered with respect to the other six in order to map the curved surface of the focal plane. The CCDs are open phase giving an improved  $Q(E)$  of 30% at carbon K (277 eV) [Holland, 1996]. The focal plane is covered by the 600 by 600 pixel imaging areas (each pixel is  $40 \mu\text{m}$  square) of the seven CCDs while the store region pixels are reduced to  $40 \mu\text{m}$  by  $12 \mu\text{m}$ .

The EPIC when combined with the XMM focusing optics promises to be a facility that will combine high sensitivity with a wide energy band-pass and good spatial, spectral and temporal resolution (down to 16 ms). This ensures that XMM will be fully complementary to AXAF with a useful deep exposure sensitivity one tenth of that offered by EINSTEIN. The core science of XMM will be high throughput imaging x-ray spectroscopy. Scientific objectives will include:

- Understanding the diffuse x-ray background and establishing its principal components.
- Mapping clusters of galaxies for temperature and elemental abundance.
- Spectral surveys of galaxies and supernova remnants.
- Studies of stellar x-rays and stellar flare events.
- Study of accreting binary systems.

### **2.3.6 ASTRO-E**

ASTRO-E will be the fifth Japanese x-ray astronomy satellite and is currently scheduled to be launched early in the next millennium [Inoue, 1997]. The three experiments it will carry are; a micro-calorimeter array (X-Ray Spectrometer - XRS), four CCD cameras (X-ray Imaging Spectrometer - XIS) and a hard x-ray detector (Hard X-ray Detector - HXD). The XRS and XIS will cover the energy range 0.4 - 10 keV while the HXD will operate over the range 10 - 700 keV.

### **2.3.7 ABRIXAS**

ABRIXAS (A Broad-Band Imaging X-ray All Sky Survey) will undertake a 3 year survey of the x-ray sky in a manner similar to that achieved with ROSAT except with an energy range of 0.4 to 12 keV. It will provide a deep survey which will complement the pointed observations of its contemporary missions, XMM and AXAF. ABRIXAS will use 7 mirror systems with 27 Wolter-1 shells, sharing one  $6 \text{ cm}^2$  pn-CCD chip. The pn-CCDs will be identical to those developed at MPE, Garching, for the EPIC-Maxi detector. The advantages of the pn-CCD are high sensitivity at high energies (95% at 10 keV) and fast readout (sub-millisecond). The energy range will be 0.4 - 12 keV. The primary scientific concerns of ABRIXAS will be [Trümper, 1997]:

- Discover and investigate galactic sources obscured by photoelectric absorption.
- Map galactic ridge emission and the broad-band emissions of clusters of galaxies.
- Study time variability and extended supernova remnants.
- Provide a large sample of Quasars II and Seyfert II galaxies.

## 2.4 Conclusions

The missions Spectrum XG, XMM, AXAF, Astro-E and ABRIXAS will be the mainstays of x-ray astronomy over the next decade. The emphasis of these missions is firmly toward spectroscopy and is the route by which x-ray astronomy will develop into the mainstream of high energy astrophysics. CCDs, with their capability of medium energy resolution and high spatial resolution, will play an important role in the scientific returns of all these missions. New developments in CCD design and implementation should ensure that the CCD carries on as the workhorse for x-ray astronomical missions well into the next millennium. These developments must include improved quantum efficiency at high and low energies, reduced noise performance, increased readout speed as well as increased yields and lower fabrication costs [Holland, 1997]. Also important for the next generation of x-ray telescopes will be larger area CCDs and, increasingly, smaller pixel sizes. Larger area CCDs will be necessary to fill the focal planes of large effective area telescopes. CCDs with pixels as low as 2.5  $\mu\text{m}$  will provide the potential for extremely high resolution imaging, along with the capability of simultaneous x-ray polarisation measurements [Hill, 1997].



# 3

## The Production, Operation and Testing of CCDs

### 3.1 Introduction

In this chapter the production and operation of CCDs and the facilities used for testing the JET-X x-ray CCDs will be discussed. The demands of x-ray astronomy place some of the most rigorous constraints on the production of a CCD. The JET-X CCD is a good example of a CCD which displays many of the best solutions to these problems, including thinned electrodes, deep depletion regions and supplementary buried channels. The JET-X CCDs are “state of the art detectors” that are capable of achieving less than 3.5 electrons noise. That is the mean error on the number of electrons produced by an x-ray is only  $\sim 3.5$  electrons.

In this Chapter the work is set out as follows. Section 3.2 will describe the production techniques of CCD production and the relevant factors involved in operating them. Section 3.3 will outline the JET-X CCD design and its special features. Section 3.4 will outline the way in which CCDs are driven, both from a hardware and a software point of view. As the measurement of CCD  $Q(E)$  is such an important facet of this thesis Section 3.5 will focus on the way in which this was measured before the decision was made to take the CCD to the Daresbury Synchrotron Radiation Source (SRS), and the reasons behind that decision and the use of the SRS as a low flux x-ray source will be described in Section 3.6.

### 3.2 CCD detectors

#### 3.2.1 Introduction

In this section the fabrication and operation of CCDs will be briefly examined. Detailed descriptions of CCD production and use has been well documented in PhD theses submitted by previous postgraduate students of the University of Leicester [Holland, 1990 and Castelli, 1991].

#### 3.2.2 CCD production

A CCD consists of a regular 2-dimensional array of individual picture elements (pixels). Each pixel is defined by a set of coupled Metal-Oxide-Semiconductor (MOS) capacitors which collect charge during an integration period. Charge is constrained in the orthogonal direction by implanted channel stops. This arrangement can be seen in the schematic in Figure 3.1, where a single pixel is shown by the hatched region. This figure shows a

3-phase CCD, *i. e.* 3 coupled MOS capacitors per pixel. This is a typical CCD construction and is the technique used for the JET-X CCDs that are featured in this thesis. The 3-phase design is the most commonly used CCD fabrication technique owing to its inherently high process tolerance, and correspondingly high yield. The JET-X CCDs use heavily doped polycrystalline silicon rather than metal for the electrodes. Channel stops are used to confine collected charge, thereby defining the extent of a pixel in one dimension.

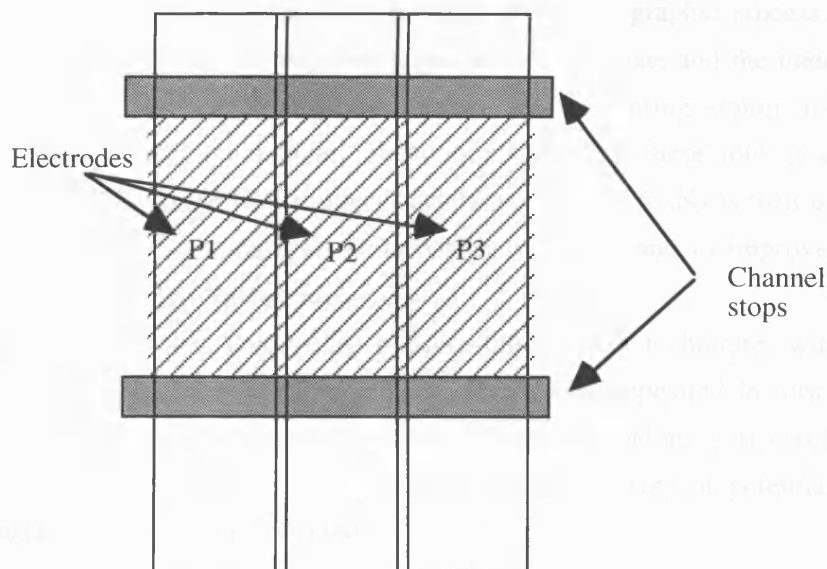


**Figure 3.1** A schematic of a single pixel of a 3-phase CCD

When a positive potential is applied to the polysilicon electrodes a potential well is formed under the pixel which collects locally ionised electrons. A typical buried channel, MOS capacitor is shown in Figure 3.2.

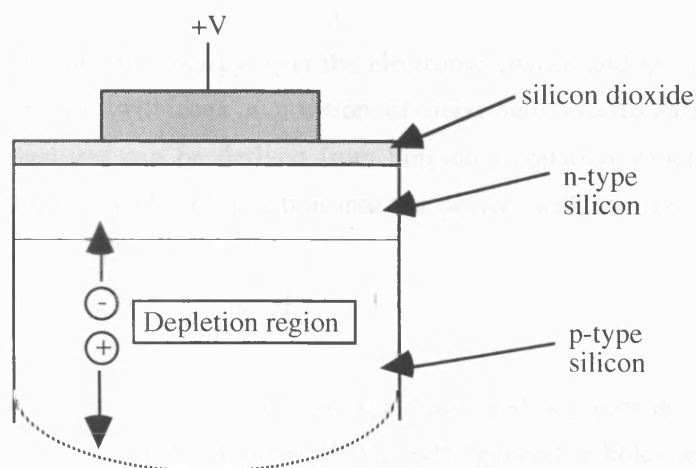


**Figure 3.2** A schematic of a buried channel MOS capacitor

MOS capacitors can be constructed in two forms: surface channel and buried channel. Virtually all modern CCDs, including the JET-X CCD, are constructed from a series of buried channel MOS capacitors, and are therefore known as Buried Channel CCDs

(BCCDs). This technology enables liberated charge to be collected well away from the surface regions, where a high density of Si-SiO<sub>2</sub> interface traps exist.

The wafer on which the CCDs are constructed consists of a p-type epitaxial layer grown over a p+ substrate. This technique has the effect of moving defects from the epitaxial region into the substrate which helps to decrease the number of sites available for bulk trapping and to reduce cosmetic artefacts such as bright pixels or bright columns. The imaging area is defined by doping with boron, using a photo-lithographic process. The silicon surface is oxidised to create an insulating layer between the gate and the underlying area. The  $\leq 1 \mu\text{m}$  n-type, buried channel is formed by implanting donor ions (usually phosphorus) through the oxide layer. The concentration of these ions is a few times  $10^{17} \text{ cm}^{-3}$ . In scientific grade CCDs another insulating layer of Si<sub>3</sub>N<sub>4</sub> is then usually added to protect the oxide from impurities, from further oxidation and to improve the overall electrical isolation between the two layers.

The electrodes are deposited using a photo-lithographic technique, with unwanted polysilicon removed by plasma etching. Each electrode is deposited in turn with a thin layer (0.3  $\mu\text{m}$ ) of oxide in between. In this way a 2-dimensional array of pixels is built up which, when the electrodes are suitably biased, present an array of potential minima in which liberated charge may be collected.

### 3.2.3 Charge storage

The application of a potential to the polysilicon electrode repels the majority carriers in the epitaxial region thereby creating a region in the silicon which is depleted of holes. The potential energy of an electron within this region is given by

$$E_b = -q|\psi| \quad 3-1$$

where  $E_b$  is the electron potential energy,  $q$  is the electronic charge and  $\psi$  is the electrostatic potential. An electron will seek a position of maximum electrostatic potential. Electrostatic potential profiles can be derived from Poisson's equation which relates the rate of change of the electric field with position into the device, with the free charge density at that point.

$$\frac{d^2V}{dx^2} = -\frac{e(N_d^+(x) - N_a^-(x) - n(x) + p(x))}{\epsilon_{si}\epsilon_0} \quad 3-2$$

where  $e$  is the electronic charge,  $N_d^+$  and  $N_a^-$  are the donor and acceptor doping concentrations respectively,  $p$  and  $n$  are the number of thermally generated holes and electrons respectively and  $\epsilon_{si}$  and  $\epsilon_0$  are the relative permittivity of silicon and the permittivity of free space respectively. This equation can be solved analytically in the simplest of cases (*i. e.* surface channel MOS capacitors with simple doping profiles) but in general must be solved iteratively using a numerical approach. Typical potential profiles in a buried chan-

nel capacitor can be seen in Figure 3.3, where a numerical solution has been used [courtesy D. J. Burt].

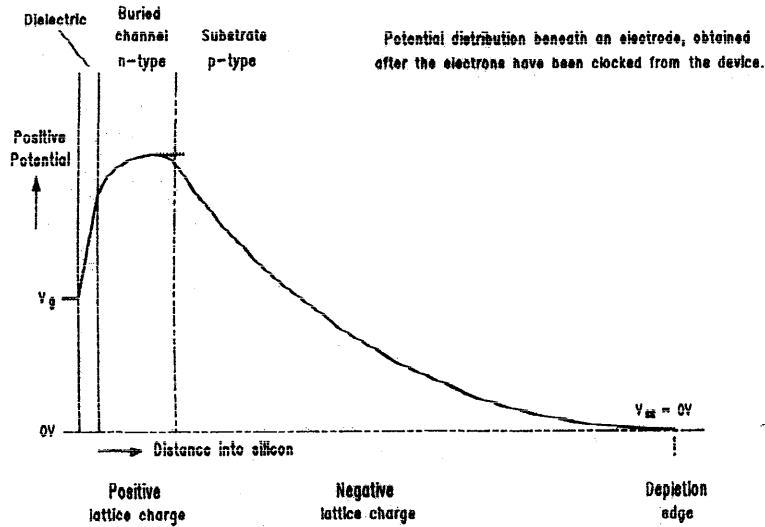
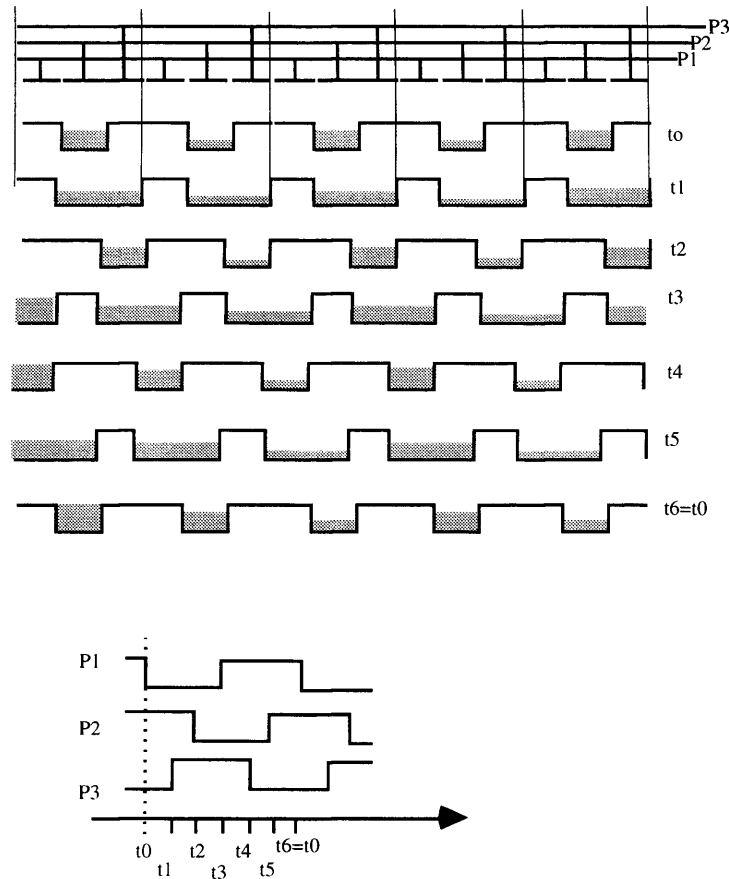


Figure 3.3 Potential profiles in a buried channel MOS capacitor [courtesy D. J. Burt]

### 3.2.4 Charge coupling

In order to be read-out there must be a mechanism by which the generated charge can be transferred to the detecting amplifier. This mechanism is clocking, where the bias on the electrodes is sequenced in order to transfer charge across the 3 phases of each pixel and into a neighbouring pixel.



**Figure 3.4** A typical clocking system to transfer charge between pixels in a CCD

A typical clocking diagram with appropriate voltage phases can be seen in Figure 3.4 for a 3-phase CCD. In Figure 3.4 the charge has been collected under the P2 electrode. At time  $t=t_1$  a positive bias equal to that on P2 is applied to P3. The charge located under P2 now diffuses and drifts under P3. At  $t=t_2$  the bias on P2 is turned off, forcing the charge to move rapidly under P3. The charge has therefore been shifted one phase to the right. Repeating this process using the P3 and P1 electrodes shifts the charge on to P1 and a further set of clocks moves the charge on to the next P2. In this manner the entire charge packet has been moved or coupled one pixel to the right. For one set of clock cycles all charge packets move one pixel to the right and the first charge packet is moved on to the readout register to be read out.  $N$  parallel clock cycles and  $M$  serial clock cycles are required to read out all the pixels of an  $N \times M$  2-dimensional array.

The efficiency with which the charge packets can be transferred depends on several factors, namely:

- Clocking speed
- Traps from mask defects and clocking potentials
- Bulk trapping sites (buried channel devices)

In practice, scientific CCDs are used at relatively slow scanning speeds and the clocking period is sufficient to enable full transfer of charge. Traps from mask defects can be

avoided by rigorous quality control, and traps from poor clocking potentials can be avoided by driving the CCD carefully. The main difficulty facing perfect charge transfer is trapping of the signal electrons by the bulk trapping sites. It can be shown that the electron trapping time is of the order of  $\sim 1 \mu\text{s}$  and the electron release time is  $\sim 1 \text{ ms}$  [Holland, 1990]. Since the clock speed is  $\sim 50 \text{ kHz}$  ( $20 \mu\text{s}$  amplifier integration time), trapped electrons are released relatively slowly compared to the pixel transfer time, resulting in charge being smeared over several pixels. The charge transfer efficiency (CTE) of most JET-X-type CCDs has been measured to be  $>99.99995\%$ , indicating that there are very few trapping sites in the CCDs.

### 3.2.5 Charge measurement

An additional linear array of pixels is laid down next, and orthogonal, to the ends of the imaging pixels. This array, known as the serial register, has a pixel next to the end of each column of imaging pixels. The serial register is connected at its end to a charge detection output amplifier. The first clock cycle transfers the first charge packets on to the serial register. These packets are then transferred, by clocking, along the serial register to the detecting amplifier. To clock all of the rows of a JET-X CCD takes in the region of 30 ms. A number of schemes exist whereby small amounts of charge can be registered and a detectable voltage output from the CCD. Figure 3.5 shows a typical on-chip output structure

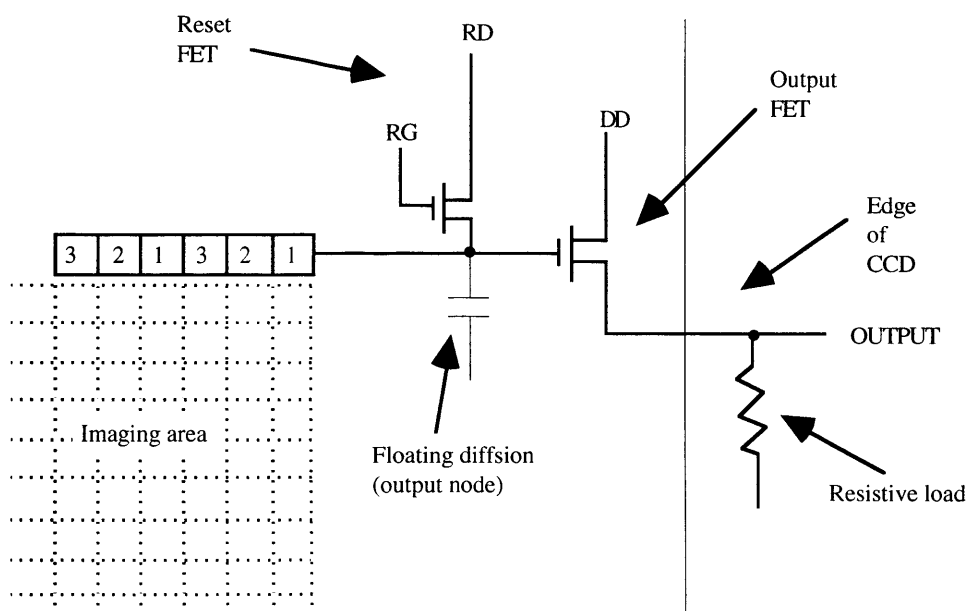


**Figure 3.5** A typical on-chip output amplifier which converts signal charge to a voltage

Read out of the charge from a pixel begins by turning on the Reset FET and allowing the output node (floating diffusion) to be set to the reset drain voltage. The output node is then isolated from the reset FET. When the final serial gate voltage is lowered the stored

electrons are free to pass on to the output node. The change in voltage can then be related to the number of electrons in the charge packet by the following relationship

$$\Delta V = \frac{\Delta Q}{C_T} G \quad 3-3$$

where  $C_T$  is the total capacitance of the output node, including the floating diffusion and the parasitic capacitance of the metal leads and the gate of the output FET.  $C_T$  is typically  $\sim 0.1$  pF.  $\Delta V$  is the change of voltage at the output FET and  $\Delta Q$  is the quantity of charge in the signal packet.  $G$  is the gain at the output FET and is typically about 0.7. For a single signal electron the output voltage changes by  $\sim 1$   $\mu$ V.

### 3.2.6 Noise

Noise in CCDs can be separated into two subsets;

- Signal related noise; photon shot noise, dark current and charge transfer noise
- Electronics related noise; reset noise and transistor noise

#### *Photon shot noise*

The absorption of x-ray photons in the CCD results in the promotion of electrons from the valence band to the conduction band. The energy of the x-ray and the number of liberated electron-hole pairs are related by the following expression

$$n = \frac{E}{\omega} \quad 3-4$$

where  $n$  is the mean number of electron-hole pairs,  $E$  is the x-ray energy and  $\omega$  is the energy required to create a single electron-hole pair ( $\omega$  is  $\sim 3.68$  eV [Bertolini, 1968]). The band gap of silicon is only 1.12 eV but the value of  $\omega$  is larger as much of the x-ray energy is dissipated in producing phonons instead of electron-hole pairs. The number of electron-hole pairs produced is subject to a statistical variation given by  $n^{1/2}$  in the case where the creation of electron-hole pairs is mutually exclusive (Poissonian case). If this were the case the fundamental resolution of a CCD at 6 keV would be  $\sim 350$  eV ( $E/\Delta E \approx 17$ ). Fortunately the observed fluctuation of  $n$  is smaller than would be expected in the Poissonian case as the secondary x-ray creations are not independent events [Fano, 1947]. Fano attributed the reduction in  $n^{1/2}$  to the restriction that the absorbing lattice places on the valence to conduction band transitions. An empirical modifier,  $F$ , the Fano factor, has been adopted to quantitatively describe this effect, *i. e.*

$$\sigma = \sqrt{Fn} = \sqrt{\frac{FE}{\omega}} \quad 3-5$$

where  $F$  is approximately 0.15, although the actual value remains an issue of continuing debate. A group at Leicester University has investigated the Fano factor in some detail, the results of which are published in [Owens, 1996]. The Fano factor reduces the fundamental resolution at 6 keV to  $\sim 100$  eV, a factor of  $\sim 3.5$  lower than the Poissonian case. It is inter-

esting to note that workers often refer to CCD response as Fano “limited” when Fano “maximised” is a better description.

#### *Dark current*

As the band gap of silicon is only 1.12 eV it is possible for thermally generated electrons to be excited into the conduction band. Depending on the type of silicon used the dark current can be very substantial. A typical CCD can have a dark current signal of as much as 30,000 electrons pixel<sup>-1</sup> s<sup>-1</sup> at room temperature, which would completely saturate the pixels, and contribute ~170 electrons to the CCD noise. Thermal electrons are generated at various sites. Listed in order of contributing power these are:

- At the Si-SiO<sub>2</sub> interface (1st term in Equation (3-6))
- In the depletion region (2nd term in Equation (3-6))
- From the neutral field-free layer (3rd term in Equation (3-6))

The current density due to thermal electrons can be written [Grove, 1967] as

$$I_d = \frac{esn_i}{2} + \frac{en_i x_d}{2\tau} + \frac{eD_n n_i^2}{L_n N_a} \quad 3-6$$

where  $n_i$  is the intrinsic carrier concentration,  $\tau$  is the effective lifetime in the depletion region,  $x_d$  is the depletion layer thickness,  $s$  is the surface recombination velocity,  $D_n$  is the diffusion constant,  $N_a$  is the dopant concentration and  $L_n$  is diffusion length for electrons. Since the intrinsic carrier concentration,  $n_i$ , is given by

$$n_i = \sqrt{N_c N_v} \exp\left(-\frac{E_g}{2kT}\right) \quad 3-7$$

where  $E_g$  is the band gap of silicon (1.12 eV),  $k$  is Boltzman’s constant,  $N_c$  and  $N_v$  are the effective density of states in the conduction and valence bands and  $T$  is the temperature, the dark current can be reduced by operating the CCD at a lower temperature. Reducing the temperature from 273 K to 173 K reduces the dark current by ~6 orders of magnitude. It is for this reason that in the laboratory astronomical CCDs are cooled with liquid nitrogen to ~-100°C.

#### *Charge transfer noise*

Imperfect charge transfer leads to an extra source of noise in the CCD. The charge transfer efficiency,  $\eta$ , of modern BCCDs usually exceeds 0.99995. The noise contribution,  $\sigma_{CTI}$ , can be calculated using

$$\sigma_{CTI} = \sqrt{nN\epsilon} \quad 3-8$$

where  $\epsilon$  is the charge transfer inefficiency (1- $\eta$ ),  $n$  is the number of electrons in the charge packet and  $N$  is the average number of charge transfers.



### *Reset noise*

A major source of noise in the system electronics is the uncertainty with which the output diode is reset to the output drain voltage after each pixel is read out. This uncertainty is caused by thermal noise in the reset potential. The noise caused by this process is given by

$$\sigma_{reset} = \frac{\sqrt{kTC_0}}{e} \quad 3-9$$

where  $k$  is Boltzman's constant,  $T$  is the temperature and  $C_0$  is the output node capacitance (typically  $\sim 0.1$  pF). The reset noise is therefore equivalent to  $\sim 100$  electrons (rms) at a temperature of  $-90^\circ\text{C}$ . This would obviously be too great a noise value with which to measure x-ray signals. The technique of correlated double sampling (CDS), whereby the signal level is measured both before and after the signal charge is moved on to the output capacitor, effectively eliminates this source of noise.

### *Transistor noise*

Noise sources that are associated with the output MOSFET are: Johnson noise from the thermal motion of the charge carriers and flicker noise, which arises from the trapping and release of electrons in the conductive drain to the source channel of the FET [Sze, 1981]. While Johnson noise has a flat frequency response, flicker noise has a response which is inversely proportional to the frequency and is therefore often referred to as  $1/f$  noise. At low frequencies the  $1/f$  noise is the dominant source of noise in the output FET. Both forms of noise can be reduced by accurate employment of CDS analogue signal processing in the dual-slope integrator.

## **3.3 The JET-X CCD design**

In 1988 the University of Leicester in conjunction with EEV Ltd, began a development programme to produce large area, radiation hard CCDs for the JET-X programme. The starting point for this work was the commercially available P8600 device, originally designed as a CCD frame transfer array for 625-line TV applications. For use as an x-ray detector the response is optimised across the soft x-ray energy range by incorporating several innovations into the design, in terms of materials, electrode structure and supplementary buried channel technologies. In order to obtain a reasonably high detection efficiency above a few keV, the CCDs are fabricated on high resistivity  $1500 \Omega\text{cm}$  epitaxial silicon,  $65 \mu\text{m}$  thick, on a  $550 \mu\text{m}$   $p^+$  substrate. The inert electrode structure on the front surface of the device is thinned to reduce the low energy cut-off to  $0.3 \text{ keV}$  (defined to be at the 5% absolute  $Q(E)$  level).

Figure 3.6 shows a schematic of a JET-X CCD, which is a P88930T device, manufactured under contract by EEV Ltd of Chelmsford, UK.

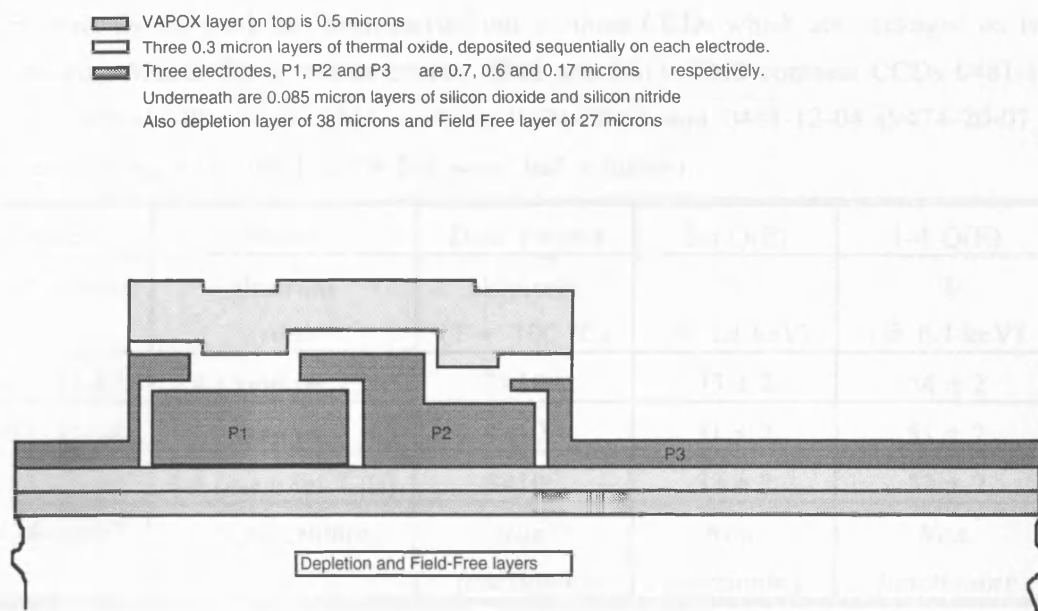


**Figure 3.6** A schematic diagram of a typical thinned electrode, JET-X CCD

It is a large area ( $20.7 \text{ mm} \times 27.6 \text{ mm}$ ),  $768 \times 1024$  pixel, three phase, front illuminated MOS device. The epitaxial silicon consists of a p-type layer, lightly doped with boron, and an n-type layer, doped with phosphorus, on top. With normal operating bias voltages a depletion layer of approximately  $38 \mu\text{m}$  is achieved with a corresponding  $27 \mu\text{m}$  field-free layer. A  $0.085 \mu\text{m}$  silicon dioxide layer is added by vapour deposition (known as a Vapox, or vapour deposited oxide layer) in order to isolate the electrode structure and passivate the surface. This has an amorphous structure. A further layer of  $0.085 \mu\text{m}$  amorphous silicon nitride is added to protect the underlying silicon from further oxidation.

The three electrodes are deposited as n-type polycrystalline silicon, one after the other, with a layer of amorphous, thermal silicon dioxide deposited on top of each electrode. Electrodes 1&2 (P1 & P2) have widths (which contact the nitride) of  $5 \mu\text{m}$  and P3 has a width of  $\sim 16.5 \mu\text{m}$  (depending on the exact thicknesses of the oxide layers, which in turn depend on temperature and crystal orientation during oxidation.) Each electrode overlaps its neighbour by  $1.5 \mu\text{m}$  from edge to edge. P1 is  $0.7 \mu\text{m}$  thick, P2 is  $0.6 \mu\text{m}$  thick and P3 is  $0.17 \mu\text{m}$  thick. All thermal oxide layers are  $\sim 0.3 \mu\text{m}$  thick. Finally a  $0.5 \mu\text{m}$  layer of Vapox is added which serves to protect the device from impurities, moisture and scratches. It possibly acquires a slight doping of phosphorus in its final processing. P3 has all of the silicon dioxide (thermal or Vapox) etched away from it, although the process which controls the final etch could possibly leave behind a few hundred Angstroms of oxide. The etch shape depends mainly on the crystal orientation but is basically vertical. There is an  $\sim 20 \mu\text{m}$  wide buried channel at the surface of the epitaxial region to improve the charge transfer process. There is in addition an  $\sim 4 \mu\text{m}$  supplementary buried channel in the flight devices which reduces the volume of the stored charge thereby reducing the possibility of the charge encountering traps.

For this thesis, work has been carried out on three CCDs which are packaged on two Engineering Model (EM) mother-boards, EM2 and EM3. EM2 contains CCDs 0481-11-07 and 0481-11-08, while EM3 contains 9474-20-07 and 0481-12-04 (9474-20-07 is non-functioning while 0481-12-04 has some bad columns).

Device	Noise	Dark current	Iso Q(E)	1-4 Q(E)
serial number	electrons (rms)	els/pixel/s (T = -100 °C)	% (@ 6.4 keV)	% (@ 6.4 keV)
0481-11-07	3.4 (Amp int 7 $\mu$ s)	$7 \times 10^{-3}$	$33 \pm 2$	$54 \pm 2$
0481-11-08	3.6 (Amp int 7 $\mu$ s)	$9 \times 10^{-3}$	$31 \pm 2$	$51 \pm 2$
0481-12-04	4.0 (Amp Int 7 $\mu$ s)	$8 \times 10^{-3}$	$33 \pm 2$	$52 \pm 2$
9474-20-07	<i>Non-functioning</i>	<i>Non-functioning</i>	<i>Non-functioning</i>	<i>Non-functioning</i>

**Table 3.1** Operating parameters of the three CCDs used for the work in this thesis [JET-X internal reports]

The scientific measurements that were carried out to characterise these devices are summarised in Table 3.1

## 3.4 CCD operation

### 3.4.1 The CCD cryostat

As was described in the Section 3.2, to be used as a single photon, x-ray detector a CCD must be cooled to low temperatures. In the lab this means that the CCD must be housed inside a vacuum cryostat, to ensure contaminants can't condense on to the CCD. A typical test cryostat is shown in Figure 3.7

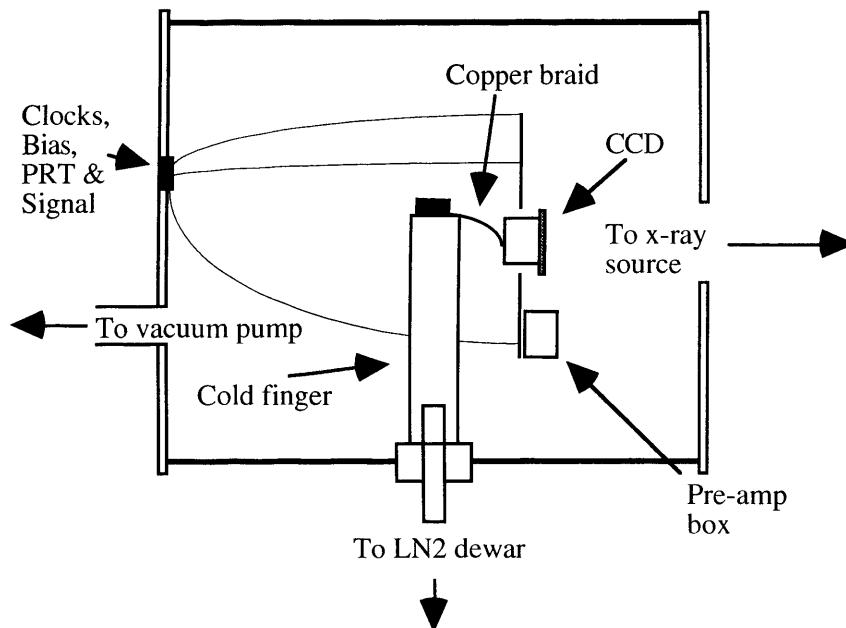


**Figure 3.7** Schematic of CCD cryostat with cold finger and CCD mounting.

The cryostat is evacuated to approximately  $1 \times 10^{-3}$  Torr by the use of a rotary vacuum pump. The CCD is cooled to approximately 170 K by a cold finger that is attached to the CCD via a copper braid. The cold finger is coupled at the other end to a liquid nitrogen reservoir. A full reservoir can keep a typical CCD at 170 K for approximately 4 hours before a refill is necessary. Dual in-line heaters mounted on the cold finger enable the temperature to be kept constant to an accuracy of  $\sim 1$  K. A block diagram of the system can be seen in Figure 3.8

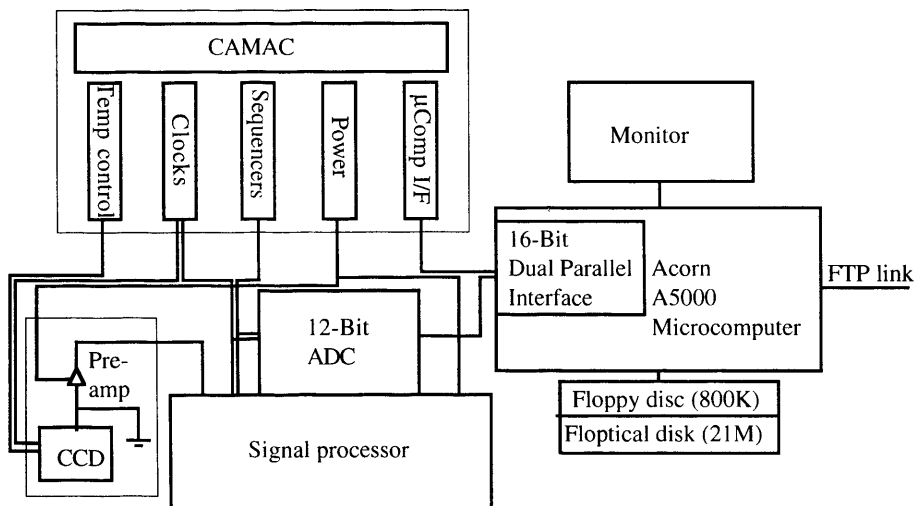


**Figure 3.8** A block diagram for a typical CCD test set-up

### 3.4.2 Drive electronics

The CCD is driven by a drive electronics and signal processing system. The correct bias voltages and clock wave-forms are provided a sequencer situated in the CAMAC.

#### *The Sequencer*

The sequencer provides the correct bit patterns and timing for the CCD clocks and analogue signal processing. The sequence begins by holding two phases of the parallel clock low to store any charge released during integration. At the end of the integration period the sequencer provides the necessary clocks to drive the signal from pixel to pixel and through the readout node, as described in Section 3.2.

#### *The pre-amp*

The output signal from the CCD is amplified by a pre-amp which is close to the CCD inside the cryostat. The pre-amp usually has a  $\times 10$  gain. The pre-amp signal is then fed to an external processor which carries out correlated double sampling (CDS) to eliminate reset noise and other noise associated with the output amplifier.

#### *Correlated double sampling (CDS)*

The CDS processor is located in a separate screened box to reduce noise pickup. There are several ways of implementing CDS, but for low noise work the dual slope integration method is usually used. A typical circuit for a dual slope integrator is shown in Figure 3.10

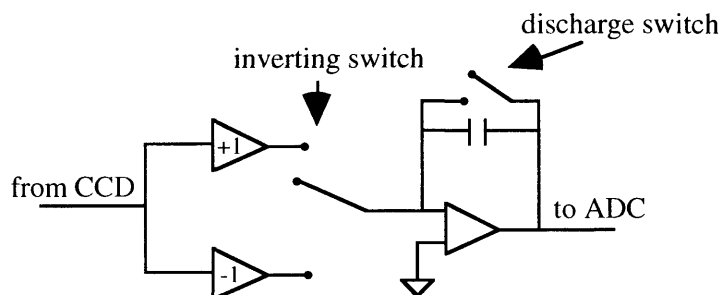


**Figure 3.10** A dual slope integrator circuit diagram

A dual slope integrator consists of an integrating amplifier and a means of inverting the incoming signal. At the beginning of the readout sequence the capacitor is discharged by shorting and it remains shorted until the reset node has settled. The switch is then opened and the output (with no signal) is integrated in inverted mode for a set time, *e. g.* 10  $\mu$ s. Then, as the signal is transferred onto the floating diffusion, the inversion is switched and the signal is integrated for another 10  $\mu$ s. The output is then the difference between the two signals and, with reset errors effectively eliminated, the signal can be sampled by the ADC.

### The ADC

The ADC is also situated in a separate, screened box. On JET-X the ADC digitises the analogue signal to 11 bits (1 - 2047), which implies a limiting resolution of  $\sim 5$  eV channel<sup>-1</sup> for a 0.1 - 10 keV energy range. In the lab a 12 bit ADC range (1 - 4095) is used. The ADC passes the signal to the parallel interface of the A5000 computer where software is employed to display CCD images and spectra.

### 3.4.3 Software

A plot of the data obtained using this system is shown in Figure 3.11. This shows a JET-X CCD which has recorded Mn K $\alpha$ , 5898 eV, x-rays at  $\sim 90$  °C. On selecting a suitable region of interest (ROI) the spectrum of all events may be formed, as in Figure 3.11.

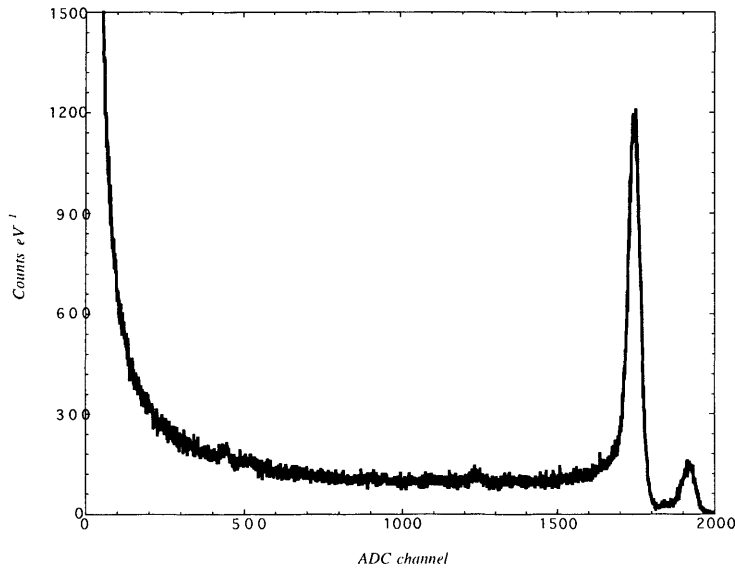


Figure 3.11 An all event spectrum of Mn K $\alpha$  x-rays

### System gain

The system gain is calibrated using the positions of the weighted mean ADC channel,  $\bar{x}$ , of the noise and x-ray peaks. The mean values are given by

$$\bar{x} = \frac{\sum_{i=n}^m x_i A_i}{\sum_{i=n}^m A_i} \quad 3-10$$

where  $A_i$  is the number of pixels in a given ADC bin. The low and high channel values are usually selected as the point at which  $A_i$  has fallen to 5% of the peak value. The calibration,  $C$ , is then given by

$$C = \frac{E_{x-ray} - E_{noise}}{x_{x-ray} - x_{noise}} \quad 3-11$$

where  $C$  is measured in  $\text{eV channel}^{-1}$ . In general the energy of the noise peak,  $E_{\text{noise}}$ , is defined to be zero.

#### Noise elimination

The system noise is evaluated from the variance of the Gaussian noise peak. The variance is found using

$$\sigma = \frac{C}{\omega} \sqrt{\overline{x^2} - (\bar{x})^2} \quad 3-12$$

where  $\omega$  is the energy needed to create an electron-hole pair (3.68 eV in Si at 173 K).

To map the distribution of x-ray events in a CCD image the software searches for pixels with  $> 5\sigma$  charge and then checks the nearby pixels for charge above threshold. X-ray events in a CCD take two different forms, isolated (single pixel) events and “summed” (split) events. Isolated events are those events in which all the liberated charge of an x-ray interaction is collected within a single pixel. Any x-ray events which create above threshold charge in more than one pixel are recorded as summed or multiple pixel events. The threshold for the discrimination of x-ray events is set as  $5\sigma$  for isolated and “summed” event spectra. Pixels which record an energy lower than this value are rejected. A “thresholded” file, derived from the data shown in Figure 3.11 is shown in Figure 3.12 for isolated or single pixel events.

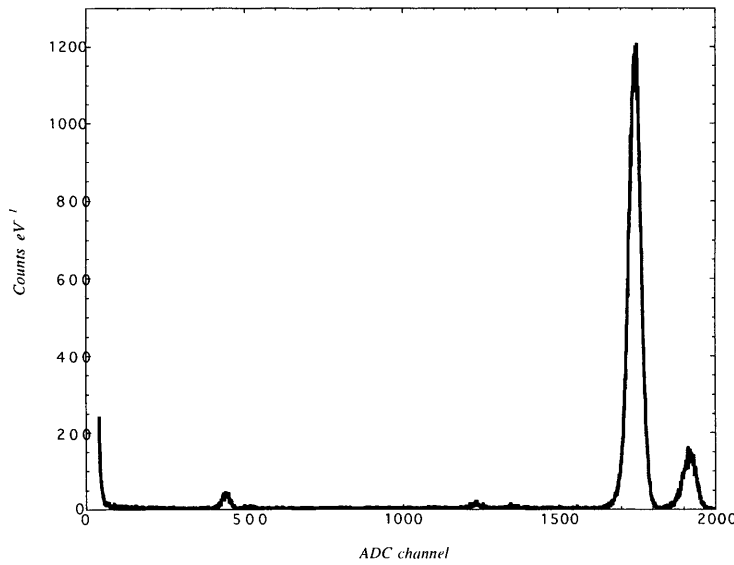


**Figure 3.12** Isolated x-ray events above the  $5\sigma$  threshold

#### X-ray events

As well as isolated pixels, an x-ray absorption event can generate a distribution of charge in which the charge is spread between two or more pixels. This can give rise to pixels in which only a fraction of the expected charge is recorded. Pixels containing only a small amount of charge, spilled over from near neighbours, are not recorded as x-ray events if

they fall below the  $5\sigma$  threshold range. Provided it is over the threshold value, the charge from neighbouring pixels can be combined to create another set of x-ray absorption events known as “summed” events. The spectrum of these types of events can also be displayed using the software. The resolution of summed event spectra are poorer than isolated spectra due to the charge trailing on the low energy side of the spectrum. Figure 3.13 shows a summed event spectrum for events which are between 1 and 63 pixels in extent.

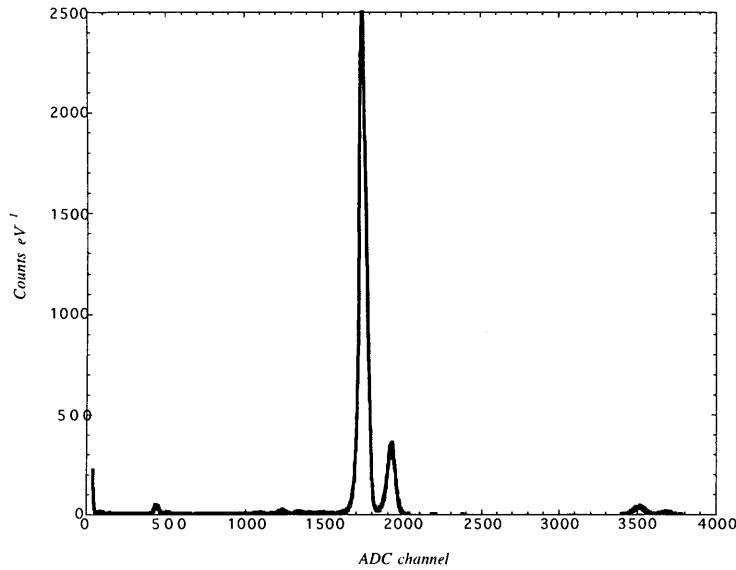


**Figure 3.13** A 1-63 pixel, summed event spectrum

In general, isolated event spectra give the highest possible spectral resolution, whilst summed event spectra give higher  $Q(E)$ .

#### *Quantum efficiency*

The  $Q(E)$  of a CCD is defined as the ratio of the number of recorded x-rays to the number of incident x-rays, and therefore takes a value between 0 and 1. The  $Q(E)$  may be non-unity mainly through the absorption of incoming photons before they reach an active part of the CCD or through a failure to absorb x-rays before they traverse the active part of the CCD. The former of these reduces the low energy  $Q(E)$  and the latter reduce the high energy  $Q(E)$ . As was seen in the previous section the JET-X CCD design incorporates both thinned electrodes for increased low energy  $Q(E)$  and high resistivity epitaxial Si for increased high energy  $Q(E)$ .

The  $Q(E)$  of a CCD as a function of x-ray energy follows smooth, well understood curves apart from at absorption edges where abrupt step-like changes in the value of  $Q(E)$  are caused by the onset of absorption in the inner shells of electrons. The absorption edges are also where the quantum mechanical nature of the photoelectron causes variations of the  $Q(E)$  which are attributable to absorption fine structures. This subject is dealt with in detail in Chapters 5 and 8. The realisation that the  $Q(E)$  of the CCD could behave in this



manner led to the experiments outlined in Chapter 4 and to the work in Chapter 7. Before this realisation occurred it was expected that the  $Q(E)$  could be established to the necessary accuracy (2%) using the test facility described in the next section, supplemented with Monte Carlo simulations of the CCD [McCarthy, 1994]. However, initial calibration work performed at the Daresbury Synchrotron Radiation Source (SRS) showed that the fine structure in the CCD  $Q(E)$  oscillates over a few eV in energy space with a magnitude of  $\sim 5\%$  above the absorption edge. This necessitated the measurement of CCD  $Q(E)$  at a synchrotron, which is tuneable in  $\sim 1$  eV steps and is highly stable.

### 3.5 The JET-X calibration facility

#### 3.5.1 Introduction

In order to calibrate JET-X CCDs to the necessary accuracy a dedicated JET-X test facility was built. It consists of a high vacuum beam line within the lab with one end extending into a class 1000 clean room. This allows spacecraft levels of cleanliness while handling the detectors and associated equipment. The detectors themselves are mounted onto their daughter boards on class 100 laminar flow benches before installation into a cryostat that can be pumped to low pressures.

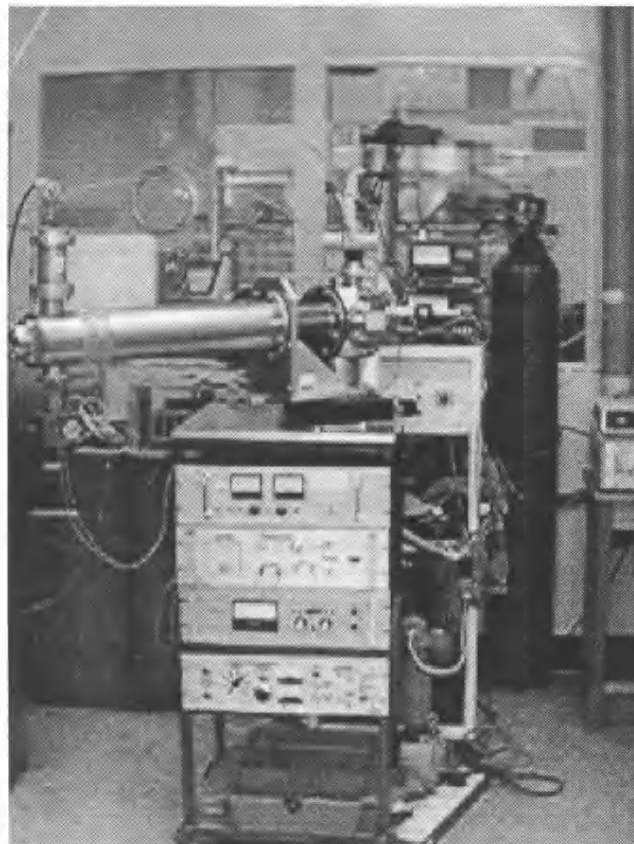


**Figure 3.14** The JET-X test facility at Leicester University

### 3.5.2 X-ray production

The facility is equipped with two x-ray sources; a soft x-ray source which can provide ~0.3 keV – 2keV x-rays, and a Kevex source for higher energy x-rays from ~2 keV – 10 keV. The soft x-ray source consists of an electron emitting element which bombards an anode causing fluorescent x-ray emission. The anode can be coated with various elements by painting on a suspension of a material in acetone, IPA or inhibisol. Characteristic x-ray lines are induced from the material which are then separated from the underlying continuum (bremmstrahlung) radiation by use of a Bragg crystal monochromator situated further down the beam line. Six Bragg crystals, mounted on a rotatable wheel, are used to provide good coverage of energy space across the 0.3 keV – 2 keV range. Higher energy x-rays are generated using a kevex electron impact source which uses fluorescence from targets on a rotating wheel.

The x-rays pass through a series of beam stops and optical filters to the cryostat containing the detector which is mounted in the clean room at the end of the beam line. The detector support table is fitted with accurate x-y tables to enable positioning of the detector within the x-ray beam. A proportional counter is used to monitor the incident beam intensity. In order that the counter can be used as a calibration standard, the relevant parameters (window area, quantum efficiency and transmission) have been accurately determined.

The energy values achievable with the test facility are listed in Tables 3.2 and 3.3.

Anode coating	Bragg crystal	Fluorescence line	Energy, eV ( $\pm 2\%$ )
SiC	PbSt	C K $\alpha$	277
CuO	PbSt	O K $\alpha$	525
MgF <sub>2</sub>	WTC	Fl K $\alpha$	677
CuO	RbAP	Cu L $\alpha$	930
MgF <sub>2</sub>	RbAP	Mg K $\alpha$	1254
SiC	RbAP	Si K $\alpha$	1740

**Table 3.2** The fluorescent lines available from the soft x-ray source.

Target element	Fluorescence line	Energy, eV ( $\pm 2\%$ )
Al	Al $K\alpha$	1487
Ti	Ti $K\alpha$	4510
V	V $K\alpha$	4952
Fe	Fe $K\alpha$	6404
Ni	Ni $K\alpha$	7478
Cu	Cu $K\alpha$	8048

**Table 3.3** The fluorescent lines available from the Kevex source.

It can be seen that the test facility provides only 12 points of reference over the whole of the operational range of the JET-X CCD.

The  $Q(E)$  is obtained absolutely with reference to a calibrated gas counter which is situated at the end of the beam line. A plot of the measured  $Q(E)$  of a JET-X CCD over the entire energy range of the test facility is shown in Figure 3.15.

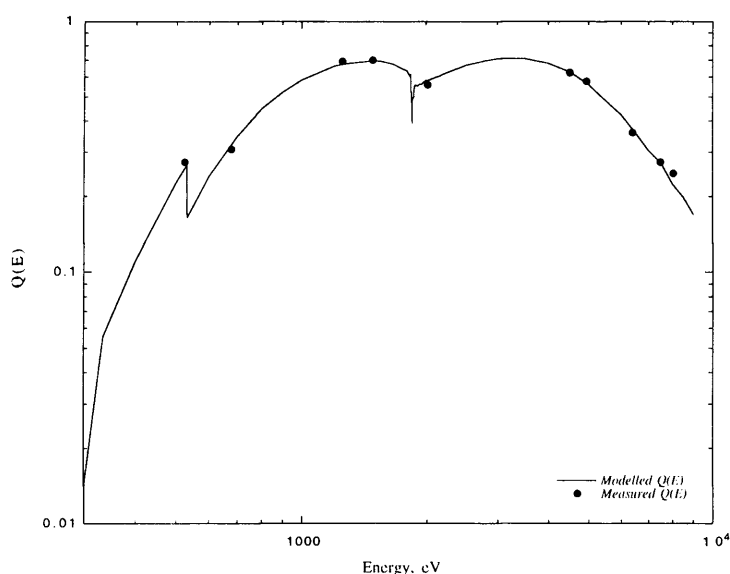


**Figure 3.15** The  $Q(E)$  of FM1 measured with the JET-X test facility along with the modelled  $Q(E)$

The continuous line in Figure 3.15 is derived by Monte Carlo modelling of the  $Q(E)$  response [McCarthy, 1994]. The measurement of  $Q(E)$  can only provide a constraint for the Monte-Carlo model, which is used to create the detector response matrix. However, the structure in the  $Q(E)$  caused by XAFS requires that measurements are made with at least 5 eV resolution around absorption edges. To do this in detail is obviously not possible with the test facility and needs a facility such as a synchrotron source.

## 3.6 The use of the SRS

### 3.6.1 Introduction

The Daresbury SRS provides high intensity, highly collimated electromagnetic radiation and when coupled to a double crystal monochromator, provides a monochromatic beam of x-rays continuously tuneable in  $< 1$  eV steps. Of these capabilities, all but high intensity are positive factors for accurate measurement of CCD  $Q(E)$ . CCDs suffer from an inability to measure the energy of an individual x-ray if a pixel receives more than one x-ray during an integration period. This “pile-up” sets the practical upper limit of the x-ray flux to  $\sim 1$  photon per 100 pixels or  $1400 \text{ x-rays cm}^{-2}$  for the JET-X CCD. The SRS provides  $\sim 1 \times 10^8 \text{ x-rays cm}^{-2} \text{ s}^{-1}$  at the experimental station which is 5 orders of magnitude higher than the CCD can cope with. A reduction of x-ray flux of  $\sim 5$  orders of magnitude is therefore necessary for CCD spectroscopy at the SRS.

Filters are not a good solution in this case for a number of reasons; i) the absorption cross-section of the filter material interferes with the flux causing a vast difference in the amount of time needed to obtain the required 1% accuracy for different x-ray energies, and as the experiments are conducted in an automatic manner this is highly impractical, ii) the flux is very sensitive to the thickness of the filter material, meaning that non-uniformities in filter thickness could jeopardise the experiment and iii) scattering, even at low energies, can be a problem.

To prevent these problems, a proposal was successfully submitted to the SRS Users Committee to reconfigure the SRS in a novel, low beam current, or “pico-beam”, mode. In this mode it was planned to reduce the beam current by five orders of magnitude to  $\sim 1 \mu\text{A}$  ( $10^6$  electrons) instead of the usual 200 mA, with a corresponding reduction in the output flux.

The SRS at Daresbury is a 3rd generation synchrotron beam. The operating parameters during normal operation are shown in Table 3.4.

Parameter	Value
First linear accelerator electron energy	2 MeV
Second booster synchrotron electron energy	600 MeV
Main storage ring electron energy	2 GeV
Storage ring current	150 mA to 300 mA
No. of electron bunches	160
Electron bunch width (FWHM)	180 ps
Circulating frequency	500 MHz
Storage ring circumference	96 m

**Table 3.4** The operating parameters of the SRS running at 200 mA beam current

Figure 3.16 shows the output of the SRS as a function of energy for operation at both 200 mA beam energy and at  $1 \mu\text{A}$ .

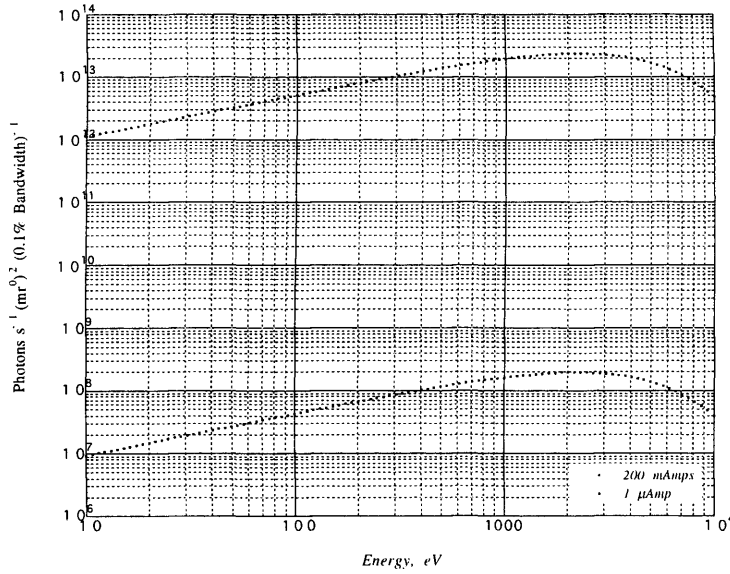


**Figure 3.16** The radiated power of the SRS.

### 3.6.2 Low beam current mode

The SRS was designed to operate with a beam current of  $\sim 200$  mA and all of the monitoring equipment is designed to match this type of operation. Under normal operation the SRS accumulates  $\sim 200$  mA quickly and delivers it to the storage ring in relatively large packets. However in low beam current mode only  $\sim 1$   $\mu$ A of circulating beam is called for and special steps are required to achieve the desired beam reduction with accurate monitoring. In fact a heavy reliance is placed on the user to provide additional beam diagnostics.

A method has been developed to accumulate a known low beam current, where a small but measurable current is injected into the storage ring. A radio frequency spectrum analyser is used to measure the magnitude of the 160th harmonic of the orbital frequency. The measurements can then be extrapolated back to the 1  $\mu$ A level. A throttled back injector is then allowed to inject beam at this level. The beam can then be stored and accelerated for the user. So far consistent results have been obtained on the four occasions that low current operation has been attempted. For example, in March 1994 the harmonic amplitude computed for the 1  $\mu$ A beam was  $-108.4 \pm 1.8$  dBm and in June 1994 it was  $-107.4 \pm 1.3$  dBm. The output of the SRS in low beam current mode is shown in Figure 3.16.

Once the basic method had been developed, further modifications were added - *e. g.*, orbital miss-steering and beam scrapping. This enabled the SRS to achieve an ultra-low current of 0.2  $\mu$ A in January 1995, with a new SRS beam record lifetime of 65.5 hours. The long lifetime was made possible because the low number of electrons circulating in the ring ensures that the inter-electron collision rate is negligible.

# 4

## Synchrotron Investigations of X-Ray CCDs

### 4.1 Introduction

The realisation that x-ray absorption fine-structure (XAFS) effects could introduce variations in the  $Q(E)$ , at the level of a few percent over a few eV in energy space, meant that the laboratory data points had to be supplemented by high resolution measurements. Since XAFS amplitudes are small (5%) compared with the overall atomic absorption, their measurement demands a very high signal to noise ratio ( $10^5$ ). Furthermore, the sharp features observed close to the edge demand high spectral resolution ( $\Delta E/E \leq 10^{-4}$ ). It is these two requirements that make synchrotron radiation sources, in conjunction with crystal monochromators or diffraction gratings, mandatory for XAFS experiments.

In this chapter the experiments carried out at the Daresbury Synchrotron Radiation Source (SRS) to measure the response of the CCD at the Si K, O K and N K edges are described in detail. In each section the experimental set-up, the measurements, the results and the conclusions are summarised.

### 4.2 First Tests

#### 4.2.1 Introduction

CCDs were taken to the Daresbury Synchrotron Radiation Source (SRS) for initial calibration tests in March 1994. These tests were carried out at Beamline 3.4 [Roper, 1992] of the SRS on a pair of CCD detectors, integrated together as EM3 - the third engineering model CCD package developed for JET-X. It was planned to systematically expose the CCD to x-ray photons with energies in the range 1830 eV - 2300 eV to measure the  $Q(E)$  and record, where possible, the XAFS modulation. Time constraints cut the upper energy range down to ~1920 eV.

#### 4.2.2 Devices

The EM3 mother-board carries two CCDs of differing construction, a thinned electrode CCD - 0481-12-04, and a thick electrode device - 9474-20-07. A diagrammatic representation of both devices can be seen in Figures 4.1a and 4.1b.

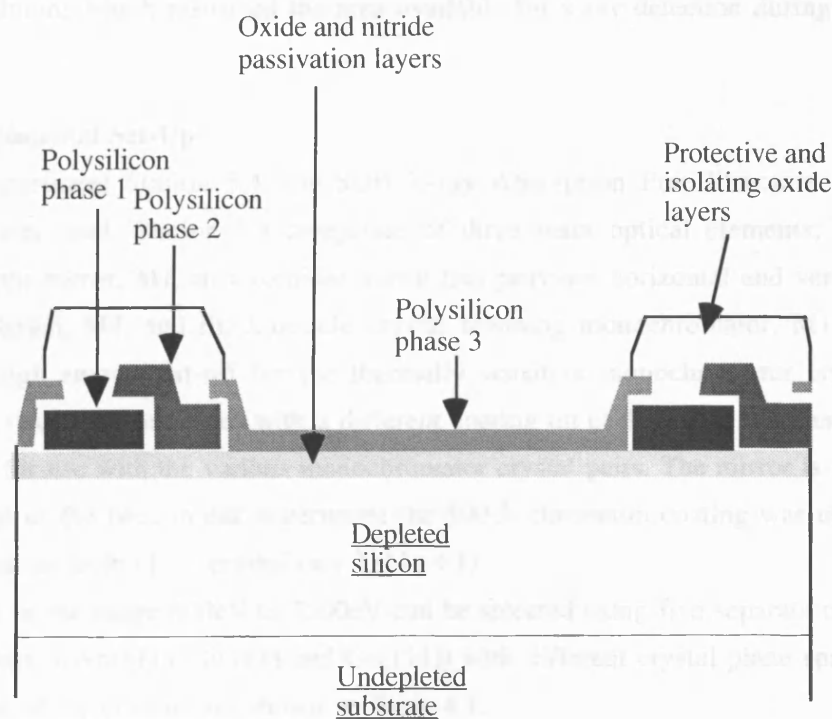


**Figure 4.1a** Cross sectional representation of the 0481-12-04 CCD showing the complex, thinned electrode structure

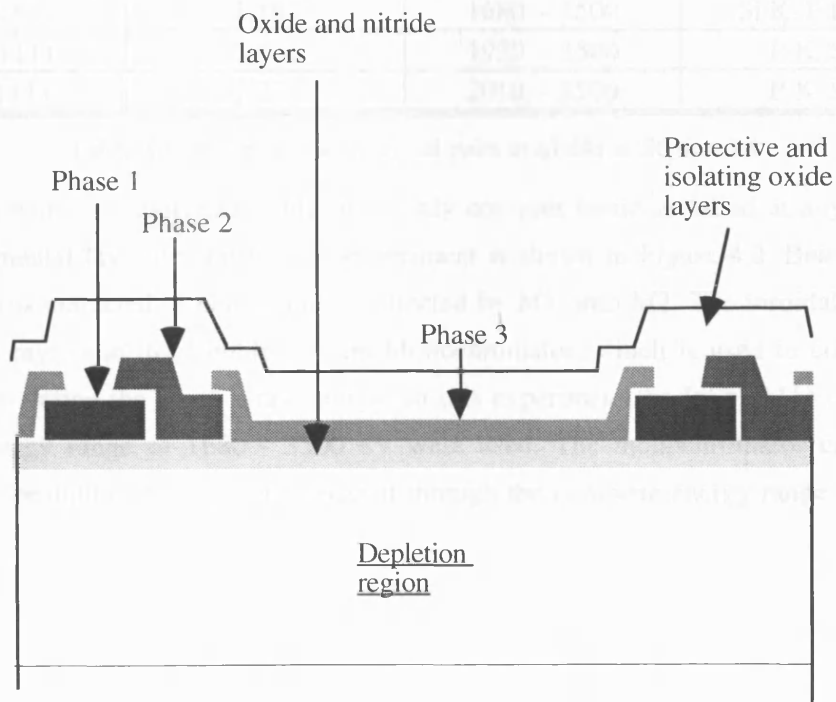


**Figure 4.1b** Cross sectional representation of the 9474-20-07 CCD showing the thick layer of oxide covering the electrode

In this experiment only the thinned, 0481-12-04 device was used. It exhibits three “bright” columns which restricted the area available for x-ray detection during the experiment.

#### 4.2.3 Experimental Set-Up

For this experiment Station 3.4, the SOft X-ray Absorption Fine Structure (SOXAFS) beam-line was used. Station 3.4 comprises of three main optical elements; i) a plane, chromium pre-mirror, M1, ii) a toroidal mirror that provides horizontal and vertical focusing of the beam, M2, and iii) a double crystal scanning monochromator. M1 is used to provide a high energy cut-off for the thermally sensitive monochromator crystals. The surface has two separate stripes with a different coating on each to give different reflectivity profiles for use with the various monochromator crystal pairs. The mirror is translatable to use either of the two. In our experiment the 500 Å chromium coating was used in conjunction with an InSb (111) crystal (see Table 4.1).

Energies in the range 800eV to 3500eV can be selected using five separate crystal pairs (Beryl, Quartz, InSb(111), Si(111) and Ge(111)) with different crystal plane spacings. The specification of the crystals are shown in Table 4.1.

Crystal type	2d spacing(Å)	Energy Range(eV)	Absorption edges
Beryl	15.954	800 - 1560	Cu L, Na K, Mg K
Quartz	8.512	1500 - 1830	Al K
InSb(111)	7.481	1680 - 3500	Si K, P K, S K
Ge(111)	6.532	1930 - 3500	P K, S K
Si(111)	6.271	2010 - 3500	P K, S K

**Table 4.1** Monochromator crystal pairs available at Station 3.4

The crystal pairs are interchangeable, with only one pair being installed at any one time. The experimental lay-out used for our experiment is shown in Figure 4.2. Beam from the synchrotron is extracted at port 3 and is reflected by M1 onto M2. The toroidal mirror focuses the x-rays onto the Double Crystal Monochromator, which is used to collimate the beam and to define the input x-ray energy. In this experiment the InSb (111) crystal pair, with an energy range of 1680 - 3500 eV were used. The monochromator can be controlled by a beamline PC in order to scan it through the complete energy range.



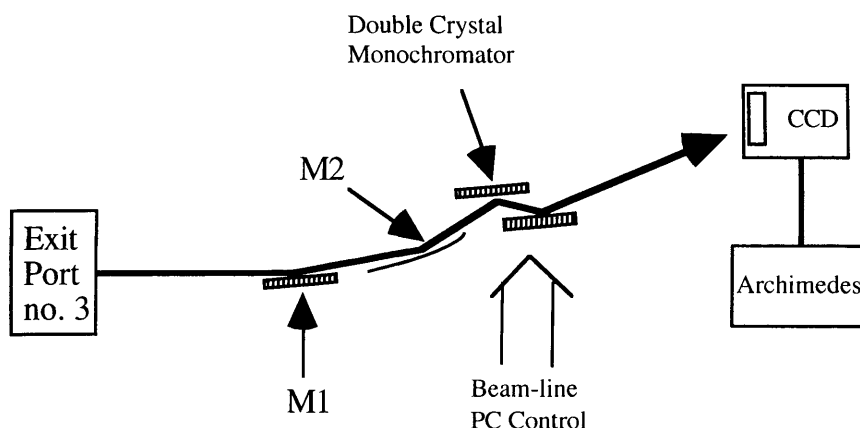


**Figure 4.2** The experimental lay-out of beam-line 3.4

The CCD control and acquisition system was essentially the same as that described in Chapter 3. The CCD was mounted in a vacuum cryostat which was turbo-pumped and coupled by a flexible bellows to the end of the beam line. The CCD was cooled to  $\sim 183$  K by a copper cold finger connected to a liquid nitrogen dewar. This eliminated CCD dark current (thermally generated, conduction band electrons) and reduced readout noise. The output signals from the CCD were fed to low-noise pre-amplifiers and then to an analogue processor which performed dual-slope-integration to remove the CCD reset noise. The resultant signal was then digitised to 12 bits and processed by an Archimedes A5000 micro-computer. The A5000 also controlled the experiment via an RS232 serial communication link with the beamline PC using software developed at Leicester, and supported data collection and analysis tasks. Table 4.2 lists the relevant parameters for the tests.

Beamline & Station	3.4
Synchrotron beam current	0.2 $\mu\text{A}$
Synchrotron beam energy	1.998 GeV
Recorded count rate @ CCD	72.7 counts $\text{s}^{-1} \text{cm}^{-2}$
Test system noise	3.69 electrons (rms)
CCD Integration time	6 s
CCD full-frame readout time	12 s
Amplifier integration time	6 $\mu\text{s}$
System calibration	1.43 eV channel $^{-1}$
Energy scan	1830 eV - 1920 eV

**Table 4.2** Summary of relevant parameters for March 1994 tests

Since the monochromator position was controlled by an IBM PC, we were able to connect together the A5000 and PC to enable experimental control via the A5000. The CCD was exposed to x-rays from 1832 eV to 1900 eV in 1 eV steps and 1900 eV to 1920 eV in steps of 2 eV. At each monochromator setting 6 frames of data were recorded at 16 s per frame giving approximately 20,000 events per energy which ensured noise statistics were less than 1%. The data were corrected *post priori* for beam decay and variation with

monochromator position. As can be seen from the table, the system noise was at the very low level of 3.69 electrons (rms). This reflects the inherent stability and low noise of the environment around Beamline 3.4 during the experiment.

#### 4.2.4 Results

##### *Data acquisition*

After the initial beam studies period the beam was reconfigured to give a monitored count rate of  $72.7 \text{ counts s}^{-1} \text{ cm}^{-2}$  at an incident x-ray energy of 1850 eV. Figure 4.3 shows a typical Pulse Height Distribution (PHD) recorded at Beamline 3.4 with the 0481-12-04 CCD. This is an isolated event PHD, recorded at 1832 eV and shows the inherent resolving power and high signal-to-noise ratio of the CCD. There are a total of 11121 counts recorded in the main absorption peak around channel 1277, with a corresponding uncertainty of 0.95%. There are 76 events in the peak centred on channel 2592 due to a small amount of pile-up photons. The number of such events has been calculated to be 0.5% which is in good agreement with the observed value of  $\sim 0.6\%$ .

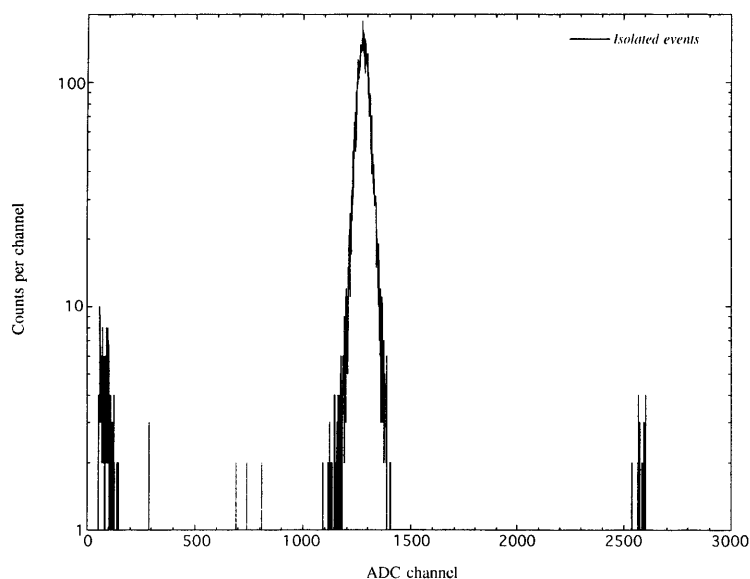


**Figure 4.3** Isolated event PHD of 1832 eV x-rays recorded at Beamline 3.4 of the SRS with the 0481-12-04 CCD in March 1994. The FWHM resolution of the main peak is 82.8 eV.

The raw, measured counts versus energy spectrum for 1-63 pixel events can be seen in Figure 4.4.

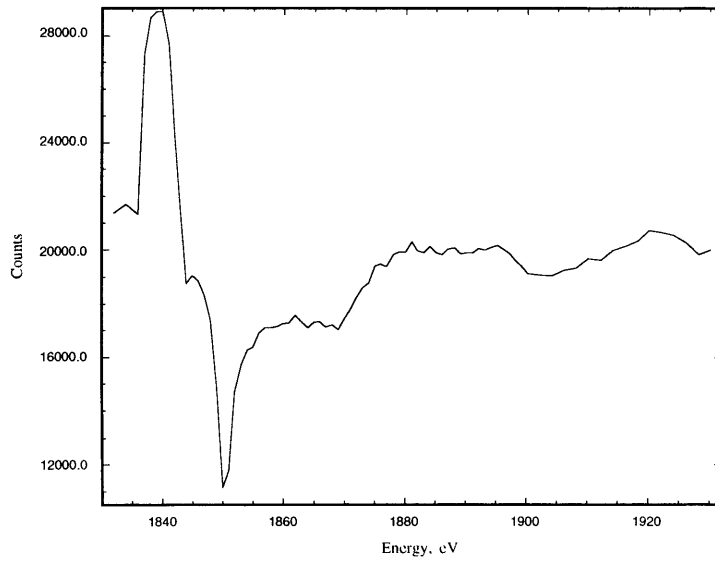


**Figure 4.4** The raw, measured counts versus energy spectrum for 0481-12-4 from Daresbury, March 1994.

*Beam decay and monochromator response: Obtaining the  $Q(E)$*

To derive the  $Q(E)$  for the device the measured counts must be corrected for the variation of the beam intensity with both time and monochromator position. The beam decay is calculated using measurements at the same energy taken at different times during the experiment. Equation (4-1) is obtained which is used to correct the measurements,

$$N_m = N_r \times \exp(-2.3303 \times 10^{-5} \times t) \quad 4-1$$

where  $N_m$  are the measured counts,  $N_r$  are the corrected counts and  $t$  is the elapsed time in seconds. The variation in beam intensity with monochromator position was taken to be that measured before the low current experiment. The normalisation was fitted with a second order polynomial over the energy range of interest here. The equation of the polynomial is

$$n = 2.89462 - (0.002596 \times E) + (8.52 \times 10^{-7} \times E^2) \quad 4-2$$

where  $n$  is the normalisation factor to be applied to the counts and  $E$  is the energy of the incident x-rays.

The measurements are then converted from counts to quantum efficiency by normalising to laboratory measurements. The  $Q(E)$  curve is shown in Figure 4.5 for multiple pixel events. As a comparison, the shape of the edge based on the attenuation coefficients found in Saloman, Hubble and Scofield [Saloman, 1988] is shown.

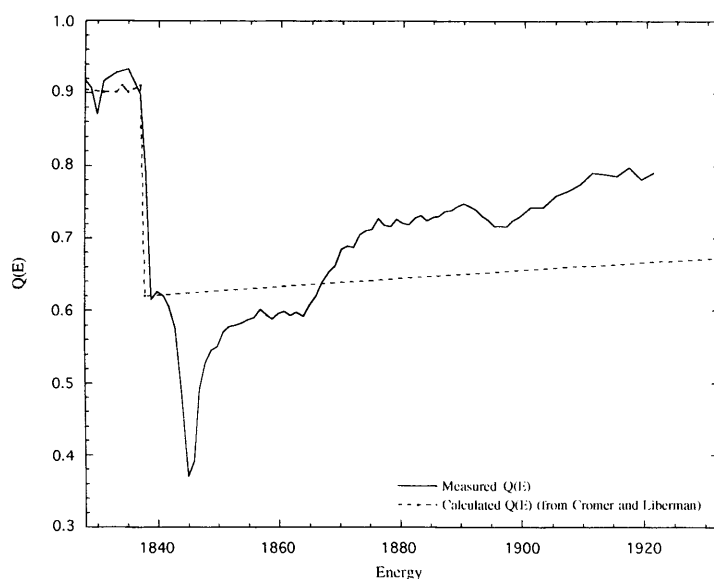


**Figure 4.5** The  $Q(E)$  of the 0481-12-04 JET-X CCD

This measurement clearly shows XAFS modulation superimposed on the absorption edge. As well as the Si absorption edge at 1838 eV, a minima due to absorption in the  $\text{SiO}_2$  at 1845 eV is also visible. A detailed discussion of this latter feature is included in Chapter 8, where a detailed analysis of this data is also described. EXAFS begin around 1850 eV and extend out to the limit of the data at 1920 eV.

### *Linearity*

The linearity,  $E_{\text{meas}}/E_{\text{real}}$  of the CCD is shown in Figure 4.6.

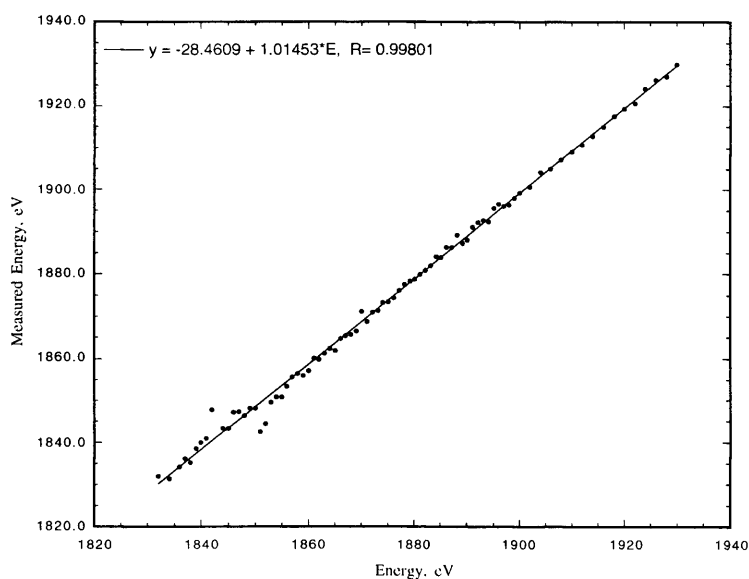


**Figure 4.6** The linearity of the CCD measured at the SRS, March 1994

An analysis of the PHDs has demonstrated that the energy required to create an electron-hole pair,  $\omega$ , is, in fact, energy-dependant [Owens, 1996]. This has confirmed the theoret-

ical predictions of Fraser [Fraser, 1994].  $\omega$  is calculated from the ratio of the measured PHD energy,  $E_{\text{meas}}$ , to the true energy,  $E_{\text{real}}$ . In Figure 4.7,  $\omega$  is plotted as a function of energy.

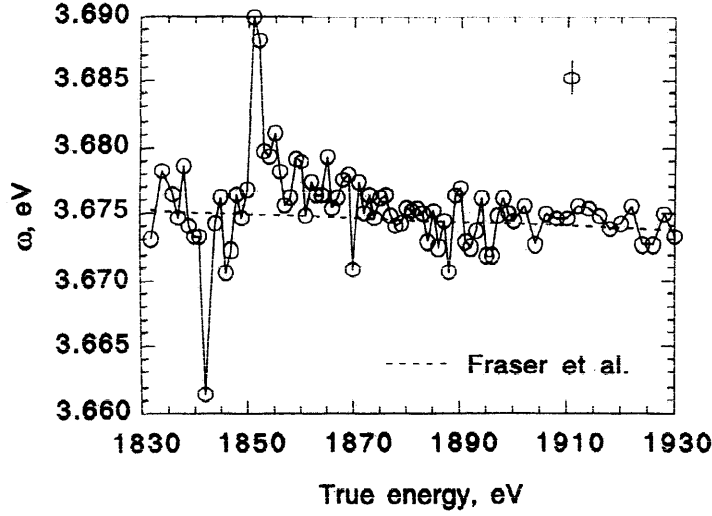


**Figure 4.7** The variation with energy of  $\omega(E)$  [Owens, 1996]

The theoretical prediction of Fraser [Fraser, 1994] is also shown for comparison. The change in  $\omega$  across the edge is +0.2%.

#### *Measured FWHM*

The Fano factor,  $F$ , can be estimated from the measured FWHM of the PHDs. Figure 4.8 shows  $F$ , extracted from the measurements at Daresbury.

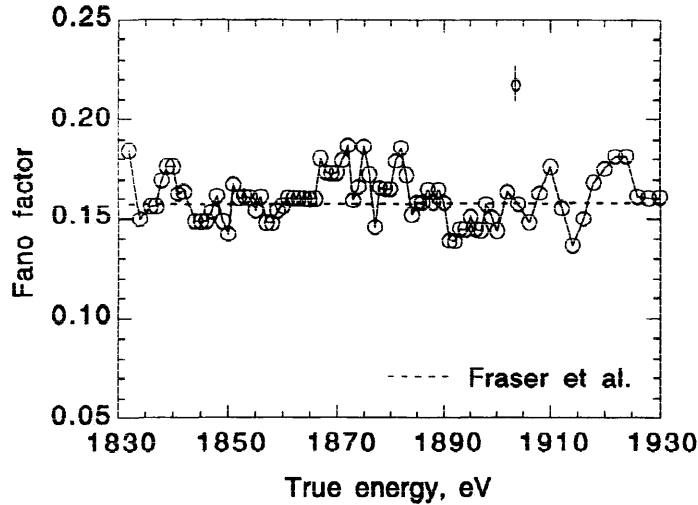


**Figure 4.8** The Fano factor as a function of energy for the 0481-12-4 CCD versus energy [Owens, 1996]

The measurements show good agreement with the theoretical predictions of Fraser [Fraser, 1994] but, because of the limited energy range, it was not possible to confirm the global energy dependence predicted by this theory, or the experimental analysis of Owens

[Owens, 1996]. However, the author has been involved in the detailed investigation of the Fano factor in silicon by the Leicester Group [Owens, 1997].

#### 4.2.5 Discussion

The  $Q(E)$  measurements taken at Daresbury in March 1994 display EXAFS and XANES, both of which had never before been seen in an x-ray CCD operated as a spectrometer. Since virtually 100% of x-rays which reach the depletion region of the CCD are absorbed, it can be concluded that these structural contributions are caused by changes in absorption in the electrodes and dead-layers. A detailed examination of the fine-structures in the CCD  $Q(E)$  is discussed further in Chapter 8. However, it is useful to point out here that the  $Q(E)$  shows minima at both  $\sim 1839$  eV due to Si, and at 1845 eV due to  $\text{SiO}_2$ . Si and  $\text{SiO}_2$  are both used in the electrodes and dead-layers above the depletion region. This reinforces the idea that XAFS are caused by changes in x-ray transmission through the inactive layers of the CCD. The work has also shown that the response of a CCD near absorption edges is more complicated than predicted by conventional modelling. Using these measurements, significant structure in  $\omega$  has been observed. The results show that  $\omega$  varies with energy and confirm the theoretical predictions of Fraser [Fraser, 1994].

### 4.3 Low Energy Tests

#### 4.3.1 Introduction

During the work on the Si K absorption edge it was realised that XAFS around other absorption edges could also affect the detailed response of the CCD. Although a CCD is manufactured from silicon, other elements are present in various amounts. Oxygen is found in the oxide layers added to the CCD for passivation and protection. A silicon nitride layer is added to the device to prevent further oxidation and to inhibit the absorption of impurities. Phosphorus and boron are used, as dopants, to provide the necessary levels of resistivity in the electrodes and the epitaxial layers. All of these materials modify the absorption of x-rays by the CCD and hence it should be possible to see absorption edges and, if measured in enough detail, XAFS from some or all of them. After silicon, the elements present in the largest proportion in the CCD are oxygen and nitrogen and consequently the energy range containing the oxygen and nitrogen K edges was analysed next.

In this section, measurements of a JET-X CCD  $Q(E)$  in the range 0.3 keV to 1.0 keV are described. In particular, attention has been paid to the O K ( $E_b = 538$  eV) and the N K ( $E_b = 408$  eV) absorption edges, where fine-structure effects can occur. A new, open electrode device, developed for the XMM project [Wells, 1989], was also taken to the SRS, to enable a comparison of the low energy  $Q(E)$ s of the two CCDs. The new mode of synchrotron operation used in the Si K edge studies was again utilised to provide x-rays at high spectral resolution ( $\Delta E/E \leq 10^{-3}$ ). The CCDs were taken to Station 1.1 of the SRS on

3<sup>rd</sup> - 6<sup>th</sup> January 1995 where they were both systematically exposed to low energy x-rays. Station 1.1 [Surman, 1992] at the Daresbury SRS provides low energy photons over the energy range 0.2 keV to 1.2 keV, with a limiting resolution of better than 1 eV. In order to fully measure the low energy  $Q(E)$  of both devices an energy spacing of  $\sim 20$  eV was required throughout the nominal energy range. To resolve fine structure, more detailed measurements around the absorption edges using the maximum spectral resolving power of the station were necessary.

#### 4.3.2 Devices

Measurements were made on two CCDs with different surface morphologies, a JET-X thinned electrode CCD [Wells, 1990] and a new open electrode CCD [Holland, 1993]. The thinned electrode devices used were those integrated in EM2, the second engineering model designed for JET-X. The two CCDs are 0481-11-07 and 0481-11-08. Both CCDs are essentially the same as the thinned electrode, 0481-12-04 device in the EM3 package which is shown in Figure 4.1a. A full description of this device is provided in Chapter 3.

Figure 4.9 shows a schematic cross section of an open electrode CCD. This device is also three-phase and front illuminated.

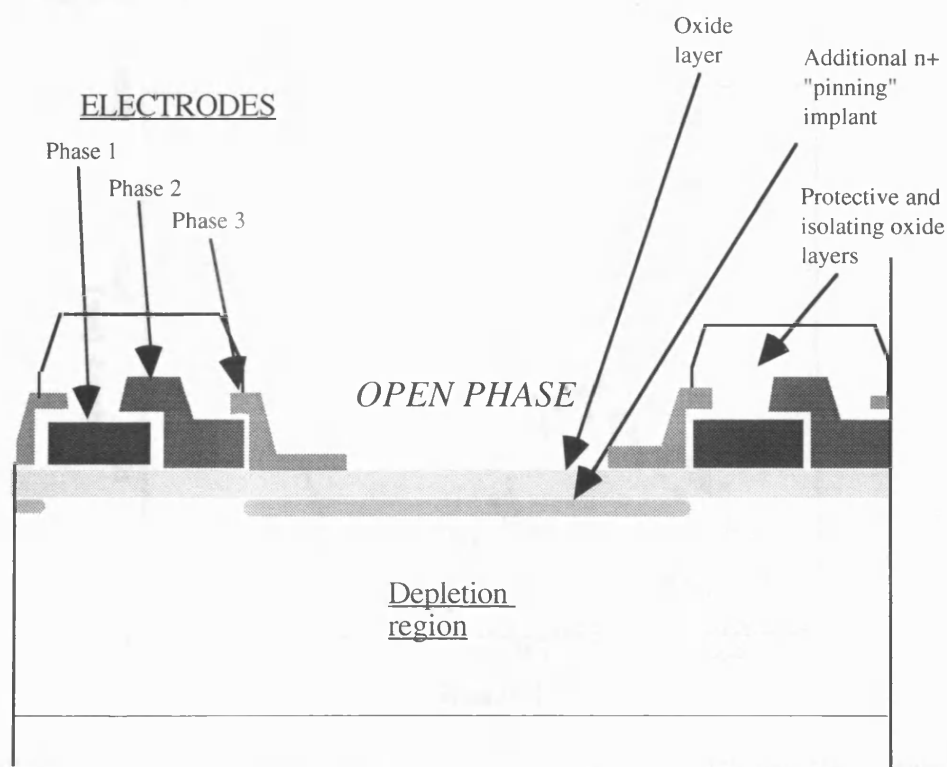


**Figure 4.9** Cross section of an open phase CCD electrode structure

The CCD is fabricated from high resistivity silicon ( $8000 \Omega\text{cm}$ ) and is fully depleted to a depth of  $85 \mu\text{m}$ . Thinned electrode technology is extended by completely opening a hole

in one electrode down to the silicon nitride layer. The open area constitutes about 30-40% of the total surface area of the CCD with the underlying oxide layer still only 0.085  $\mu\text{m}$ . The nitride layer is not present. To maintain charge transport throughout the array, the remainder of the pixel area is a conventional three-phase design.

This type of device will be used for the EPIC instrument on XMM [Holland, 1993], it is very transmissive to low energy x-rays and provides an extension to the usable response of a CCD down to the EUV region at  $\sim 20$  eV. Discrete line measurements have shown that open electrode technology greatly improves the quantum efficiency of the CCD to  $\sim 35\%$  at 300 eV [Holland, 1995], whereas the  $Q(E)$  of a conventional, thinned electrode CCD rolls off to  $\sim 5\%$ . The hole in the electrodes prevents the application of bias, so a pinning implant is used to control the potential within the device. This is essential to promote the correct field structure and to allow generated charge to be efficiently collected in the potential minima under the electrodes. However, the presence of the pinning implant adversely reduces both the mean, achievable depletion depth, and the charge transfer efficiency (CTE) of the CCD. The imperfect CTE degrades the PHD of the open electrode device, producing both broadened gaussian distributions and partial event tailing, and the reduced depletion depth affects the high energy response.

Figure 4.10 shows measured PHDs for both types of device to carbon  $K_{\alpha}$  x-rays (277 eV) [Holland, 1995].

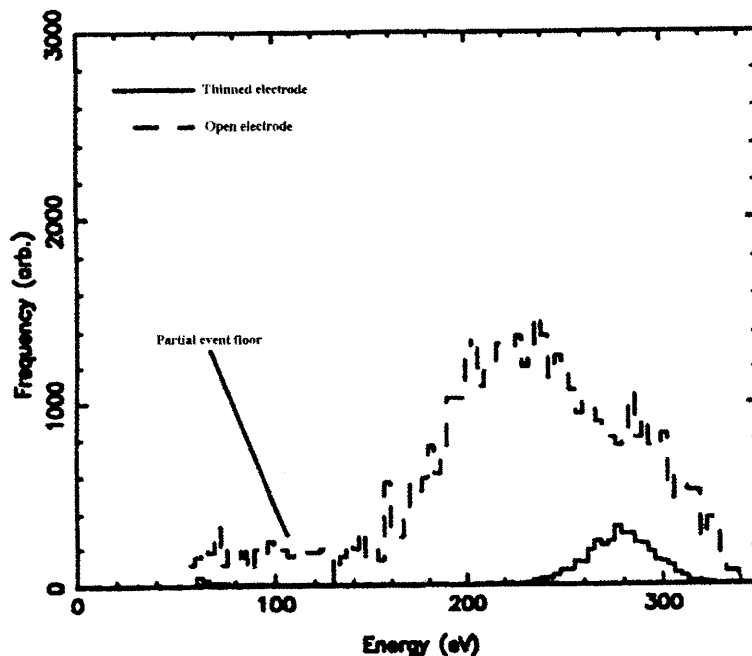


**Figure 4.10** Spectra recorded at carbon K edge (277 eV) with open and thinned electrode devices [Holland, 1995].

The thinned electrode device gives an ideal spectral performance with FWHM resolution near the theoretical minimum of 50 eV, but the  $Q(E)$  of the device at this energy is only  $\sim 2\%$ . The open electrode device has a  $Q(E)$  of  $\sim 30\%$  at  $\sim 300$  eV but it has a degraded



spectral response due to the presence of the pinning implant. In the open electrode device the response at carbon can be resolved into two gaussian peaks plus a partial event floor, the lower of the peaks and the partial events are from interactions in the implant layer [Holland, 1995]

### 4.3.3 Experimental Set-Up

Measurements were carried out on Station 1.1 at the Daresbury SRS. This is an Ultra-High-Vacuum (UHV) beamline, providing monochromatic x-ray photons suitable for surface x-ray absorption, photo-emission and photoelectron diffraction experiments, and studies in the area of structural material science (XAFS). The heart of the beamline is the High Energy Spherical Grating Monochromator (HESGM), an entrance slitless instrument providing high photon flux and coverage of the energy range 200 eV to 1400 eV. The layout of the beamline is shown in Figure 4.11

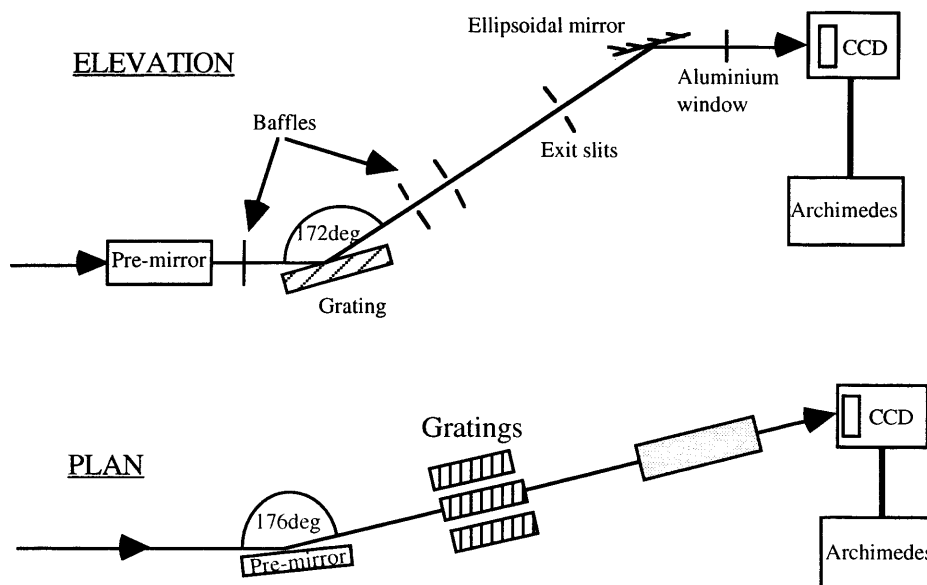


**Figure 4.11** A schematic of the layout of Beamline 1.1

The optical elements are: a horizontally deflecting water cooled cylindrical mirror (Pt-coated SiC), three interchangeable, spherical, gold coated gratings of line density 1050, 1500 and 1800 lines  $\text{mm}^{-1}$  respectively, and a post-focusing mirror (Pt coated ellipsoid with 2:1 demagnification). A series of exit slits are provided at exit arm lengths tailored to the true radius of each individual grating. A permanently installed vessel behind the post-focusing mirror allows continuous monitoring of the ' $I_0$ ' signal - the photon flux passing into the user's end chamber [Surman, 1992].

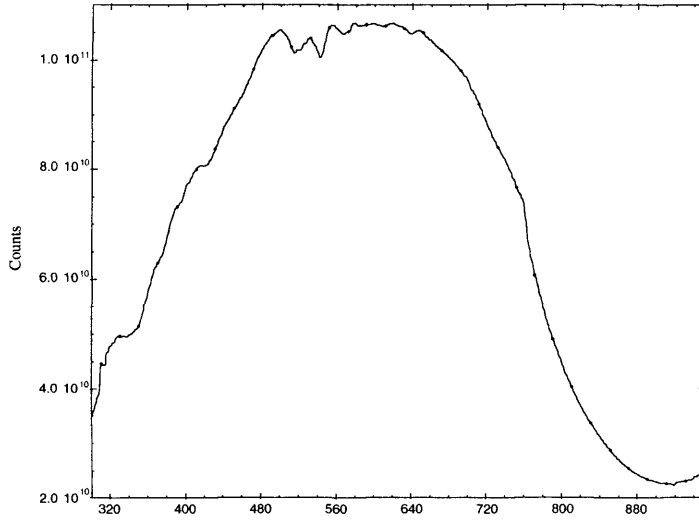


**Figure 4.12** The output flux from Beamline 1.1 for the 1050 mm<sup>-1</sup> grating measured as a function of selected x-ray energy during normal beam operation [Surman, 1992].

For these experiments the 1050 mm<sup>-1</sup> grating was used, it has a usable response from ~200 eV to ~1000 eV. The output flux from the grating in normal operation is shown in Figure 4.12. This was measured during normal beam operation as the 'I<sub>0</sub>' monitor did not function under the novel conditions of the low beam current operation. The resolution of the 1050 mm<sup>-1</sup> grating is shown in Figure 4.13, again this was measured during normal operation.

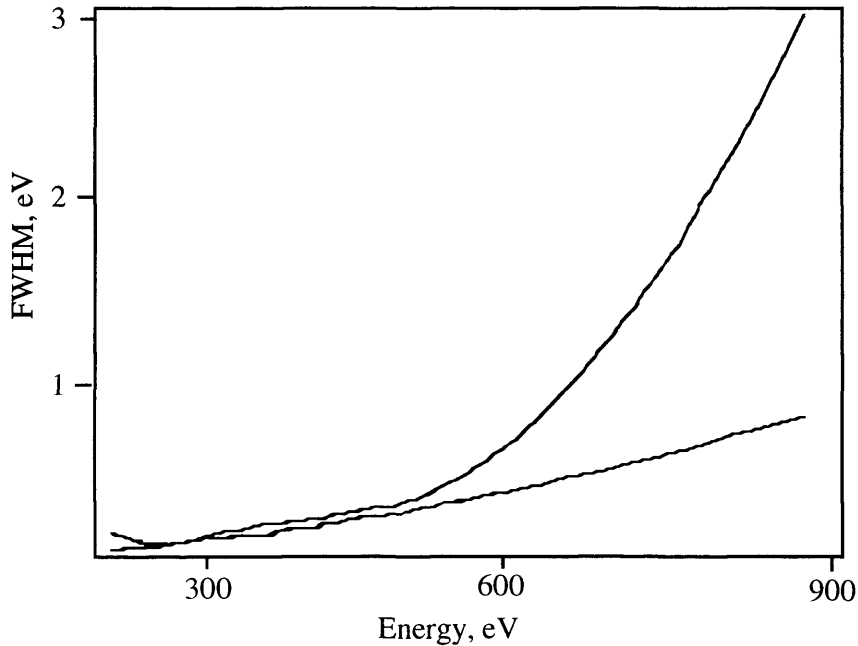


**Figure 4.13** The FWHM resolution of the 1050 mm<sup>-1</sup> grating as a function of x-ray energy. The upper curve is the calculated resolution including defocus, and the lower curve is the source-size limited resolution [Surman, 1992].

The photon flux from the synchrotron was extracted from bending magnet 1. The beam was then focused on to the grating using the cylindrical mirror where it was vertically diffracted. The light emerging from the exit slit was refocused to the CCD position by the ellipsoidal, post-focusing mirror. Adjustable baffles within the beam pipes reduced the zero order scattered radiation to a negligible level.

Beamline control was provided by a dedicated PC-CAMAC-GPIB-RS232 system, running software developed at Daresbury Laboratory, this is shown in Figure 4.14. For non-UHV experiments, such as our CCD measurements, the end chamber is installed behind a thin (0.15  $\mu\text{m}$ ) aluminium window which protects the integrity of the beamline vacuum.

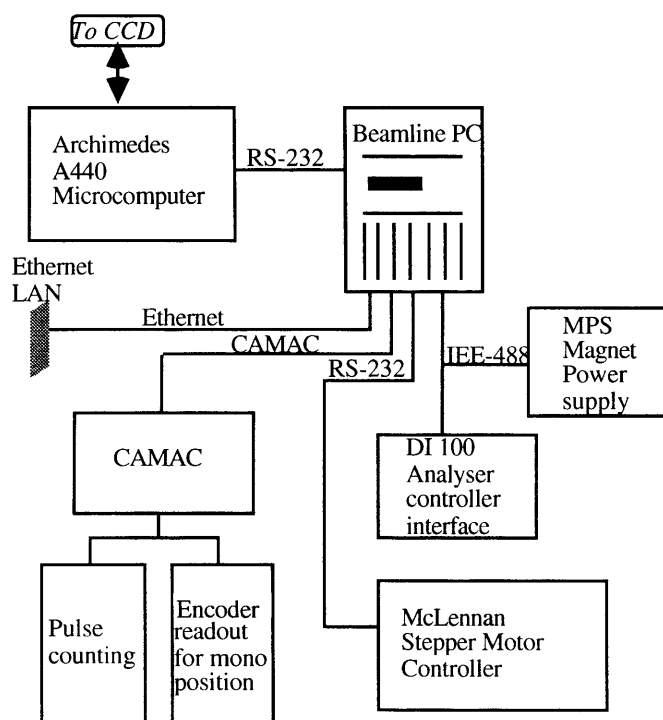


**Figure 4.14** The beamline control system and integration with CCD experimental equipment.

The CCD was mounted in the vacuum cryostat already described in the Chapter 3. The beam spot was centred on the CCD with the aid of an adjustable stand designed for use at this beamline. As is usual in CCD operation, to minimise read-out noise the CCD was cooled to  $\sim 180$  K by a copper cold finger connected to a liquid nitrogen dewar. The average readout noise during the experiment was 3.40 electrons (rms), reflecting the stability and low noise of the environment around Station 1.1. The main experimental parameters are summarised in Table 4.3.

The output signals from the CCD were fed to low-noise pre-amplifiers and then to an analogue processor which performed dual-slope-integration to remove the CCD reset noise. The resultant signal was digitised to 12 bits, implying a limiting resolution of  $<1\%$ , which compares well with the grating resolution shown in Figure 4.13. The digital signal was then processed by an Archimedes A440 microcomputer. The A440 also controlled the

experiment via an RS232 serial communication link with the beamline PC using software developed at Leicester, and supported data collection and analysis tasks.

Beamline & Station	1.1
Synchrotron beam current	0.2 $\mu\text{A}$
Synchrotron beam energy	1.998 GeV
Beam lifetime	~65 hours
Recorded count rate @ CCD	116 counts $\text{s}^{-1} \text{cm}^{-2}$ (77 counts $\text{s}^{-1} \text{cm}^{-2}$ , 1st order events)
Test system noise	3.40 electrons (rms)
CCD Frame time	6 s
CCD Readout time	12 s
Amplifier integration time	10 $\mu\text{s}$
System calibration	1.35 eV channel <sup>-1</sup>
Energy scans	300 eV - 1000 eV at low resolution Around the edges at high resolution

**Table 4.3** Summary of relevant test parameters for January 1995 tests at the Daresbury SRS

#### 4.3.4 Results

##### *Data acquisition*

After an initial beam studies period, the synchrotron was reconfigured to give a beam current of  $\sim 0.2 \mu\text{A}$ , which provided a recorded x-ray flux of  $\sim 117 \text{ cm}^{-2}\text{s}^{-1}$  at the detector, of which  $77 \text{ cm}^{-2}\text{s}^{-1}$  were first order events. This was achieved by reducing the beam current and then deliberately mis-steering the beam. At this low beam current the 'I<sub>0</sub>' flux monitor would not function, so the response of the grating was recalibrated prior to beginning the experiment (see Figure 4.12).

During the experiment the grating was scanned in 20 eV steps from 300 eV to 1000 eV. Near the absorption edges the spacing between contiguous measurements was reduced to 10 eV, then to 2 eV and finally to 1 eV in the region where structural effects are most important, *i. e.* immediately after the edges. At most monochromator settings a single PHD was recorded, while more than one PHD was recorded for a few energies to check the beam decay. The integration time for each PHD was chosen to reduce statistical uncertainty to the  $\sim 1\%$  level or below, *i. e.* at least  $10^4$  events were recorded in each PHD. However as the  $Q(E)$  of the devices drop to very low levels around the absorption edges this became increasingly difficult due to time constraints. Therefore a compromise was achieved where approximately 20 frames of data were accumulated at each setting, corresponding to a total integration time of approximately 7 minutes per recorded file.

Figure 4.15 shows a typical isolated event PHD measured during the experiment with the JET-X CCD at 600 eV. For an isolated event detection criterion, x-rays are defined to be those events in which the released charge is confined to a single pixel. For soft x-ray photons this registers 100% events whilst rejecting  $> 99\%$  of high energy x-rays and

charged particle events. In Figure 4.15 the 1st, 2nd and 3rd orders of radiation from the gratings are clearly resolved. The measured FWHM resolution of the main x-ray peak is 56.94 eV ( $E/\Delta E = 10.54$ ), the grating resolution at this energy is  $\sim 0.5$  eV.

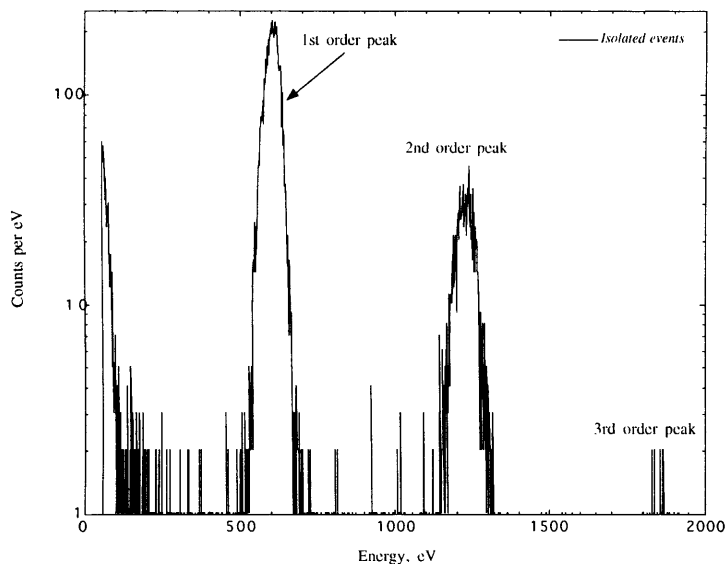


**Figure 4.15** Incident x-ray spectrum of 600 eV events recorded with the JET-X CCD at Beamline 1.1 of the SRS in January 1995. The different orders of radiation from the monochromator are clearly resolved. The FWHM energy resolution is 56.94 eV

Figure 4.16 shows the array of measured, multiple pixel event counts versus energy recorded in the JET-X CCD. This is completely raw data and, apart from being normalised to the same number of recorded frames, in this case 20, have not been corrected for any experimental factors. This measurement shows the nitrogen K edge at  $\sim 400$  eV and the oxygen K edge at  $\sim 540$  eV with associated structure.

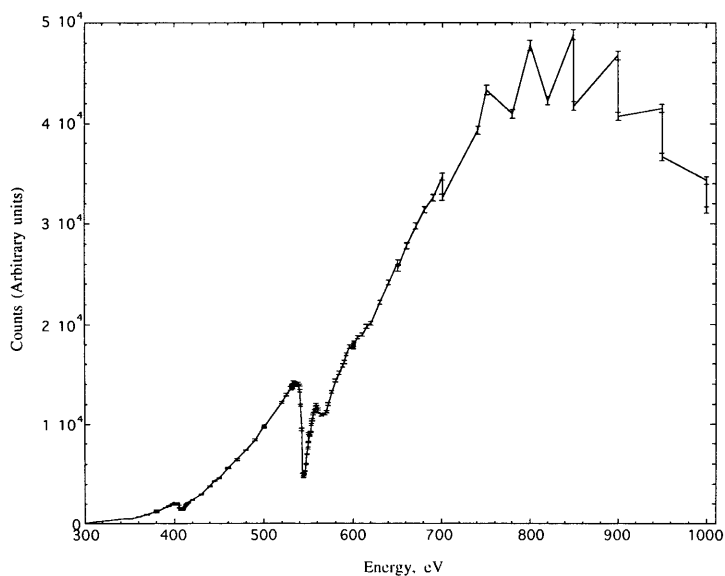


**Figure 4.16** The measured counts versus energy for the JET-X CCD.

There are several ‘glitches’ in this data, most noticeably at high energies, this is because the effects of beam decay have not yet been removed. The high energy variation in counts is due to the measurements being recorded at different times during the experiment.

*Beam decay, grating and filter response, and deglitching*

To obtain an accurate measurement of counts versus energy and to enable proper normalisation, artefacts in the spectra from sources other than the CCD had to be removed. For beamline 1.1 such effects can be caused by the gratings, the aluminium window and the reduction in the flux from the beam due to its natural decay. The low current, or pico-beam, mode of synchrotron operation has already been documented in Chapters 3. One of the side-effects of only circulating  $\sim 1 \mu\text{A}$  in the ring is the low number of electron collisions that occur. This causes the lifetime of the beam to be significantly prolonged. For the calibration campaign carried out in January 1995 a beam current of only  $0.2 \mu\text{A}$  was achieved with a new SRS record lifetime of 65.5 hours. As the beam decays, the flux from the synchrotron is exponentially reduced and the  $1/e$  lifetime can be estimated using measurements at the same energy recorded at different times. Equation (4-3) is obtained and applied to the measured counts to correct for beam decay.

$$N_0 = \frac{N}{\exp(-0.000254452 \times t)} \quad 4-3$$

where  $t$  is time of measurement relative to a given start time,  $N$  and  $N_0$  are the measured and the corrected counts. Once this process had been applied to the data there were still some spurious points where the correction was imperfect or where the data was corrupted for some other reason. Where there was more than one measurement at a given energy these glitches were removed by substituting conflicting data points with more reasonable ones. When only one measurement existed it was replaced by the average value of the neighbouring points on either side. Caution must be exercised when correcting values in the regions near the absorption edges, but fortunately glitches were found only at energy values far removed the edges. Figure 4.17 shows the results of the beam decay subtraction and deglitching described above. It can be seen that the wildly varying values at high energies have been completely corrected by applying the beam decay correction while the rest of the spectrum retains integrity.

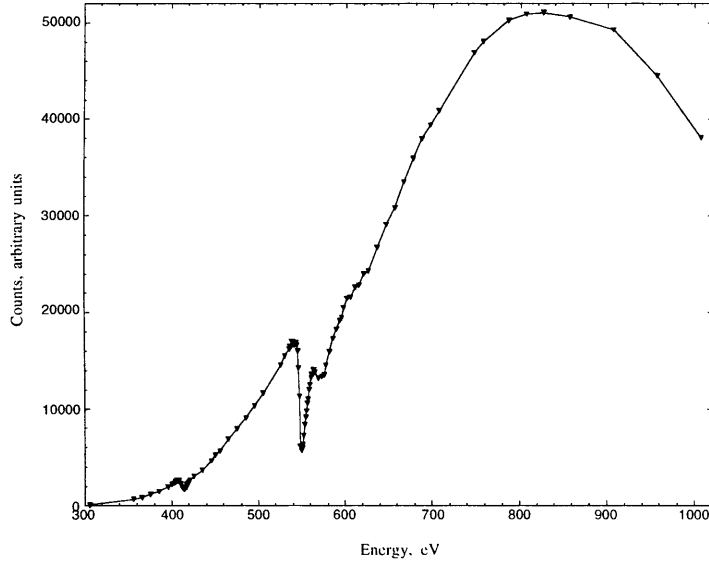


**Figure 4.17** The measured counts versus energy plot for the JET-X CCD after the beam decay correction and deglitching process have been applied.

To maintain the high vacuum of the beamline, our experiment was installed behind a  $0.15 \mu\text{m}$  Aluminium window. The window preferentially transmits higher energy x-ray photons as can be seen from the plot of the window transmission in Figure 4.18.

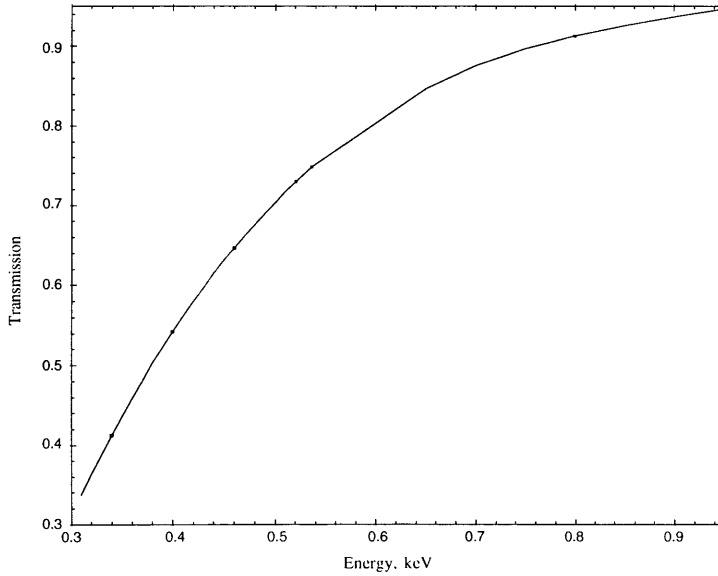


**Figure 4.18** Transmission of the  $0.15 \mu\text{m}$  Aluminium window.

To remove the effect of the window transmission from the Daresbury data-sets, a model of the transmission of the Al window was obtained which had the functional form

$$T = -0.93938 + (0.0058347 \times E) - (6.257 \times 10^{-6} \times E^2) + (2.3223 \times 10^{-9} \times E^3) \quad 4-4$$

where  $T$  is transmission and  $E$  is the energy of the incident x-ray photons. This equation was then used to adjust the CCD measurements. The CCD measurements were corrected for the grating response by dividing them by the normalised flux from the grating at each energy point. The normalised flux from the grating, derived from the data shown in Figure 4.12, is shown in Figure 4.19.

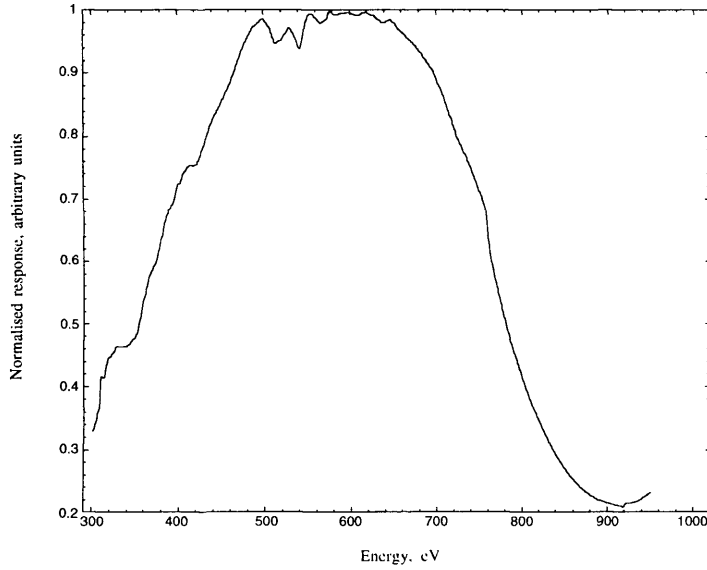


**Figure 4.19** The normalised response of the monochromator with the 1050 mm<sup>-1</sup> grating in pico-beam mode.

The fully corrected counts versus energy plot for the JET-X device can be seen in Figure 4.21.

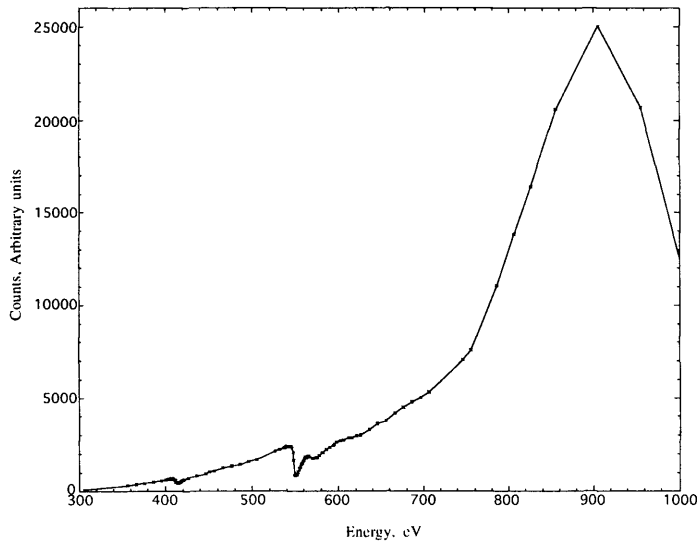


**Figure 4.20** Counts versus energy for the JET-X CCD. The data have been corrected for beam decay, the aluminium window transmission and the response of the grating.

Comparing this plot with Figure 4.22, which shows the modelled  $Q(E)$  of the JET-X CCD, it is clear that decoupling the grating response has not been entirely successful. The nor-



malisation process has created some spurious points at high energies (950 eV and 1000 eV) and also given a curve which is much too steep after ~650 eV. This is probably caused by an error in the grating response used to correct the data implying that the real grating response for low beam current operation was different from that measured while the beam was operating in its normal mode (Figure 4.12). The most likely cause is that the abnormally low flux rates at the grating provided a different heating load on the grating thereby causing a change in the response, particularly at higher energies. A similar effect using the same beamline in low beam current mode, but with a different grating has been described by the Micro Channel Plate (MCP) Group at Leicester University [Pearce, 1996]. Many methods were attempted to resolve this problem without significant success so it was decided that if the effect of the grating on the CCD response around the absorption edges was small it would be safer not to correct for the grating at all. Figure 4.21 shows the comparison of the CCD response before and after correcting for the grating, the y-axis uses a logarithmic scale to reveal any differences between the plots in more detail.

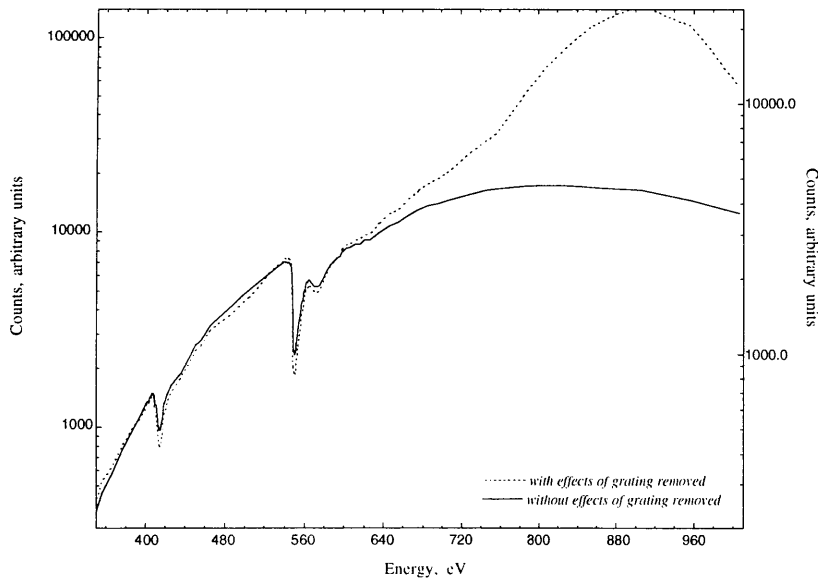


**Figure 4.21** Comparison of counts versus energy plots before and after decoupling the grating response.

It is clear from Figure 4.21 that the grating normalisation is causing a change in the response after 650 eV but that, importantly, it does not affect the response around the absorption edges. In fact the largest effect was measured for the oxygen white line where the size of the line in the uncorrected data was only ~0.5% smaller than the corrected data. Based on this evidence it was decided to use the uncorrected data set to obtain the  $Q(E)$  of both devices.

#### *Obtaining the $Q(E)$ of the devices*

The next step was to obtain the absolute  $Q(E)$  of the two CCDs. As no absolute measurement of incident flux was possible during the run, this had to be accomplished by normal-

ising the experimental data to modelled values. Using this method one must ensure the normalisation points are far enough away from the potential effects of EXAFS *i. e.* above and below the N and O K edge absorption energies. The model used was a standard Monte-Carlo model, developed especially for determining the response of the JET-X CCD for the device calibration program [McCarthy, 1995]. The model is optimised to fit absolute measurements of CCD  $Q(E)$  from the JET-X test facility. The results of a simulation are shown in Figure 4.22, for both isolated and summed (1-63 pixel) events. The proximity of both plots indicates that at these energies virtually all x-ray interactions give rise to charge which is confined to a single pixel.

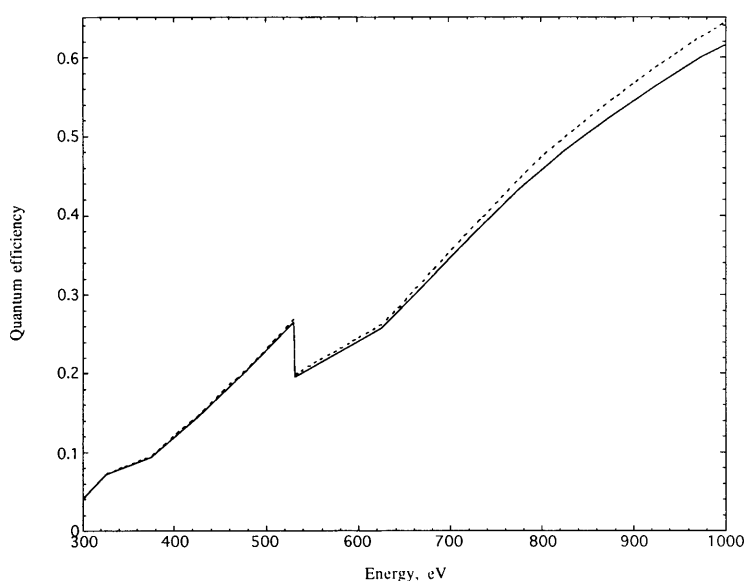


**Figure 4.22** The modelled response of the JET-X CCD in the energy range 0.3 keV to 1.0 keV. The solid line plots the isolated event values while the dotted line plots the values for summed (1-63 pixel) events.

A number of measurements at energies including 390 eV, 450 eV, 530 eV and 800 eV, were used to normalise the CCD counts. The counts are divided by the modelled  $Q(E)$  and the resultant numbers are fitted with a linear curve fit. This fitted curve is then used to convert the counts into  $Q(E)$ . The derived, absolute  $Q(E)$  curves for both devices are shown in Figure 4.23. Both plots are for single pixel interactions.

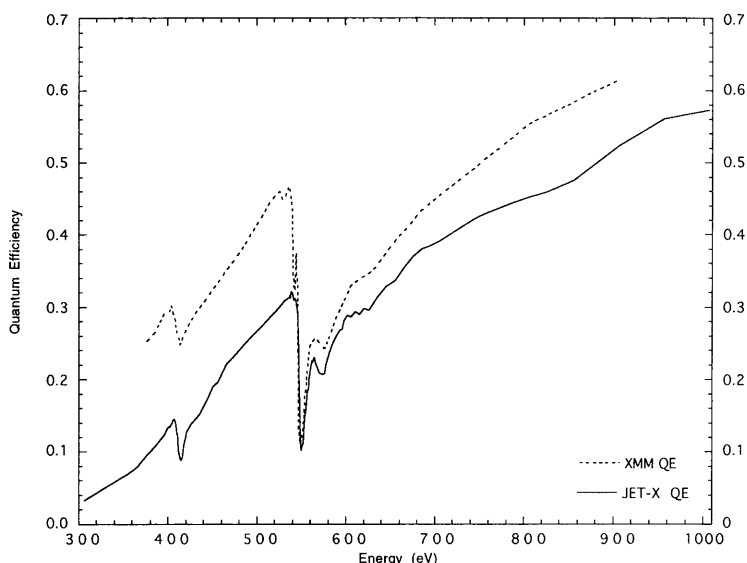


**Figure 4.23** The absolute  $Q(E)$  measurements of the JET-X thinned electrode CCD and the XMM open electrode CCD. The data has been normalised to modelled  $Q(E)$ s.

#### 4.3.5 Discussion

It can be seen from the plots of the final  $Q(E)$  that in both devices a number of expected features including the O K and N K edges, are clearly resolved. In both cases the oxygen edge displays typical absorption edge behaviour with considerable structure including the characteristic strong white line resonance at 551 eV, and EXAFS, particularly in the JET-X CCD, extending from ~590 eV to the end of the data set. The oxygen white line is caused by the presence of O-Si bonds, which provide additional states with energies very close to conduction band to which the oxygen inner-core electrons can be excited. The large population of such states gives rise to a increase in the density of allowed states, and hence the x-ray absorption coefficient, near the atomic absorption edge.

The nitrogen edge shows no structure in the open electrode device and even the white line appears to be unresolved, however there is some evidence to suggest the presence of a small white line in the JET-X data. The lack of structure at the N K edge is to be expected for two reasons i) nitrogen is present in the CCDs in a much smaller concentration than oxygen - the ratio of the amount of  $\text{Si}_3\text{N}_4$  to  $\text{SiO}_2$  in the CCDs is approximately 1:14, and ii) the poor  $Q(E)$  of the CCDs around the nitrogen edge. The relatively higher efficiency of the open electrode device is also obvious in Figure 4.23. This is due to the superior low energy x-ray transmission of the open electrode design compared to the thinned electrode technology.

There are a number of features in the plots which were not foreseen, including pre-edge dips at both ~530 eV and ~542 eV in the open electrode device and a strong dip in the  $Q(E)$  at ~565 eV in both devices. The most significant of these features is the pre-edge dip in the  $Q(E)$  of the open electrode CCD at ~540 eV. The strength of this feature is con-

siderable, reducing the  $Q(E)$  from  $\sim 0.48$  to  $0.33$ , and the shift from the absorption edge at  $\sim 548$  eV is  $\sim 6$  eV which is indicative of the resonance line caused by a hydrogen-oxygen bond. Since there should be no residual hydrogen left from the manufacturing process, the strength of this feature strongly suggests water or ice build up on the front surface of the CCD.  $H_2O$  can condense onto a CCD if the cryostat pressure is too high when the CCD is cooled. Supporting this hypothesis is the experimental log which showed that the XMM device was cooled to  $\sim 163$  K at a relatively poor vacuum of  $\sim 3 \times 10^{-2}$  Torr whereas the JET-X CCD was cooled to a similar temperature at a lower pressure of  $1 \times 10^{-3}$  Torr.

The feature in the  $Q(E)$  of the open electrode device at  $\sim 530$  eV is attributed to an unidentified additional line, related to the presence of other contaminants on the front surface of the CCD. As well as  $H_2O$  it is possible for materials, such as hydrocarbons and other out-gassed substances, to be adsorbed onto the CCD during cooling at relatively high vacuum pressures. The presence of small amounts of carbon and nitrogen, for instance, would provide O-C, O-N bonds that could give rise to other resonance absorption lines.

The strong dip in the  $Q(E)$  of both devices near  $\sim 565$  eV has been deduced to be evidence of x-ray absorption near edge structure, or XANES. XANES, like EXAFS, is a resonance effect, caused by the interference of the emitted photoelectron wave with the wave reflected back from neighbouring atoms. However, unlike EXAFS which concerns only single scattering processes, XANES is caused by interactions from multiple scatter type events where the reflected wave interacts with more than one atom before returning to the excited atom. This type of event occurs for very low photoelectron energies, *i. e.* very close to the absorption edge, when the interaction of the photo-electron with its surroundings are strong. For  $SiO_2$  the cut-off between the XANES region of the spectrum and the EXAFS region has been calculated to be  $\sim 55$  eV above the absorption threshold (see section 5.2.3) so clearly the strong dip in the  $Q(E)$  of both devices is well within the XANES region. In these CCDs this feature is probably caused by the multiple scatters from the silicon atoms bonded to the excited oxygen atoms, in the tetrahedrally co-ordinated, amorphous  $SiO_2$  at the CCD surface.

## 4.4 Extended Energy Range, Si K Edge Tests

### 4.4.1 Introduction

In January 1996 the Leicester group obtained another allocation of beam time at the Daresbury SRS. Amongst other work it was decided to take two JET-X engineering model CCDs packages (EM2 & EM3), previously used in March 1994 and January 1995, to Daresbury for further  $Q(E)$  measurements. As well as providing a chance to confirm the results of the first experiment in March 1994, it was planned to augment those early mea-

surements by extending the range to 1700 eV - 2500 eV. In practise the range was limited by the allowed beam-time to 1780 eV - 2300 eV.

#### 4.4.2 Devices

Both EM2 and EM3 were taken to the SRS, but only EM3 was used due to set-up problems with EM2. Of the two devices on the mother-board of EM3 only the 0481-12-04 device is thinned, therefore this device was used for these tests. A schematic representation of the device can be seen in Figure 4.1a.

#### 4.4.3 Experimental Set-Up

Station 3.4 was used for this test [Roper, 1992]. The set-up was identical to that used in the previous Si K edge test (see Section 4.2 of this Chapter). Table 4.4 shows the relevant experimental parameters for the experiment.

Beamline & Station	3.4 / 1.1
Synchrotron beam current	1 $\mu$ A
Synchrotron beam energy	1.998 GeV
Beam lifetime	~80 hours
Recorded count rate @ CCD	43 counts s <sup>-1</sup> cm <sup>-2</sup>
Test system noise	3.78 electrons (rms)
CCD Frame time	4 s
CCD Readout time	12 s
Amplifier integration time	2 $\mu$ s
System calibration	2.84 eV channel <sup>-1</sup>
Energy scans	1780 eV - 2000 eV at high resolution 2000 eV - 2300 eV at low resolution

**Table 4.4** Summary of relevant test parameters for January 1996 tests at the Daresbury SRS

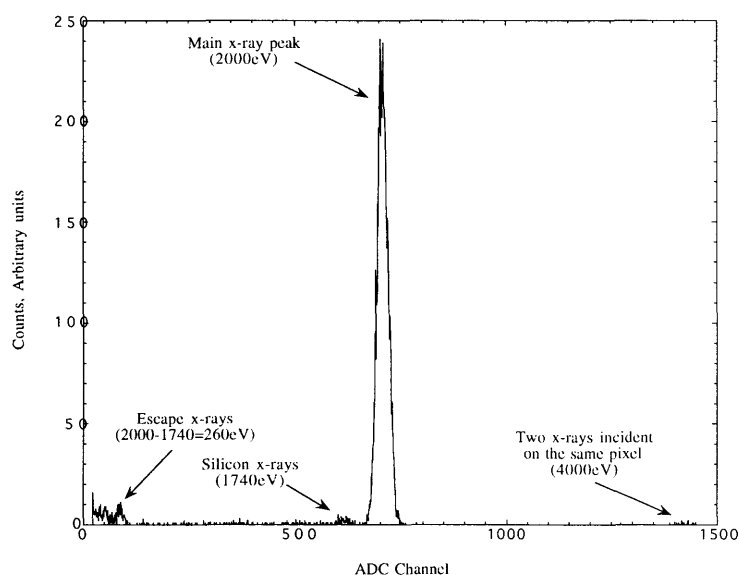
The CCD was again mounted in a vacuum cryostat which was turbo-pumped and coupled by a flexible bellows to the end of the beam line. The CCD was cooled to ~160 K by a copper cold finger connected to a liquid nitrogen dewar. This enabled elimination of CCD dark current and reduced readout noise. The output signals from the CCD were fed to low-noise pre-amplifiers and then to an analogue processor which performed dual-slope-integration to remove the CCD reset noise. The resultant signal was digitised to 12 bits and processed by an Archimedes A440 microcomputer. The A440 also controlled the experiment via an RS232 serial communication link with the beamline PC using software developed from the program described by Holland [Holland, 1990], and supported data collection and analysis tasks. Since the monochromator position was controlled by an IBM PC, we were able to connect together the A440 and PC to enable experimental control via the A440.

#### 4.4.4 Results

##### Data Acquisition

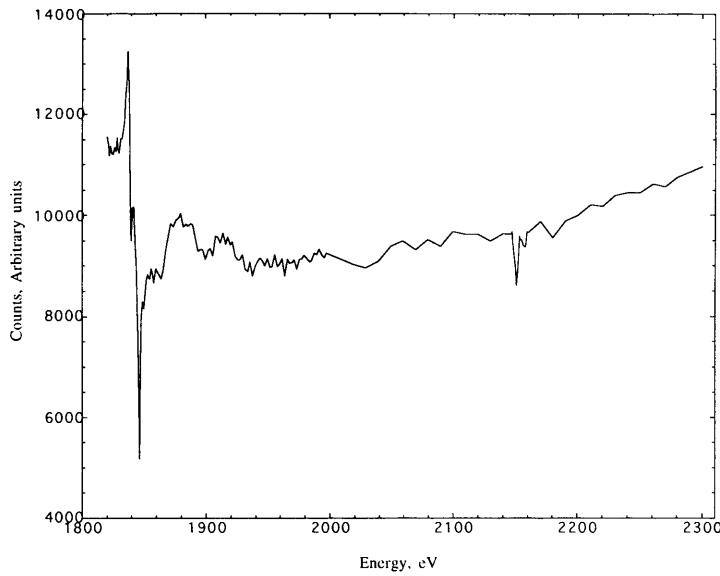
After initial beam studies the beam was reconfigured to give an incident x-ray flux of  $43 \text{ counts s}^{-1} \text{ cm}^{-2}$  at the detector. This low level of flux was achieved by a subtle miss-steering of the beam as in previous experiments at the SRS. The monochromator was scanned from 1780 eV to 1820 eV in 2 eV steps, from 1820 eV to 1860 eV in 1 eV steps, from 1862 eV to 2000 eV in 2 eV steps from 2000 eV to 2300 eV in 10 eV steps. Additional data were also recorded around the energy of the phosphorus K edge at  $\sim 2150 \text{ eV}$ . At each energy we tried to ensure enough data was acquired to restrict statistical noise below the 1% level (10,000 counts). This meant recording approximately 18-20 frames of data at  $\sim 600 \text{ events frame}^{-1}$ . In practise the average number of counts recorded across the Si K edge was  $\sim 9000$ , *i. e.* statistical noise  $\approx 1.05\%$ . As can be seen from the table, the system noise was at the very low level of 3.69 electrons (rms), again reflecting the inherent stability and low noise of the environment around Station 3.4.

Figure 4.24 shows a typical isolated event PHD recorded during the run at 2 keV. The FWHM resolution of the main x-ray peak is 85 eV.



**Figure 4.24** A PHD recorded with the 0481-12-04 device at the SRS in January 1996

Figure 4.25 shows the recorded counts versus energy spectrum in its completely raw state for isolated events, uncorrected for beam decay.



**Figure 4.25** The raw counts versus energy spectrum recorded at the SRS in January 1996

The EXAFS and XANES at the Si K edge are very clearly defined. There is evidence of structure at the P K edge as well. Although the CCD does contain P as a dopant it is also possible that the beamline grating could also have been contaminated with phosphorus.

#### *Beam Decay*

The lifetime of the stored beam during the run was ~80 hours which dictates the use of Equation (4-5) to correct for beam decay

$$N_m = N_r \times \exp(-0.0000035 \times t) \quad 4-5$$

where  $N_m$  are the measured counts,  $N_r$  are the corrected counts and  $t$  is the time elapsed since the beginning of the run. Unfortunately it was not possible to measure the response of the monochromator as the incident beam monitor would not operate at the low fluxes that were being used in this experiment.

#### *Obtaining the $Q(E)$ of the device*

The measurements are converted from counts to quantum efficiency by dividing by the expected incident count rate and normalising at energies away from the edge. The  $Q(E)$  curve is shown in Figure 4.26 for multiple pixel events.

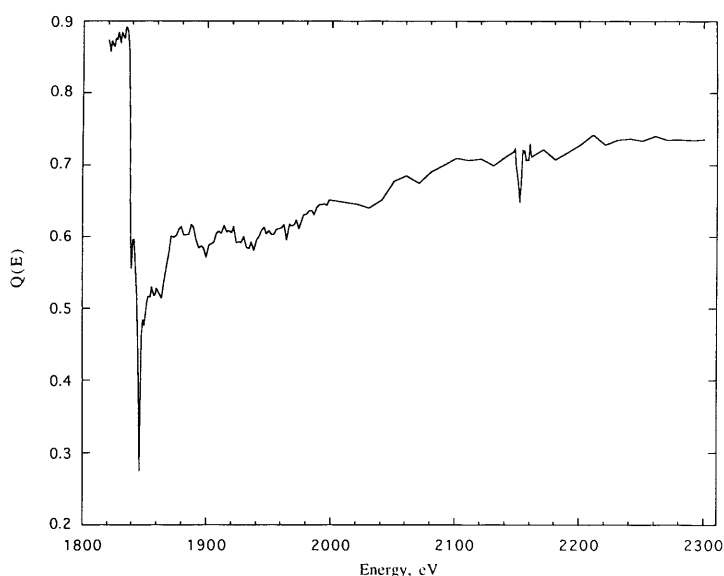


**Figure 4.26** The  $Q(E)$  of the 0418-12-4 device as measured at the SRS in January 1996

#### 4.4.5 Discussion

The measurements recorded at the SRS in January 1996 confirm the earlier, March 1994, investigations of the Si K edge and again highlight the power of synchrotron radiation for investigating XAFS in CCDs. At the Si K edge EXAFS, XANES and “white lines” are all clearly delineated. The extension of the energy range to 2300 eV has allowed data to be recorded well away from the effects of XAFS, and has enabled the P K edge to be seen. Further analysis of these data have been carried out in Chapter 8 to elicit information about the structure of the chemicals in the CCD. These are also important measurements in terms of the calibration requirements of JET-X.

### 4.5 Conclusions

In this chapter CCD calibration measurements performed at the Daresbury SRS have been described. The high resolution measurement of CCD  $Q(E)$  has, for the first time, enabled XAFS to be observed at the absorption edges of silicon and oxygen in a CCD operated as a x-ray spectrometer. The conclusion drawn is that the change in transmission through the electrodes and dead-layers causes XAFS in the  $Q(E)$  at the Si K and O K edges. This has led to the body of work described in Chapter 8. The fact that the  $Q(E)$  at absorption edges is much more complicated than predicted by conventional models has also led to the work in Chapter 7.

The work carried out at the SRS and described in this chapter has also been beneficial in other areas. The measurements carried out on the two devices at the O K edge were an important examination of the enhanced  $Q(E)$  provided by the new, open electrode device, designed for the XMM project. There is clear evidence of EXAFS and XANES at the O K



edge in the  $Q(E)$ s of both the XMM and the JET-X devices, which is caused by the  $\text{SiO}_2$  molecules in the VAPOX and oxide covering on the electrodes. The presence of a pre-edge dip at 542 eV in the XMM  $Q(E)$  is good evidence for ice contamination on the front side of the CCD and this conclusion correlates with the fact that the device was cooled down in a relatively poor vacuum. This is the first time contaminants on a CCD have been measured in this manner.

The high resolution measurements at the Si K edge in March 1994 have also enabled the energy required to generate an electron-hole pair,  $\omega$  [Owens, 1996] and the Fano factor,  $F$  [Owens, 1997] to be investigated. Those works have shown that  $\omega$  decreases with energy, which is in agreement with the theoretical work of Fraser *et. al.* [Fraser, 1994].

# 5

## X-ray Absorption Fine Structure

### 5.1 Introduction

Although XAFS have been known about and understood for a long time, only a few investigations of XAFS in solid state x-ray detectors have been carried out. Krumrey studied the  $Q(E)$  of a Si(Li) detector using synchrotron radiation and found EXAFS related variations at the ~3% level [Krumrey, 1989] while Cho reported an EXAFS modulation in the current response of both a silicon surface barrier detector and a lead silicate micro-channel plate, above the Si K edge [Cho, 1988]. In the field of x-ray astronomy other workers are beginning to realise that the current generation of detectors are capable of resolving detector-induced XAFS. For instance Kraft and co-workers used Si K shell EXAFS data to improve a model of their detector's response to continuum synchrotron radiation [Kraft, 1995].

The term XAFS describes a range of phenomena, including EXAFS, XANES, “white lines” and “edge shifts”. EXAFS and XANES are caused by a modulation of the absorption coefficient due to the effect that near neighbour atoms have on the photo-electron emitted during x-ray absorption. EXAFS can be explained by a single reflection from a neighbouring atom, whereas an explanation of XANES is more complicated since it involves the photo-electron interacting with more than one neighbouring atom. “White lines” and edge shifts are molecular effects. “White lines” are caused by electron excitations to molecular bound states while edge shifts occur either as a consequence of the atoms in a molecule having different electronegativities or because the band-gap is changed by the strength of the bonding. It is because of the relative simplicity of the EXAFS theory that the phenomena has become a useful tool for analysing chemical structures whereas XANES and “white line” effects are less useful.

In this chapter a theory of EXAFS will be developed. This will be used in Chapter 8 to help analyse the chemical structures in the CCD. To do this a quantum mechanical treatment of the absorption of x-rays will be required. This treatment will be described in Section 5.2. Absorption fine structure effects will be outlined in Section 5.3. In Sections 5.4, 5.5 and 5.6 the different types of fine structures will be explained. In Section 5.7 the absorption coefficient formed in Section 5.2 will be heuristically developed to obtain an expression for the EXAFS function,  $\chi(E)$ .

## 5.2 X-ray absorption

X-ray photons of energies between 100 eV and 100 keV are absorbed predominantly by photo-electric absorption, with Compton absorption as an important secondary process. The magnitudes of both these absorption mechanisms can be seen in Figure 5.1

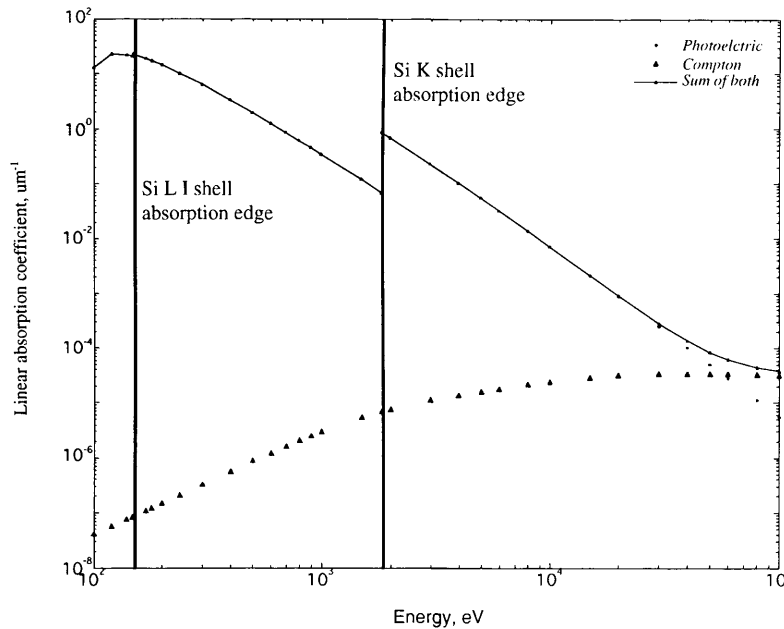


**Figure 5.1.** The linear absorption coefficients for photo-electric and Compton interactions in silicon. The photo-electric absorption edges at 1839 eV (1s electron is ejected) and at 149 eV (2s electron is ejected) are shown.

At energies of less than about 60 keV the primary mechanism for the interaction of x-ray photons with matter is the photo-electric effect. A schematic representation of photon absorption by the photo-electric effect is shown in Figure 5.2.

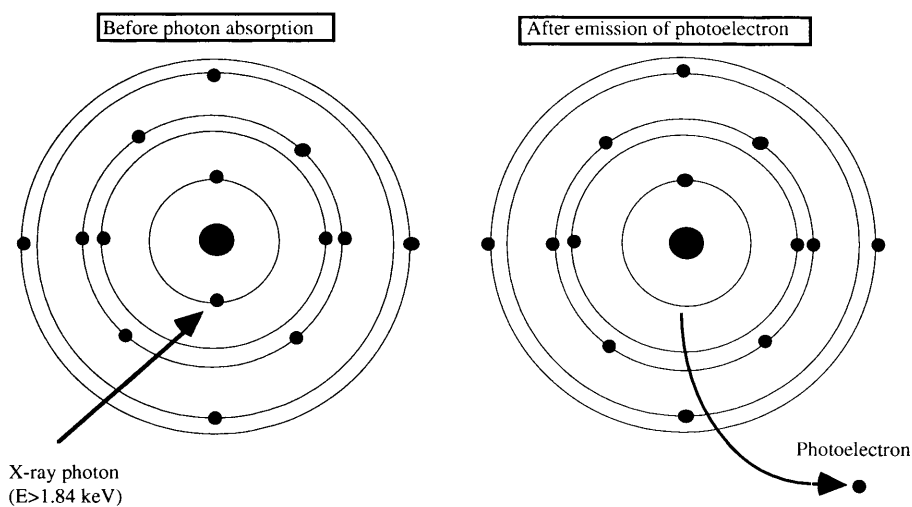


**Figure 5.2** Schematic picture of x-ray photon absorption in silicon by the photo-electric effect. Provided the energy of the x-ray is greater than the K-shell binding energy (1839 eV) the most likely outcome is the emission of a K-shell electron.

In a photo-electric absorption event a photon is captured by a “bound” atom with the subsequent promotion of a “free” photo-electron. In the EXAFS regime the momentum,  $p$ , can be determined by the free electron relation

$$\frac{p^2}{2m} = T = h\nu - E_b \quad 5-1$$

where  $m$  is the rest mass of the photo-electron,  $T$  is its kinetic energy,  $h$  is Planck’s constant,  $\nu$  is the frequency of the photon and  $E_b$  is the binding energy of the given state. Some of the XANES structure, particularly “white lines”, depend explicitly on bound-bound transitions, and the momentum of the photo-electron cannot therefore be determined using Equation (5-1). Provided the energy of the photon,  $h\nu$ , exceeds the binding energy of the K-shell of the atom, the most probable (92%) x-ray interaction is with a K(1s)-shell electron [Fraser, 1994]. For x-ray photons of energy less than 1839 eV absorption in silicon is a combination of components from the L<sub>I</sub>, L<sub>II</sub>, L<sub>III</sub> and M<sub>I</sub> shells.

Quantum mechanically the photoelectron can be treated as a wave whose wavelength,  $\lambda$ , is given by the de Broglie relation

$$\lambda = \frac{h}{p} \quad 5-2$$

An expression for the photo-electric absorption coefficient in terms of the initial-state and the final-state electron wave-functions,  $\psi_i$  and  $\psi_f$  is necessary. For the absorption of an x-ray we have the following “Bohr” relationship.

$$\omega \equiv 2\pi\nu \equiv ck = \frac{1}{\hbar}(E_f - E_i) \quad 5-3$$

where  $\hbar$  is the “rationalised” Planck’s constant,  $h/2\pi$ ,  $c$  is the speed of light in a vacuum,  $\omega$  is the angular frequency of the photon,  $k=2\pi/\lambda$  is the photon wave number and  $E_i/E_f$  are the energy of the initial-state and the final-state respectively. The absorption coefficient is obtained from

$$\mu(k) = N\sigma(k) \quad 5-4$$

where  $\mu(k)$  is the photo-electric absorption coefficient, *i. e.* the probability per unit path length that a given photon is absorbed,  $N$  is the number of atoms per cm<sup>3</sup> and  $\sigma(k)$  is the absorption cross section. The absorption cross section is defined [Bethe, 1957] as

$$\sigma(k) = \frac{2\pi e^2 \hbar^2}{m^2 c \nu} \left| \int \psi_f^* \sum_j \exp(ikr_j) \frac{\partial \psi_i}{\partial x_j} d\tau \right|^2 \quad 5-5$$

where  $-e$  is the charge on an electron,  $m$  is the electron rest mass,  $\psi_f^*$  is the complex conjugate of the final-state electron wave-function,  $r_j$  is the radius of the  $j$ -th atomic electron and the integral is in three dimensions. The equation can be simplified by expanding the exponential term,  $\exp(ik \cdot r)$  in Equation (5-5) as a power series

$$\exp(ik \cdot r) \approx 1 + ik \cdot r + \frac{1}{2!}(ik \cdot r)^2 + \dots \quad 5-6$$

here  $r$  is typically  $10^{-9}$  or less for the core electrons and  $6 \times 10^5 \leq k \leq 6 \times 10^9$  for x-rays with energies  $100 \text{ eV} \leq E \leq 10 \text{ keV}$ . This is known as the “dipole” approximation; terms other than the first one are very small. Equation (5-5) thus becomes

$$\sigma(k) = \frac{2\pi e^2 \hbar^2}{m^2 c v} \left| \int \psi_f^* \sum_j \frac{\partial \psi_i}{\partial x_j} \partial \tau \right|^2 \quad 5-7$$

using Equation (5-4) and Equation (5-7) along with a number of quantum mechanical relations, Bethe has shown that the absorption coefficient can be related to the initial- and final-state electron wave functions by

$$\mu(k) = \frac{\pi e \mu_0 c \omega_{fi}}{2 \hbar} \left| \int \psi_f^*(\epsilon \cdot r_j) \psi_i d^3 r \right|^2 \quad 5-8$$

where  $\mu_0$  is the permeability of free space and  $\epsilon$  is the electric field polarisation vector [Bethe, 1957]. Equation (5-8) is sometimes written in an alternative form [Gurman, 1990] as

$$P = \frac{2\pi^2 e^2}{mc^2 \omega} \left| \int \psi_f^*(\epsilon \cdot r_j) \psi_i d^3 r \right|^2 \rho(E) \quad 5-9$$

where  $P$  is the probability of x-ray absorption and  $\rho(E)$  is the density of allowed states at  $E_f$ . For the free-electron assumption for  $\rho(E)$  (see Equation (5-1)) the only factor which contributes to the EXAFS signal is the matrix element given by

$$\int \psi_f^* \epsilon \cdot r_j \psi_i d^3 r \equiv \int_0^\infty \int_0^\pi \int_0^{2\pi} \psi_f^*(r, \theta, \varphi) \epsilon \cdot r_j \psi_i(r, \theta, \varphi) r^2 \sin \theta dr d\theta d\varphi \quad 5-10$$

### 5.3 Absorption Fine Structure

Absorption fine structures have been known about for over 70 years but only recently has their relationship to chemical structures been fully realised. The first observations of fine structure in the absorption spectra of solids were made in 1920 by Fricke and Hertz [Fricke, 1920; Hertz, 1920]. The first structure observed was near-edge structure, which came to be known as Kossel structure [Kossel, 1920] but is now more commonly called X-Ray Absorption Near-Edge Structure or XANES. Later Kronig observed that the absorption spectra of many molecular solids exhibited oscillatory structure extending many hundreds of eV above absorption edges [Kronig, 1931]. This structure came to be known as Extended X-Ray Absorption Fine Structure, or EXAFS. In his 1931 paper, Kronig announced a theory which attempted to explain this oscillatory structure in terms of the excitation of a single electron from within large, ordered, crystal lattices. His theory used the

idea of long-range order (LRO) in solids but it was unable to explain the EXAFS signal quantitatively. The following year he introduced a contrasting theory based on scattered waves [Kronig, 1932] rather than on LRO. This new theory came to be known as a Short-Range-Order (SRO) theory [Azaroff, 1963] and, although there was much confusion at the time [Azaroff and Pease, 1974], SRO theories are now known to be the more accurate.

Kronig had developed his SRO theory to explain EXAFS in molecules and the theory, although lacking in some aspects, remain essentially the same as modern theories, which explain EXAFS in terms of the modulation of the final-state wave-function when the photoelectron wave is back-scattered from surrounding atoms. A significant addition to Kronig's theory was made by Petersen who realised the potentials of both the excited and the back-scattering atom could cause an effective shift in the phase of the wave [Petersen, 1932]. Other additions were made by Kostarev [Kostarev, 1941 & 1949], Sawada [Sawada, 1959 & 1957] and Shmidt [Shmidt, 1961 & 1963]. Kostarev extended EXAFS theory to condensed matter, Sawada developed the theory to take into account the lifetime of the core hole and the photoelectron, and Shmidt was able to introduce a factor that accounted for lattice vibrations.

The application of EXAFS as an experimental tool was slow to take-off until it was pointed out [Sayers, 1971] that, based on a theoretical expression, a Fourier transform of EXAFS with respect to the photoelectron wave number should peak at distances corresponding to the position of the nearest-neighbour co-ordination shells of atoms. This insight promoted EXAFS from an interesting peculiarity to a serious non-destructive, non-invasive tool for determining chemical structures. At the same time it demonstrated the correctness of the SRO theory, since a Fourier transform revealed only the first few shells of atoms. The availability of high intensity, highly stable synchrotron radiation was an important next step forward for EXAFS analysis because the time needed to obtain a spectrum dropped from weeks to minutes thus enabling very dilute samples to be analysed.

The advantages of EXAFS analysis are:

- SRO theory shows that long-range order in materials is not required, which implies that non-crystalline materials exhibit EXAFS and can therefore be analysed. The corollary to this is that EXAFS contains no long range information and so traditional methods (*e. g.* diffraction, diffuse elastic scattering) are still necessary.
- EXAFS analysis can determine the local atomic arrangement around each atom in a material, quickly and accurately.
- The structural information can be obtained simply and directly from EXAFS by an analysis of the Fourier transform.
- EXAFS is a non-destructive technology, *i. e.* the material is left unchanged by the measurement.

## 5.4 Extended X-ray Absorption Fine Structure

As was shown in Section 5.2, x-ray absorption is a quantum mechanical process which involves the initial- and final-state electron wave-functions. When the final-state wave function is perturbed by the presence of near neighbours, EXAFS can occur. EXAFS, is the term used to describe the sinusoidal, oscillatory structure seen in absorption spectra some way above the absorption threshold of molecules or solids. Figure 5.3 shows an absorption spectrum from a rhodium metal foil, the EXAFS signal can be seen extending up to 1500 eV above the absorption edge. When the kinetic energy of the photo-electron is large compared to its interaction energy with the surrounding atoms ( $\sim 3$  eV) the photon interaction can be treated as a perturbation about an isolated atom. The final-state of the photo-electron is modified by scattering from the surrounding atoms but the initial state, in a deep core level, is almost completely unaffected.

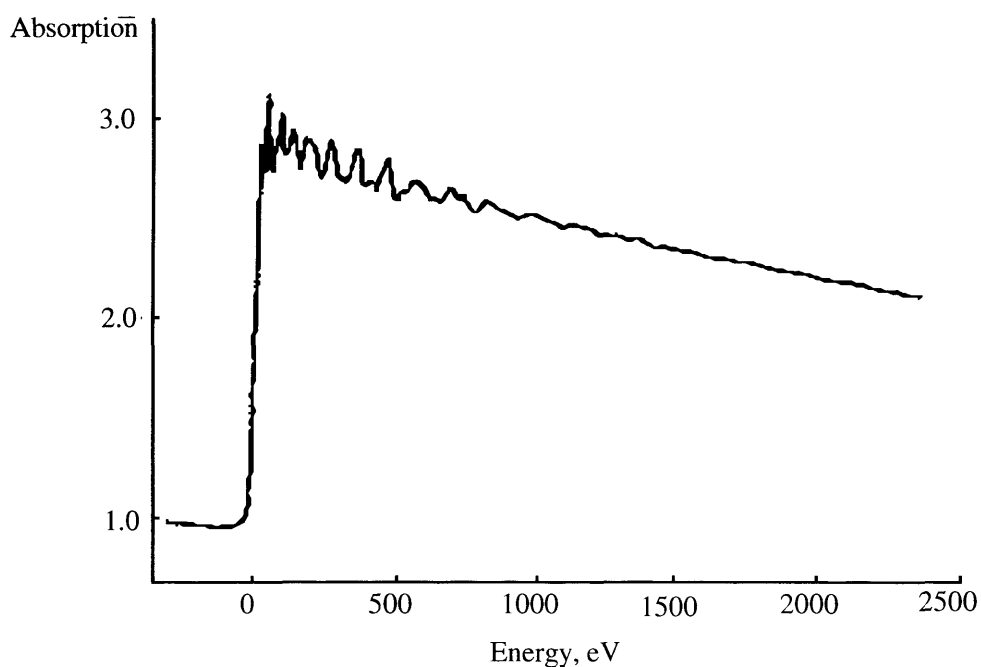


**Figure 5.3.** Fine structure in the raw absorption spectrum of a rhodium metal foil at 80 K. The x-axis is x-ray energy in eV, relative to the Rh K absorption edge at 23220 eV. EXAFS can be seen beginning just after the absorption edge and extending as far as 1500 eV above [Sayers, 1988].

For isolated atoms the photo-electron is represented as an outgoing wave as shown in Figure 5.4 by the dark lines. In a solid or molecule the outgoing waves will be scattered from co-ordinated neighbours as shown in Figure 5.4 by the lighter lines. The back-scattered waves in Figure 5.4 add to or subtract from the outgoing wave depending on their relative phase. The final-state is a superposition of the outgoing and scattered waves and the total amplitude of the final-state electron wave function is modulated, modifying the probability of x-ray absorption. As the energy of the x-ray is varied, the relative phase of

the waves changes. Thus the variations in the absorption due to EXAFS are the direct consequence of the wave-like nature of the photo-electron. Since the variation in phase also depends on the distance between the centre and scattering atoms, and since the strength of the back-scatter depends on the type, and number of atoms involved, it can be seen that the EXAFS signal contains information on the atomic surroundings of the excited atom. In order to quantify EXAFS it is necessary to obtain the EXAFS function,  $\chi(E)$ . This process is described in Section 5.7. In general the structure after the absorption edge is split into three areas; i) the low-energy-XANES region extending over the first 8 eV, described in Section 5.6, ii) the multiple scattering or XANES region and iii) the EXAFS region, described in this section.

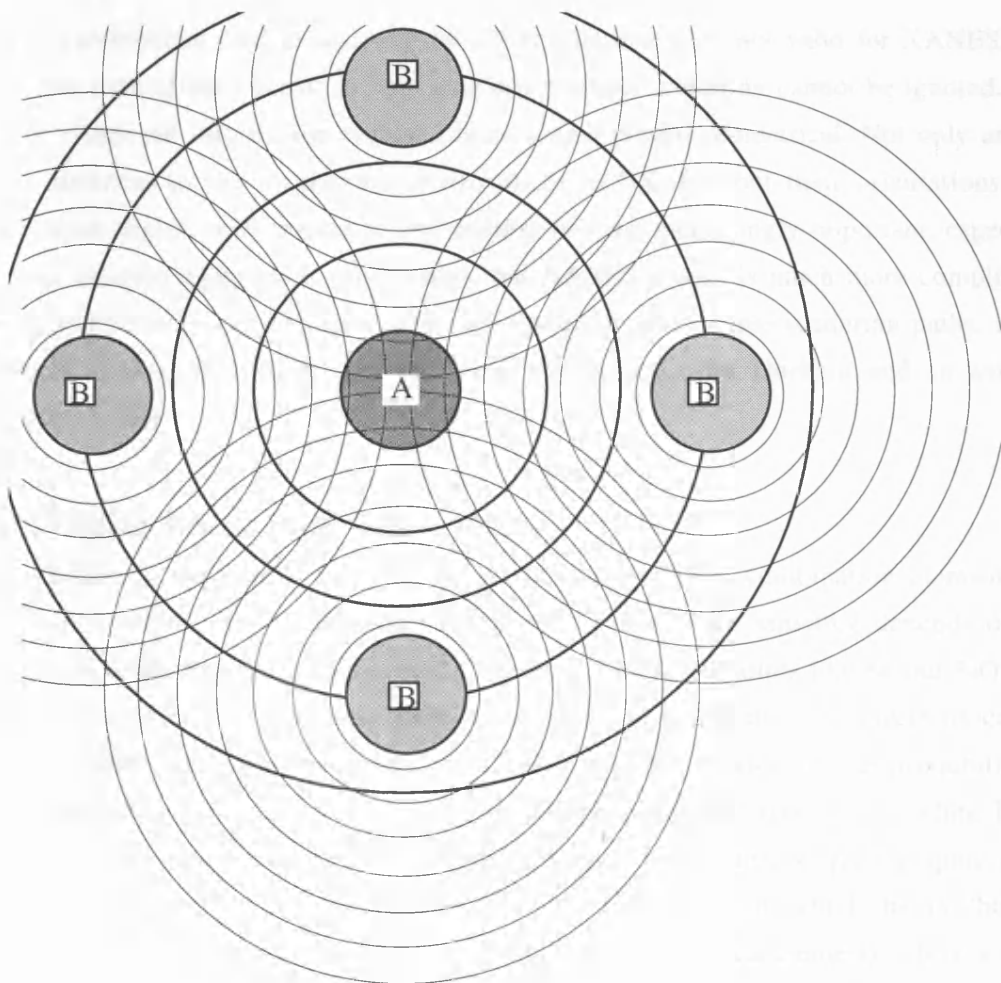


**Figure 5.4.** Process of photoelectron back scattering by near neighbour atoms causing modulation of attenuation near the centre of the absorbing atom, A. In this figure A is the excited atom and B are the back-scattering atoms. The shaded areas are the 1s regions for each atom. The concentric circles represent photoelectron waves where the distance between each consecutive circle represents the wavelength of the photoelectron.



## 5.5 X-ray Absorption Near-Edge Structure

The multiple scattering XANES region is normally stated as extending from  $\sim 8$  eV to  $\sim 50$  eV, above the absorption threshold. An accurate method of calculating the extent of the XANES region was suggested by Bianconi, who proposed that the energy division between XANES and EXAFS is the energy at which the wavelength of the excited electron is equal to the distance between the absorbing atom and its nearest neighbour [Bianconi, 1980]. For example in silicon, with a nearest neighbour at  $2.35 \text{ \AA}$ , the corresponding partition energy is  $\sim 24.5$  eV ( $k=2.7 \text{ \AA}^{-1}$ ), while in silicon dioxide where the nearest neighbour to a silicon atom is an oxygen atom at  $1.6 \text{ \AA}$ , the energy is  $\sim 55$  eV ( $k=3.9 \text{ \AA}^{-1}$ ).

The assumptions used in deriving the EXAFS equation are not valid for XANES. The mean free path of the electron is very long and multiple scattering cannot be ignored. This in turn means the information obtained is no longer purely geometrical. Not only are the radial distances to the neighbours important, as in EXAFS, but their orientations, and hence bond angles, with respect to one another become increasingly important, especially at lower electron energies. It can be seen that XANES theory is much more complicated than EXAFS theory and requires a full description of all multiple-scattering paths. A description of XANES theory may be found in the paper by Durham and co-workers [Durham, 1982]

## 5.6 “White lines” and edge shifts

The structure in the first  $\sim 8$  eV after the absorption edge is a combination of resonance transitions (“white lines”) and “edge shifts”. The cause of the structure depends on the class of materials that are being studied [Bianconi, 1988]. For solids like Si and  $\text{SiO}_2$ , the molecular/covalent bonds provide unoccupied levels to which the core electrons can be excited. These “bound-bound” transitions cause a large increase in the probability of x-ray absorption and hence give rise to absorption peaks, referred to as “white lines” since they were first observed as large, underexposed white lines on photographic negatives. In  $\text{SiO}_2$  there are a large number of empty  $3p/3s$  states to which the  $1s$  “bound” electrons can be transferred. This can be seen in our CCD measurements where a large  $\text{SiO}_2$  “white line” is visible at  $1846$  eV which merges with the absorption edge since the resolution needed to separate them is beyond the limit of the experimental capability. This also makes it difficult to observe the true edge position, a problem which is exacerbated by the shift in the absorption threshold in  $\text{SiO}_2$ .

The absolute position of the absorption threshold in a molecule depends on the chemical state of the atoms. There are two contributions, namely; widening of the band-gap and screening. Band-gap widening usually dominates for the core electron absorption thresholds. The strength of the bond between atoms moves the conduction band states to

higher energies and the valence band states to lower energies. When the band gap widens, the core electrons need more energy to excite them into the conduction band and hence the threshold is moved. This is the reason that the SiO<sub>2</sub> K absorption threshold is shifted relative to the Si K threshold in our CCD measurements.

Screening is caused by the imbalance in the strengths of the electronegativities of the elements in a molecule. It is usually associated with the absorption threshold of the L and M shells whose density of states overlap the valence states that are being interfered with. The element with higher electronegativity attracts the bonding electrons more strongly toward it, subtly increasing the attraction toward the nucleus felt by the L and M shell electrons of the less electronegative atom. This effect is most easily seen when elements are oxidised, *i. e.* the edge shifts to higher energies with greater oxidation states.

## 5.7 Heuristic derivation of the EXAFS function, $\chi(E)$

It has been established that EXAFS is a modulation of the final-state wave-function by the back-scattered photoelectron wave as shown pictorially in Figure 5.4. In this section the EXAFS function,  $\chi_j(E)$ , for atomic type,  $j$ , will be derived heuristically. For the purpose of this derivation only the effects of single scattering are considered, this being a valid approximation in the EXAFS region where the kinetic energy of the photoelectron is larger than its interaction energy with its surroundings. To obtain the EXAFS function the value of the back-scattered wave is calculated at the origin and is then multiplied by the outgoing wave to obtain the final-state wave-function,  $\psi_f$ . From Equation (5-8)

$$\mu(k) \propto \left| \int \psi_f^* \mathbf{E} \cdot \mathbf{r}_j \psi_i d^3r \right|^2 \quad 5-11$$

For an isolated atom the final-state,  $\psi_f$ , would be a function of an outgoing, unperturbed spherical wave,  $\psi_o$  only. As has been described, in solids and molecules, the final-state is a sum of the unperturbed outgoing wave,  $\psi_o$  and a scattered wave,  $\psi_s$

$$\psi_f = \psi_o + \psi_s \quad 5-12$$

$\psi_s$  is a function of the outgoing wave-function,  $\psi_o$  and is proportional to  $(kr)^{-1} \exp(ikr)$  where we take  $\exp(ikr)$  as the complex form of a plane wave. The initial value of the outgoing wave is therefore

$$\psi_s = \psi_o \frac{1}{kr} \exp(ikr) \quad 5-13$$

This outgoing wave travels out to its neighbour where it is scattered. This introduces the atomic scattering factor,  $F_j(k)$ , and creates another wave, with the neighbour atom as its origin, that travels away from the scattering atom.  $\psi_s$  thus becomes,

$$\psi_s = \psi_o \frac{\exp(ikr_j)}{kr_j} kF_j(k) \frac{\exp(ik|r-r_j|)}{k|r-r_j|} \quad 5-14$$

where  $r_j$  is the distance to atoms of type  $j$ . The potentials of both the excited and the scattering atoms interact with the wave and, after Petersen [Petersen, 1932], introduce a total phase-shift,  $2\delta_j$ , to the scattered wave which gives

$$\psi_s = \psi_o \frac{\exp(ikr_j)}{kr_j} kF_j(k) \frac{\exp(ik|r-r_j|)}{k|r-r_j|} \exp(2i\delta_j(k)) \quad 5-15$$

The matrix element is non-zero only near the centre of the absorbing atom *i. e.* at  $r=0$ , so Equation (5-12) can be rewritten as

$$\psi_f = \psi_o \left[ 1 + \frac{\exp(2ikr_j)}{kr_j^2} F_j(k) \exp(2i\delta_j(k)) \right] \quad 5-16$$

Now Equation (5-11) can be rewritten by substituting Equation (5-16) for  $\psi_f$  to get

$$\left| \int \psi_f^* \epsilon \cdot r_j \psi_i d^3r \right|^2 \propto \left| \int \psi_o^* \epsilon \cdot r_j \psi_i d^3r \right|^2 \left| 1 + \frac{\exp(2ikr_j)}{kr_j^2} F_j(k) \exp(2i\delta_j(k)) \right|^2 \quad 5-17$$

where the final term has been separated as it is not a function of radial position. Equation (5-18) which defines the EXAFS function [Gurman, 1990] is used to extract  $\chi_j(k)$ .

$$\mu(k) = \mu_o(k) [1 + \chi_j(k)] \quad 5-18$$

The first part of the right-hand side of Equation (5-17) can be equated to  $\mu_o$ , the smooth monotonic variation of the absorption coefficient seen in isolated atoms. The modulus squared term on the right of Equation (5-17) can then be expanded and equated to the EXAFS function

$$\begin{aligned} \left| 1 + \frac{\exp(2ikr_j)}{kr_j^2} F_j(k) \exp(2i\delta_j(k)) \right|^2 &= 1 + 2 \frac{\exp(2ikr_j)}{kr_j^2} F_j(k) \exp(2i\delta_j(k)) \\ &\quad + \left| \frac{\exp(2ikr_j)}{kr_j^2} F_j(k) \exp(2i\delta_j(k)) \right|^2 \end{aligned} \quad 5-19$$

The final term in Equation (5-19) is much smaller than the other terms and so is ignored, leaving, with reference to Equation (5-18),

$$1 + \chi_j = 1 + \frac{\exp(2ikr)}{kr_j^2} F_j(k) \exp(2i\delta_j(k)) \quad 5-20$$

and therefore

$$\chi_j = \frac{\exp(2ikr_j)}{kr_j^2} F_j(k) \exp(2i\delta_j(k)) \quad 5-21$$

Now the real part of this equation can be taken, which gives

$$\chi_j(k) = \frac{F_j(k)}{kr_j^2} \sin(2kr_j + 2\delta_j(k)) \quad 5-22$$

The EXAFS signal consists of single scattering events only, this enables the total effect of neighbouring atoms to be simply taken as the sum of their individual contributions. However, it is important to point out that, in general, multiple scatters give rise to peaks in the Fourier transform which are at much greater atomic distances than those from single scatters. Therefore one can say that the first peak in the Fourier transform will contain no contributions from multiple scatter events. In fact for the study of silicon and silicon dioxide which have diamond-like crystal structure, the first two peaks are free from multiple scatters (For a thorough treatment see [P. J. Durham, 1988]). Making the single-scatter approximation, and hence summing over all atoms gives

$$\chi(k) = \sum_j \chi_j(k) = \sum_j \frac{F_j(k)}{kr_j^2} \sin(2kr_j + 2\delta_j(k)) \quad 5-23$$

which is an expression for  $\chi(k)$ , the total EXAFS function.

This equation can now be refined by taking into account the effect of the core hole lifetime (*i. e.* the probability that the core hole is filled) and the lifetime of the photoelectron (*i. e.* the probability of an electron scatter) [Petersen, 1932]. This is done by introducing a mean-free-path term which qualitatively describes the probability,  $P$ , that the electron returns to an atom which is still excited. If  $\Lambda$  is the mean free path of the electron then  $P$  is given by

$$P = \exp\left(\frac{-2r_j}{\Lambda}\right) \quad 5-24$$

where  $2r_j$  is the total distance travelled by the photo-electron and the EXAFS equation then becomes

$$\chi(k) = \sum_j \frac{F_j(k)}{kr_j^2} \exp\left(\frac{-2r_j}{\Lambda}\right) \sin(2kr_j + 2\delta_j(k)) \quad 5-25$$

The more commonly used form of the EXAFS equation is obtained by summing over co-ordination shells rather than individual atoms. This is done by summing over atoms that have the same distance from the centre atom,  $r_j$ . In a particular co-ordination shell not all of the atoms will have precisely the same,  $r_j$ , and hence their contribution to the interference will not be exactly in phase. The random disorder of atoms in a given shell is, if small, Gaussian and therefore adds a factor

$$N_j \exp(-2k^2 \sigma_j^2) \quad 5-26$$

to the EXAFS equation where  $N_j$  is the number of atoms of type  $j$  in the co-ordination shell and  $\sigma_j$  is the rms. deviation from the mean distance,  $r_j$ . Equation (5-25) then becomes

$$\chi(k) = \sum_j \frac{N_j F_j(k)}{k r_j^2} \exp\left(\frac{-2r_j}{\Lambda}\right) \exp(-2k^2 \sigma_j^2) \sin(2k r_j + 2\delta_j(k)) \quad 5-27$$

This expression, although obtained heuristically, is valid for all polycrystalline samples, cubic crystals, amorphous and liquid materials [Stern, 1988]. This expression will be used in the analysis of EXAFS in a silicon CCD in Chapter 8.

# 6

## The JET-X Focal Plane Cameras

The work in this thesis has been primarily carried out on the CCDs designed for the JET-X project. This has meant that much of it has overlapped with project work, often with positive results. For instance the measurement of XAFS in the response of the CCDs, has fed through to the calibration of the JET-X CCDs. Chapter 6 is a report of aspects of the calibration of the JET-X telescope that have occurred during the period taken to complete this thesis. The areas included in the chapter have nearly all led, through work with other participants in the project, to the release of data for the thesis. In this chapter data from test calibration work on JET-X are reviewed. Where the author of this thesis has not been directly involved the sources have been duly referenced.

As with any project which seeks to extend the frontiers of observational science beyond what is termed “state of the art”, JET-X requires accurate calibration. For JET-X the overall target accuracy is 3% for the essential parameters of collecting area, efficiency, and spatial and spectral resolution. Therefore each element in the optical train, *i. e.*, mirrors, filters and detectors must be calibrated to  $\sim 2\%$  accuracy.

### 6.1 Introduction

#### 6.1.1 JET-X

JET-X [Wells, 1990] consists of two identical, co-aligned x-ray imaging telescopes with spatial resolution  $\approx 20''$ . The field of view (FOV) of the two telescopes is  $20^\circ$ . The focal plane detectors are thinned electrode, high resistivity CCDs with x-y spatial resolution of  $27\ \mu\text{m}$  which oversamples the image of a focused point source by  $\sim \times 10$  for  $20''$  spatial resolution. The focal plane, detector assembly consists of two CCDs mounted on alumina daughter boards which are bonded to an alumina mother board using conductive epoxy resin. The two CCDs are butted along their serial readout register edges, to form a single focal plane array. The dead strip width between neighbouring image sections is  $< 250\ \mu\text{m}$  which is comparable with the Half Energy Width (HEW  $\sim 12''$ ) of the JET-X telescope. To avoid a dead-band in the reconstructed sky image, the CCD arrays in the two JET-X telescopes are offset by  $1/2$  of a single CCD height. The daughter board functions as a mechanical support for the CCD and provides the electrical connections from a double row of pins along each side of the daughter board to the CCD, via metal tracks. Connections are made from the CCD to the metal tracks by  $25\ \mu\text{m}$  aluminium wires ultrasonically wedge bonded at both ends.

The two telescopes are co-aligned in a common structure together with an attitude monitor which provides an independent attitude solution to  $\leq 5$  arc-seconds. The detailed specifications for JET-X are listed in Table 6.1 and the operating modes of the telescope are shown in Table 6.2. The 20 " angular resolution corresponds to a focal plane resolution of 0.340 mm (HEW). For long,  $10^5$  s, observation times, spacecraft drift and thermal distortion can lead to image blurring and a consequent loss of sensitivity. However the attitude monitor provides a measurement of instrument pointing which is accurate to 5 ". This allows any drift between frames of data to be corrected *post facto* during data analysis. The attitude monitor measures the position of the telescope relative to up to four stars in its field of view. An attitude solution, with  $\sim 5$  " precision, can then be established during data processing.

OBJECTIVES	To carry out detailed imaging and spectroscopic observations of weak and cosmological sources in the soft x-ray band.
TYPE	X-ray optics employing 12 nested mirrors in Wolter Type I geometry. CCD focal plane detectors with spatial resolution of 27 $\mu\text{m}$ .
DETECTORS	2 EEV P88930T CCDs; Dimensions; $20.7 \times 27.7 \mu\text{m}^2$ each with an active depth $\sim 65 \mu\text{m}$ .
ENERGY RANGE	300 eV to 10 keV.
ENERGY RESOLUTION	130 eV @ 6.4 keV ( $E/\Delta E = 50$ ).
ANGULAR RESOLUTION	$\sim 20$ "
FIELD-OF-VIEW	$20 \times 30$ '
SENSITIVITY	Better than $10^{-13}$ ergs $\text{cm}^{-2}$ for $10^4$ s source observation.
SUBSYSTEMS	2 x-ray telescopes
	Command and Data Handling System
	Telescope Alignment Monitor
	Power Distribution Unit
	Background Monitor
	Attitude Monitor ( $4 \times 5.4$ ' FOV)
CRYOGENICS	Single stage passive radiator of area $\sim 1600 \text{ cm}^2$
	Detector temperature $\sim -110$ °C.
	Detector/cryostat focal plane assembly weight 21 kg.
TEMPORAL RESOLUTION	25 s in full-frame mode, 2.5 s in frame store mode, 400 $\mu\text{s}$ in timing mode
MEMORY SIZE	60 MB.
BIT RATE	1 Mbit/sec (fast telemetry), 16 kbit/sec (slow telemetry).
TOTAL WEIGHT	551 kg.
OVERAL SIZE	4 m long $\times$ 1 m diameter.
TOTAL POWER	260 W total: 130 W heater power.

**Table 6.1** The principal characteristics of the JET-X telescope

Mode	Imaging	Bright object	Timing	Back-up
Configuration of detectors	2 CCDs in each telescope	1 CCD in either telescope, 2nd telescope in imaging mode	1 CCD in either telescope, 2nd telescope in imaging mode	1 or 2
Spectroscopy	Full resolution	Full resolution	Full resolution	Full resolution
Imaging	Both telescopes	Both telescopes	Imaging in 1 telescope, none in timing telescope	Both telescopes
Time resolution (s)	2.5	2.5 - 0.1	$10^{-3}$	5 - 25
Maximum count rate (counts s <sup>-1</sup> )	2	50	400	0.4
Maximum source brightness (mCrab)	3.6	90	718	> 0.7
Imaging Field of view (arcmins)	13.8 × 20.3 (overlap) 41.3 × 20.3 (combine)	13.8 × 20.3 27.4 × 20.3 (2nd)	No imaging in timing telescope 27.4 × 20.3 (2nd)	

**Table 6.2** Principal operating modes of the JET-X telescope

A radiation detector is provided to monitor the level of cosmic radiation incident on the CCDs. This will allow the CCDs to be turned off during solar flares and as the telescope passes through the Earth's radiation belts. Although the original specification for JET-X included an optical monitor, which was to have provided simultaneous monitoring of x-ray sources to a limiting magnitude of  $m_v \sim 22$ , this item was deleted because of budgetary and schedule constraints, and was replaced by a back-up attitude monitor.

The telescope itself is constructed from three carbon fibre sections which i) contain the instruments, ii) act as an optical bench - maintaining focal length and iii) provide mutual co-alignment between the two telescopes and the attitude monitors. Any mis-alignments between the mirrors and the focal bulkheads can be measured by a Telescope Alignment Monitor (TAM).

Figure 6.1 shows the system block diagram for the JET-X telescope.



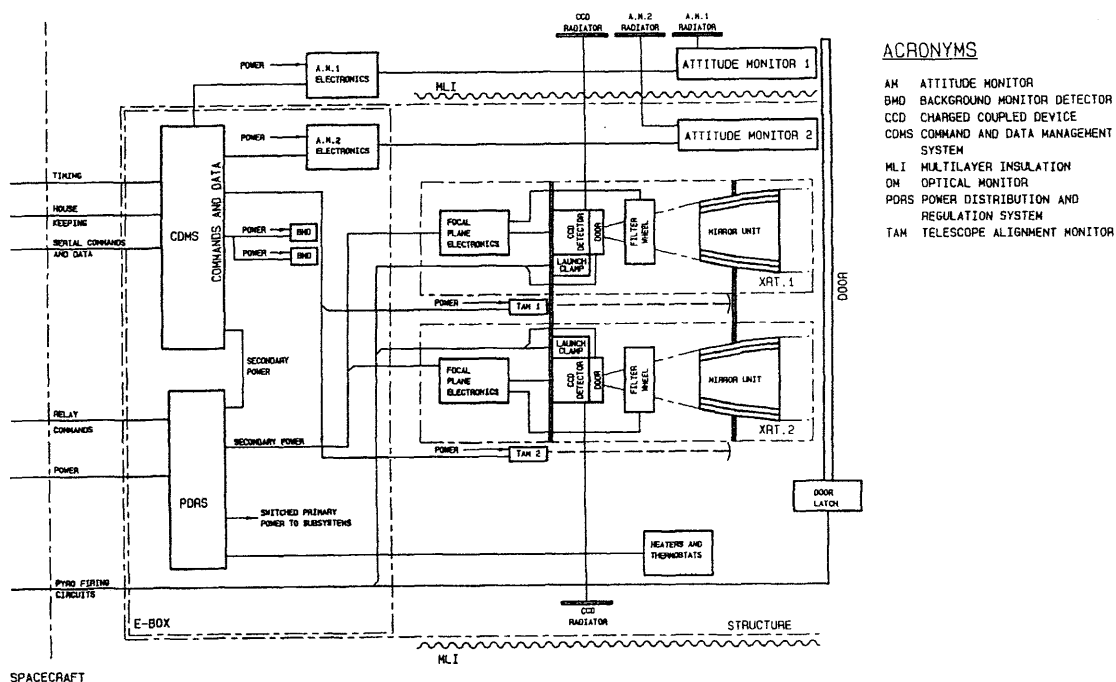


**Figure 6.1** The system block diagram of JET-X

### 6.1.2 Status of JET-X

Since December 1994 the following major targets in the JET-X programme have been achieved [JET-X/FDR, 1995]:

- Delivery of the EM instrument to Russia and completion of acceptance and complex tests
- Completion of STM (Structural Thermal Model) qualification and delivery of the STM to Russia
- Delivery of FM (Flight Model) structure, CCD arrays and TEs (Test Electronics) to Leicester
- Completion of calibration work on the six delivered FM CCD arrays and investigation of a number of instrumental calibration effects
- Completion of the FDR (Flight Design Review) in February 1995

During this period JET-X (along with NASA's MOXE) has been defined to be the most advanced instrument on the Spectrum-X-Gamma payload and will therefore be used to define the standards and procedures for the other instruments aboard Spectrum RG to adopt.

## 6.2 Instrumental performance

Some of the following information was gathered from JET-X design reviews that have been attended by the author during the period 1994 - 1996. These include the JET-X

Flight Design Review, held at the University of Leicester, 20th - 22nd February 1995 and the Design Review which was held at The Cosener's House, Abingdon, 27th - 28th November 1995. The reports from these meetings may be found in the following references [JET-X/FDR, 1995] and [JET-X/(95)RAL-184].

### 6.2.1 Mirror system

The two x-ray telescopes consist of 12 nested, co-axial and con-focal mirrors of Wolter-I geometry. The outer mirror is 0.30 m in diameter, the inner mirror is 0.19 m in diameter and the focal length is 3.5 m. Each shell is manufactured by electro-form nickel on a gold-plated, aluminium mandrel. The surfaces are gold coated to provide high reflectivity over a wide dynamic range as well as a stable surface [Citterio, 1994]. The combined on-axis effective area for the two telescopes is  $\sim 360 \text{ cm}^2$  at 1.5 keV falling to  $\sim 140 \text{ cm}^2$  at 8.0 keV. The thickness of the shells varies from 0.7 mm for the inner shell to 1.1 mm for the outermost. These values have been selected to ensure high stiffness, resonant frequency  $\geq 200 \text{ Hz}$  and negligible gravitational degradation of the image when the mirrors undergo testing in a horizontal position.

The response of the JET-X mirrors is built up from three discrete components:

- The simulated response (discussed in Section 6.3.2)
- Au M edge energies and widths measured using synchrotron radiation
- Discrete measurements from tests carried out at the Panter x-ray test facility in March 1995.

#### *Synchrotron measurements*

The detailed response of mirror samples around the Au M absorption edges have been measured within the group [Owens, 1996]. To put the work in the next Chapter into context the experiment, results and conclusions will be discussed briefly here. The measurements were derived from an extensive set of photo-current and reflectivity measurements made on Au-coated mirror samples at the SRS and the NSLS [Graessle, 1992; Owens, 1994]. Figure 6.2 shows the photo-yield measurements made at the SRS on a mirror sample along with the first derivative of the data. The shape and edge energies can be clearly seen as well as the onset of the edge, denoted by  $\epsilon_p$ .

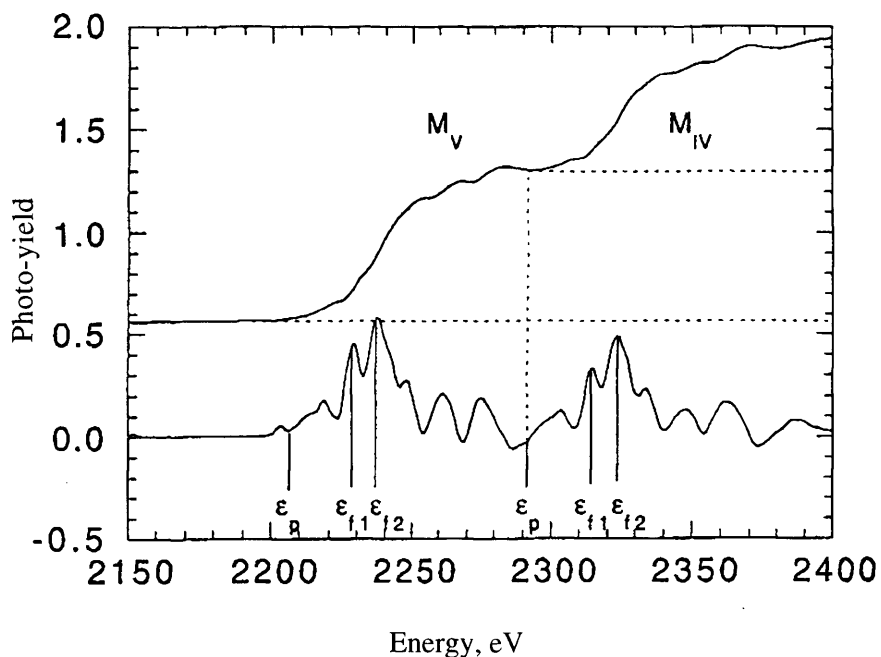


**Figure 6.2** The photo-yield from a mirror sample [Owens, 1996]

Reflectivity measurements were made at the SRS at 12 incident angles over the range  $0.1^\circ$  to  $2^\circ$ , scanned in 1 eV steps from 2100 eV to 3600 eV. Figure 6.3 shows the un-normalised reflectivity from a mirror sample across a range of angles.

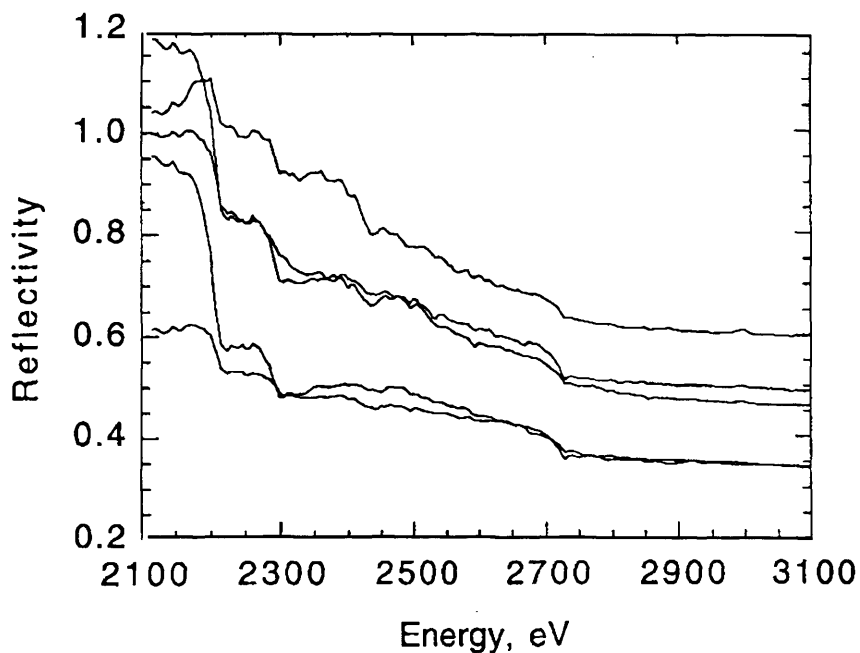


**Figure 6.3** Un-normalised mirror reflectivity data [Owens, 1996]

Figure 6.4 shows the predicted reflectivity of a mirror sample across the Au M edges.

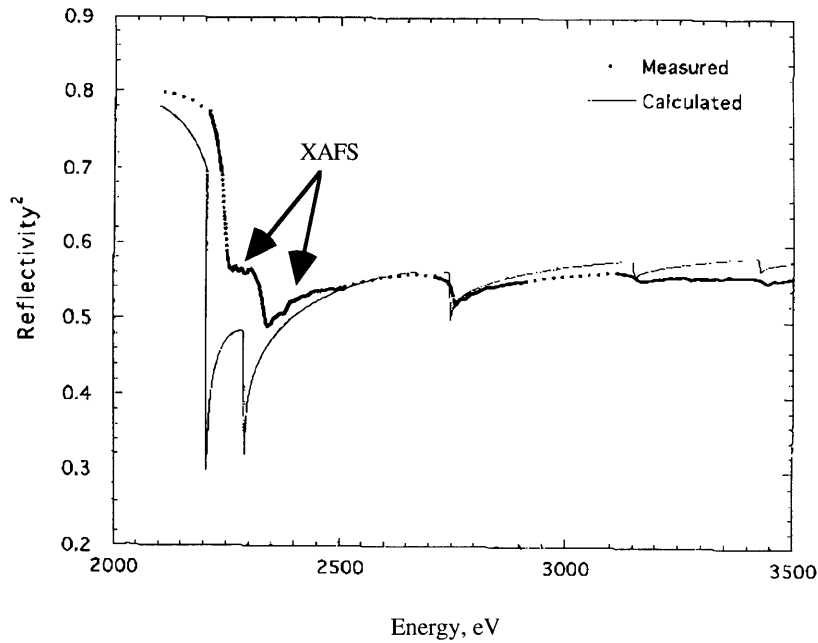


**Figure 6.4** Predicted mirror reflectivity for an incident angle of 27.375 arcmins [Owens, 1996]

These data were derived from single reflectivity measurements using an incident grazing angle of 27.375 arcmins at the NSLS [Graessle, 1992]. For comparison the calculated response based on the calculations of Cromer & Liberman [Cromer, 1970] is also shown. Deviations at the low and high energies have been attributed to contamination and density effects, respectively [Owens, 1996]. It should be noted that the energy resolution for these measurements is  $\leq 1$  eV so the width of the edges and apparent lack of detail is real. The reflectivity is deviant from the calculated values around the  $M_V$  and  $M_{IV}$  edges, both in amplitude and position. The measured edge energies of the  $M_V$  and  $M_{IV}$  edges are shifted from their tabulated values by about 30 eV [Owens, 1996], an effect that has also become apparent in Ir, Pt and Pb.

This edge shift is an important result for the calibration of x-ray astronomical telescopes since the detailed shape and energy position of edges used in their response functions have until now, been based on tabulated data [*e. g.*, Henke, 1982; Saloman, 1988], and the next generation of focal plane instrumentation will easily be capable of resolving 30-40 eV shifts. The shift in edge energies has been attributed to a combination of three effects; i) the use of limiting absorption values derived from XPS data, ii) the finite width of the edges due to core hole lifetime effects and iii) the possible slow onset of the main absorption edge [Owens, 1996]. XAFS can be seen in the response after the onset of the  $M_V$  and  $M_{IV}$  edges

#### *Panther measurements*

The JET-X mirrors have been extensively tested for focusing quality, *i. e.* angular resolution and HEW, at the Panther test facility, near Munich, which belongs to the Max Planck Institute fur Extraterrestrische Physik. The facility consists of a large vacuum chamber,

130 m distant from a point-like source which produces photons in the range 0.3 - 8.0 keV. The optics are supported by a stage which can translate and tilt inside the test chamber, allowing three-axis manipulation of the mirrors for alignment purposes. The results of these tests have been published [Citterio, 1996] and are summarised here. Figure 6.5 shows a typical mirror response image showing the angular resolution of the mirrors. In this figure the point spread function (PSF) is plotted for a double exposure of x-rays where the CCD has been moved by 20 " half way through the integration. At both 1.5 keV and 8.1 keV the two sources are clearly resolved showing the excellent angular resolution of JET-X [Citterio, 1996].

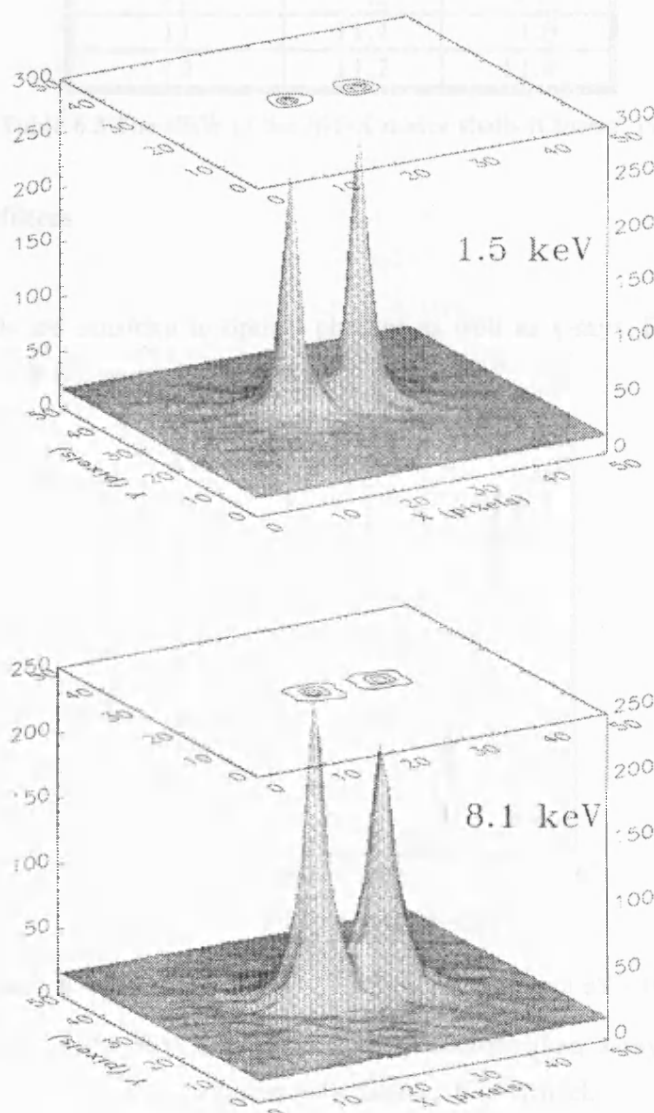


**Figure 6.5** The PSF of the JET-X mirrors [Citterio, 1996]

Table 6.3 shows a prediction from UV measurements of the x-ray HEW due to the geometry of the JET-X mirror shells [Citterio, 1996].

Mirror No.	HEW FM1 arcsec	HEW FM2 arcsec
1	7.2	7.3
2	11.8	11.8
3	9.3	10.2
4	10.9	10.1
5	11.7	10.3
6	10.8	10.7
7	10.4	9.4
8	9.9	11.2
9	11.9	10.6
10	11.2	9.7
11	11.4	11.0
12	11.7	11.9

**Table 6.3** The HEW of the JET-X mirror shells [Citterio, 1996]

### 6.2.2 The x-ray filters

#### *Introduction*

The JET-X CCDs are sensitive to optical photons as well as x-rays. Figure 6.6 shows the Q(E) of a CCD over the range 1 - 10,000 eV.

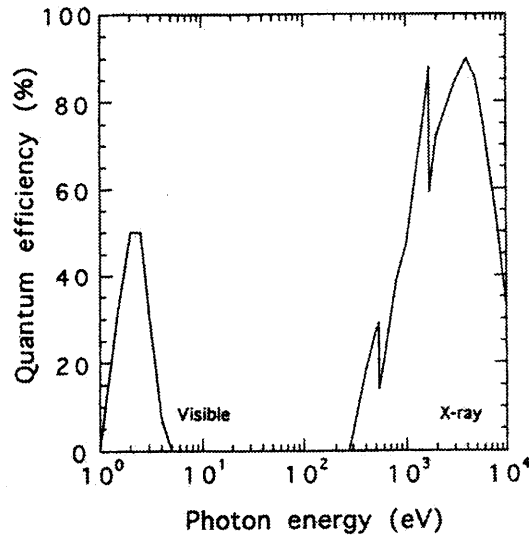


**Figure 6.6** The Q(E) of a JET-X CCD over the range 1 eV - 10 keV.

Since most objects in the sky emit more optical photons than x-ray photons both telescopes will carry optical filters mounted on a rotating filter wheel.

If optical photons are not filtered out they will be focused on to the CCD at the same spot as the x-rays and give rise to excessive dark current, spectral broadening, peak shifts and decreased telescope throughput. The optical photons provide an extra term in the CCD resolution equation *i. e.*

$$\Delta E = \sqrt{(8 \ln 2)(\omega F E + \sigma_r^2 + \sigma_o^2)} \quad 6-1$$

where  $\omega$  is the energy required to create an electron hole pair,  $F$  is the Fano factor,  $\sigma_r^2$  is the variance in the readout noise and  $\sigma_o^2$  is the variance in the optical noise component.

### *Design*

To maximise the soft x-ray response of JET-X, the original filter specification [JETX-(92) UL142] was for one thick (low x-ray transmission) and one thin filter (high x-ray transmission). The thick filter was to be 800 Å of Al on 2000 Å Lexan (C<sub>16</sub>H<sub>14</sub>O<sub>3</sub>) and the thin filter was to be 400 Å of Al with the same Lexan support. The filters were to be double sided and an ~85% transmitting nickel support mesh was to be provided in both cases. The filter design was based on the filters designed for the ROSAT WFC which were manufactured by Rutherford Appleton Laboratory. Al/Lexan was chosen because the combination provided the best mixture of high optical attenuation with x-ray transmission. The original design was for a circular filter with an inside diameter of 52 mm. This first design failed under vibration test. The filters were then redesigned with a square filter area within a circular support mesh to enhance stiffness and relieve stress at the filter/holder boundary. This design also failed vibration testing.

The manufacture and use of optical filters in x-ray telescopes has since been extensively investigated [Castelli, 1997]. These investigations have showed that although most of the thin filters achieved optical transmission specification, the thick, 800 Å, filters failed to achieve a satisfactory optical transmission of 10<sup>-5</sup>. This has been accounted for by the presence of optically transparent Al<sub>2</sub>O<sub>3</sub> on the surface of the Al filters. This oxide is formed during manufacture in the coating facility, a problem which is exacerbated by the double sided, 400 Å per side, technique. Recent broad band measurements have confirmed this conclusion and also shown that interference effects arising from Lexan/double sided Al layers contribute to increased transmission in the blue/UV part of the spectrum. The solution has a single sided Al filter, with an increased thickness of 1100 Å and a Polyimide substrate material which is UV opaque below 350 nm. Further work has shown that the thin filter provides only an ~3% increase in integrated transmission in the x-ray band and it has been decided to fly only the thick filter design. The 1100 Å Al/2000 Å Polyimide filters will be provided by Luxel Corporation. Thus far these filters have passed acceptance level vibration tests with no performance degradation.

### *X-ray response*

To map the x-ray response of the JET-X filters samples of both thick and thin designs were taken to the Daresbury SRS for transmission measurements. Figure 6.7 shows the transmission of the filter as a function of energy. In this figure both calculated values and SRS measurements, normalised to discrete-line values, are shown.

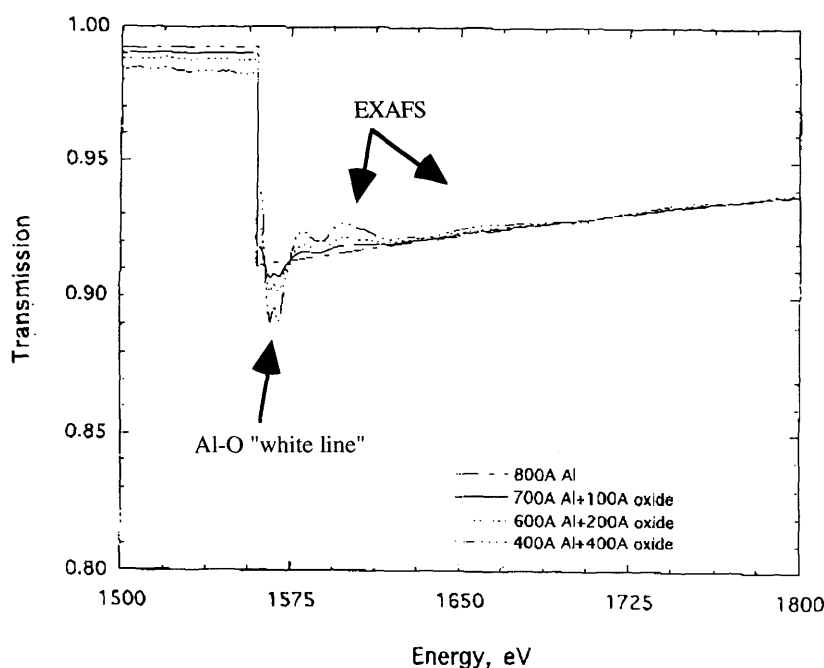


**Figure 6.7** The x-ray transmission of the JET-X optical filters

Figure 6.7 shows that there is considerable structure around the Al K absorption edge. This structure has been attributed to XAFS and XANES, similar to that seen in the  $Q(E)$  of the CCD. A large absorption feature can be seen at the onset of the edge that has been correlated with the presence of  $\text{Al}_2\text{O}_3$  on the surface of the filter. This feature is caused by the “white line” or resonance line, due to electron transitions to molecular states provided by Al-O bonds. These transitions can be thought of as electron transitions to a large population of  $3p/3s$  hybrid orbital states caused by the Al-O bond, similar to those seen in the case of Si-O bonds, described in Chapters 5 and 8. Ripples seen modulated on the post-edge absorption are interpreted as EXAFS although the background noise makes it difficult to be conclusive. These synchrotron measurements are limited to the region around the Al K edge. This was not thought to be a problem as the carbon edge is outside the active range of JET-X and the effective thickness of oxide in the filters is small ( $\sim 200 \text{ \AA}$ ) compared to the thickness of oxide on the CCD ( $\leq 1.2 \text{ }\mu\text{m}$ ).

### 6.2.3 The x-ray detectors

The focal plane detectors are the deep depletion, thinned electrode CCD devices described in detail in Chapter 3. They are specifically designed to study x-ray emission over the energy range 0.3 keV to 10 keV. The FWHM energy resolution of a typical JET-X CCD is  $\sim 130 \text{ eV}$  at 6.4 keV,  $E/\Delta E \approx 50$  @ 173 K.

#### *CCD quantum efficiency*

The quantum efficiency curve of the CCDs is built up from SRS, Panter and test facility measurements and simulation results. All values are normalised absolutely to the Panter



measurements. In between absorption edges a simulation program [Holland, 1990 and McCarthy, 1994] is used to generate smooth curves. XAFS and “white line” measurements from the absorption edges of N, O and Si are added. At, and near to, the Si K absorption edge, XAFS effects are added from tables obtained by semi-empirical best-fitting to SRS measurements (see Chapter 8), using attenuation coefficients abstracted from Si, SiO<sub>2</sub> and Si<sub>3</sub>N<sub>4</sub> photo-yield data obtained in a separate SRS experiment [JETX-(94) UL-241]. Figure 6.8 shows the measured Si K absorption edge Q(E) along with the modelled edge based on standard absorption coefficients and those abstracted from SRS photo-yield measurements.

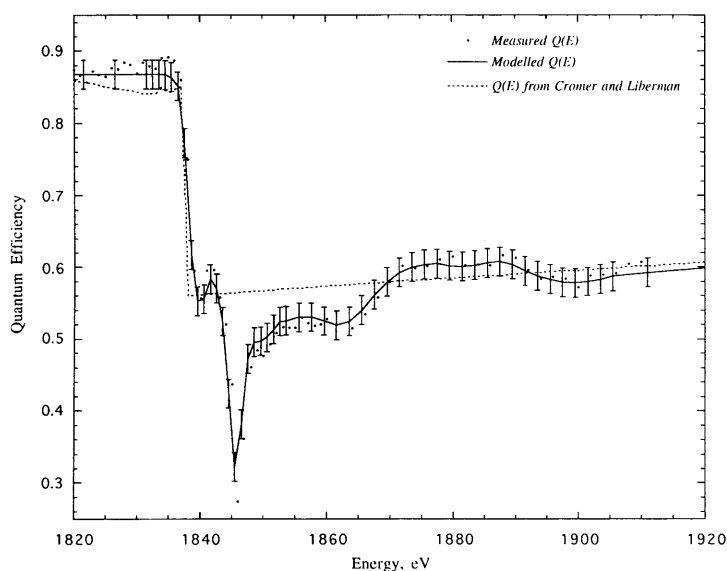


**Figure 6.8** Measured and modelled Q(E) at the Si K absorption edge of the JET-X CCD.

At the O and N K edges, XAFS information is added to the Q(E) curve by fitting normalised SRS data to the modelled edges. Figure 6.9 shows the Q(E) of the JET-X CCDs at the O and N K edges.

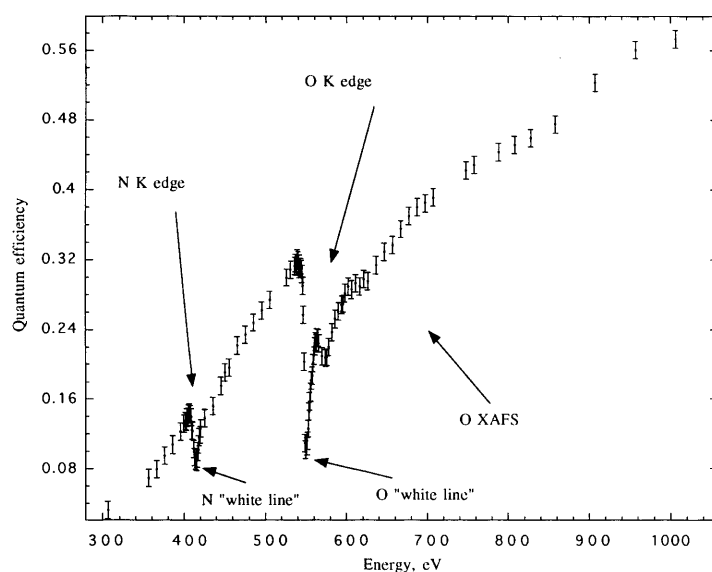


**Figure 6.9** The  $Q(E)$  of the CCDs at the O and N K edges.

Figure 6.10 shows a plot of the  $Q(E)$  of a CCD over the energy range 300 eV to 10,000 eV. This plot includes data from the SRS, the test facility and from calculations. In this case the data have been normalised to the test facility values

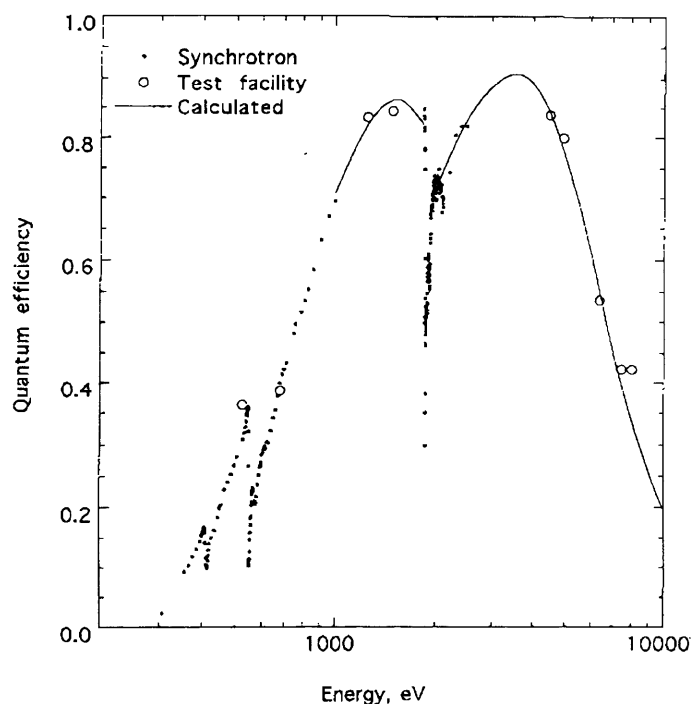


**Figure 6.10** Measured and modelled CCD  $Q(E)$

### *CCD energy resolution*

Measurements of the resolution of the CCDs are fitted with a function of the form

$$\Delta E = a_1 \sqrt{a_2 + E}$$

6-2

where  $a_1$  is typically  $1.525 \text{ eV}^{1/2}$  and  $a_2$  is  $\sim 440.5$  averaged over all nodes of the CCDs for isolated x-ray events and a given read noise [Owens, 1995]. Data will be taken for all n-pixel class events. Figure 6.11 shows the FWHM of the JET-X CCDs.

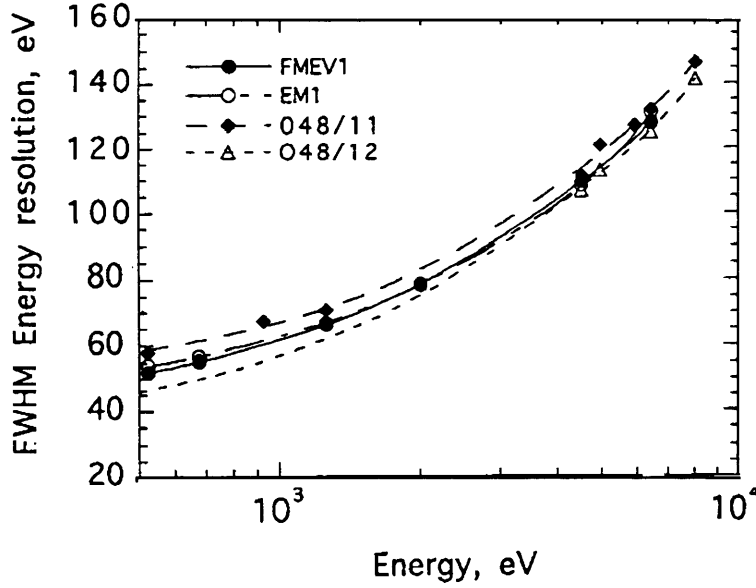


**Figure 6.11** FWHM energy resolution of JET-X CCDs as a function of energy [Owens, 1995]

#### *Other CCD effects*

Electronic thresholding affects the charge loss in CCDs. Although the energy deposition is strongly peaked in deep depletion devices, a proportion of the charge is deposited in pixels outside of a 4 pixel limit. For a 6.4 keV x-ray,  $\sim 5\%$  of the charge is spread out over thousands of pixels in a Lorentzian-like distribution. Charge loss is therefore very sensitive to the selection of the charge threshold [Owens, 1995]

### **6.3 The instrument response matrix**

The calibration data-set for JET-X, that will be delivered to the observer, will feature two levels of files, Basic Calibration Files (BCFs), including, for example, the CCD response matrix and the CCD  $Q(E)$ , and Calibration Product Files (CPFs), including, for example, the point response function of the telescope [Denby, 1996]. BCFs are the lowest level (unit) calibration files and contain the raw results of ground or in-flight calibrations. CPFs combine the unit levels into response files suitable for scientific applications. All of the above files will be in a Flexible Image Transport System, or FITS, format. Relevant BCF and CPF files can be seen in Tables 6.4 and 6.5.

Parameter	Functional dependence	Notes
CCD linearisation	-	Conversion of CCD pixel co-ordinates into angular offsets
Filter transmission on-axis	Energy	The on-axis filter transmission
Filter transmission off-axis	Energy, angular off-set	The off-axis filter transmission
Mirror effective area on-axis	Energy	The on-axis area of the telescope mirrors
Mirror effective area off-axis	Energy, angular off-set	The off -axis area of the telescope mirrors (relative to the centre of the field)
Pixel defect table	-	Locations of bad pixels excluded from processing
CCD Q(E) spatial location	Energy, angular off-set	Q(E) at a grid of CCD locations
CCD gain	CCD/node/ADC combination	Energy scales of a given event path
Bore-sight alignment	-	Rotation of JET-X in each of 3 axes relative to spacecraft
Attitude Monitor calibration	Angular off-set	Converts AM pixel data to angular off-set

**Table 6.4** List of BCF files

Parameter	Functional dependence	Notes
Point response function	Energy, angular off-set, event rate	Constructs spatial and energy dependence of the mirror response
On-axis area	Energy	Total on-axis effective area for the telescope
Off-axis area	Energy, angular off-set	Total off-axis effective area for the telescope
Spectral redistribution matrix (see below)	Event class, event rate	Describe redistribution of photon energy for each event class and for given event rate

**Table 6.5** List of CPF files

### 6.3.1 CCD redistribution matrix

A theoretical CCD response to incoming photons is built up from multiple component Gaussian approximations. A BCF file is created for each CCD/Readout node/ADC channel/Event Class combination by combining the detector gain and the detector energy resolution (including the response to monochromatic x-rays/escape peaks etc.). For a given combination the response is stored in a single “sparse” 2-D matrix<sup>2</sup> of Energy versus PHA channel whilst the energy range of each channel is stored in a second “sparse” matrix. Work done within the group has shown that the response of the JET-X CCDs to soft x-rays can be described to the required 1% accuracy by a double Gaussian fit [Castelli, 1997]. Figure 6.12 shows a typical JET-X CCD redistribution matrix.

<sup>2</sup>a sparse matrix is a matrix where only those channels with a non-zero value are stored, along with the number of zero channels.

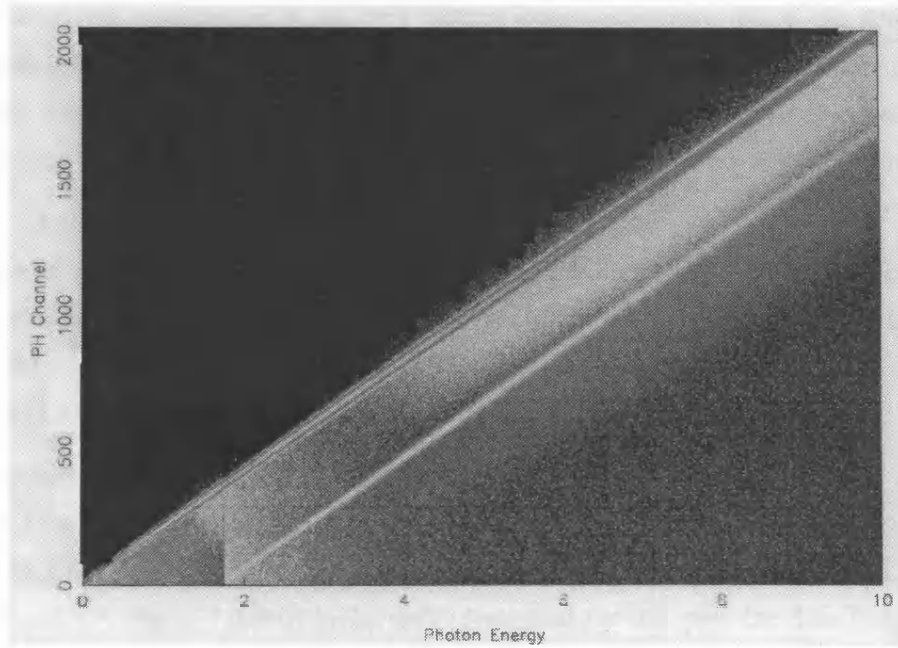


**Figure 6.12** The redistribution matrix for multi-pixel events

### 6.3.2 Telescope response

The JET-X simulation code consists of three modules, the CCD redistribution matrix, the optics and the filters. The simulation works by transporting a photon through the mirror and filter modules. The photon, if not absorbed, is then convolved with the CCD redistribution matrix. After convolution with the CCD response matrix a list of detector counts, defined by the energy and the x and y spatial co-ordinates, is output. Various charge particle backgrounds, whose energies and positions are randomly sampled, can be added.

#### *The mirror response*

The mirror simulation consists of a ray-tracing routine that predicts the path of a photon from its entry into the telescope until it reaches the focal plane or is absorbed. Reflection from mirrors surfaces is described by Fresnel's law and the reflective index is described by the theory developed by Kramers, Kallman and Mark [see Giacconi, 1969].

Scattering due to surface micro-roughness is described by a simplification of the vector and scalar theory of Beckman and Spizzichino [Beckman and Spizzichino, 1963]. The number of scattered photons is given by

$$\frac{I_s}{I_0} = 1 - \exp\left(-\left(\frac{4\pi\sigma \sin \alpha}{\lambda}\right)^2\right) \quad 6-3$$

where  $I_0$  is the number of incident photons,  $I_s$  is the number of scattered photons,  $\sigma$  is the rms surface micro-roughness,  $\alpha$  is the grazing angle and  $\lambda$  is photon wavelength.

Parameters input to the simulation are; number of mirror shells, coefficient for the surface equations, mirror length, diameter and thickness, geometry of the mounting system

and the scattering parameters;  $\sigma$ , the rms surface micro-roughness, and  $\tau$ , the auto-correlation coefficient for the statistical distribution of the micro-roughness of the mirror surface.

XAFS, from synchrotron measurements, are added to the effective area curves after normalisation at the appropriate absorption edges, *i. e.* the Au M edges (see Figure 6.4).

#### *The filter response*

The filter is simulated using a simple transmission model which takes into account the x-ray transmission of Al, Al<sub>2</sub>O<sub>3</sub>, and Lexan/Polyimide (C and O) as well as the support mesh. XAFS are normalised and added to the filter transmission around the Al absorption edge (1560 eV).

#### *All-up effective area*

Figure 6.13 shows the effective area of JET-X from the simulation code over the range 0.3 keV to 10 keV. The inset shows the effective area over the range of the Al K, Si K and Au M V and IV edges, 1.5 keV to 2.5 keV. Note that for this plot the data from the synchrotron measurements have not been added. Effective areas including the measurements from the SRS and NSLS will be seen in the next chapter.

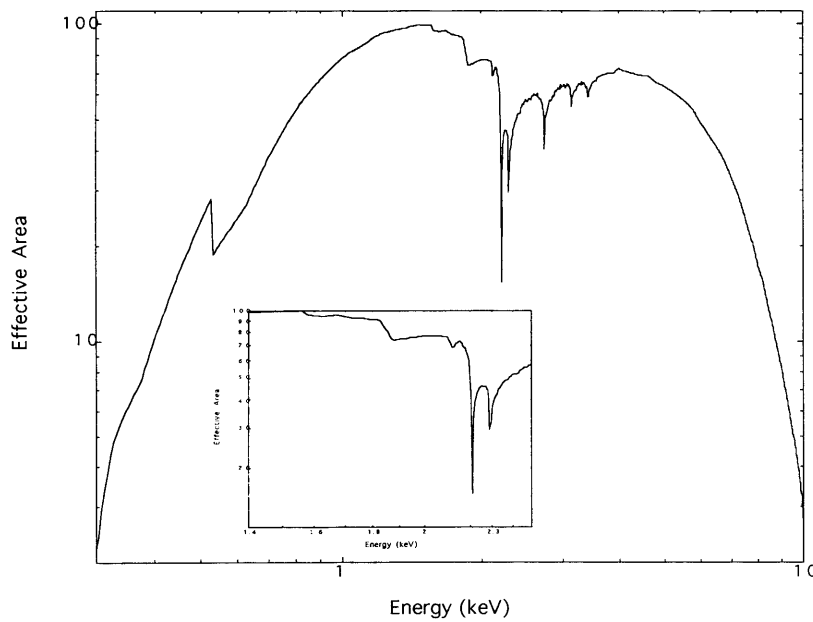


**Figure 6.13** The effective area of JET-X calculated using the simulation code.

## 6.4 In-orbit calibrations

A set of cosmic x-ray sources have been selected that will be observed to provide extra, in-orbit calibrations of the JET-X telescope. The parameters to be calibrated and the object(s) required are summarised in Table 6.6.

Parameter	Object(s)
Bore-sighting	Medium strength (10 mCrab), non diffuse sources
Mirror PSF	Stable sources; Bright (~100 mCrab), Medium (10 mCrab)
Vignetting (off axis)	Medium strength (10 mCrab) sources
Flat fielding	Clusters of galaxies ( <i>e. g.</i> Coma)
Spectral response	Stable source, point-like with well characterised spectrum
XAFS	Sources with flat spectra in the 0.5 - 3 keV range
Optical/UV leaks	A-type stars
Timing	Flare stars, binary systems
Background	Blank fields, well characterised diffuse sources

**Table 6.6** The additional, in-orbit calibration sources necessary for JET-X

## 6.5 Conclusions

In this chapter the calibration of JET-X has been briefly summarised. This has been done to establish a context for the work reported in remaining chapters of this thesis, especially the following chapter. It has been shown where the studies of CCD Q(E) have fitted into the overall calibration program of JET-X. A brief summary of data from project sources has been made and the observation of fine structures in the responses of the optical sub-systems has been described. An account of the response matrix for the JET-X CCDs and for the whole telescope has been included in this chapter and will be used further in the Chapter 7.

## XAFS and the Interpretation of Astronomical X-Ray sources

### 7.1 Introduction

In this chapter it will be shown that because of the large improvement in spectral resolution and sensitivity brought by CCD detectors, the search for important astrophysical features in cosmic spectra can be compromised by the detectors themselves. This is because the detectors are able to discern X-ray Absorption Fine Structure (XAFS) and shifts in the absorption edges in the critical 100 eV - 10 keV energy band, features that are produced within the detector sub-systems. It will be seen that the magnitude of these features can be large enough to introduce artefacts into pulse height data at the 5 % level. These in turn, can cause errors in the unfolded source spectra of the order of a few percent. Since astrophysical reflection spectra, edges and line features are to be found at the same statistical level ( $\sim 5\%$ ), it is obvious that a good understanding of this instrument induced structure is essential. Recent high resolution, in-orbit measurements by soft x-ray telescopes have revealed inextricable low-level fine structure in cosmic spectra that is difficult to ascribe to an astronomical source using current models. For example, Figure 7.1 shows a high resolution measurement of the Crab Nebula obtained with NASA's Broad Band X-ray Telescope (BBXRT) [Weaver, 1985].

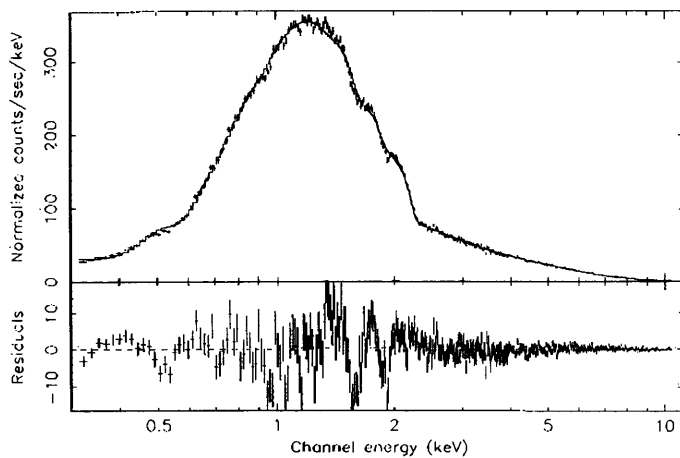


**Figure 7.1** The measured BBXRT spectrum of the Crab Nebula.



In this figure the solid line is a best-fit absorbed power law spectrum. The lower panel shows the residual spectrum after the model has been subtracted. From the figure, it can be seen that the normally “feature-less” Crab spectrum displays considerable structure between 0.2 keV and 3 keV. A significant fraction of this structure reveals itself as emission lines and absorption features at energies appropriate for the O-K ( $\sim 0.5$  keV), Al K (1.4 keV) and Si K (1.8 keV) edges, and at  $\sim 2$  keV. However, current theory suggests that the x-ray spectrum of the Crab nebula should be a smooth power law. This is because the emitted radiation can be accounted for by synchrotron radiation from relativistic electrons moving within the  $\sim 10^{-9}$  T magnetic field of the nebula [Mitton, 1979].

### 7.1.1 Calibration of JET-X

In the early stages of the calibration program of JET-X, the effect of XAFS had not been considered. However concern over structure in the response of detectors in the vicinity of atomic absorption edges was not entirely new. For example, Lamb reported a discontinuity in the gain of the Space Lab 1 GSPC around the Xe L edges (4.78 keV to 5.45 keV) which gave rise to a narrow line feature at 4.8 keV in an x-ray spectrum from the Crab nebula [Lamb, 1987]. More recently, Jahoda and McCammon have reported response discontinuities in an Ar-CH<sub>4</sub> proportional counter across the Ar LI & LII edges ( $\sim 250$  eV) [Jahoda, 1988].

With the realisation that gain changes (*i. e.* changes in the value of  $\omega$  and  $F$ ) could effect the response of the CCD at an absorption edge, the group at Leicester, in 1993, decided to undergo a series of tests to measure these effects. It was quickly realised however that XAFS were more significant. The group then turned its efforts to mapping the response of the CCDs [Keay, 1995; Owens, 1996] while carrying on the program to understand the x-ray response of silicon [Fraser, 1994]. At the same time the response of the mirrors and the filters were investigated [JET-X/FDR, 1995]. In this chapter it will be shown that the three components in the optical chain of JET-X, the mirrors, the filters and the CCDs, can create artefacts in recorded spectra. It will be shown that these features are similar, in both magnitude and energy, to artefacts from cosmic sources. Some of this work has also been published [Owens, 1997]

The scientific goals of JET-X, which were outlined in Section 2.4, depend critically on the ability of JET-X to study sources using good spectral resolution. In this chapter it will be shown that if these goals are to be met, then structure in the response of the telescope sub-systems will need to be thoroughly understood.

### 7.1.2 Future missions

In this chapter it will also be argued that the artefacts caused by the telescope not only hinder model fitting but also introduce line and emission features that can confuse the

search for astrophysical absorption and emission lines if the telescope is not accurately calibrated.

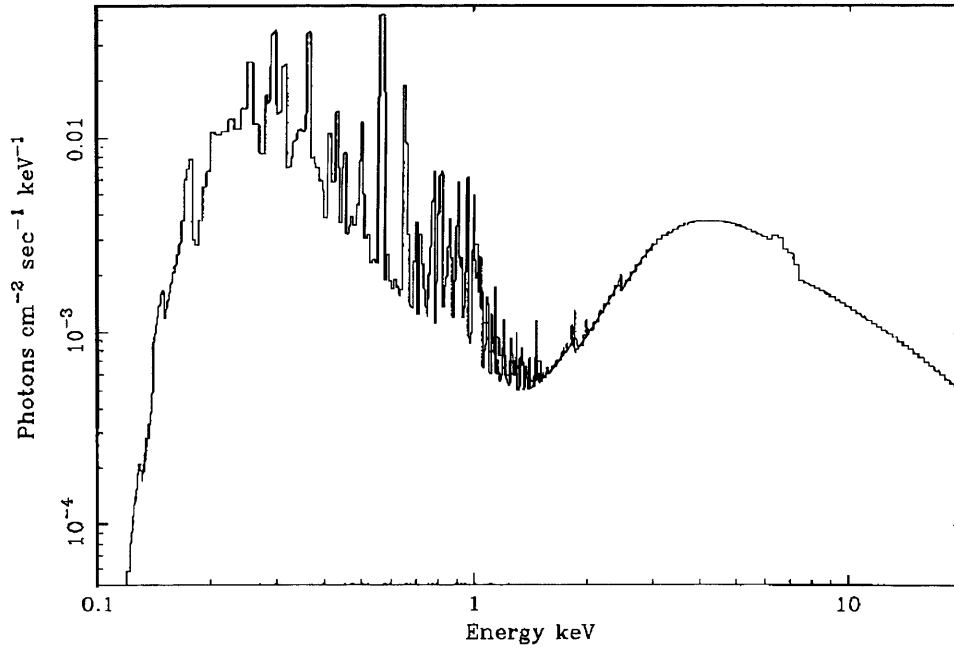


**Figure 7.2** The predicted x-ray spectrum of NGC 4151 [Warwick, Done and Smith].

Accurate calibration will be especially important for missions launched in the next decade, since theoretical models of Active Galactic Nuclei (AGN) predict considerably more structure in these regions than hinted at by previous instrumentation. Figure 7.2 shows an example of the type of spectrum that can be expected. In this figure a predicted x-ray spectrum of the Seyfert galaxy NGC4151, based on the model of Warwick, Done and Smith [Warwick, 1995] is shown. The presence of multiple emission features in the 0.3 keV - 2.5 keV energy range is clear.

Using measurements detailed in Chapters 4 and 6, it will be shown that unfolding celestial source spectra using a “standard” response function in which the edge shapes are calculated from atomic absorption cross-sections can lead to the generation of spectral artefacts at, and above, absorption edges. It will be shown that, in turn, these artefacts produce unacceptably high values of chi-square in model fits and statistically significant line-like features in residual plots, that is plots of the measured data - the modelled data. The largest deviations in the residuals are shown to arise near  $\sim 0.5$  keV, associated with XAFS produced in the  $\text{SiO}_2$  layers of the CCD, at  $\sim 1.84$  keV associated with the Si K absorption edge, and at  $\sim 2.2$  keV caused by the gold reflective surface of the mirrors. It will be shown that these results are significant for data interpretation tasks with the ASCA, JET-X, XMM and AXAF telescopes.

In Section 7.2 the models developed to analyse the data will be explained. In Section 7.3 the results of the computer modelling are described and in Section 7.4 the implications of the results are discussed.

## 7.2 Modelling

### 7.2.1 Introduction

The effect of XAFS on cosmic x-ray source spectra has been investigated using the x-ray spectral fitting program, XSPEC, in combination with the JET-X simulation code. The simulation code, which is described in the previous chapter, is a collection of modules which detail the response of the individual sub-systems of the JET-X telescope, and combines them into an “all-up” system response. Figure 7.3 shows the “all-up” system response reproduced from Chapter 6. The figure shows the all-up effective area of the JET-X telescope, including an 800 Å filter, both with and without the effect of XAFS and edge-shifts.

### 7.2.2 XSPEC

The x-ray spectral fitting program XSPEC has been used to analyse XAFS introduced by the response of the JET-X telescope. XSPEC is an interactive, command-driven program designed to be used with virtually any system response [Schafer, 1990]. XSPEC allows the user to fit data with models that can be constructed from many components. These components may be additive or multiplicative. Multiplicative components can be applied to other components, a group of components or the entire model. Data-sets were created using the XSPEC *fakeit* command. *Fakeit* allows a user-defined response matrix and a representative model spectrum to be convolved in order to create a set of realistic, “fake” data. Statistical noise, based on the simulated observation time, and background noise may be optionally added. For the purpose of this work “fake” data was then deconvolved using different representative response matrices to analyse the residual signal caused by XAFS and edge shifts. The standard XSPEC optimisation command, *fit*, was used to perform a chi-squared minimisation based on the Levenberg-Marquadt algorithm [Press, 1992].

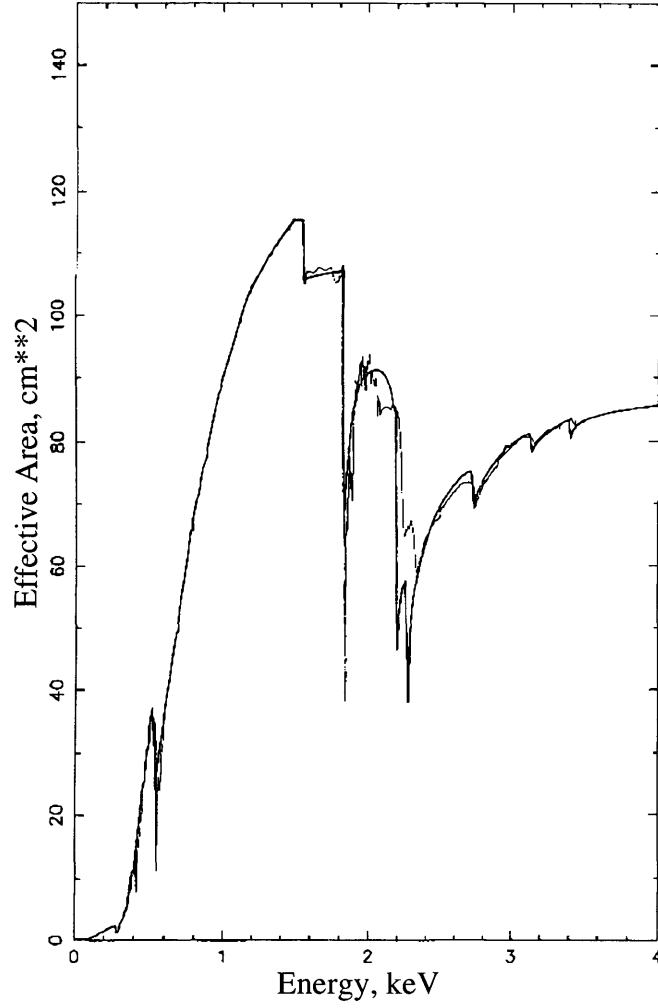


**Figure 7.3** The effective areas of the JET-X telescope with the 800 Å Al filter

#### *Model Spectra*

A number of different representative input spectra were used for this work. Two examples include the Crab nebula and a typical AGN, 3C273. In each case the photon spectrum was adequately described by an equation of the form

$$\frac{df}{dE} = \alpha E^{-\gamma} \quad 7-1$$

where  $df/dE$  is the photon flux,  $\alpha$  is the normalisation in photons  $s^{-1} cm^{-2} keV^{-1}$ ,  $E$  is the photon energy and  $\gamma$  is the power-law slope. The relevant parameters are given in Table 7.1.

Parameter	Source	Value
$\alpha$	Crab nebula	10
	3C273	0.016
$\gamma$	Crab nebula	2.1
	3C273	1.4

**Table 7.1** The model parameters for the Crab Nebula and 3C273. used in this work.

The high throughput of JET-X limits the maximum observable source strength in Imaging Mode to  $\leq 2$  mCrab [Eyles, 1995]. In contrast, the maximum source strength in the non-imaging, Timing Mode is  $\leq 700$  mCrab. For the purpose of this work the Crab-like source was arbitrarily normalised to  $0.18 \text{ photons s}^{-1} \text{ cm}^{-2} \text{ keV}^{-1}$ , *i. e.* 18 mCrab. This level of flux is well above the maximum for imaging but is well below the limit in Timing Mode. Equation (7-1) thus becomes

$$\frac{df}{dE} = 0.18E^{-2.1} \quad 7-2$$

in this case. The modelling also took into account an absorbing hydrogen column between the source and the observer by adding an exponential component which is given by

$$f(E) = f_0(E) \exp(-n_h \times \sigma(E)) \quad 7-3$$

where  $f(E)/f_0(E)$  is the reduction in photon number due to absorption,  $n_h$  is the equivalent column density of hydrogen ( $10^{22} \text{ cm}^{-2}$ ) and  $\sigma(E)$  is the photo-electric absorption cross-section ( $\text{cm}^2$ ). Using Equation (7-2) and Equation (7-3) the incident photon spectrum for the 18 mCrab source can be written

$$f(E) = 0.18E^{-2.1} \times \exp(-0.3 \times 10^{22} \times \sigma(E))dE \quad 7-4$$

where  $n_h = 0.3 \times 10^{22} \text{ cm}^{-2}$  for a representative galactic hydrogen column density.

Once the input spectrum has been modelled, the “fake” data are created using the *fakeit* command. Equation (7-5) is used to determine the number of counts recorded in each detector PHA channel

$$C(I) = \int_0^\infty f(E) \otimes R(E, I) dE \quad 7-5$$

where  $C(I)$  are the detected counts in the  $i^{\text{th}}$  PHA channel ( $\text{counts s}^{-1} \text{ keV}^{-1}$ ),  $f(E)$  is incident model spectrum ( $\text{photons s}^{-1} \text{ cm}^{-2} \text{ keV}^{-1}$ ) and  $R(E, I)$  is the system response matrix ( $\text{counts photon}^{-1} \text{ cm}^{-2}$ ). The system response matrix,  $R(E, I)$ , shown in Figure 6.12, has been determined using the JET-X simulation code with an effective telescope area both with and without the effect of XAFS

For most of this work a “complex” telescope response, including the effects of XAFS and edge shifts, was first convolved with the model using *fakeit*. Using *fakeit*, the background file and poissonian photon statistics were then added. The “fake” data were then deconvolved using the “standard” response matrix, which did not include the effect of

XAFS and edge shifts. Using this procedure, artefacts in the de-convolved spectrum that were wholly due to XAFS in the system response were monitored. The appearance of lines in residual spectra were recorded, while the quality of fits of the model to the data were assessed using the *fit* function.

## 7.3 Results

### 7.3.1 The effect of Si K edge XAFS on deconvolved cosmic x-ray spectra

In this section the effect of XAFS at the Si K edge on x-ray spectra has been analysed using the method outlined in the previous section. Initially a simulated observation was carried out with a model of 3C273 as the input spectrum and a “standard” JET-X response matrix for both convolution and deconvolution. The model and response were convolved with the appropriate statistical noise using the XSEPC procedure *fakeit*. Figure 7.4 shows a plot of the measured spectrum (*i. e.* convolved with *fakeit* and then deconvolved) and the modelled spectrum of the simulated source, observed for  $\sim 10^6$  s.

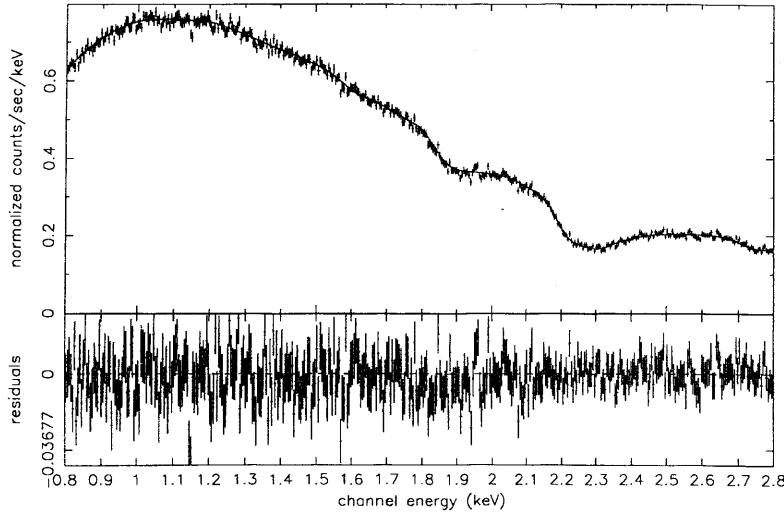


**Figure 7.4** The x-ray spectrum of 3C273 recorded for  $10^6$  s

As expected this spectrum shows only the background and statistical noise with no trace of lines in the residual spectra.

To examine the effect of the “complex” response matrix, including XAFS at the Si K edge, an observation of an 18 mCrab source was then simulated. For this observation the source was convolved with the “complex” response, as well as the background and statistical noise. The data were then deconvolved using the “standard” response matrix. Figure 7.5 shows the measured (*fakeit*) and modelled x-ray spectrum of an 18 mCrab source integrated for  $10^6$  s,  $\sim 10^7$  counts.

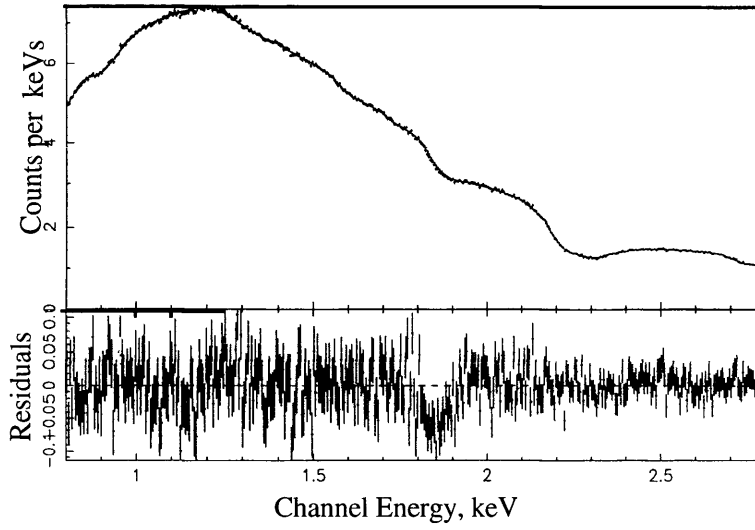


**Figure 7.5** The x-ray spectra of an 18 mCrab source, note the residuals caused by Si K edge anomalies in the CCD Q(E) response

This figure illustrates the effect of Si K edge XAFS on x-ray spectra recorded with JET-X. In the plot of the residuals versus energy (lower panel) it is clear that structure has been induced by using the “standard” response function to unfold the recorded data. The source of this structure is the deviation of the “complex” effective area in the region of the SiO<sub>2</sub> “white line”, which can be seen in Figure 7.3. This spectral artefact appears as an absorption-like feature, with amplitude ~4%, centred at an energy of ~1840 eV.

Interestingly this feature is of the same amplitude relative to the continuum and is at approximately the same energy as residual features measured by the BBXRT telescope (*i. e.*, up to 4% of the source counts). In fact structure of up to 10% of continuum is seen across the whole of the 0.2 to 3 keV range in the BBXRT Crab spectrum (see Figure 7.1). It is therefore clear from the result shown in Figure 7.5, that the structure seen in Figure 7.1 can be interpreted as telescope-induced features from the Si solid-state detectors, the filters and the mirrors of BBXRT.

The significance of this residual line-like feature seen in Figure 7.5 was then measured for different observation times with an 18 mCrab spectrum. The summary of these results can be seen in Figure 7.6.

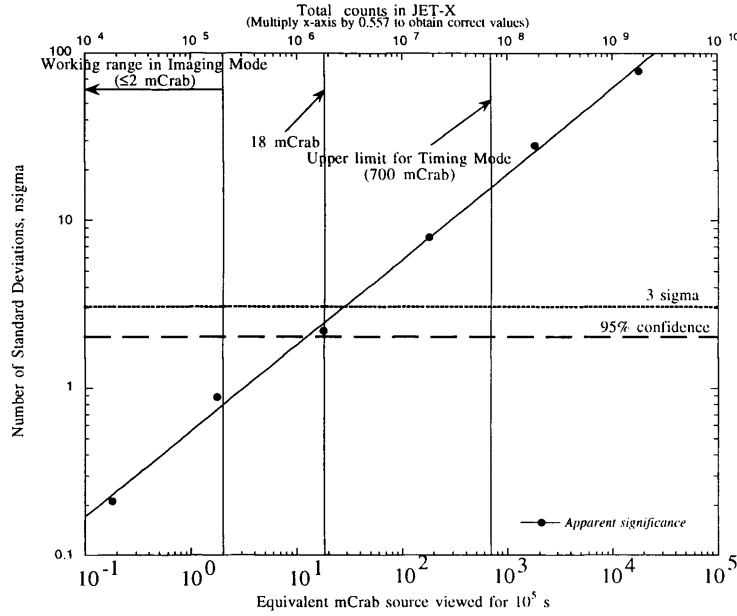


**Figure 7.6** Apparent significance of Si K edge residuals in the JET-X response

This figure shows the apparent significance of the residuals in 18 mCrab source spectra caused by XAFS at the Si K edge. The JET-X working range in Imaging and Timing Modes is shown, along with the 95 % confidence and  $3\sigma$  levels. The total source counts on the upper x-axis should be multiplied by 0.557 to account for the JET-X conversion factor of  $1 \text{ mCrab} = 0.557 \text{ counts s}^{-1}$ . From Figure 7.6 it can be seen that residuals in spectra appear above the  $3\sigma$  level for total source counts  $> \sim 1.7 \times 10^6$ , and above the  $2\sigma$  (95% confidence) level for  $> \sim 6 \times 10^5$  counts. These levels are equivalent to an 18mCrab source observable with JET-X being observed for  $\sim 1.7 \times 10^5 \text{ s}$  and  $\sim 7 \times 10^4 \text{ s}$  respectively. Therefore, Si K edge residuals should be measured in cosmic spectra at the  $2\sigma$  level for an observation of an 18 mCrab source with JET-X operating in Timing Mode, in a typical observation period of  $\sim 1 \times 10^5 \text{ s}$ .

### 7.3.2 Further results of modelling: N K edge, O K edge, Al K edge and Au M edges.

#### *Appearance of lines*

After the initial Si K edge results the work was expanded to include an analysis of structure at other absorption edges of interest (N, O and Al K, and Au M) using a response matrix which included XAFS and edge-shifts from all of the telescope sub-systems, *i. e.* the mirrors and filters, and the O and N edges of the CCD. Figure 7.7 shows a  $\sim 10^5 \text{ s}$  observation of a 10 mCrab source. Again *fakeit* was used to convolve the “complex” response matrix with a model spectrum and the resulting data was then deconvolved using the “standard” response matrix.



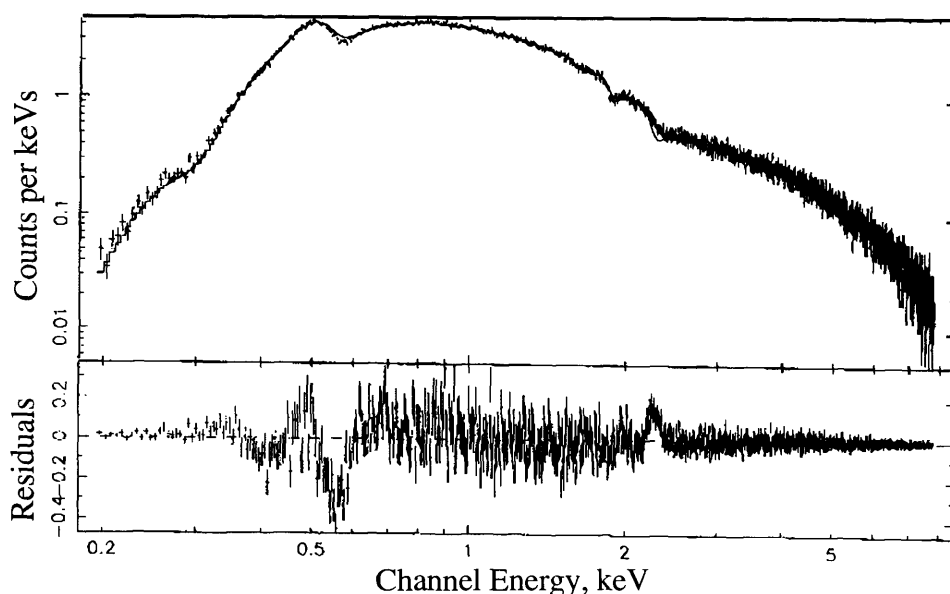


**Figure 7.7** A  $\sim 10^5$  s observation of a 10 mCrab source, deconvolved with a response matrix which did not include XAFS and edge-shifts

Again the effect of XAFS, and now edge shifts in the mirror response as well, are clearly shown in the lower of the two plots which shows the residuals when the incorrect response matrix is used. The Si K edge residuals are now difficult to discern above the noise as one would expect from the results shown in Figure 7.6. However there are absorption-like and emission-like features at 0.43 keV (6% of counts), 0.5 keV (5%) and at  $\sim 0.55$  keV ( $\sim 10\%$ ) and at 2.2 keV (14%). These features can be attributed to edge structure from the oxide surface layers of the CCD ( $\sim 0.5$  keV) and the gold surface of the mirrors ( $\sim 2.2$  keV) respectively.

The features in the low energy regions, 0.4 - 0.7 keV, can all be associated with Q(E) variations in the CCD. The absorption-like feature at  $\sim 430$  eV can be attributed to the N K absorption edge of the  $\text{Si}_3\text{N}_4$  in the passivation layers of the CCD. Although there is only a little structure in the N K edge data from the Daresbury data (see Figure 4.23) the deviation is still enough to cause structure to appear at the  $\sim 6\%$  level, due to the presence of a small “white line” in the data which is not accounted for in the model. The small emission-like feature around 0.5 keV is due to small deviations of the measured CCD Q(E) from the model just below the O K edge. The large  $\sim 10\%$  artefact at 0.55 keV is the effect of the “white line” in the CCD Q(E) at the O K edge (see Section 8.2.1 for a thorough description of this feature). The “white line” is caused by the thermal and vapour deposited  $\text{SiO}_2$  in the surface layers of the CCD.

The most significant feature at 2.2 keV is due to the large discrepancy between the measured and modelled shapes of the Au M V edge in the mirror response. This is described in Section 6.2.1 and can be seen in Figure 6.4 where the onset of the M V and the M IV differs from the tabulated values in both amplitude and position. In Figure 7.8 the

significance of the line feature at 2.2 keV as a function of integrated source counts is plotted. The upper x-axis should be multiplied by 0.557 to account for the JET-X conversion factor of  $1 \text{ mCrab} = 0.557 \text{ counts s}^{-1}$ .

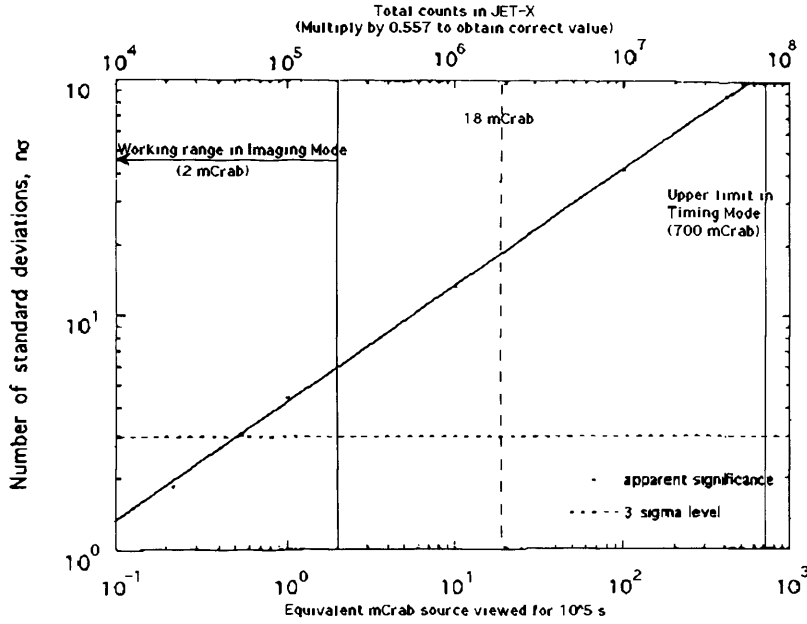


**Figure 7.8** Apparent significance of the 2.2 keV residual feature

The dotted line shows the  $3\sigma$  level. It can be seen that the 2.2 keV feature exceeds the  $3\sigma$  noise level for total source counts  $> 2.8 \times 10^4$  counts *i. e.* a 0.4 mCrab source observed for  $10^5$  s.

#### Model fits

Another aspect of this work, shown in Figure 7.9, is that instrument induced structure can adversely affect model fits for all observation times  $> \sim 10^4$  s. Figure 7.9 shows the reduced chi-squared quality of fit,  $\chi^2_r$ , as a function of total source counts for 10 mCrab spectra that have been unfolded with both the “complex” and the “classical” response. The dotted horizontal line shows the  $2\sigma$  ( $\sim 95\%$  confidence) level. The upper x-axis should be multiplied by 0.557 to account for the JET-X scaling factor of  $1 \text{ mCrab} = 0.557 \text{ counts s}^{-1}$ . It can be seen from the plot that spectra unfolded using the “complex” response matrix (dot-dashed line) fall within the  $2\sigma$  level for all observation times. However, spectra unfolded with the “standard” response (solid line) are poorly fitted by the model for any observation  $> \sim 2.8 \times 10^4$  counts. This means that any relatively strong source, an AGN for example, would produce enough counts during a typical,  $10^5$  s, observation, that XAFS and edge-shifts would have a deleterious effect on the  $\chi^2_r$  value. The concern must then be that this may lead the user to try to fit false emission or absorption features in order to improve the  $\chi^2_r$ .

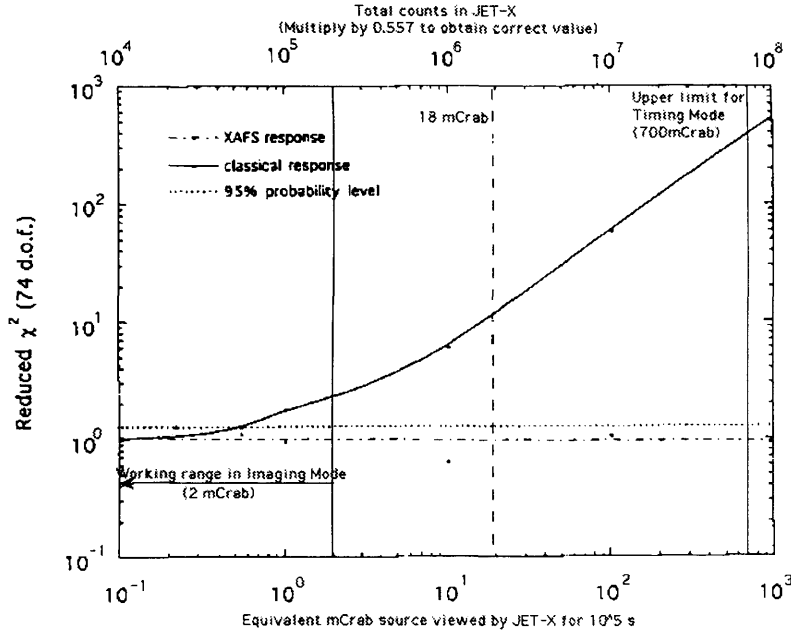


**Figure 7.9** Apparent significance of residuals in source spectra caused by the JET-X response

## 7.4 Discussion

In this chapter the effect of the JET-X telescope response on data interpretation tasks has been examined and described. The effect of complex edge structure in the  $Q(E)$  of the CCD at the Si K edge was initially examined. It was shown that Si K edge XAFS will produce an absorption-like artefact with an  $\sim 2\sigma$  significance in cosmic sources stronger than 10 mCrab, in a typical observation period, if not accurately calibrated. This effect will be of serious consequence when JET-X is operated in Timing Mode, although it should not be a problem when in Imaging Mode. This is because the counting statistics are limited by photon pile-up in the CCDs, and JET-X will not therefore be able to view a source as bright as 10 mCrab.

In the light of this important result the effect of anomalies in the response of the rest of the telescope sub-systems were investigated. It was shown that unfolding source spectra using a “standard” response matrix, yields line-like artefacts at almost every absorption edge of interest. This leads to poor model fits for source fluxes  $> 2 \times 10^4$  counts, *i. e.* a  $10^5$  observation of a 0.4 mCrab source. It has been shown that the largest deviations in the residuals arise at 0.55 keV and 2.2 keV and are attributed to structures produced in the oxide surface layers of the CCD and the gold reflective surface of the mirrors, respectively.

The work in this chapter shows that the intrinsic, instrument-induced structure, caused by XAFS, will be a serious threat to the scientific objectives of JET-X if not properly corrected for. The work has also shown that particular care must be taken in the treatment of XAFS during calibration and that a comprehensive program to derive the relevant absorption cross section should be carried out. In fact it is the work done to establish the impact

of XAFS on JET-X that has led to the Si K edge absorption coefficients used for the interpretative tasks in the next chapter. This database also ensures that, at the Si K edge, JET-X should not suffer from the effects of XAFS, as is shown by the accurate modelling shown in Chapter 8.

This work has shown that XAFS and edge shifts are significant for data interpretation tasks with the ASCA, XMM and AXAF telescopes as well as JET-X. This will be particularly true for XMM because of its significantly greater effective area [Bignami, 1990]. The number of counts recorded by an x-ray telescope can be related by the expression

$$C(E) = \sum_{0.03}^{10} f(E)Q(E)At\Delta E \quad 7-6$$

where  $C(E)$  is the total number of counts in the energy band 0.03 - 10 keV,  $f(E)$  is the source strength,  $A$  is the telescope area and  $t$  is the observing time. Therefore the statistical error on the number of counts recorded in a given channel for a given observation period is given by the square root of this number, *i. e.*

$$\sigma = \sqrt{f(E)Q(E)At\Delta E} \quad 7-7$$

Given that JET-X and XMM will have very similarly constructed mirrors and detectors (with similar fine structure effects), if both observe the same source for the same amount of time, the ratio of counts (or residuals) to noise in XMM will be higher than that in JET-X by a factor given by

$$\left(\frac{C}{\sigma}\right)_{XMM} = \left(\frac{C}{\sigma}\right)_{JET-X} \times \left(\frac{A_{XMM}}{A_{JET-X}}\right)^{\frac{1}{2}} \quad 7-8$$

Since at ~1.8 keV,  $A_{XMM}/A_{JET-X} \approx 16$  then  $(C/\sigma_{XMM})/(C/\sigma_{JET-X}) \approx 4$ . Now, the observation time,  $t \propto (C/\sigma)^2$ , so the time needed to perceive instrument induced structure with XMM will be reduced a factor of  $\approx 16$ , *i. e.* an observation above the  $3\sigma$  level in  $\sim 10^4$  s at the Si K edge, and  $< 10^3$  s at the Au M edges.

XAFS and other edge-related phenomena will potentially be an even greater cause for concern for the next generation of detectors. This is because they will need to differentiate between instrumentally-induced structure and structure produced in cosmic matter. This is particularly true for future detectors with increased energy resolution such as calorimeters and those based on Superconducting Tunnel Junction (STJ) technology [Kraus, 1997]. As an example of the type of structure that these detectors will be capable of measuring, Figure 7.10 shows an SMM X-Ray Polychromator spectrum of the 6.6 keV, Fe XXV - Fe XXII, “iron line” complex with varying spectral resolutions [Schmitt, 1990]. This region is of prime interest in x-ray astronomy because it provides such useful physical constraints for cosmic plasmas.

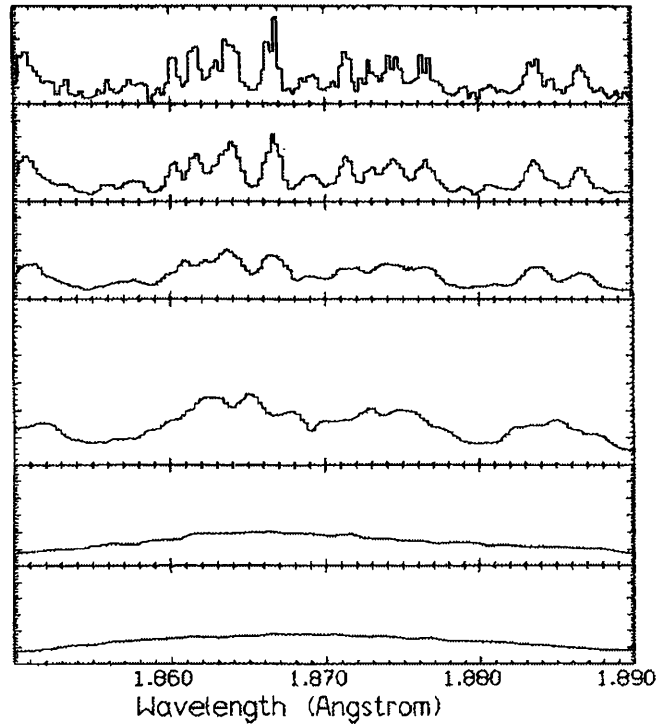


**Figure 7.10** The effect of reducing instrumental resolution from 0.7 eV to 60 eV on the 1.85 Å “iron line” complex [from Schmitt, 1990].

The effect of spectral resolution can clearly be seen as the resolution is reduced from 0.7 eV at the top through 2.1 eV, 5 eV, 10 eV and 30 eV, to 60 eV at the bottom. At 10 eV, close to the resolution that calorimeters can currently achieve, the spectral resolution has blended together most of the satellite lines. However at ~1 eV, the theoretical limit for STJs, the wealth of information is clear. The problem for these detectors will be how to discern instrument induced structure from that produced by cosmic plasmas.

This work in this chapter suggests that interpretation of existing data has probably already been complicated by artefacts in cosmic spectra which are attributable to the telescope sub-systems. Instrument induced structure can be introduced at a level similar to the inexplicable residuals seen in instruments such as BBXRT (see Figure 7.1). It is clear therefore to interpret structure from cosmic plasmas at this level one must be confident that it is not caused by the telescope itself. This can only be done if the instrument response is fully understood, and calibrated, a task that will become increasingly difficult for future missions based on more advanced photon capture and detection systems.

Interestingly, recent work by Woo [Woo, 1995] has shown that at the levels of resolution mentioned earlier ( $E/\Delta E \approx 1000$ ) it is possible to derive the compositional and crystal structures of interstellar grains from the XAFS signal imprinted on the spectra of highly extincted, bright stars. EXAFS at the Mg K and Si K absorption edges, from Magnesium Silicate in interstellar grains, can be seen in Figure 7.11, which is a simulated spectrum from a highly extincted x-ray star.

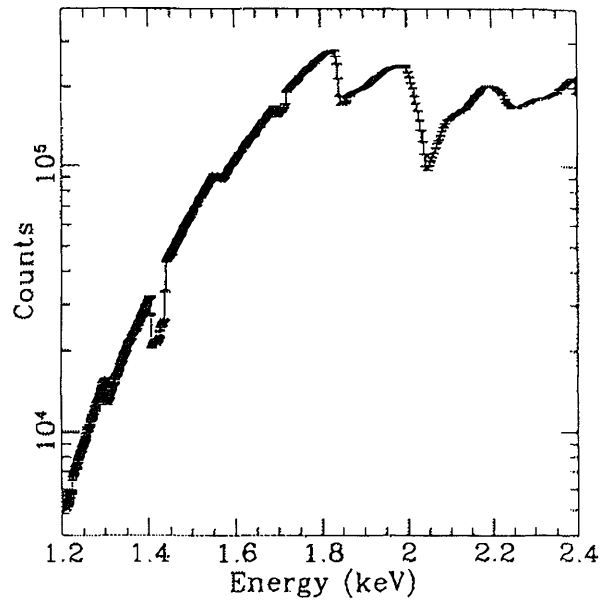


**Figure 7.11** EXAFS above the Mg K edge (1.30 keV) and the Si K edge (1.84 keV) from a simulation of a highly extincted x-ray star.

In the conclusion of his paper, Woo states that he, “simply wants to emphasise that EXAFS features will be detectable in the spectrum of bright and highly extincted stars”. In conclusion to this chapter it should be pointed out that XAFS features will indeed be discernible in cosmic spectra, especially at higher resolutions, but these features are equally as likely to be have been produced in the detector as the cosmic source.

# 8

## Investigating the Composition and Structure of Materials in an X-Ray CCD

### 8.1 Introduction

During the course of the CCD calibration work at Daresbury it was realised that the large amount of detail in the  $Q(E)$  at the silicon K absorption edge could provide accurate information about the structure and composition of the chemicals found in the CCD. Initially it was envisaged that this information would come from the simple comparison of CCD  $Q(E)$  with Si,  $SiO_2$  and  $Si_3N_4$  photo-current measurements, measurements that had been obtained concurrently in a separate experiment. However, as knowledge of XAFS in CCDs improved, it was realised that the  $Q(E)$  measurements were potentially a more powerful investigative tool than such a simple analysis allowed.

In previous chapters it has been shown that the absorption of x-rays in a CCD involves many processes. CCDs have extensive dead-layer and electrode structures situated on the front surface that absorb x-rays before they reach the depletion layer. In fact one of the major problems in x-ray spectroscopy is determining the energy dependant correction for absorption in these inactive layers. This is a complex exercise because CCDs have inactive regions consisting of many independent layers. The composition and thicknesses of these layers are not accurately known for a variety of reasons; i) the complex form of the MOS construction, ii) the fact that details of construction are proprietorial information that manufacturers do not wish to make public and iii) the presence of residual materials left over after processing, particularly etching. Scanning Electron Microscopy (SEM) of sectioned CCDs can be used to measure the thicknesses of the layers but not, in general, their composition. Alternatively the thicknesses can be determined using a Monte-Carlo model, where estimated thicknesses of the inactive regions are adjusted until a good fit to experimental  $Q(E)$  measurements is obtained. This procedure can usually provide an accuracy of ~5% for the thicknesses of the electrode structures and dead-layers.

Modelling has already shown that the response of the CCD just below the Si K absorption edge is dominated by the depletion depth, whereas above the edge, it is dominated by the overlying structures [McCarthy, 1991]. This ensures that the structure seen in the  $Q(E)$  above the edge is almost entirely caused by the electrodes and dead-layers and is dependant on the chemical environment in which the absorbing atom is situated. The structure in the  $Q(E)$  very near the edge (up to ~30 eV) is attributable to XANES and in the next section it will be shown that XANES measurements can be used to obtain the thicknesses of

the electrodes and dead-layers. The fine-structure in the rest of the spectrum is caused by EXAFS and, as is shown in Section 8.3, measurements of the EXAFS can be analysed to obtain information on the composition of the chemicals in the overlying region.

The cause of x-ray absorption near edge structure, has already been described in Chapter 5. In 8.2.1 of this chapter, XANES in the CCD Q(E) will be described in more detail. Sections 8.2.2 and 8.2.3 describe the initial, phenomenological work using photocurrent measurements which showed that the structure at the edge could be attributed to the attenuation in Si, SiO<sub>2</sub> and Si<sub>3</sub>N<sub>4</sub> in the overlying regions. The subsequent work using more accurate absorption coefficients and the conclusions drawn about the CCD composition are given in 8.2.4. In particular it was possible to analyse the near-edge structure and the “shape” of the edge, to derive the thicknesses of the inactive layers of the CCD to a higher degree of accuracy than can be obtained by modelling Q(E) data or by SEM measurements.

Section 8.3 describes the work done in extracting the EXAFS signal from Q(E) measurements. The EXAFS signal has been extracted and then analysed, using a standard technique, to provide information on the structural chemistry in the inactive layers of the CCD. This technique is powerful enough to supply accurate bond lengths for the three nearest neighbours of the absorbing atoms, which in turn has allowed the crystalline state of the materials in these layers to be confirmed.

## **8.2 Utilising XANES in the Q(E) to investigate an x-ray CCD**

In this section it will be shown how the XANES signal in Q(E) measurements can be used to ascertain the thicknesses of the inactive layers in a CCD. It must be pointed out that a single, unique set of parameters for the electrodes and dead-layers are difficult to obtain since structures in the Q(E) are not attributable to an individual source. However, it will be shown that starting with a reasonable approximation of the electrode structure, it is possible to constrain the parameters and hence determine their value to a reasonable degree of accuracy. The analyses are carried out on data obtained at the Daresbury SRS in March 1994 and in January 1996. Details about the experiment, the data collection and the data reduction are provided in Chapter 4. The CCD, which can be seen in Figure 4.1a, is described in detail in Chapter 3.

### **8.2.1 Measurements of near-edge structure**

Figure 8.1 shows the CCD Q(E) measured at Daresbury in March 1994. The near-edge structures of interest are the absorption thresholds at ~1836 eV for Si and ~1841~eV for SiO<sub>2</sub>, the SiO<sub>2</sub> “white line” at ~1846 eV and an additional resonance line centred at ~1865 eV.



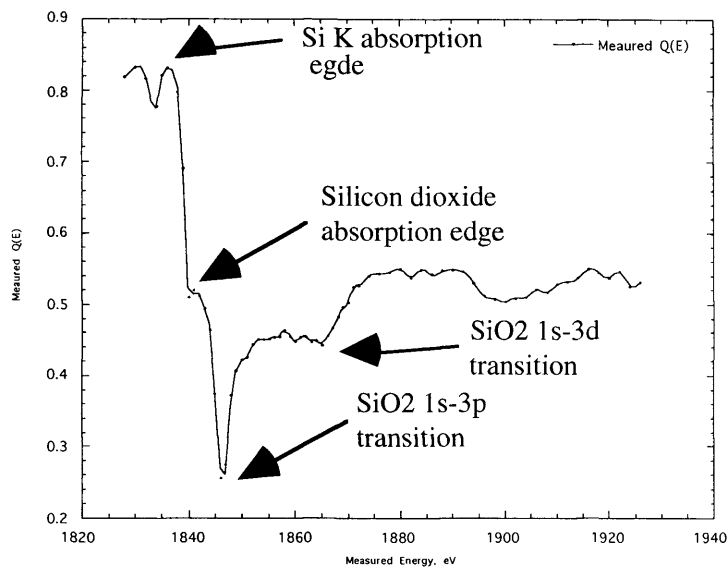


**Figure 8.1** The  $Q(E)$  of the EM3 device measured at Daresbury in March 1994.

The Si K absorption threshold begins at  $\sim 1836 \text{ eV} \pm 0.5 \text{ eV}$  and the absorption edge (defined as the maximum slope) is at  $1839.4 \text{ eV} \pm 0.3 \text{ eV}$ . This corresponds well with values of the Si K absorption edge from the literature which are usually quoted as  $1839 \text{ eV}$  [see for instance, Saloman, 1988]. The  $\text{SiO}_2$  absorption threshold begins at  $\sim 1841 \text{ eV} \pm 1.5 \text{ eV}$  and has a maximum slope some eV above, although it is difficult to deduce accurately as the “white line” begins around the same energy. However it can be seen that there is a shift from the Si K absorption edge of  $\sim 4 \text{ eV} \pm 2 \text{ eV}$ . A shift of 4 - 5 eV is a good indication of an oxygen atom bonded to the silicon absorbing atom [Gurman, private communication]. This shift is due to the widening of the band gap in silicon caused by the Si-O bonds, which increases the energy required for a K shell electron to be excited into the conduction band (see Chapter 5).

The  $\text{SiO}_2$  “white line” at  $1846 \text{ eV} \pm 1 \text{ eV}$  is caused by the increase in absorption that occurs when the K shell electrons are excited into bound states, created by the presence of the oxygen atoms (again, see Chapter 5). Li and co-workers concluded that the feature in  $\text{SiO}_2$  spectra at  $1846.8 \text{ eV}$  is caused by a 1s to 3p/3s transition [Li, 1993]. The 3p/3s bound state in the conduction band is created when the 3p and 3s level combine into  $sp^3$  hybrid orbitals which then interact with  $\phi_1/\phi_2$  oxygen hybrid orbitals. There is an additional, broader line in the CCD spectrum at  $1864.7 \text{ eV} \pm 1 \text{ eV}$ . This is approximately the energy of a broad feature seen in  $\text{SiO}_2$  spectra, which is usually quoted as  $1863.8 \pm 0.1 \text{ eV}$ . This line has been attributed to 1s to 3d/3p hybrid state transitions, which occur via a spin forbidden transition [Li, 1993]. These 3d/3p hybrids occur when the Si 3d states mix with Si 3p levels in the distorted  $\text{SiO}_4$  tetrahedra.

### 8.2.2 Phenomenological interpretation of near-edge structures

In order to identify and quantify the features observed in the CCD  $Q(E)$ , use has been made of photocurrent measurements of Si, SiO<sub>2</sub> and Si<sub>3</sub>N<sub>4</sub>. Total photo-currents were measured from the front and back side of a non-functioning CCD and on samples of silicon nitride and polycrystalline silicon. These measurements were made on Station 3.4 of the Daresbury SRS, by recording the replacement current required to restore charge neutrality in samples of the materials exposed to x-rays [Owens, 1994]. Results are shown in Figure 8.2. The measurements were then converted to total photo-yields using the measured current in, and known photo-yield of, the reference counter. Photocurrent measurements were also made by irradiating a non-functioning CCD, both on front and back surfaces. These measurements gave signatures identical to the SiO<sub>2</sub> sample indicating that both surfaces of the CCD are composed mainly of silicon dioxide.

The photo-currents can be related to the quantum efficiency as follows. To first order, the total photo-current,  $\gamma(E)$ , is proportional to the product of the energy,  $E$ , and the absorption coefficient,  $\mu(E)$  and they are related by the function,

$$\gamma(E) = \mu(E)[\alpha + \beta E] \quad 8-1$$

Over a small energy range,  $\Delta E$ , such that,  $E > \Delta E$ ,

$$\gamma \propto \mu(E) \quad 8-2$$

Let  $\mu_d$  be the absorption coefficient of the depletion region of the CCD and let  $d$  be its thickness.

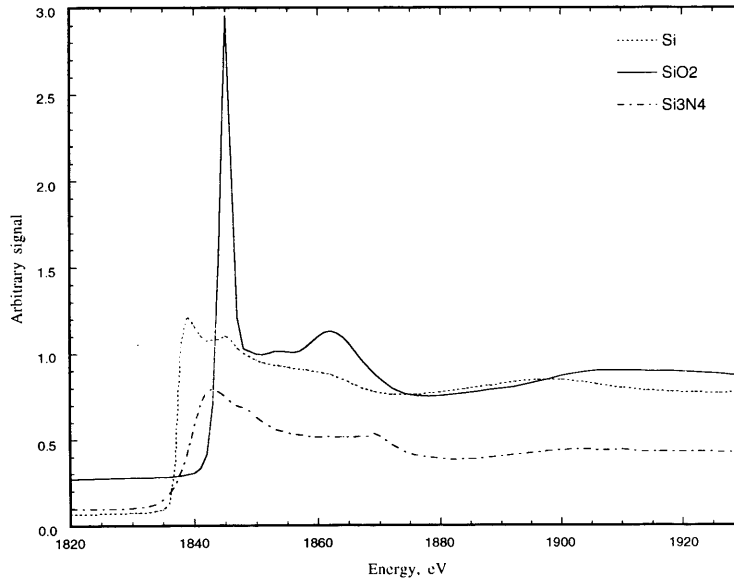


**Figure 8.2** Photocurrent measurements of the CCD constituent materials.

The quantum efficiency for detecting photons of energy,  $E$ , is then given by

$$Q(E) = \frac{1}{p} \left[ 1 - \exp(-\mu_d d) \right] \int \prod_{i=1,0}^p \exp \left[ -a_i(x) (\mu_e)_i t_i \right] \quad 8-3$$

where  $p$  is the pixel width,  $a_i(x)$  is a weighting factor which accounts for the presence or absence of the  $i^{\text{th}}$  overlayer at co-ordinate  $0 < x < p$  within a 1-dimensional section of the CCD pixel, width  $p = 27 \mu\text{m}$ .  $a_i = 0$ , if the  $i^{\text{th}}$  layer is absent and  $a_i = 1$  if it is present.  $(\mu_e)_i$  is the absorption coefficient of the  $i^{\text{th}}$  component of the electrode structure or dead-layers and  $t_i$  it's thickness. In a CCD, the amount of surface structure is dependent on position, and this is the reason for the product summation in Equation (8-3). In order to establish the link between photo-current and quantum efficiency it will be assumed that the complex electrode structure can be approximated by a single uniform layer across the CCD of thickness  $t_{el}$  and attenuation coefficient  $\mu_{el}$ . In this case, Equation (8-3) reduces to

$$Q(E) = [1 - \exp(-\mu_d d)] \times [\exp(-\mu_{el} t_{el})] \quad 8-4$$

Since  $\mu_d d$  is large,

$$Q(E) \approx \exp(-\mu_{el} t_{el}) \quad 8-5$$

and since  $\mu_{el} t_{el}$  is much less than 1

$$Q(E) \approx 1 - \mu_{el} t_{el} \quad 8-6$$

Combining (8-6) with (8-2) we find that,

$$Q(E) \approx a - b\gamma \quad 8-7$$

Typically,  $a \approx 1$ ,  $b \approx 10^{-3}$  and so we have,

$$Q(E) \approx 1 - b\gamma \quad 8-8$$

*i. e.*, the quantum efficiency is essentially the complement of the photo-current. Using this result it is justified, to first order, in directly comparing photo-yield data with the quantum efficiency measurements.

In Figure 8.3 a comparison of the total photo-yield plots of Figure 8.2 and the CCD spectrum can be seen. The initial comparison shows the CCD spectrum to be very similar to the plot produced by the combined photo-current data over the range from 1830 eV to 1930 eV. The first Si peak and the SiO<sub>2</sub> white peak match well and the peak and troughs agree broadly. However, the overall slopes of the plot after the edge are different but this has been found to be due to calibration errors in the monochromator response. A phenomenological analysis, comparing the photocurrent data directly as the complement of the quantum efficiency (but where in Equation (8-8)  $b(\text{SiO}_2) = \sim 2.3 \times b(\text{Si})$ ), has revealed there to be Si (32%), SiO<sub>2</sub> (62%) and Si<sub>3</sub>N<sub>4</sub> (6%) contributing the observed structure. The errors on these figures have been estimated to be at the 5% level. It is believed that all the structure is contributed by the dead layers and electrodes as changes in the absorption coefficient of the silicon in the depletion layer cause negligible changes in the amount of x rays absorbed. This is because the size of the layer is relatively large at 35  $\mu\text{m}$  which ensures that 100% of x-rays with energies from 1838 eV ( $I_d/I_0 = 2 \times 10^{-4}$ ), to the limit of our experiment ( $I_d/I_0 = 2.2 \times 10^{-10}$  at 1930 eV), are absorbed. It can be seen, therefore, that the

Si XAFS must arise from the electrodes above the depletion layer, the SiO<sub>2</sub> XAFS must originate in the Vapox layer and the thermal oxide layers on each electrode and Si<sub>3</sub>N<sub>4</sub> XAFS must come from the passivation layer.

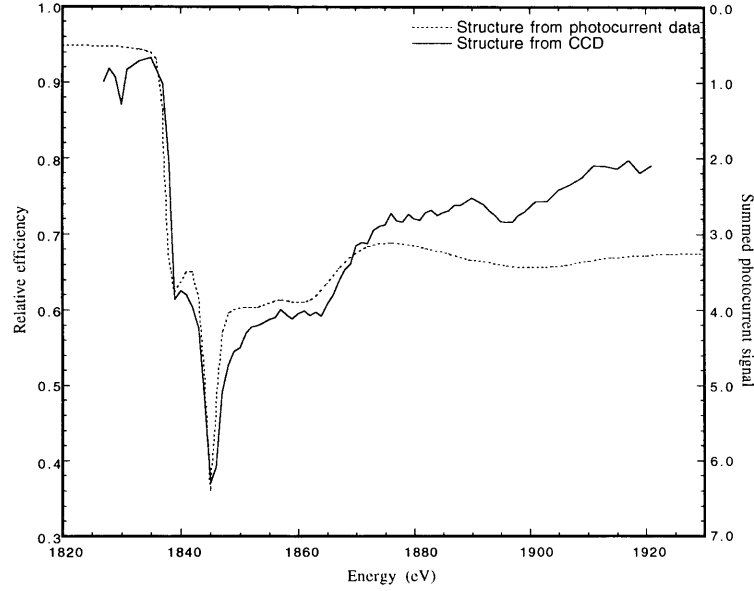


**Figure 8.3** Photo-current measurements fitted to the CCD Q(E)

### 8.2.3 A more detailed analysis of the near-edge structure

In a later low-beam-current study of the CCD, in January 1996, an improved set of Q(E) measurements were obtained. This has been described in Chapter 4. In this section it will be shown that the thicknesses of the electrodes and dead-layers can be extracted from these detailed measurements. To derive these parameters it was necessary to use accurate absorption coefficients of Si, SiO<sub>2</sub> and Si<sub>3</sub>N<sub>4</sub>. Our group has been able to derive absorption coefficients for Si-c, Si-a, SiO<sub>2</sub>-a and Si<sub>3</sub>N<sub>4</sub>-a. from the photo-current measurements shown in Figure 8.2, this data has been published in tabulated form [Owens, 1994]. The attenuation coefficients were derived from photo-current measurements using the expression,

$$\gamma(E) = \mu(E) \{ \alpha + \beta E \} \quad 8-9$$

where  $\gamma(E)$  is the total photo-yield at an energy, E, and  $\mu(E)$  is the corresponding attenuation coefficient.  $\alpha$  and  $\beta$  were determined by normalising  $\mu(E)$  to the classical values far enough above the edges to be free of the effects of XAFS.

The attenuation coefficients from all four materials are shown in Figure 8.4 below.

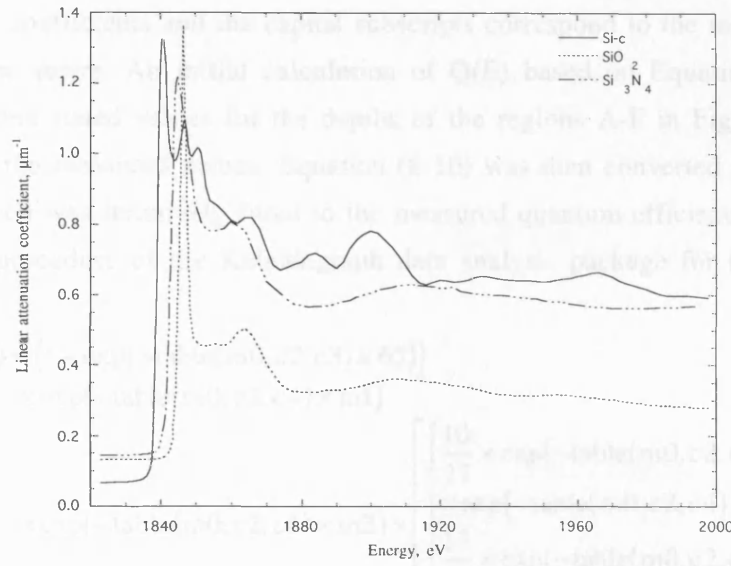


**Figure 8.4** Linear attenuation coefficients for the CCD constituent materials as a function of energy

Using these coefficients as the input, an analytical model was derived based on a simplification of Equation (8-3). In this model the CCD composition was approximated as in Figure 8.5 below

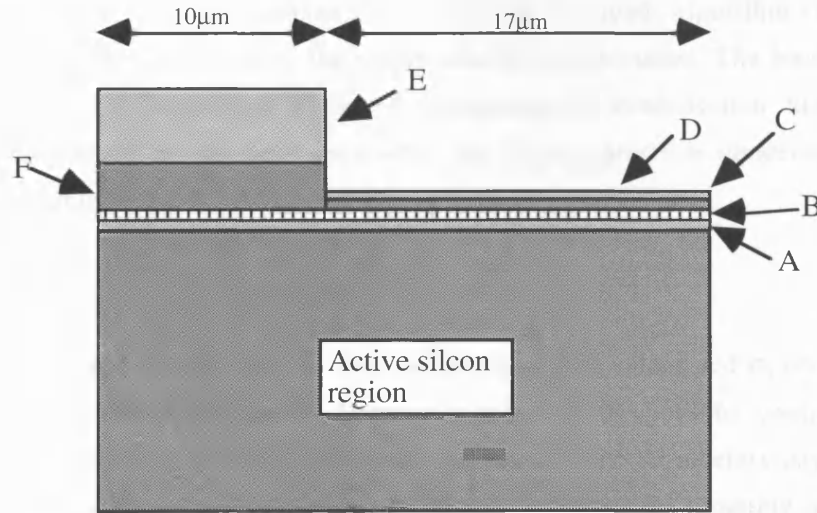


**Figure 8.5** Schematic of CCD model used in the analytical simulation. A is the  $\text{SiO}_2$  passivation layer thickness, B is the  $\text{Si}_3\text{N}_4$  passivation layer thickness, C is the P3 thinned electrode thickness, D is the thickness of the remnant oxide on P3, E is the thickness of the VAPOX and LTO on P1/P2 and F is the thickness of the combined P1/P2 electrode.

Assuming all the pixels are identical, the quantum efficiency of the CCD, Equation (8-3), can be approximated by,

$$Q(E) = \left| \frac{10}{27} \left( \exp(-\mu_{\text{Si}} z_F) \exp(-\mu_{\text{Ox}} z_E) \right) + \frac{17}{27} \left( \exp(-\mu_{\text{Si}} z_C) \exp(-\mu_{\text{Ox}} z_D) \right) \right| \times \exp(-\mu_{\text{Ox}} z_A) \exp(-\mu_{\text{nit}} z_B) (1 - \exp(-\mu_{\text{Si}} z_{\text{act}})) \quad 8-10$$

where 10/27 and 17/27 are the relative areas of coverage of each region,  $\mu$  represents the attenuation coefficients and the capital subscripts correspond to the regions represented in the diagram above. An initial calculation of  $Q(E)$  based on Equation (8-10) using the manufacturers stated values for the depths of the regions A-F in Figure 8.5 gave a very poor fit to the measured values. Equation (8-10) was then converted to a form (Equation (8-11)) which was iteratively fitted to the measured quantum efficiency using the General Curve-Fit procedure of the Kaleidagraph data analysis package for the Macintosh computer.

$$Q(E) = (1 - \exp(-\text{table}(m0, c2, c3) \times 65)) \times \exp(-\text{table}(m0, c2, c4) \times m1) \times \exp(-\text{table}(m0, c2, c5) \times m2) \times \left[ \left\{ \frac{10}{27} \times \exp(-\text{table}(m0, c2, c3) \times m3) \right\} + \left\{ \frac{17}{27} \times \exp(-\text{table}(m0, c2, c3) \times m5) \right\} \right] \quad 8-11$$

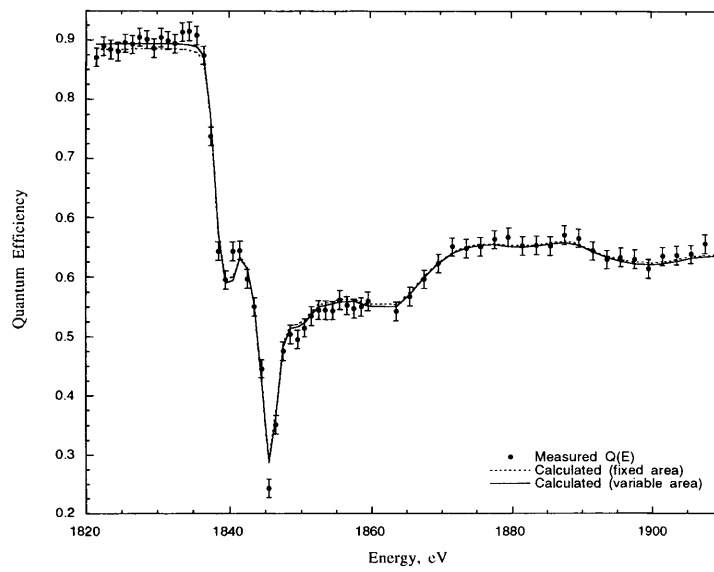
In Equation (8-11) the Kaleidagraph "Table" command is used to interpolate between values of attenuation coefficients stored in a data file, c2 is the energy column, c3-c5 are the columns containing the attenuation coefficients for Si-c, SiO<sub>2</sub> and Si<sub>3</sub>N<sub>4</sub>, and m1-m6 are the free parameters, in this case, the depths of the overlying regions. General Curve-Fit uses a minimisation routine based on the Levenberg-Marquadt algorithm [Press. 1992]. The initial values were taken to be the manufacturer best estimates. The routine defines a  $\chi^2$  merit function and determines the best-fit parameters by minimisation. Since there is a non-linear dependence on the input parameters the fit then proceeds iteratively. The merit function,  $\chi^2$ , is defined as

$$\chi^2 = \sum_i^N \left( \frac{y_i - f(x_i)}{\sigma_i} \right)^2 \quad 8-12$$

where  $y_i$  are the experimental values,  $f(x_i)$  are the modelled values and  $\sigma_i$  are the standard errors for each experimental point. Since a number of the regions contain the same chemical it is possible for the routine to try to reduce some parameters beyond feasible levels (*i. e.* to negative values) while increasing others. However, inputting initial guesses which give values of  $\chi^2$  near the local (realistic) minimum can prohibit this.

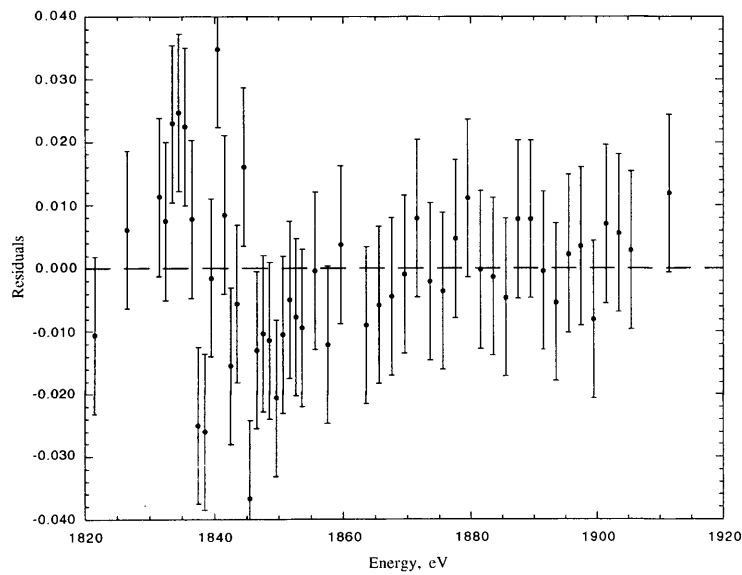
#### 8.2.4 Results

Figure 8.6 shows the quantum efficiency of the EM3 CCD for two different models, calculated using the method described above. Fit (a) has been derived from a model with pixel areas set to 10/27 and 17/27, which are the nominal manufacturers values. In fit (b) the pixel areas have been allowed to vary.



**Figure 8.6** Measured and modelled  $Q(E)$  of the EM3 CCD.

Figures 8.8a and 8.8b show the residuals (*i. e.* the measured values - simulated values) for the curves in Figure 8.6.



**Figure 8.7a** The residuals (measured - calculated) of fit (a) in Figure 8.5.

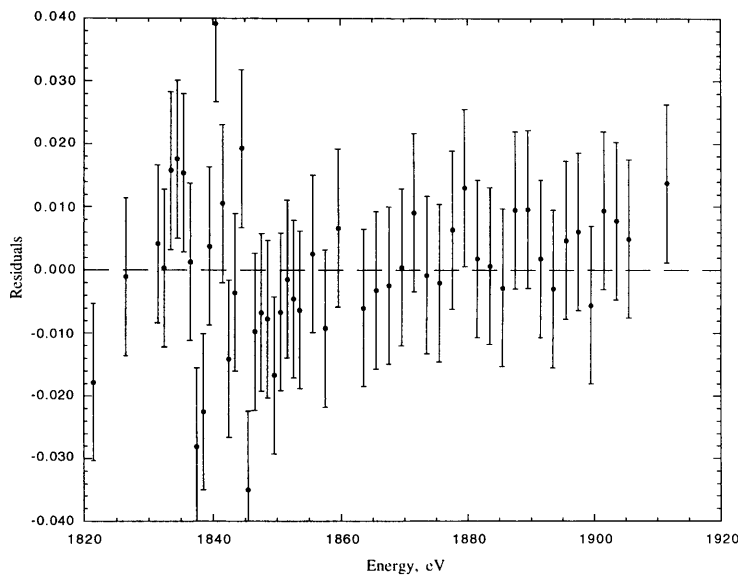


**Figure 8.7b** The residuals (measured - calculated) of fit (b) in Figure 8.5.

For both models the residuals have no systematic trends with energy and are randomly spread around zero. Since the average errors are 0.992% in fit (a) and 0.888% in fit (b) it is justified in saying that all features in the CCD  $Q(E)$  have been accounted for.

Table 8.1 shows the best-fit values for the depths of the regions shown in Figure 8.5, for both fit (a) and fit (b). The  $\chi^2$  values are 51.06 for fit (a) and 44.87 for fit (b), both fits were for 65 degrees of freedom so that  $\chi_r^2(a) = 0.79$  and  $\chi_r^2(b) = 0.69$ . During the fitting procedure the average errors on the measured points were taken to be 1.25%. In fact the  $\sqrt{n/n}$  statistical errors on the number of recorded counts, from which the  $Q(E)$  measurements are derived, varied between 1.45% and 0.95%. The  $\chi^2$  value is very close to 1 if the standard errors in Equation (8-12) are taken to be  $\sim 0.9$ . It can therefore be deduced that there has been an over-estimate of the experimental errors combined with a slight over-fitting of the data.

### 8.2.5 Deductions from this analysis

The results of the fitting procedure are very encouraging and agree well with the values quoted by the manufacturer. However the modelling has produced systematically higher values for the P3 electrode and the oxide covering on P3. In the case of the oxide on P3, subsequent SEM work has shown that although a  $0.01 \mu\text{m}$  oxide was supposed to be covering the electrode, there was in fact a much larger,  $0.10 \mu\text{m} \pm 0.02 \mu\text{m}$  layer. The higher values for the other parameter is not in agreement with the manufacturer's target specifications. These specifications were designed for the JET-X Flight CCDs and do not appear to have been as strictly adhered to in this Engineering Model (EM) device (see Chapter 3). The precision with which some of the regions, especially the thinner areas, can be laid down, is low. One of the benefits of this work is that it confirms the ability of accu-



rate Q(E) measurements to investigate the thicknesses of the surface regions of CCDs. The errors on the parameters in Table 8.1 show that the accuracy with which these parameters are deduced is higher than that generally achieved by Process Control.

Parameter	Manufacturer <sup>3</sup>	Best-Fit (with constrained areas)	Best-Fit (with variable areas)
Depth of F (P1/P2) $\mu\text{m}$	$0.65 \pm 0.13$	$0.629 \pm 0.020$	$0.618 \pm 0.017$
Depth of C (P3) $\mu\text{m}$	$0.17 \pm 0.03$	$0.222 \pm 0.006$	$0.225 \pm 0.006$
Depth of E (Oxide (on P1/P2)) $\mu\text{m}$	$1.20 \pm 0.24$	$1.193 \pm 0.040$	$1.199 \pm 0.034$
Depth of D (Oxide (on P3)) $\mu\text{m}$	$<0.01$ $(0.1 \pm 0.02)^4$	$0.145 \pm 0.020$	$0.132 \pm 0.012$
Depth of B (Nitride passivation) $\mu\text{m}$	$0.085 \pm 0.017$	$0.081 \pm 0.005$	$0.076 \pm 0.005$
Depth of A (Oxide passivation) $\mu\text{m}$	$0.085 \pm 0.017$	$0.192 \pm 0.009$	$0.177 \pm 0.009$
Linear extent of P1/P2 $\mu\text{m}$	10	10	$11.367 \pm 0.013$
Linear extent of P3 $\mu\text{m}$	17	17	$15.957 \pm 0.009$
Chi-Squared value	-	51.06	44.81
Ratio of chemicals <sup>5</sup> (Si/SiO <sub>2</sub> /Si <sub>3</sub> N <sub>4</sub> ) %	36/55/9	32/62/6 ( $\pm 5$ )	32/62/6 ( $\pm 5$ )

**Table 8.1** Comparison of best-fit CCD parameters with manufacturers values.

<sup>3</sup> The absolute tolerances for process control are  $\pm 20\%$

<sup>4</sup> The original specification for the oxide on P3 was  $<0.01 \mu\text{m}$ , however, subsequent SEM investigations showed that P3 did in fact have a  $0.10 \mu\text{m} \pm 0.02 \mu\text{m}$  oxide layer.

<sup>5</sup> c. f. 7.2.2

### 8.3 Analysis of chemical structures using EXAFS

As well as XANES, the CCD  $Q(E)$  displays oscillatory structure further away from the absorption edge known as EXAFS or Extended X-Ray Absorption Fine Structure. In this section it will be shown that the EXAFS signal can be used to provide information about the chemical structure in the inactive layers of the CCD. In order to analyse the EXAFS signal the absorption of the inactive layers has to be separated from the response of the active region of the CCD. This process is described in Section 8.3.1. The EXAFS signal was then extracted from the underlying absorption features, such as the absorption edge itself. This work is described in Section 8.3.2. The data was then analysed to extract the relevant parameters from the EXAFS signal. This was achieved by a Fourier transformation followed by a best-fit analysis of the data. This analysis is described in Section 8.3.3

#### 8.3.1 Reducing CCD $Q(E)$ to inactive layer absorption

Figure 8.8 shows the measured quantum efficiency of the CCD as a function of energy for isolated events, recorded at the SRS in January 1995. In this experiment the energy range was extended up to 2000 eV in order to map all the long range EXAFS features in the response. For comparison the modelled quantum efficiency derived from atomic attenuation coefficients [Cromer, 1970] is also shown.

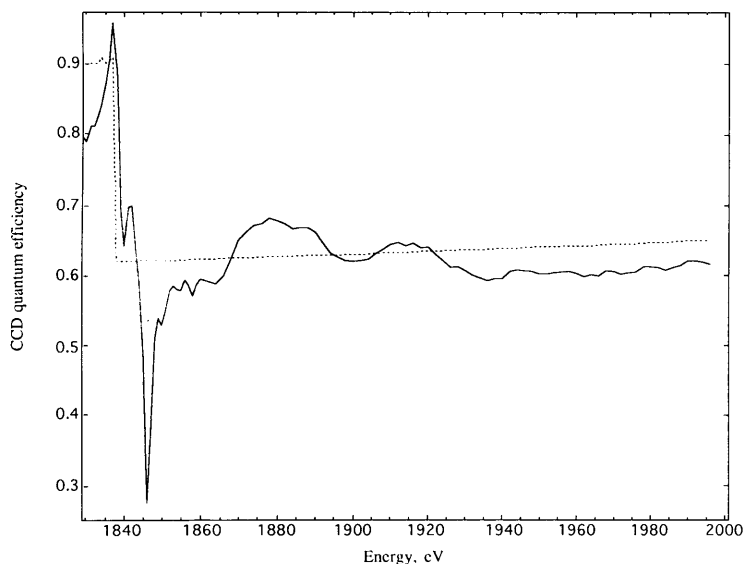


**Figure 8.8** The measured quantum efficiency of the JET-X CCD as a function of x-ray energy around the Si K absorption edge for isolated events. The dotted line is the modelled efficiency obtained using data from Cromer and Liberman.

The CCD measurements have been corrected for beam decay and variation of incident flux intensity with monochromator position, as described in Section 3.3. They were then

converted to quantum efficiency by normalising the measured efficiency to theoretically determined values at energies well below (1820 eV) and well above (2000 eV) the K edge region. For the purpose of this analysis single pixel (isolated) events were used. For x-ray events of one pixel extent which interact in the depletion layer, the CCD quantum efficiency is given by Equation (8-3). The transmission,  $\tau$ , of the electrodes and dead-layers is the integral term on the right hand side of Equation (8-3), so the absorption,  $A=1-\tau$ , can be written as

$$A = 1 - \tau = 1 - \frac{1}{p} \int_0^p \prod_{i=1,n} \exp[-a_i(x)(\mu_e(E))_i(x_e)_i] dx \quad 8-11$$

and therefore, also from Equation (8-3)

$$A = \frac{Q(E)}{[1 - \exp(-\mu_d(E)x_d)]} \quad 8-12$$

Since  $a_i(x_e)(\mu_e)_i(x_e)_i < 1$  at these photon energies, a binomial expansion can be used so that Equation (8-12) is simplified to,

$$A \approx 1 - \frac{1}{p} \int_0^p \prod_{i=1,n} (1 - a_i(x)(\mu_e(E))_i(x_e)_i) dx \quad 8-13$$

For the purpose of this work it has been assumed that the absorption of the inactive layers can be approximated by the absorption from a single uniform layer across the CCD of thickness,  $x_{el}$ , and absorption coefficient,  $\mu_{el}$ . Using this simplification in Equation (8-13) gives

$$A \approx 1 - (1 - \mu_{el}(E)x_{el}) \approx \mu_{el}(E)x_{el} \quad 8-14$$

Hence from Equations (8-12) and (8-14)

$$\mu_{el}(E)x_{el} \approx 1 - \frac{Q(E)}{[1 - \exp(-\mu_d(E)x_d)]} \quad 8-15$$

The absorption of the electrodes and dead-layers can therefore be extracted by normalising the CCD quantum efficiency with the depletion layer absorption.

EXAFS cause the absorption coefficient,  $\mu(E)$ , to vary from the classical absorption coefficient,  $\mu_0(E)$ , by as much as  $\pm 5\%$  on the high energy side of the edge. Therefore the absorption coefficient of Si in the depletion layer will, in principle, be modulated by EXAFS. However the effects are negligible because the large depth of the depletion layer ensures the effect of EXAFS on the absorption of x-rays within this region are essentially attenuated. In fact x-ray absorption within the depletion region is complete to within 1 part in  $10^4$  at 1838 eV rising to 1 part in  $10^{10}$  at 1930 eV. Based on this fact a model was used to simulate the depletion layer absorption for single pixel events, and used to decouple the response.

A Monte-Carlo model was used to simulate the CCD response. The model is a three-dimensional simulation of the charge generation, loss and transport processes in the CCD

[McCarthy, 1995]. The simulation is broken down into four key processes; i) x-ray absorption in the active silicon, ii) generation of photo-ionisation electrons, iii) drift and diffusion of these electrons through the CCD and iv) collection and transfer of the electrons to the read-out register. For this work the response of the CCD has been simulated ignoring the effects of the electrodes and dead-layers so as to obtain a measure of x-ray absorption within the depletion and field-free layers. The input attenuation coefficients were obtained by the group in a separate experiment and included XAFS effects [Owens, 1994]. Figure 8.9 shows a simulation of the absorption in the depletion region as a function of x-ray energy. It can be seen that there is no evidence of an XAFS signal in the absorption spectrum. To extract the absorption of the dead-layers and electrodes from the CCD  $Q(E)$  measurements, the CCD  $Q(E)$  is divided by the depletion region  $Q(E)$  (Figure 8.9 and Equation (8-15)). Figure 8.10 shows the absorption in the electrodes and dead-layers as a function of x-ray energy, derived by this process. Both XANES and EXAFS features can clearly be seen.

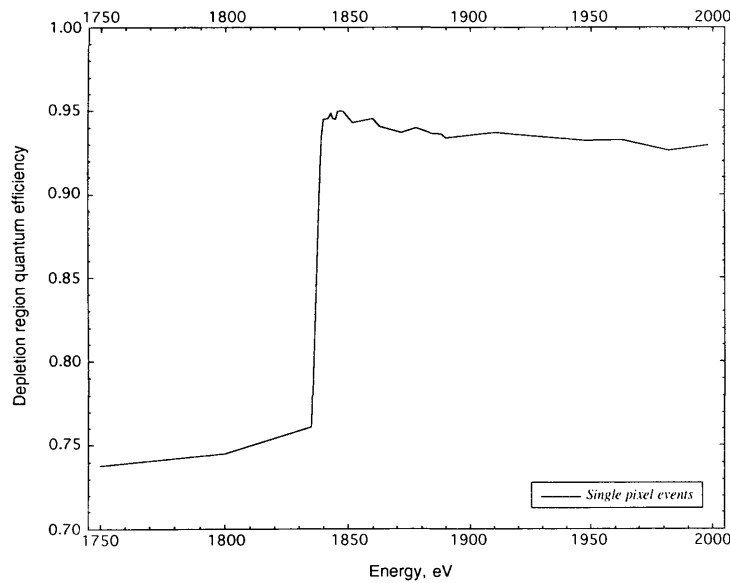


**Figure 8.9.** The result of the “Monte Carlo” simulation of the depletion region absorption. The  $Q(E)$  of the depletion region is displayed as a function of x-ray energy around the Si K absorption edge

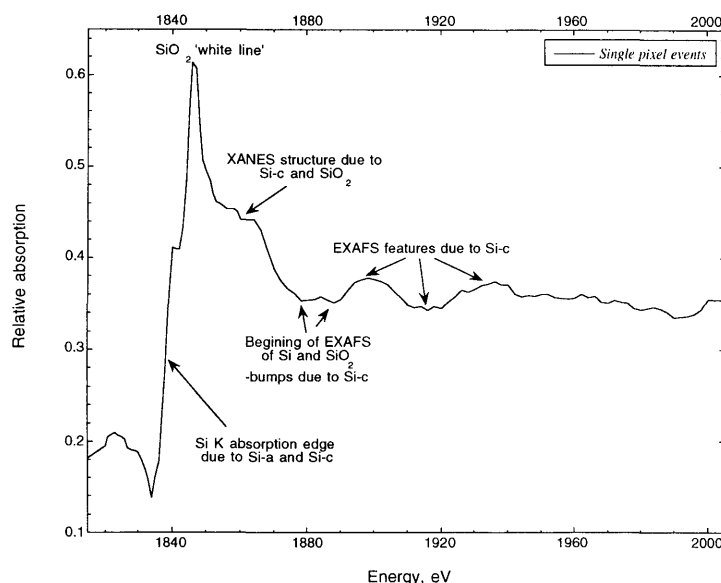


**Figure 8.10** The absorption of the electrodes and dead-layers as a function of x-ray energy. The main features of importance have been pointed out in this diagram.

### 8.3.2 Extracting and analysing the EXAFS signal

The next step in the analysis was to extract the EXAFS function,  $\chi(E)$ , from the dead-layer absorption coefficient,  $\mu_{el}$ . Daresbury's EXBACK program [Morrel, 1986] was used for all aspects of initial processing of the raw data. In order to isolate the EXAFS signal the raw data has to have the pre-edge and post-edge trends removed, and it must be normalised. The fine-structure can then be isolated. The region below the absorption edge is only affected by lower energy transitions and other processes that are not of interest in this analysis, so it is subtracted from the data. The pre-edge background absorption can be fitted either with a "Victoreen" function which has the empirical form,  $A/E^3 - B/E^4$ , or a more simple quadratic equation, and then subtracted. In Figure 8.10 the absorption spectrum input to the EXBACK program is shown. The pre-edge trend is fitted, in this case, with a polynomial function. The post-edge background absorption is removed by fitting the slowly varying background variation with a cubic least-squares-spline fit. This entails fitting the post-edge absorption with 2 or 3 joined polynomial curves in order to model the atomic absorption. Utilising Equation (8-16) the total absorption,  $\mu_{el}(E)$  can be normalised by the smooth monotonically varying absorption coefficient due to an isolated atom,  $\mu_0(E)$ , to remove the effects of sample thickness.

$$\chi(E) = \frac{\mu_{el}(E) - \mu_0(E)}{\mu_0(E)} \quad 8-16$$

The isolated EXAFS are then transformed into k-space, weighted with a  $k^3$  factor and plotted to reveal the normalised EXAFS signal.

Further analysis is carried out using Daresbury's EXCURV92 [Morrel, 1986] EXAFS analysis computer program. A Fourier analysis technique is used to isolate the data from different co-ordination shells. Using an accurate model the data can be iteratively fitted to obtain the best-fit structural parameters. The fitting procedure used is to minimise the sum of the squares of the residuals in the following equation

$$S^2 = \sum s_i^2 = \sum (\chi_i^T - \chi_i^E)^2 W_i \quad 8-17$$

where the sum is taken over all data points,  $i$ , being used for the analysis,  $\chi^T$  and  $\chi^E$  are the theoretical and experimental EXAFS functions and  $W_i$  is a weighting function that can be used to take into account the changing accuracy of the data points.

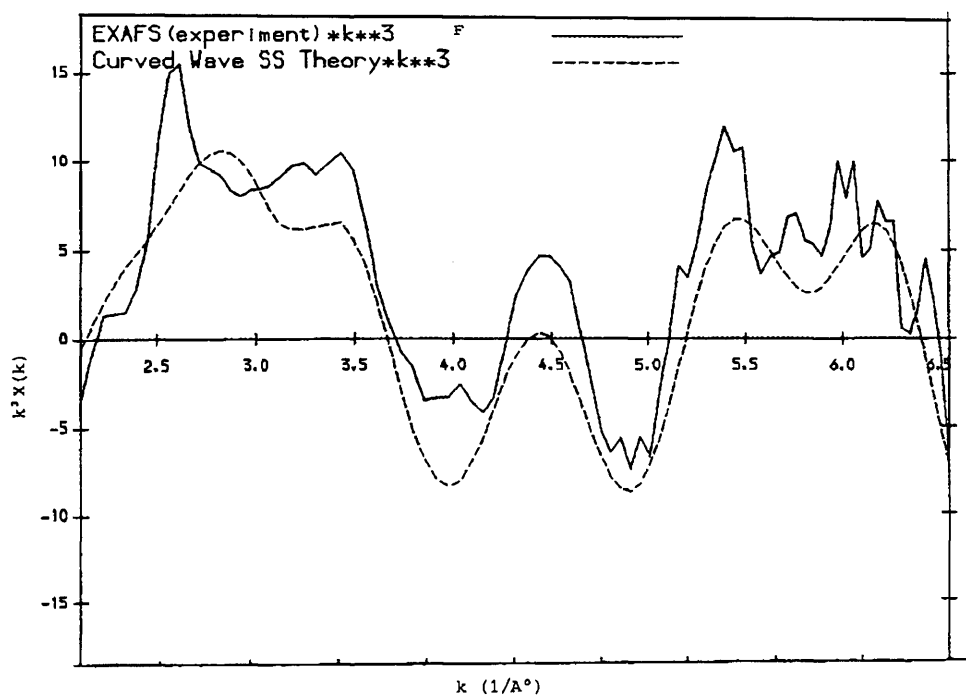
As has been shown in Chapter 5, the EXAFS function,  $\chi(E)$ , can be related to the structural parameters in Equation (8-18) using the following expression, which is based on a single scattering, Plane Wave Approximation (PWA) (for a detailed discussion see [Gurman, 1990, Stern, 1988]). Although the EXCURV92 program is based on a more complex, Fast Curved Wave expression [Gurman, 1990] which takes into account wave curvature effects, a PWA theory is used allowing the basic principles involved, which are unchanged in either theory, to be more easily understood.

$$\chi(E) = \sum_j \frac{N_j F_j(k)}{k r_j^2} \exp\left(\frac{-2r_j}{\Lambda}\right) \exp(-2k^2 \sigma_j^2) \sin(2k r_j + 2\delta_j(k)) \quad 8-18$$

It can be seen from Equation (8-18) that  $\chi(E)$  contains information about i) the distance,  $r_j$ , ii) the number,  $N_j$ , iii) the chemical type, from  $F_j(k)$  and  $\delta_j(k)$ , of the excited atom's near neighbours, and iv) the average fluctuation,  $\sigma_j^2$ , of the position of the atoms in the  $j^{\text{th}}$  co-ordination shell.

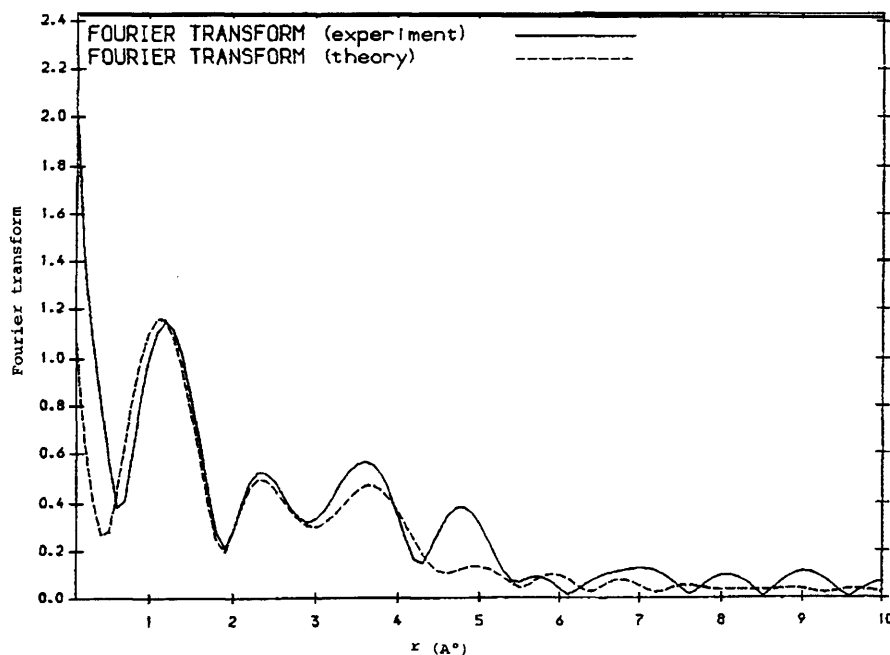
### 8.3.3 Results

Figure 8.11 shows the extracted EXAFS plotted in  $k$ -space and the best fit model based on the Fast Curved Wave Theory [Gurman, 1990] of EXAFS.



**Figure 8.11** The EXAFS spectrum extracted from CCD Q(E) measurement, compared with theoretical EXAFS of a Si/SiO<sub>2</sub> structure

In Figure 8.12 a Fourier transform of the EXAFS and the model are plotted together. In this plot the peaks due to the distinct co-ordination shells are clearly separated with usable peaks from three discrete radial distances.



**Figure 8.12** A Fourier transform of both the experimental and theoretical EXAFS showing the contribution of radial shells of atoms to the EXAFS spectrum in Figure 8.11

The model and data were iteratively fitted using Equation (8-17) to obtain the best-fit structural parameters shown in Table 8.2

Co-ordination shell	Distance (Å)	Fluctuation (Å <sup>2</sup> )	Bond type	Co-ordination number
1 <sup>st</sup>	1.5 ± 0.15	0.025 ± 0.013	Si-O	4.0 ± 2.0
2 <sup>nd</sup>	2.3 ± 0.23	0.009 ± 0.05	Si-Si	3.3 ± 1.7
3 <sup>rd</sup>	3.7 ± 0.33	0.001 ± 0.0005	Si-Si	10.0 ± 5.0

**Table 8.2.** The best-fit configuration parameters for the EXAFS of the CCD electrodes and dead-layers

To deduce any structural information, only the type and distance parameters have been used. The distance parameter has an estimated error of ~10%. The fluctuation parameter, which is related to the Debye-Waller factor was found to be difficult to estimate, especially at greater shell distance. This causes large errors, as high as 50%, in the calculation of the co-ordination parameter. Therefore the co-ordination number has only been used as an approximate guide where appropriate. These parameters are less accurate than a standard EXAFS analysis, which would have typical errors of 0.5% for the distance and 10% for co-ordination, due to the limited accuracy with which the EXAFS function can be derived from quantum efficiency measurements. Nevertheless, the analysis allows the atomic type and separation to be established with sufficient precision that it is possible to determine, unequivocally, the chemical structure that is responsible for extended x-ray absorption fine structure features found in the CCD quantum efficiency measurements.

### 8.3.4 Deductions about structural chemistry from the best-fit analysis

#### *Silicon dioxide*

The 1<sup>st</sup> co-ordination shell seen in Figure 8.12 has a best-fit species of oxygen (*i. e.* suggesting a Si-O bond) and has a calculated spacing of 1.5 Å. This is very close to the bond distance expected for [SiO<sub>4</sub>] tetrahedra in SiO<sub>2</sub> with four co-ordinated Si, where the mean bond distance is usually taken to be ≈1.61 Å [see for example Liebau, 1985]. This deduction is reinforced by the best-fit co-ordination number of 4.0. Taking this together with the lack of evidence for any other Si-O shells in the data, it follows that only amorphous SiO<sub>2</sub> (SiO<sub>2</sub>-a) is found in the surface layers. This is confirmed by reference to Chapter 3 where it can be seen that all oxides of Si are either thermally grown or vapour deposited and *should* therefore be amorphous. There is no evidence for other, energetically less favourable, phases, such as [SiO<sub>6</sub>] octahedra, or SiO<sub>x</sub> phases of silicon oxide, where 0 < x < 2.

#### *Silicon*

The 2<sup>nd</sup> co-ordination shell has a best-fit spacing of 2.3 Å and a best-fit species of a Si shell. Within error, this is a typical value of bond distance for a Si-Si bond, with the Si in



tetrahedral, diamond-like, co-ordination, and a corresponding bond length of 2.35 Å [for example, Blakemore, 1989]. The 3<sup>rd</sup> co-ordination shell at a distance of 3.7 Å, with a best-fit type of Si, indicates another Si shell further from the excited atom. This value for the distance of the 3<sup>rd</sup> shell is in good agreement, again within error, with the calculated value of 3.77 Å for a tetrahedral arrangement. Combined with the co-ordination number of ~10 this is a good indicator of the second nearest Si shell in a tetrahedrally co-ordinated Si lattice. The short-range order of the 1<sup>st</sup> Si co-ordination shell and longer-range-order of the 2<sup>nd</sup> Si co-ordination shell are indicative of the presence of crystalline Si. This is exactly what one would hope to see as the electrodes themselves are grown as crystalline grains of Si (again see Chapter 3)

## 8.4 Discussion

In this chapter it has been shown that the structure in the  $Q(E)$  of an x-ray CCD at the silicon K absorption edge depends critically on the chemical nature of the surface layers of the CCD. The interpretation of this structure, known as x-ray absorption fine structure or XAFS, is described. The analysis of the XAFS has led to the possibility of measuring detailed structural parameters associated with the CCD. Two separate studies of fine structure in the  $Q(E)$  have been made, the first using XANES and the second using EXAFS.

It has been shown that x-ray absorption near edge structure, or XANES, which extends up to ~45 eV from the Si K threshold in the CCD, can be used to investigate the thickness and linear extent of the regions in the inactive layers. The detailed shape of the edge has been modelled in order to derive values for the electrodes and passivation layers and it has been shown that these are more accurate than the values obtained from process control. The errors on the values obtained using the XANES analysis are ~±8% whereas process control inaccuracies can be as high as ±20%.

In this chapter it has also been shown for the first time that the EXAFS function,  $\chi(E)$ , can be extracted from high resolution, synchrotron measurements of the  $Q(E)$  of a Si CCD. The EXAFS signal has been used to analyse the chemical structures in the inactive layers of the CCD. The use of the EXAFS analysis package has enabled detailed atomic parameters to be extracted. The parameters obtained are in close agreement with the theoretical values. Because of the relatively poor quality of the data a number of alternative structural models could conceivably fit the data. However, whilst different models were fitted to the data it was found that the best fit model, shown in Table 8.2, is very representative of the structures expected in a silicon CCD and the fitted parameters are in very close agreement with theory. In particular the presence of both Si and SiO<sub>2</sub> have been confirmed by the accurate measurements of bond distances and chemical type. The lack of any higher co-ordination other than a single shell at ~1.5 Å for SiO<sub>2</sub> clearly demonstrates that there is only amorphous silicon dioxide (SiO<sub>2</sub>-a) present in the dead layers of the

CCD. The presence of two co-ordination shells at 2.3Å and 3.7Å with a best-fit type of Si confirms that Si is present in the dead-layers as crystalline silicon (Si-c).

The work in this chapter describes in detail the use of XAFS as a non-destructive CCD analysis tool. The use of these measurements for this purpose is a novel and exciting application. They provide the ability to examine chemical structures at the atomic level from a relatively simple measurement carried out at using a monochromatic source of x-rays. There is therefore a potential application of this work in the field of non-destructive examinations of detectors. Also, as an analysis tool in the semiconductor industry these measurements could be used as a quality control tool, as they provide non-destructive investigations that are sensitive to low levels of concentration. The accuracy of the information from the XANES analysis is higher than that obtained from process control and less destructive than that obtained by the more traditional technique of Scanning Electron Microscopy (SEM).

An EXAFS analysis of the oxygen K edge could provide an independent analysis tool for SiO<sub>2</sub>. The data used so far in this analysis does fall short of the standard usually used for EXAFS analysis. This is an inherent problem due to the necessity of low photon count rates in a CCD combined with lack of experimental time, and could only be improved by integrating for longer to obtain statistically better data. This would enable other structural parameters, such as co-ordination numbers and perhaps even relative amounts of materials, to be obtained with more accuracy. However this work has shown that even with limited quality of data EXAFS is a valid structural determination tool for CCDs.

This work has also enabled a more complex model of CCD response around absorption edges to be developed. This in turn will lead to an improved interpretation of cosmic source spectra recorded with silicon CCDs.

## Conclusions and Future Work

### 9.1 Conclusions

The work in this thesis has been concerned with the development of CCDs for use as x-ray astronomical detectors on JET-X. This involved particularly the extensive experimental investigation of x-ray absorption fine structure (XAFS) in CCDs and the effect of XAFS on CCD data.

In the final chapter, the interpretation of fine structure in the quantum efficiency in terms of EXAFS (Extended X-ray Absorption Fine Structure) and XANES (X-ray Absorption Near Edge Structure) was described. It was found that fine structures in the CCD quantum efficiency could be accounted for by the variation in the transmission through its surface layers. Absorption fine structures in the quantum efficiency were analysed to obtain both the thickness and the chemical composition of the inert structures on the surface of the CCD. Detailed models were fitted to the quantum efficiency using new absorption coefficients [Owens, 1994]. The quality of the fitting procedure was such that the thicknesses of the various sections of the surface layers and the amount of material present were obtained with greater accuracy ( $\pm 8\%$ ) than could be predicted by the manufacturer ( $\pm 20\%$ ). Indeed, the fitting procedure showed that the P3 electrode was covered by an unexpectedly thick oxide covering which, at  $0.145 \pm 0.020 \mu\text{m}$ , was a factor 14 greater than the thickness predicted for the final etch ( $< 0.01 \mu\text{m}$ ). Subsequent SEM analysis of the CCD by the manufacturer confirmed that the CCD did indeed have an oxide covering of  $0.1 \pm 0.02 \mu\text{m}$  on the P3 electrode.

A more detailed analysis of the quantum efficiency variations of the CCD in terms of the EXAFS caused by the Si and  $\text{SiO}_2$ , in the surface layers of the CCD, was then conducted. The absorption in these layers was deconvolved from the CCD quantum efficiency and analysed using Daresbury's suite of EXAFS analysis software [Morrel, 1986]. It was found that this procedure could elicit detailed structural information on the chemicals found in the surface layers. In particular the average bond lengths between Si-Si and Si-O were estimated to be  $2.3 \pm 0.2 \text{ \AA}$  and  $1.5 \pm 0.2 \text{ \AA}$  respectively. Further evidence of a second co-ordination shell of Si-Si bonds was discovered to be at a distance of  $3.7 \pm 0.3 \text{ \AA}$ , while no such evidence was found for Si-O. These bond distances were found to agree with published values. The information showed that both Si and  $\text{SiO}_2$  are present on the surface of the CCD, the Si in crystalline form and the  $\text{SiO}_2$  in a less structured amorphous form.

These conclusions were found to be in agreement with the expected nature of the CCD surface layers.

As well as showing that XAFS can provide a useful method for analysing CCDs, this thesis has shown that by discovering the effects of XAFS on the instrument response and thereby taking the effects into account, the scientific quality of astronomical data can be improved. This was achieved by analysing the simulated data from a representative JET-X instrument response. The all-up instrument response was created both with and without fine structures in the CCD, filter and mirror calibration files. Initially it was shown that XAFS at the Si K edge could be introduced into simulated data at the  $\sim 4\%$  level. The simulation was then used to show that Si K edge XAFS would appear at the  $2\sigma$  level in typical cosmic spectra recorded with JET-X operating in timing mode (*i. e.* 18 mCrab) for typical integration times (*i. e.*  $1 \times 10^5$  s). This is an important result for JET-X and other future x-ray missions based on solid state detectors with reasonable spectral resolution.

The next step was to include measurements from the K absorption edges of nitrogen ( $\sim 400$  eV), oxygen ( $\sim 540$  eV), aluminium ( $\sim 1.56$  keV) and the gold M edges (2.2 - 3.5 keV) in the simulation. It was shown by simulation that the Au M edges appear in cosmic spectra for total recorded source counts as low as  $2 \times 10^4$  counts, *i. e.*, a  $10^5$  s observation of a 0.4 mCrab source. This will obviously be of serious concern for JET-X and other missions using grazing incidence optics. The simulation showed that there were instrumental artefacts associated with the other absorption edges as well. It was also shown that for observations of  $> 5 \times 10^4$  counts, the fitting of models to data could be hampered by instrumental artefacts.

All of the work in this thesis has come about because of the tight specifications placed on the calibration of the JET-X x-ray telescope (CCD resolution and efficiency, filter efficiency and mirror response all to a limiting precision of better than 2% and an overall telescope precision of better than 3%). The calibration program at the SRS, carried out over the period March 1994 to January 1996, was initially prompted by the realisation that gain changes, *i. e.*, changes in the value of  $F$ , the Fano factor, and  $\omega$ , the energy required to generate an electron/hole pair and electronics drift, could affect the measured energy resolution of the CCD. During the first calibration run, XAFS were seen in the response of a CCD for the very first time and it was found that EXAFS effects on the JET-X CCD quantum efficiency, which could be as high as  $\pm 5\%$ , were more significant than changes in  $\omega$  or  $F$ . This result showed that the detailed response of the CCD around absorption is more complicated than predicted by conventional modelling based on atomic absorption coefficients [*e. g.* Saloman, 1988].

The data recorded during this period has had a significant impact on both JET-X calibration programme [JET-X(94)UL-230] and wider experimental investigations of these effects [Fraser, 1994; Owens, 1996a]. The data has been used to investigate XAFS [Keay,

1995; Owens, 1996b],  $F$  [Owens, 1997],  $\omega$  [Owens, 1996a; Fraser, 1994] and escape peak ratios in Si CCDs [McCarthy, 1997]. The low energy calibration run in January 1995 allowed the new, open electrode CCD developed for the EPIC on XMM to be tested for the first time along with a JET-X CCD. Detailed fine structure was seen in the response of both devices, including EXAFS, XANES and strong “white lines”, particularly at the O K edge ( $\sim 550$  eV). The higher quantum efficiency of the open electrode device compared to the JET-X CCD was seen. Also measured was a strong pre-edge ( $\sim 540$  eV) dip in the quantum efficiency of the open electrode device. This was deduced to be caused by the build up of contaminants on the front surface of the CCD whilst it was being cooled in a partial vacuum of likely in-orbit contaminants ( $H_2O$  and hydrocarbons).

The extended energy range of the test conducted in January 1996 allowed phosphorus to be measured, as an absorption feature, in the CCD response. The source of this feature is likely to be the phosphorus used in the doping of the electrodes and the phosphorus acquired by the VAPOX layer in the final stages of processing. However, some phosphorus may have been present on the beam line grating and it is therefore difficult to be certain. The data at the Si K edge was used further for the detailed analysis of EXAFS in Chapter 8.

As part of this PhD programme it also became necessary to understand XAFS in terms of detector performance. The information gathered during the programme is reviewed in Chapter 5. A survey of the history of absorption fine structure was made along with a study of EXAFS, XANES and “white lines” as applied to silicon CCDs, which contain mainly Si and  $SiO_2$ . In order to understand EXAFS more fully a heuristic method for deriving the EXAFS function,  $\chi(E)$ , was developed and this is seen in Section 5.7. This work led directly to the investigation of CCD quantum efficiency variations which culminated in the chemical analysis of the CCD seen in Chapter 8.

## 9.2 Future work

CCDs will continue to be used on x-ray missions in the next generation of x-ray telescopes. Developments that will be necessary for their continued success may be separated into 5 major areas: i) quantum efficiency improvements, ii) lower noise, iii) larger areas, iv) radiation hardening and v) smaller pixels. Fabricating devices on high resistivity silicon improves high energy quantum efficiency. The increased depletion depth thereby achieved (40 - 70  $\mu m$ ) increases the quantum efficiency to 25 - 40% at 10 keV. Low energy quantum efficiency is improved by the use of thinned or open electrodes, or by using rear side illumination of the CCD. At Leicester work will concentrate on improving existing thinned/open electrodes and investigating alternative techniques. Lower noise in CCDs will improve the low energy resolution. A reduction to 1 electron (rms) from current values of  $\sim 4$  electrons (rms) would improve the resolution to  $\sim 30$  eV (10%) at 300 eV

compared to  $\sim 50$  eV (17%) obtained in present devices [Holland, 1997]. Low noise work at Leicester will concentrate on methods of reducing output node capacitance. It will also examine the use of floating gate amplifiers, where the charge packet is non-destructively sampled  $n$  times, reducing noise by a factor  $n^{1/2}$  [Holland, 1997]. Large area CCDs will be needed to cover the large focal plane of the next generation of x-ray observatories. To this end, wafer scale CCDs have been recently produced on both 4" and 6" wafers [Meidinger, 1996; Kreider, 1995]. Another main area of concern in the future will be the degradation of charge transfer efficiency (CTE) by radiation damage. Investigations in this area will focus on i) defect engineering, where benign traps are introduced to offset the potential effects of harmful traps and ii) field profiling combined with rapid clocking, where charge packets are held away from trapping sites by accurate field profiles and clocked before they have time to be trapped [Holland, 1997]. An investigation of the use of small pixel CCDs as polarimeters is currently being carried out by a colleague as part of a PhD programme [Hill, 1997]. Pixels as small as  $3 \times 6 \mu\text{m}$  have been tested and modelled, and CCDs with  $2.5 \mu\text{m}$  pixels will soon be available [Hill, 1997]. If  $3 \times 6 \mu\text{m}$  pixel CCDs can be combined with the type of mirrors currently planned for missions such as XMM, then polarimetry at 10 keV to the 5% level down to 5 mCrab in  $10^5$  s should be possible [Holland, 1997].

The work in Chapter 7 has shown that XAFS is an important physical process in CCDs that has proved to be significant for JET-X and all current and future x-ray missions. In order that the solid state detectors on these missions do not compromise their own capabilities they should be calibrated to at least 1% in efficiency, especially around the absorption edges of the elements that the CCD is constructed from. This will be particularly important as astronomers begin to investigate XAFS from cosmic sources [*e. g.* Woo, 1995]. This is because they will need to be confident that they can deconvolve the detector response accurately enough to leave only the XAFS due to the source.

This work has also shown that XAFS in the CCD quantum efficiency provides information that can be used as a method of non-destructive analysis of CCD electrode and inert layer thickness. As it is inherently non-destructive, this potential tool would have significant advantages over invasive techniques, such as Scanning Electron Microscopy (SEM), whilst providing details of the surface composition to a higher degree of accuracy than process tolerances. As was seen in the discovery of the much larger oxide covering of the P3 electrode, XAFS will prove an essential tool for quality control of CCDs, especially as the technology moves on to more advanced electrode structures. This will provide a major benefit in large scale device programmes where XAFS could be used to inspect sample devices for anomalies and thereby allow the manufacturer to correct costly mistakes at an early stage in production.

## Bibliography

### Chapter 1

- P. Gorenstein & M. Zombeck, Proc. IAU Coll. **115** (1990) Preface
- E. G. Chowanietz, D. H. Lumb and A. Wells, Proc SPIE **597** (1986) 381
- M. C. Weisskopf, Astrophys. Lett. Commun. **26** (1987) 1
- A. Wells, *et. al.*, Proc IAU Coll. **115** (1990) 318
- G. F. Bignami, *et. al.*, Proc. SPIE **1344** (1990) 144
- H. Inoue, Proc ISAS Sym. on Astrophys. (1992) 149
- W. S. Boyle & G. E. Smith, *The Bell System Technical journal*, Vol. 49 **4** (1970) 593
- I. S. McLean, *Electronic and Computer-Aided Astronomy; from eyes to electric sensors*,  
John Wiley & Sons (1994)
- P. S. Heyes, P. J. Pool and R. Holtom, Proc SPIE 1234 (1997) TBC
- C. M. Castelli, The soft x-ray performance of CCD detectors, Ph. D. thesis, University of  
Leicester (1990)
- E. G. Chowanietz, Advances in CCDs for x-ray imaging and spectroscopy, Ph. D. thesis,  
University of Leicester (1986)
- H. Schnopper, Proc. IAU Coll. **123** (1990) 119
- W. C. Friedhorsky, C. E. Moss, E. E. Fenimore, R. L. Kelley, S. S. Holt, Proc. SPIE **1159**  
(1989) 177
- A. M. Cruise, R. Holdaway, J. W. Curtis, Journ of the Brit. Interplanet. Soc. **43** (1990) 139
- S. I. Babichenko *et. al.*, Cosmic Res. **28** (1990) 587 (translated **28(4)** (1990) 503)
- R. Sunyaev *et. al.*, Adv. Space Res. **10(2)** (1990) 41
- J. Roques, J. Paul, P. Mandrou and F. Lebrun, Adv. Space Res. **10(2)** (1990) 223
- A. Owens, M. Denby, M. R. Sims, O. Terekhov and A. Wells, JET-X(92) UL-146 WP:2220  
(1992)

D. H. Lumb, X-ray imaging and spectroscopy with CCDs, Ph. D thesis, University of Leicester (1983)

A. D. Holland, Radiation effects in CCD x-ray detectors, Ph. D. thesis, University of Leicester (1990)

## Chapter 2

R. Giacconi, H. Gursky, F. Paolini, B. Rossi, Phys. Rev. Lett. **9** (1962) 439

H. V. D. Bradt, T. Ohashi, K. A. Pounds, Ann. Rev. Astron. Astrophys. **30** (1992) 391

K. A. Pounds, Proc. American Philos. Soc. **141** (1997) 67

J. C. Raymond, Proc. IAU Coll. **115** (1990) 1

F. Haberl, T. R. Kallman and N. E. White, Proc. IAU Coll. **115** (1990) 201

J. L. Culhane, Proc. IAU Coll. **115** (1990) 281

H. E. Mason, Proc. IAU Coll. **115** (1990) 11

P. F. Winkler *et. al.*, Astrophys. Jour. Lett. **246** (1981) L27

A. H. Gabriel and H. E. Mason, in Appl. Atom. Coll. Phys. **1** (1982) 345

C. R. Canizares, Proc. IAU Coll. **115** (1990) 136

S. S. Holt, Proc. IAU Coll. **115** (1990) 346

G. W. Fraser, *Detectors in X-Ray Astronomy*, Cambridge University Press, New York (1989)

B. D. Ramsey, R. A. Austin, R. Decher, Space Sci. Rev. **69** (1994) 139

A. Wells, unpublished (1997)

J. L. Linsky, Proc. IAU Coll. **115** (1990) 94

R. Giacconi, *et. al.*, Astrophys Jour. **230** (1979) 540

R. M. Joyce, R. H. Becker, F. B. Birsa, S. S. Holt and M. P. Noordzy, IEEE Trans. on Nucl. Sci. **NS25**(1) (1978) 453

K. A. Weaver *et. al.*, Astrophys. Jour. Suppl. **96** (1995) 303

A. A. Wells, R. Willingale and D. Lumb, ESA workshop on a cosmic x-ray spectroscopy mission, **ESA SP-239** (1985) 299

Y. Tanaka, H. Inoue and S. S. Holt, Publ. Astron. Soc. Japan **46** (1994) L37

M. C. Weisskopf, Astrophys. Lett. Commun. **26** (1987) 1



- G. W. Fraser, J. E. Lees, J. F. Pearson, S. E. Pearce, P. R. Houghton, J. Page, Leicester University Internal Report for the period May 1993 to April 1995 (1996) 43
- M. Weisskopf, *Space Sci. Rev.* **47** (1988) 47
- A. Wells, *et. al.*, *Proc IAU Coll.* **115** (1990) 318
- G. F. Bignami *et. al.*, *Proc SPIE* **1344** (1990) 132
- A. Holland, *Nucl. Instr. and Meth.* **A377** (1996) 334
- H. Inoue, *The next generation of x-ray observatories: Workshop proceedings Leicester X-Ray Astronomy Group Special Report XRA97/02* (1997) 161
- J. E. Trümper, *The next generation of x-ray observatories: Workshop proceedings Leicester X-Ray Astronomy Group Special Report XRA97/02* (1997) 201
- M. J. L. Turner, G. G. C. Palumbo, J. A. M. Bleeker, G. Hasinger, A. Peacock, J. E. Trümper, *The next generation of x-ray observatories: Workshop proceedings Leicester X-Ray Astronomy Group Special Report XRA97/02* (1997) 165
- A. D. Holland, *The next generation of x-ray observatories: Workshop proceedings Leicester X-Ray Astronomy Group Special Report XRA97/02* (1997) 99
- J. E. Hill, A. D. Holland, C. M. Castelli, A. D. T. Short, M. J. L. Turner and D. J. Burt, to be published in *Proc. SPIE* **3314** (1997)

### Chapter 3

- A. D. Holland, *Radiation effects in CCD X-Ray Detectors*, Ph. D. thesis, University of Leicester (1990)
- C. M Castelli, *The Soft X-Ray performance of CCD Detectors*, Ph. D. thesis, University of Leicester (1991)
- G. Bertolini and A. Coche, *Semiconductor devices*, Elsevier-North Holland Amsterdam 1968
- U. Fano, *Phys Rev.* **72** (1947) 26
- A. Owens , JET-X(96) UL-300 WP:2220 (1996) and to appear in *Nucl. Instr and Meth.*
- A. S. Grove, *Physics and Technology of Semiconductor Devices*, Wiley (1967)
- S. M. Sze, *Physics of Semiconductor Devices*, Wiley (1981)

K. J. McCarthy, A. Owens, A. D. Holland and A. Wells, Nucl. Instr. and Meth. **A346**  
(1994) 353

## Chapter 4

E. B. Saloman, J. H. Hubble and J. H. Scofield, Atom. and Nucl. data tables **38** (1988) 1

G.W. Fraser, A.F. Abbey, A. Holland, K.J. McCarthy, A. Owens and A. Wells, Nucl. Instr.  
and Meth. **A350** (1994) 365

A. Owens, G. Fraser, A. Keay and K. McCarthy, to appear in Nucl. Instr. and Meth. (1997)

G. W. Fraser, A. Abbey, A. Holland, K. J. McCarthy, A. Owens and A. Wells, Nucl. Instr.  
and Meth. **A350** (1994) 365

A Wells and D. H. Lumb, Proc. SPIE v. **1159** (1989) 372

A. Wells, *et. al.*, Proc IAU Coll. **115** (1990) 318

A. D. Holland, to be published in Nucl Instr. and Meth. (1995)

A. D. Holland, M. J. L. Turner, D. J. Burt and P. J. Pool, Proc. SPIE **2006** (1993) 2

S. E. Pearce, *Synchrotron Calibration of Microchannel Plates for X-Ray Astronomy*, Ph. D.  
thesis, University of Leicester (1997) to be published

K.J. McCarthy, A. Owens, A. D. Holland and A. Wells, Nucl. Instr. and Meth. **A362**  
(1995) 538

A. D. Holland, *Radiation effects in CCD x-ray detectors*, Ph. D. thesis, University of  
Leicester (1990)

## Chapter 5

M. Krumrey, E. Tegeler and G. Ulm, Rev. Sci. Instr. **60** (1989) 2287

T. Cho, N. Yamaguchi, T. Kondoh, M. Hirata, S. Miyoshi, S. Aoki, H. Maezawa and M.  
Nomura, Rev. Sci. Instr. **59** (1988) 2453

R. P. Kraft, J. A. Nousek, D. H. Lumb, D. N. Burrows, M. A. Skinner and G. P. Garmire,  
Nucl. Instr and Meth. **A366** (1995) 192

G.W. Fraser, A.F. Abbey, A. Holland, K.J. McCarthy, A. Owens and A. Wells, Nucl. Instr.  
and Meth. **A350** (1994) 365

- H. A. Bethe and E. E. Salpeter, *Quantum Mechanics of two electron systems*, Springer-Verlag (1957) 296
- S. J. Gurman, in *Synchrotron Radiation and biophysics*, Ellis Horwood (1990) Chapter 1
- H. Fricke, Phys. Rev. **16** (1920) 202
- G. Hertz, Z. Phys. **3** (1920) 19
- W. Kossel, Z. Phys. **1** (1920) 119; **2** (1920) 470
- R. de L. Kronig, Z. Phys. **70** (1931) 317
- R. de L. Kronig, Z. Phys. **75** (1932) 468
- L. V. Azaroff, Rev. Mod. Phys. **35** (1963) 1012
- L. V. Azaroff and D. M. Pease, in X-Ray Spectroscopy, McGraw-Hill (1974) Chapter 6
- H. Petersen, Z. Phys. **76** (1932) 768
- A. I. Kostarev, Zh. Eksp. Teor. Fiz. **11** (1941) 60; **19** (1949) 413
- M. Sawada, Rep. Sci. Work. Osaka University **7** (1959) 1; T. Shiraiwa, T. Ishimura, and M. Sawada, J. Phys. Soc. Japan **12** (1957) 788
- V. V. Shmidt, Bull. Acad. Sci. USSR Phys. Ser. **25** (1961) 998; **27** (1963) 392
- D. E. Sayers, E. A. Stern, and F. W. Lytle, Phys. Rev. Lett. **27** (1971) 1204
- D. E. Sayers and B. A. Bunker, in X-ray absorption-Principles, applications, techniques of EXAFS, SEXAFS, and XANES, Wiley-Interscience **92** (1988) 211
- A. Bianconi, Appl. Surf. Sci. **6** (1980) 392
- P. J. Durham, J. B. Pendry and C. H. Hodges, Comput. Phys. Commun. **25** (1982) 193
- P. J. Durham, in X-ray absorption-Principles, applications, techniques of EXAFS, SEXAFS, and XANES, Wiley-Interscience **92** (1988) 53
- E. A. Stern, in X-ray absorption-Principles, applications, techniques of EXAFS, SEXAFS, and XANES, Wiley-Interscience **92** (1988) 3

## Chapter 6

- A. Wells, *et. al.*, Proc. IAU Coll. **115** (1990) 318
- O. Citterio *et. al.*, Proc. SPIE **2279** (1994) 480
- A. Owens, S. C Bayliss, P. J. Durham, S. J. Gurman and G. W. Fraser, Astrophys. Jour. **468** (1996) 451

- D. E. Graessle *et. al.*, Proc SPIE **1742** (1992) 203
- A. Owens, S. C. Bayliss, G. W. Fraser, S. J. Gurman, D. Hutt, K. J. McCarthy and A. Wells,  
Proc. SPIE **2279** (1994) 325
- D. T. Cromer & D. Liberman, J. Chem. Phys. **53** (1970) 1891
- B. L. Henke *et al.*, Atomic Data and Nucl. Data Tables **27** (1982) 1
- E.B. Saloman, J.H. Hubble & J.H. Scofield, Atomic and Nuclear Data Tables **38** (1988) 1.
- O. Citterio *et. al.*, Proc. SPIE **2805** (1996) 56
- C.M. Castelli, to be published in Proc. SPIE (1997)
- A. D. Holland, *Radiation effects in CCD X-Ray Detectors*, Ph. D. thesis, University of  
Leicester (1990)
- K. J. McCarthy, A. Owens, A. D. Holland and A. Wells, Nucl. Instr. and Meth. **A346**  
(1994) 353
- A. Owens, presented at the JET-X/FDR (1995)
- M. Denby D. J. Allan and M. J. Ricketts, Astron Data Anal. Software and systems V, ASP  
conf. series **101** (1996) 236
- C.M. Castelli, to be published in Proc. SPIE (1997)
- R. Giacconi *et. al.*, Space. Sci. Rev. **9** (1969) 3
- P. Beckman and A. Spizzichino, *The Scattering of electromagnetic waves from rough sur-  
faces*, Oxford Pergamon (1963)

## Chapter 7

- K. A. Weaver, Ph. D. Thesis, University of Maryland (1983)
- S. Mitton, *The Crab Nebula*, Faber and Faber, London (1979) 87
- P. Lamb, G. Manzo, S. Re, G. Boella, G. Villa, R. Andersen, M. Sims and G. Clark,  
Astrophys. Space Sci. **136** (1987) 369
- K. Jahoda and D. McCammon, Nucl. Instr. and Meth. **A272** (1988) 800
- A. Keay, A. Owens, S. J. Gurman, G. W. Fraser, K. J. McCarthy and A. Wells, Nucl. Instr.  
and Meth. **B97** (1995), 316
- A. Owens, G. Fraser, A. Keay, A Wells, K. McCarthy, S. Hill, E. Hughes, A. Smith, V. Suller  
and M. Surman, X-Ray Spectrometry **25** (1996) 33

- G. W. Fraser, A. F. Abbey, A. Holland, K. J. McCarthy, A. Owens and A. Wells, Nucl. Instr. and Meth. **A350** (1994) 368
- A. Owens, M. Denby, A. Keay, A. Wells, R. L. Blake and D. E. Graessle, Astrophys. Jour. **476** (1997) 924
- R. S. Warwick, C. Done & D. A. Smith, Mon. Not. Royal Astron. Soc. **275(4)** 1995 1003
- R. Schafer *et al.*, *XSPEC, An X-ray Spectral Fitting Package* ESA TM-09 (1991)
- W. H. Press, S. A. Teukolsky, W. T. Vetterling and B. P. Flannery, *Numerical recipes; The art of scientific computing 2nd edition*, Cambridge University Press (1992) 678
- C. Eyles, presented at the JET-X/FDR (1995)
- G. F. Bignami *et. al.*, Proc SPIE **1344** (1990) 132
- H. Kraus, *The Next Generation of X-Ray Observatories: Workshop Proceedings Leicester X-Ray Astronomy Group XRA97/02* (1997) 75
- J. H. M. M. Schmitt, , Proc IAU Coll. **115** (1990) 110
- J. W. Woo, Astrophys. Jour. Lett. **447** (1995) L129

## Chapter 8

- K. J. McCarthy and A. A. Wells, Proc. 10th Symp. on Photoelectric Imaging Devices (1991) 17
- E.B. Saloman, J.H. Hubble & J.H. Scofield, Atomic and Nuclear Data Tables **38** (1988) 1
- S. J. Gurman, private comm. (1996)
- D. Li , G. M. Bancroft, M. Kasrai, M. E. Fleet, X. H. Feng, K. H. Tan and B. X. Yang, Solid State Commun., **87** (1993) 613
- A. Owens, S. C. Bayliss, G. W. Fraser and S. J. Gurman, JET-X(94) UL-241 WP:2220 (1994) and submitted to Nucl. Instr. and Meth.
- W. H. Press, S. A. Teukolsky, W. T. Vetterling and B. P. Flannery, in *Numerical recipes; The art of scientific computing*, 2nd edition, Cambridge University Press (1992) 678
- D.T. Cromer & D. Liberman, J. Chem. Phys., **53** (1970) 1891
- K.J. McCarthy, A. Owens, A. D. Holland and A. Wells, Nucl. Instr. and Meth. **A362** (1995) 538

- C. Morrel, J. T. M. Baines, J. C. Campbell, G. P. Diakun, B. R. Dobson, G. N. Greaves and S. S. Hasnaín, *EXAFS Users' Manual*, Daresbury Laboratory, Warrington WA4 4AD (1986)
- S. J. Gurman, in *Synchrotron Radiation and biophysics*, Ellis Horwood (1990) 9
- E. A. Stern, in *X-Ray absorption; Principles, Applications, Techniques of EXAFS, SEXAFS and XANES*, **92** in Chemical Analysis, Springer-Verlag (1988) 3
- F. Liebau, *Structural chemistry of silicates; Structure, bonding and classification*, Springer-Verlag (1985) 14
- J. S. Blakemore, *Solid-state physics - 2nd edition*, Cambridge University Press (1989) 24

## Chapter 9

- A. Owens, S. C. Bayliss, G. W. Fraser and S. J. Gurman, JET-X(94) UL-241 WP:2220 (1994) and submitted to Nucl. Instr. and Meth.
- C. Morrel, J. T. M. Baines, J. C. Campbell, G. P. Diakun, B. R. Dobson, G. N. Greaves and S. S. Hasnaín, *EXAFS Users' Manual*, Daresbury Laboratory, Warrington WA4 4AD (1986)
- E.B. Saloman, J.H. Hubble & J.H. Scofield, Atomic and Nuclear Data Tables **38** (1988) 1
- G.W. Fraser, A.F. Abbey, A. Holland, K.J. McCarthy, A. Owens and A. Wells, Nucl. Instr. and Meth. **A350** (1994) 365
- A. Owens, G. Fraser, A. F. Abbey, A. Holland, K. McCarthy, A. Keay and A. Wells, Nucl. Instr. and Meth. **A382** (1996a) 503
- A. Keay, A. Owens, S. J. Gurman, G. W. Fraser, K. J. McCarthy and A. Wells, Nucl. Instr. and Meth. **B97** (1995), 316
- A. Owens, G. Fraser, A. Keay, A Wells, K. McCarthy, S. Hill, E. Hughes, A. Smith, V. Suller and M. Surman, X-Ray Spectrometry **25** (1996b) 33
- A. Owens, G. Fraser, A. Keay and K. McCarthy, to appear in Nucl. Instr. and Meth. (1997)
- K. McCarthy, A. Owens and A. Keay, Nucl. Instr. and Meth. **A 384** (1997) 403
- A. D. Holland, to be published in Proc. SPIE **3314** (1997)
- N. Meidinger, *et. al.*, Proc. SPIE **2808** (1996) 492
- G. Kreider, *et. al.*, IEDM Technical Digest (1995) 155

J. E. Hill, A. D. Holland, C. M. Castelli, A. D. T. Short, M. J. L. Turner and D. J. Burt, to  
be published in Proc. SPIE **3314** (1997)

J. W. Woo, *Astrophys. Jour. Lett.* **447** (1995) L129